



Design of oxide based nanomaterials by ALD : from sensors to membrane application

Adib Abou Chaaya

► To cite this version:

Adib Abou Chaaya. Design of oxide based nanomaterials by ALD : from sensors to membrane application. Material chemistry. Université Montpellier II - Sciences et Techniques du Languedoc, 2014. English. NNT : 2014MON20117 . tel-01563358

HAL Id: tel-01563358

<https://theses.hal.science/tel-01563358>

Submitted on 17 Jul 2017

HAL is a multi-disciplinary open access archive for the deposit and dissemination of scientific research documents, whether they are published or not. The documents may come from teaching and research institutions in France or abroad, or from public or private research centers.

L'archive ouverte pluridisciplinaire **HAL**, est destinée au dépôt et à la diffusion de documents scientifiques de niveau recherche, publiés ou non, émanant des établissements d'enseignement et de recherche français ou étrangers, des laboratoires publics ou privés.

THÈSE

Pour obtenir le grade de
Docteur

Délivré par **UNIVERSITE MONTPELLIER 2**

Préparée au sein de l'école doctorale **ENSCM**
Et de l'unité de recherche **IEM**

Spécialité : **Chimie et Physicochimie des matériaux**

Présentée par **Adib Abou Chaaya**

TITRE DE LA THESE

**Conception de nanomatériaux à base d'oxyde par ALD: de
la détection aux membranes**

**Design of oxide based nanomaterials by ALD: from
sensors to membrane application**

Soutenue le 09/09/2014 devant le jury composé de

Prof Philippe Miele, IEM
Dr Mikhael Bechelany, IEM
Dr IVO Utke, EMPA (Thun, suisse)
Prof Julien Bachmann, FAU (Erlangen, Allemagne)
Dr Lionel Santinacci, CINAM (Marseille, France)

Directeur de thèse
Co-encadrant
Rapporteur
Rapporteur
Examineur

Acknowledgment

Summary

General introduction.....	3
Chapter1.Bibliography.....	7
Chapter2.Synthesis of ALD Zinc oxide thin film and zinc oxide/Aluminium oxide nanolaminates: studies of their structural and optical properties.....	48
Chapter 3: Atomic layer deposition on nanostructured materials for sensor applications.....	110
Chapter4.Mechanical properties of Al₂O₃/ZnO nanolaminates	158
Chapter5. ALD modified PET and PC membranes for different applications.....	193
General Conclusion.....	244
Annex-a-.....	249
Annex-b-.....	278
Annex-c-.....	285

General introduction

“Nano” is one of the most used word in the research community today. Nanomaterials by definition are materials having at least one dimension lower than 100 nm. One of the first scientific reports on nanostructured materials is the colloidal gold particles synthesized by Michael Faraday in 1857. By the early 1940’s, precipitated and fumed silica nanoparticles were being manufactured and sold in USA and Germany as substitutes for ultrafine carbon black for rubber reinforcements.

Nanostructure science and technology is a broad and interdisciplinary area of research and development that has been growing explosively worldwide in the past few years. It is already having a significant commercial impact, which will assuredly increase in the near future. Nanostructure materials are of interest due to their unique optical, magnetic, electrical, and other emerging properties. These properties allow great impacts in electronics, medicine, energy harvesting, sensors and other fields. Engineered nanomaterials are resources designed at the molecular (nanometer) level to take advantage of their small size and novel properties which are generally not seen in their conventional, bulk counterparts.

The two main reasons why materials at the nanoscale can have different properties are: (i) increased relative surface area and (ii) new quantum effects. Nanomaterials have a much greater surface area to volume ratio than their conventional forms, which can lead to greater chemical reactivity and affect their strength. Also at the nanoscale, quantum effects can become much more important in determining the materials properties and characteristics, leading to novel optical, electrical and magnetic behaviors. According to Siegel, nanostructured materials can be classified as:

- Zero dimensional (spheres and clusters)
- One dimensional (nanofibers, wires, rods, etc.)
- Two dimensional (films, plates, and networks)
- Three dimensional nanostructures (nanophase materials consisting of equiaxed nanometer sized grains).

Among nanomaterials, nanostructured semiconductors are known to show various non-linear optical properties. Semiconductor Q-particles also show quantum confinement effects which may lead to special properties that can be promising in solar cells, UV sensing and others applications. Nanostructured metal-oxide thin films for instance are receiving a growing

attention for the realization of gas sensors (NO_x , CO, CO_2 , CH_4 and aromatic hydrocarbons) with enhanced sensitivity and selectivity.

Nanomaterials designing can be basically described by two approaches:

- **The top down approach** refers to slicing or successive cutting of a bulk material to get nanosized particle.
- **The bottom up approach** refers to the approach to build a material up from the bottom: atom-by-atom, molecular-by molecular or cluster-by-cluster.

Using these 2 approaches, many different methods have been used to design nanostructures such as wet chemical synthesis of nanomaterials, mechanical grinding, heating and gas phase synthesis of nanomaterials (CVD, PVD, ALD, laser ablation and others). The gas-phase synthesis methods are of increasing interest because they allow controlling process parameters in order to be able to design the size, the shape and the chemical composition of the obtained nanostructures. Among the gas phase synthesis methods, the Atomic layer deposition (ALD) shows several advantages in the synthesis of nanostructured materials such as:

- A wide range of deposition materials: oxide, nitride, carbide and others
- A conformal coating ability on high aspect ratio templates
- A thickness control on the angstrom range
- A high chemical purity of the deposited films
- A high chemical composition control of the deposited layer

In this context, the aim of this PhD work is the synthesis of different nanostructured materials based on ALD oxide thin film (Al_2O_3 , ZnO and $\text{Al}_2\text{O}_3/\text{ZnO}$ nanolaminates) deposited on different types of substrates such as silicon substrate, glass, nanofibers, multipores and monopores membranes, PET and gold coated nickel dogbones. ALD deposition was performed on those substrates with changing the film thickness (number of cycles), the deposition temperature, and the film composition (doping, multilayers etc.). After the ALD deposition chemical, structural, optical, electrical and mechanical characterization were performed on the ALD deposited layer in order to study the influence of the deposition parameters on the thin film properties.

The deposited and characterized ALD films were investigated on different fields:

- Optical properties for solar cell applications (Chapter 2)
- UV detection (Chapter 3)
- Protective coating and gas barrier (chapter 4)
- Ionic transport, water desalination, Mass spectrometry, DNA sequencing and Gas purification (chapter 5)

The atomic layer deposition technique combined with nanostructured templates show several advantages on several application fields that will be reported on this thesis. The structural and properties evolution of the ALD thin film with the deposition parameter evolution led to a doped ZnO layer and Al₂O₃/ZnO multilayer with tunable optical, electrical and mechanical properties that can be interesting for different applications such as solar cell and UV detection. The conformal coating on high aspect ratio template with the angstrom range thickness control offered by the atomic layer deposition technique meted our target on nanopores diameter tuning for different applications on the nanometeric range such as gas purification. Moreover the compatibility of the deposited materials with some biological function led to a combination between nanostructure materials and biological function that shows promising results for different applications such as ionic transport, water desalination, mass spectrometry and DNA sequencing.

Chapter 1. Bibliography

Bibliography

1.Introduction.....	10
2.Thin film preparation methods.....	11
2.1.Liquid phase deposition.....	11
2.1.1.Spin-coating.....	11
2.1.2.Dip-coating.....	11
2.1.3.Electrodeposition.....	12
2.1.4.Electroless deposition.....	12
2.2.Physical vapor deposition.....	12
2.2.1.Evaporation.....	13
2.2.2.Laser ablation.....	13
2.2.3.Sputtering.....	13
2.3.Chemical vapor deposition (CVD).....	14
3.Atomic Layer Deposition (ALD).....	15
3.1.ALD setup.....	16
3.2.ALD of Al_2O_3 as typical ALD model.....	17
3.3.ALD deposited materials.....	17
3.4.ALD Growth characteristics.....	19
3.5.ALD precursors.....	20
3.6.Parametric study of ALD deposition.....	23
3.6.1.Parametric study of ALD window.....	23
3.6.2.Parametric study of ALD deposition setup.....	24
3.7.The growth per cycle.....	24
3.8.ALD reactor.....	26
4.ALD nanostructuring and applications.....	28
4.1.ALD on high aspect ratio structures.....	29
4.2.Nanolaminates structures by Atomic layer deposition.....	29
5.ALD for energy application.....	30
5.1.ALD for solar cell applications.....	31
5.2.ALD for catalysis applications.....	32
5.3.ALD for photocatalysis applications.....	32
5.4.ALD for Batteries.....	33

5.5.ALD for thermoelectric materials application.....	34
6.ALD for sensor application	34
7.ALD for membrane applications.....	35
8.General conclusion.....	37
9.Thesis objectives.....	38

1. Introduction

Device miniaturization, enhancement of device efficiency and low cost fabrication present the largest interest of the innovation research. Nanotechnologies are the new technology brand that deal with small size structures materials (sub-nanometer to several hundred nanometers). The concept of nanotechnology is attributed to the Nobel Prize winner in 1959 Richard Feynman. However the first scientific report on a nanomaterial elaboration is the colloidal gold particles synthesized by Michael Faraday as early as 1857 [1]. The development of nanotechnologies has been enabled by the invention of two techniques: the Scanning Tunneling Microscopy and the Atomic Force Microscopy in 1986 [2]. Recent developments in the field of nanomaterials have resulted in exciting of new possibilities in numerous applications, such as energy application, pollution, electronic device and others. 0D, 1D and 2D nanomaterials presents particular properties versus the bulk materials due their unique structure in term of chemical composition and geometry. Optical, electrical and mechanical properties of those nanomaterials can be tuned at the nanometric scale. Nanostructure materials include nanoparticles, nanorods, nanowires and thin film have been widely investigated on the last 10 years due to their large application field. Many technologies have been used to fabricate nanostructures and nanomaterials based on two approaches:

- **The top down approach** refers to slicing or successive cutting of a bulk material to get nano sized particle.
- **The bottom up approach** refers to the approach to build a material up from the bottom: atom-by-atom, molecular-by molecular or cluster-by-cluster.

Among the different techniques used to fabricate nanostructures we can note [3]:

- Vapor phase growth: including laser reaction pyrolysis for nanoparticle synthesis, chemical vapor deposition of thin films, atomic layer deposition and so on.
- Liquid phase growth: including colloidal processing for the formation of nanoparticles and self-assembly of nanolayers, and the sol-gel method for the preparation of metallic nanoparticles
- Solid phase formation: including phase segregation to make metallic particles in glass matrix and two photon induced polymerization for the fabrication of three dimensional photonic crystals
- Hybrid growth: including vapor-liquid-solid (VLS) growth of nanowires

Among different kinds of nanomaterials, thin layers are a nanomaterial category widely used and investigated for different applications in electronic field, optical field, energy, environment and others. Different thin layer materials are largely used today due to their needs for the nanotechnologies evolution. In this chapter we will introduce different thin film deposition techniques and then we will focus on the Atomic Layer deposition which is the deposition technique investigated during this PhD thesis.

1. 2. Thin film preparation methods

Thin film deposition methods were largely investigated and used for laboratories study and industrial applications. Thin film depositions methods can be divided into two sections: a liquid phase deposition process and a gas phase deposition process.

2.1. Liquid phase deposition

2.1.1. Spin-coating

Spin coating is a deposition method used to deposit uniform thin films on flat substrates. A droplet of the coating liquid is applied on the center of the substrate. The substrate is then rotated at high speed in order to spread the coating material by centrifugal force. Alternatively the liquid solution may be applied while the substrate is spinning. The thickness, morphology and surface topography of the final film obtained from a particular material in a given solvent at a given concentration is highly reproducible. Rotational speed, spinning time, viscosity, volatility, diffusivity, molecular weight and concentration of the solutes are 7 parameters to investigate during the spin-coating deposition process[4].

2.1.2. Dip-coating

The dip coating process is a deposition technique based on the immersion of a substrate in the coating solution fixed it for a while inside the solution then pulls it up with a constant speed. The thin layer deposits itself on the substrate while it is pulled up. This setup can be repeated several times to increase the layer thickness. The immersion speed, resident time, solution viscosity, and solvent volatility are parameters to investigate during the dip-coating deposition process. The surface activity and morphology of the substrate influent the deposition process [5].

2.1.3. Electrodeposition

Electrodeposition process is a deposition technique based on an electrical field applied between a cathode and an anode immersed into a solution that contains a salt which incorporate in his molecule the desired element to be deposited. Only conductive element can be deposited using this technique. Metals, metal alloys and semiconductors materials can be deposited using the electrodeposition technique. The electrodeposition technique has been widely used for surface recovery to enhance electrical, mechanical and optical properties for different applications. Due to its unsophisticated setup, large production scale, highly reproducibility, and total surface recovery, this technique is largely used for industrial application [5].

2.1.4. Electroless deposition

Electroless plating is a non-galvanic plating method that involves several simultaneous reactions in an aqueous solution, which occur without the use of external electrical power. The most common electroless plating method is the electroless nickel plating, although silver, gold and copper [6].

Liquid phase deposition techniques are of such importance due to their large scale production ability with low fabrication coast and time. Those techniques are widely used for different industrial applications. Despite their advantages liquid phases techniques present several disadvantages in term of conformal coating and thickness control in the nanometric range.

2.2. Physical vapor deposition

2.2.1. Evaporation

Evaporation under Vacuum is based on two basic processes: the evaporation of the source and the condensation of the evaporated material on the substrate. The deposition process is carried out at low pressure (10^{-3} - 10^{-10} Torr). Heating the source is performed by

passing an electric current or by an electron gun. This deposition technique offer a non-conformal coating due to the one directional deposition process [3].

2.2.2. Laser ablation

Laser assisted deposition or laser ablation involves the vaporization of the material under the laser impact. The evaporated species are ejected perpendicular to the surface of the target and then deposited on the substrate. During deposition, the atmosphere is controlled by a dynamic pressure of gases (O_2 , O_3 , Ar, N_2 ...). Laser ablation shows a large ability in the deposition of complex thin film. The control of the vapor phase composition is one of the laser ablation advantage however the complex system design is a disadvantage [3].

2.2.3. Sputtering

Sputtering involves bombarding a target consisting of the desired material with ions of inert gas (generally Ar^+). Particles are detached from the target and form a vapor that is deposited on the substrate placed in the opposite side. The polarities of the target (cathode) and the wall (anode) are selected to accelerate ions from the anode to the target to create the vapor phase [3].

There are two kinds of sputtering techniques:

- DC sputtering: A DC voltage is applied between the target and the walls of the deposition chamber. It can then sputter conductive materials even weakly conductors, as well as metal alloys. However a dielectric material sputtering is not possible since the charges provided by the ions cannot flow through the insulating material of the target, which results in the creation of defects layer.
- RF sputtering: This method uses an electric field of very high frequency allows the flow of charges on the surface of insulating material so we can deposit all types of dielectric materials (oxide and nitride). We can sputter directly a dielectric target or a metallic one under reactive gas like oxygen or nitrogen.

The necessity of ultrahigh vacuum is the main disadvantage of the sputtering technique. However this method has different advantages; For instance, the deposition can be achieved at low temperature and the obtained material is not contaminated. Due to her directional deposition process, the sputtering technique cannot be used on high aspect ratio substrate.

2.3. Chemical vapor deposition (CVD)

Chemical Vapor Deposition (CVD) technique consists of growing a solid phase material from a gas phase material. The precursors are introduced simultaneously into the reactor; they react together on gas phase to give the final film. The secondary products of this reaction must be on the gas phases to be removed from the reactor. The CVD technique can be coupled with a plasma system as activation energy instead of thermal activation and it is called PECVD [3]. The CVD technique presents several advantages and disadvantages.

Advantages of CVD

- Complex Materials formulation can be deposited.
- The films exhibit good compliance against the PVD.
- Deposits can be selective in some cases (deposit on certain materials and not others).

Disadvantages of CVD

- The material obtained is sometimes contaminated by elements contains in the precursors (often carbon).
- The precursors react in the gas phase which can lead to the formation of parasitic deposits in the gas phase (homogeneous nucleation) and contamination by particles on the substrate.

Liquid phase deposition, physical vapor deposition and chemical vapor deposition are different thin film deposition techniques widely used for laboratory and industrial applications that present different advantages such as conformal coating thin film deposition ability in the micrometric range, low deposition temperature, and a non-contaminated film. Despite those advantages, the miniaturization process needs a super-deposition technique with nm and angstrom resolution having a 3D deposition ability with high chemical properties for different material types such as conductive materials, semiconductors and insulators which is difficult with the methods described above.

3. Atomic Layer Deposition (ALD)

Atomic Layer deposition (ALD) is a vapor deposition method of ultrathin layers. It was known for his debut under the name of ALE (Atomic Layer Epitaxy) [7]. Some sources give the origins of ALD to Professor Aleskovskii and his team in 1960 that realized the deposition of TiO_2 from TiCl_4 and H_2O , as well as deposits of GeO_2 from GeCl_4 and H_2O [8]. Atomic layer deposition is a deposition technique derivate from the CVD (Chemical Vapor Deposition) technique. It based on 2 self-limiting reactions absolutely separated in gas phases [9]. When 2 precursors A and B react on gas phases during the CVD deposition to produce a thin film on the surface of the substrate, the same precursors react separately in ALD with the substrate surface to produce a uniform coating. ALD deposition principle is based on the splitting of the deposition reaction in 2 separated self-limiting reactions (Figure 1) due to the deposition mechanism described in Figure 1. No other thin film technique can approach the conformity achieved by the ALD on high aspect ratio structures.

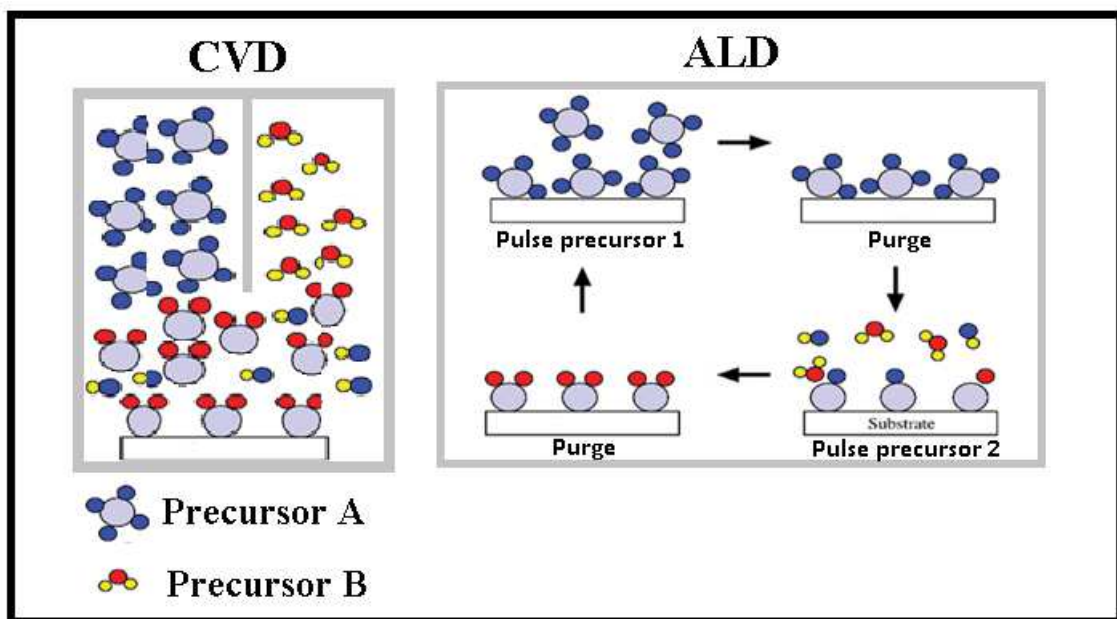


Figure1. Schematic representation of both CVD and ALD Process

Table 1. Difference between ALD and CVD

CVD	ALD
Reactants with low reactivity are preferred	The high reactivity of the reactants is preferred
The reactants react together on the surface and also on the gas phase	The reactants react separately with surface: surface limited reaction
The precursors can decompose at the deposition temperature	Precursors should not decompose at the temperature of deposition.
An uniform reactants flow are needed to obtain an uniform deposition	The deposition uniformity is ensured by a saturation mechanism
The thickness is controlled by the process time.	The thickness is controlled by the number of cycles.

3.1. ALD setup

As we described before the ALD is a deposition technique based on 2 self-limiting reactions absolutely separated in gas phases [9]. To be able to perform those two self-limiting reactions, 4 steps were required [10]:

Step 1: Pulse precursor 1 (introducing the first precursor to the deposition chamber to react with the substrate surface and form a chemisorbed and physisorbed layer)

Step 2: Purge to eliminate both of the physisorbed layer and the by-products of the reaction.

Step 3: Pulse precursor 2 (introducing the second precursor to react with the chemisorbed layer resulting by the reaction of the first precursor with the substrate. As for the step 1 the chemisorbed and physisorbed layers were formed).

Step 4: Purge to eliminate both of the physisorbed layer and the by-products of the reaction.

The Self-limiting reaction on the surface of the substrate make from the ALD a special technique for the deposition on high aspect ratio [9]. ALD films remain extremely smooth and conformal to the original substrate because the reaction are driven to completion during every reaction cycle [9]. Due to the necessity to decompose the reaction in 2 separate reactions to be able to limit the deposition on the surface of the substrate, 2 purge steps were needed after the exposition of the substrate to both precursors. This mechanism makes from ALD cycle a long

cycle with a deposition in the angstrom range, that's means a slow deposition rate. This disadvantage of ALD is an advantage for some applications that needs a high degree of thickness control in the angstroms range.

3.2. ALD of Al_2O_3 as typical ALD model

Atomic Layer Deposition of aluminum oxide (Al_2O_3) using Trimethylaluminum (TMA) and water as precursor has been developed as a model for the ALD system [9]. The surface reaction during the ALD deposition mechanism can be described by those two surface reactions:



Where the asterisks denote the surface species.

The overall reaction is:



This reaction has one of the highest ALD reaction enthalpies. The growth per cycle for one AB reaction is about 1.1-1.2 Å [11, 12]. This value has been obtained using various techniques such as ellipsometry and SEM.

3.3 ALD deposited materials

Different materials have been deposited using the ALD technique such as oxide, nitride, carbide, chloride and others. Table 2 adapted from the review published by M. Ritala and J. Niinisto, in Chemical Vapor Deposition (Royal Society of Chemistry, 2009) [13] presents the different materials deposited by ALD.

Table2. Different types of materials deposited by ALD adapted from the review published by M. Ritala and J. Niinisto[13]

Oxide dielectrics	Al ₂ O ₃ , TiO ₂ , ZrO ₂ , HfO ₂ , Ta ₂ O ₅ , Nb ₂ O ₅ , Sc ₂ O ₃ , Y ₂ O ₃ , MgO, B ₂ O ₃ , SiO ₂ , GeO ₂ , La ₂ O ₃ , CeO ₂ , PrO _x , Nd ₂ O ₃ , Sm ₂ O ₃ , EuO _x , Gd ₂ O ₃ , Dy ₂ O ₃ , Ho ₂ O ₃ , Er ₂ O ₃ , Tm ₂ O ₃ , Yb ₂ O ₃ , Lu ₂ O ₃ , SrTiO ₃ , BaTiO ₃ , PbTiO ₃ , PbZrO ₃ , Bi _x Ti _y O, Bi _x Si _y O, SrTa ₂ O ₆ , SrBi ₂ Ta ₂ O ₉ , YScO ₃ , LaAlO ₃ , NdAlO ₃ , GdScO ₃ , LaScO ₃ , LaLuO ₃ , LaYbO ₃ , Er ₃ Ga ₅ O ₁₃
Oxide conductors or semiconductors	In ₂ O ₃ , In ₂ O ₃ :Sn, In ₂ O ₃ :F, In ₂ O ₃ :Zr, SnO ₂ , SnO ₂ :Sb, Sb ₂ O ₃ , ZnO, ZnO:Al, ZnO:B, ZnO:Ga, RuO ₂ , RhO ₂ , IrO ₂ , Ga ₂ O ₃ , VO ₂ , V ₂ O ₅ , WO ₃ , W ₂ O ₃ , NiO, CuO _x , FeO _x , CrO _x , CoO _x , MnO _x
Other ternary oxides	LaCoO ₃ , LaNiO ₃ , LaMnO ₃ , La _{1-x} Ca _x MnO ₃
Nitride dielectrics or semiconductors	BN, AlN, GaN, InN, Si ₃ N ₄ , Ta ₃ N ₅ , Cu ₃ N, Zr ₃ N ₄ , Hf ₃ N ₄ , LaN, LuN
Metallic nitrides	TiN, Ti-Si-N, Ti-Al-N, TaN, NbN, MoN, WN _x , WN _x C _y , Co _x N, Sn _x N
II-VI semiconductors	ZnS, ZnSe, ZnTe, CaS, SrS, BaS, CdS, CdTe, MnTe, HgTe
II-VI based phosphors	ZnS:M (M=Mn,Tb,Tm); CaS:M (M=Eu, Ce, Tb, Pb); SrS:M(M=Ce,Tb, Pb)
III-V semiconductors	GaAs, AlAs, AlP, InP, GaP, InAs
Fluorides	CaF ₂ , SrF ₂ , MgF ₂ , LaF ₃ , ZnF ₂
Elements	Ru, Pt, Ir, Pd, Rh, Ag, Cu, Ni, Co, Fe, Mn, Ta, W, Mo, Ti, Al, Si, Ge
Other semiconductors	PbS, SnS, In ₂ S ₃ , Sb ₂ S ₃ , Cu _x S, CuGaS ₂ , WS ₂ , SiC, Ge ₂ Sb ₂ Te ₅
Others	La ₂ S ₃ , Y ₂ O ₂ S, TiC _x , TiS ₂ , TaC _x , WC _x , Ca ₃ (PO ₄) ₂ , CaCO ₃

3.4. ALD Growth characteristics

The saturation of the surface is determined by the exposure to the reactant (the flow and the time of exposure). These factors may affect the increase of the thickness for one ALD cycle. Under saturated conditions, all the chemical reactive groups at the surface are occupied which creates new species on the surface. Reactive sites change at each half-reaction to allow the growth of the film. The adsorbed material must not be desorbed during the purge phase.

Adsorption can be done through two mechanisms [14]:

- The physical adsorption is the low energy interaction between the substrate and the molecule $\Delta H_{\text{ads}} = 20\text{-}80 \text{ KJ/mol}$. However this reaction is reversible and it is not considered in the ALD growth. It is eliminated during the purge process between cycles.
- The chemical adsorption is the new chemical bonds formed between the molecule and the surface with high energy $\Delta H_{\text{ads}} = 300\text{-}400 \text{ KJ/mol}$. It is the non-reversible reactions that contribute to the ALD growth. The "chemisorption" is a single layer on each cycle.

The chemisorption process can be achieved through three mechanisms:

- By ligand exchange: When the precursor molecules arrive on the surface, they react with the functional groups (active sites). The molecule of the reagent interchanges one or more ligands with those active sites (Figure 2a).
- By Dissociation: The molecule is associated with the active sites on the surface (Figure 2b).
- By association: The reactant molecule forms bonds with the reactive site on the surface without decomposition (Figure 2c).

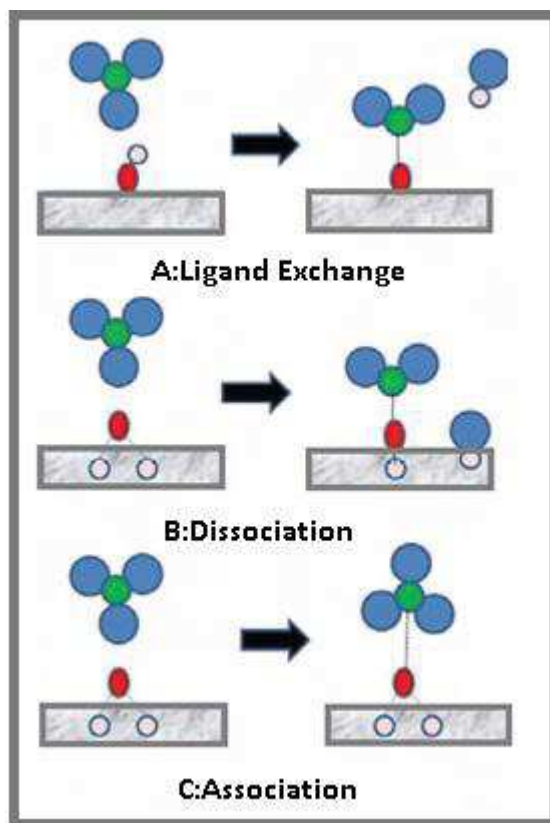


Figure2. Chemisorption process mechanisms: a) by ligand exchange, b) by dissociation, and c) by association.

3.5. ALD precursors

Due to the necessity of a surface limited reaction to assure a good ALD process the ALD precursors must have[15]:

- Sufficient volatility at the deposition temperature.
- No self-decomposition allowed at the deposition temperature.
- Precursors must react with the surface sites.
- Sufficient reactivity towards the other precursors, e.g. H_2O .
- No etching of the substrate or the growing film.
- Availability at a reasonable price.
- Safe handling and preferably non-toxicity.

ALD precursors can be divided into two main sections: ALD precursors for metals and ALD precursors for non-metal

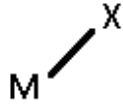
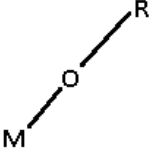
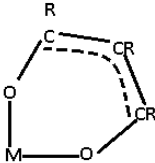
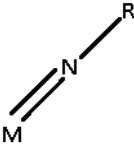
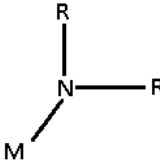

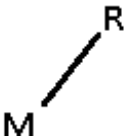

- Non-metals ALD precursors can be divided to different sections: oxygen based precursors, Nitrogen based precursors, carbon based precursors and fluorine based precursors. We have also Sulfur, Selenium, Tellurium, Phosphorus, Arsenic and Antimony based precursors. Table3 reports the different ALD precursor's types.[16]

Table3. Non-metals ALD precursors adapted from ALD Precursors and Reaction Mechanisms book [16].

Oxygen based precursors	H ₂ O, H ₂ O ₂ , CH ₃ OH, C ₂ H ₅ OH, O ₃ , O ₂ plasma
Nitrogen based precursors	NH ₃ , NH ₄ , N ₂ , NO
Carbon based precursors	Acetylene gas, Formic acid vapor
Fluorine based precursors	HF, WF ₆
Sulfur	Sn, H ₂ S
Selenium	H ₂ Se, (Et ₃ Si) ₂ Se
Tellurium	(Et ₃ Si) ₂ Te
Phosphorus	PH ₃
Arsenic	AsH ₃
Antimony	SbCl ₃ , tris(dimethylamido)antimony

- Metals ALD precursors can be divided to different categories (Table4) [16]:

Table4. Metals ALD precursors adapted from ALD Precursors and Reaction Mechanisms book [16].

Halides	
Alkoxides	
β -diketonate-complexes	
Alkylimides	
Alkylamides	
Amidates	
Alkyls	
Cyclopentadienyls	

3.6. Parametric study of ALD deposition

Different parameters should be studied before starting an ALD deposition. One of those most important parameters is the ALD windows. The precursor pulse time, exposure time and purge time are also important parameters to investigate.

3.6.1. Parametric study of ALD window

The ALD deposition mechanism can be performed on a temperature range called ALD Windows (Figure 3). We call a ALD window, a temperature interval inside of it we assure a constant growth per cycle and we avoid other undesirable phenomena such as condensation, decomposition, incomplete reaction, desorption or loss of surface species [9].

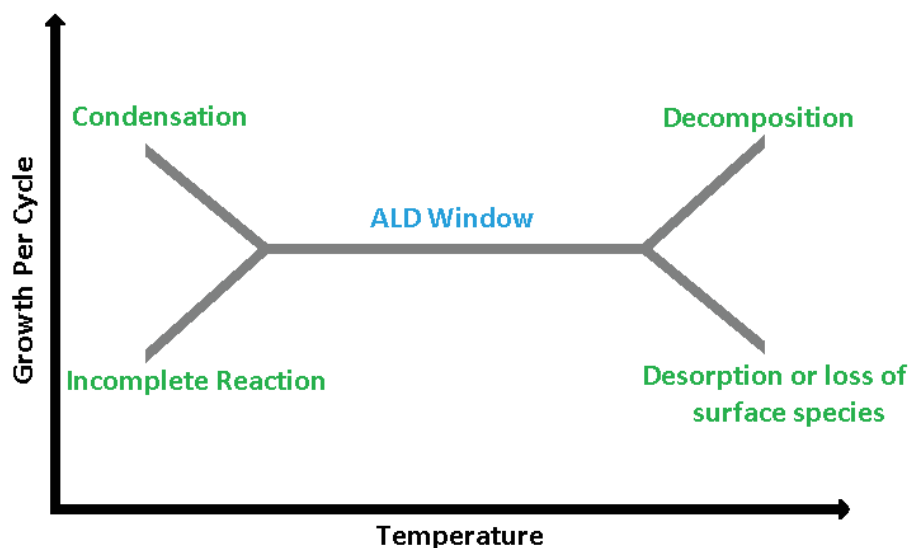


Figure3. ALD Windows

Actually low temperature privileges 2 undesirable phenomena: the first one is precursors or by-products condensation because of a thermal energy lack to desorb the reactants, than we are in a CVD process. In the same case, low temperature could lead to an incomplete reaction and then only a fraction of monolayer will be formed in an ALD cycle.

Same that for the low temperature, high temperature can privilege 2 other undesirable phenomena: the first one is the decomposition of the precursors that is not desirable in an

ALD process and the second one is the desorption of chemisorbed layer due to the crack on the chemical bonds under the high temperature effect.

We must note here that the ALD Window is not valid for all ALD systems because in some case, we have precursors decomposition on the minimum temperature required for the surface reaction. TiN using tetradimethylaminotitanium (TDMAT) and NH_3 can be one of those systems.

3.6.2. Parametric study of ALD deposition setup

To assure a 100% ALD growth film with no CVD, we should optimize a number of parameters:

- Pulse time: the pulse time should be optimized in order to assure the saturation of the surface with both precursors: that's means optimizes the pulse of precursors to assure a perfect saturation of the surface with no precursors waste.
- Exposure time: the exposure time should be controlled to assure an adequate exposure time to both precursors and allow the maximum of reaction with the surface.
- Purge time: it is necessary to assure that no by-product or no physisorbed phases stay in the reactor chamber or on the substrate surface.

3.7. The growth per cycle

During the ALD process the chemical composition of the surface changes due to the deposition of new materials. The first cycles occur on the original substrate, the following cycles will occur on two materials: the substrate and the ALD film, and after several cycles, deposition occurs only on the deposited material. Since the surface chemistry changes, the growth rate per cycle may evolve during deposition.

The evolution of the ALD growth based on number of cycles can be classified into four groups [9] as shown in Figure 4. In all cases, it is recognized that growth reaches a steady state where the growth rate is constant as a function of the number of cycles.

- Linear growth [17, 18]: The growth rate is constant from the first cycles. This regime may appear if the number of active sites remains unchanged throughout the deposition.

- Growth activated by the substrate [19, 20]: In this mode there is one transition state where the growth rate is higher in the first cycles and then it decreases after to reach a steady state. We can meet such mode if the number of active sites on the substrate is higher than the number of active sites on the deposited material.
- Growth inhibited by the substrate [21, 22]: In this mode, the growth rate is lower at the beginning of the growth, it means that the number of active sites is greater on the material deposited than the initial substrate.

Based on this classification, tow behavior are observed: In type II [23], the growth rate passes through a maximum before returning to the steady state. In type I [24] we do not have this maximum. It has been reported in the literature that the growth inhibited by the substrate (type II) is due to a preliminary islets growth [25].

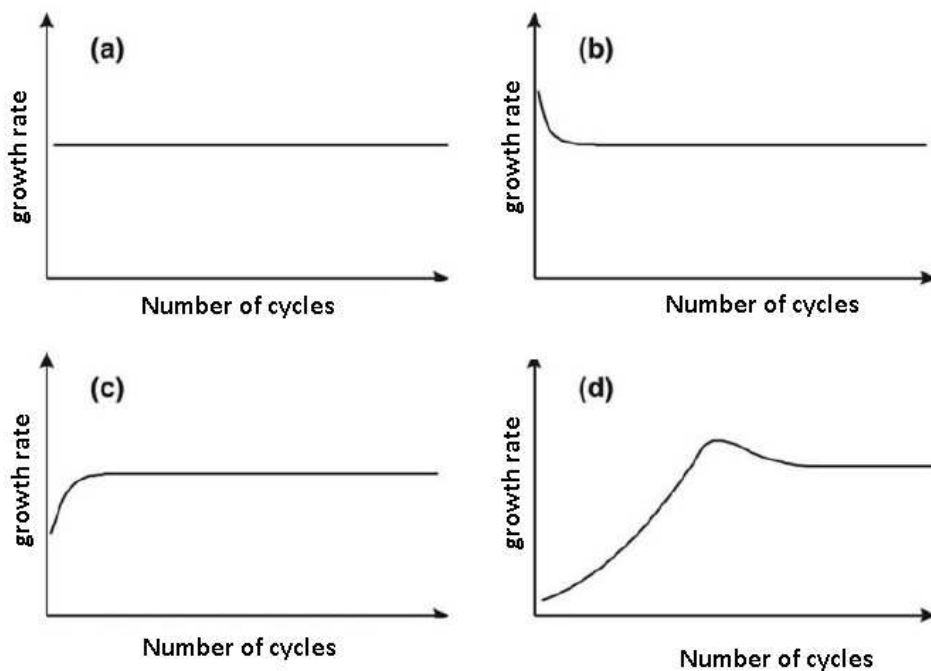


Figure4. Evolution of the growth rate depending on the number of cycles [9] a) Linear growth b) Growth activated by the substrate, c) Growth inhibited by the substrate (type I), and d) Growth inhibited by the substrate (type II)

3.8. ALD reactor

In 1977 and 1983, T. Suntola describes in his patents many ALD reactor designs [26] then he discussed different new versions of ALD reactors in his reviews [10, 27].

Those reactors can be divided to 2 categories:

- Viscous flow reactors
- Vacuum reactors

In the viscous flow reactors type, the reactants are exposed with a carrier gas flow, than a carrier gas has been used in the purge step. The optimum pressure for viscous flow reactors (with nitrogen as carrier gas) is around 1 Torr because this pressures value corresponds to a mean free path of N_2 about 50 μm . This small mean free path of N_2 indicates that N_2 gas is in a viscous flow at 1 Torr. The advantage of this type of reactors is their much shorter ALD cycles comparing with the second reactors types (without carrier gas).

In the second type, the reactant is exposed without using a carrier gas and sometimes with throttled pumping. In the next step the reactant is evacuated by completely opening the pump. The absence of the carrier gas leads to slow ALD cycles comparing with the first type.

Different types of reactors based on those 2 categories have been designed for industrial application. Figure 5 adapted from reference [28] shows those different reactors types. Both reactors are industrial type reactors; they can coat multiple samples in the same time (Figure 5-b). This type of reactors can improve the cost and the time. In-line spatial ALD reactor as designed by SoLayTec [28] (Figure 5c), in-line spatial ALD reactor as designed by Levitech (figure 5d), roll-to-roll ALD reactor as designed by Lotus Applied Technology [142] (Figure 5e), and roll-to-roll ALD reactor as designed by Beneq [29] (Figure 5f), are other industrial types of ALD reactors.

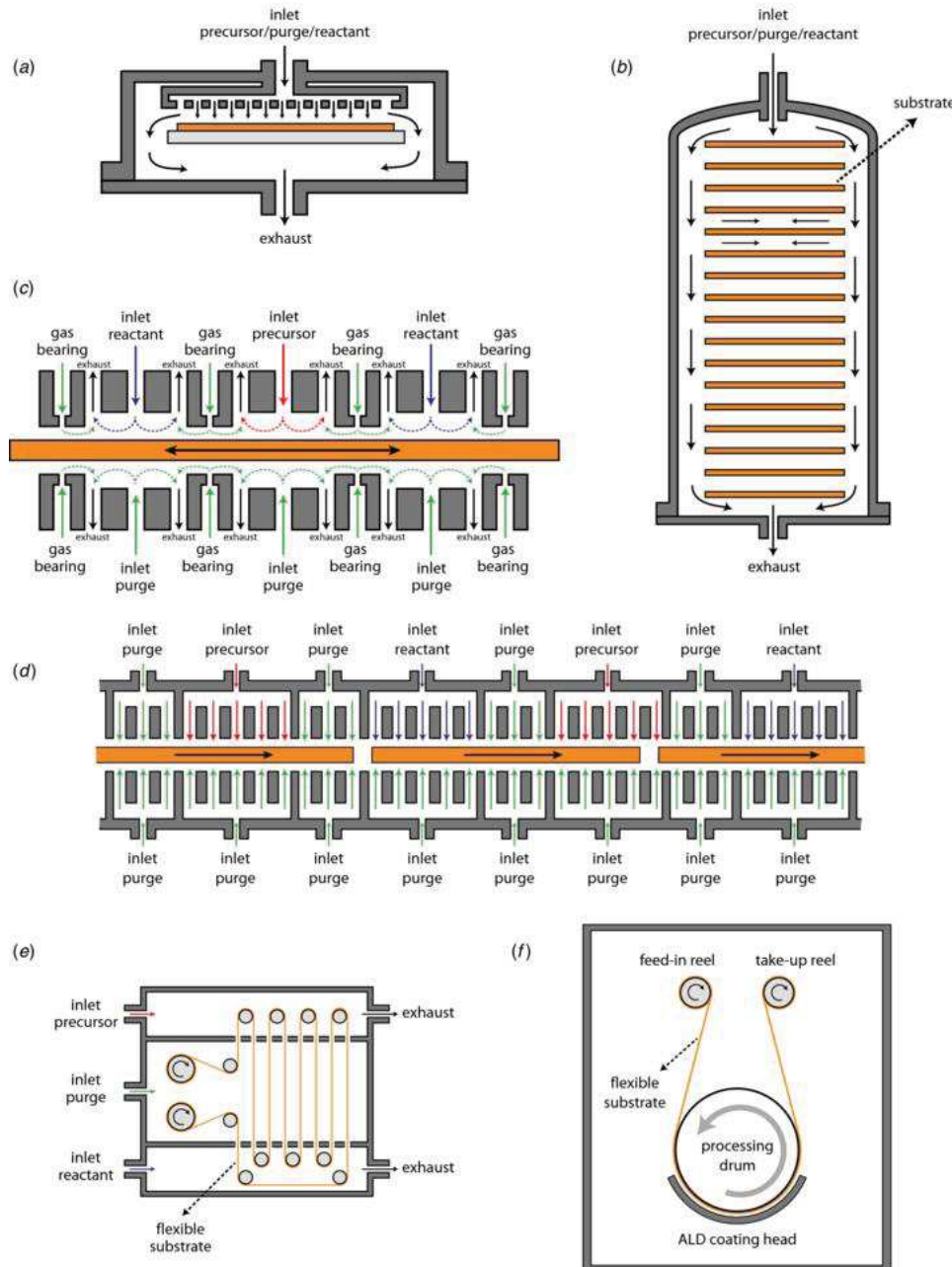


Figure 5. Schematic representations of various ALD reactor designs: (a) showerhead type single wafer ALD reactor; (b) batch ALD reactor [30]; (c) in-line spatial ALD reactor as designed by SoLayTec[31]; (d) in-line spatial ALD reactor as designed by Levitech [134];(e) roll-to-roll ALD reactor as designed by Lotus Applied Technology [142]; (f) roll-to-roll ALD reactor as designed by Beneq[29]: Adapted from reference [28].

After that we introduce the growth mechanism used in the ALD technique and the different deposition parameters to be optimised before to start the ALD deposition and the different types of ALD reactors, we will illustrate now a bibliographical study on the different applications of ALD.

4. ALD nanostructuring and applications

Thin film coating for high aspect ratio substrate for electronic industry has been one of the main motivations for the recent development of ALD. High permittivity gate oxide Al_2O_3 , ZrO_2 and HfO_2 have been developed by ALD for MOSFET applications. Three dimensional DRAM capacitor development with a new dielectrics gate with high conformal coating to be an alternative to SiO_2 with a permittivity value above 200 pushes the researcher for the elaboration of a new ternary and quaternary compounds using the ALD technique like SrTiO_3 [32] BaTiO_3 [33]. Low electron leakage dielectrics for magnetic read and write heads has almost developed by ALD[34]. ALD deposition was used also for copper diffusion barriers in backend interconnects[35]. A large number of metal oxides are used in ALD for different applications such as sensor [36, 37], solar cells[38, 39], fuel cells [40-44] photocatalytic[45-50], gas diffusion barriers [51-59], encapsulate organic light emitting diodes [60, 61], organic solar cells [62, 63], a dielectric gate for polymer-based transistors [64], to the Enhancement of the photoprotection and nanomechanical properties of polycarbonate[65]. Due to the ability to achieved low temperature deposition using the ALD technique, ALD has been used on polymers substrate to functionalize the polymer surface, to create inorganic/organic polymer composites [9] and to deposit gas diffusion barriers on polymers [9]. Low temperature ALD was also used on biological templates [66] such as tobacco mosaic virus (TMV) and ferritin [67].

Transition metal nitrides like TiN and TaN was also deposited by ALD [68, 69] and used as metallization barriers to avoid Cu diffusion into the surrounding insulators and the silicon substrate and to prevent Cu contamination due to the reverse diffusion from the insulators to Cu, both are also used as metal gates for MOSFET applications. TiN has been deposited from TiCl_4 and NH_3 at 400°C . However the HCl by-product of this reaction is a disadvantage [68]. Metal films by ALD are a big challenge due to the unsuccessful trials to use CVD precursors on the ALD Metal system. Despite that many metals have been deposited

by the ALD technique like amorphous tungsten from WF_6 and Si_2H_6 , Ru and Pt from organometallic precursors and Oxygen [70, 71].

4.1. ALD on high aspect ratio structures

As a typical prove on the ability of the ALD to do homogeneous film on high aspect ratio materials, anodic aluminum oxide with an aspect ratio of 1000 approximately reduced by different types of oxide using the ALD technique can improve the capacity of the ALD on high aspect ratio substrates [72-87]. ALD was also used in polycarbonate porous membrane to tune the pores size [88]. ALD on particles was achieved as well. ALD has been used to modify the surface chemistry of particles, to deposit protective and insulating coating on particles to prevent particles oxidation [89], to improve electrical conductivity [90], and to modify the optical [91] and mechanical properties [92]. A fluidized bed maintaining particles under agitation to allow the gas precursor to reach all the particles surface and to avoid particles agglomeration during the deposition has been used [93].

4.2. Nanolaminates structures by Atomic layer deposition

Nanolaminates materials are nanocomposites materials formed by alternating layers of different materials. Those nanolaminates often show physical, chemical and electrical properties which are not observed in the constituent layer materials alone. Due to her precise thickness and control ability, the ALD can be an important technique for such materials fabrications. Nanolaminates and alloys of different types of oxides with different ratio has been developed using the ALD technique. $\text{HfO}_2/\text{Ta}_2\text{O}_5$ nanolaminates was been used as low leakage dielectric film [94], $\text{Al}_2\text{O}_3/\text{Ta}_2\text{O}_5$ and $\text{Hf}_x\text{Al}_y\text{O}_z$ for dram capacitors application [95]. $\text{Al}_2\text{O}_3/\text{TiO}_2$ with layer thicknesses smaller than the wavelength of light have been used to tune the optical refractive index of the nanolaminate films from 2.4 (TiO_2) to 1.6 (Al_2O_3) [96]. Aluminium oxide/titanium oxide deposited on silicon wafer by ALD than characterized by TEM cross-section assure the ability of parallel nanolaminate deposition using the ALD technique [97]. $\text{ZnO}/\text{Al}_2\text{O}_3$ nanolaminates synthetized by ALD [98, 99] show a smooth surface compared to the monolayer of ZnO and this roughness decreases when the bilayers thicknesses decreases. This roughness change has been associated with a ZnO crystalline phases disappearing. Fundamental properties of ZnO can be tailored by doping. It is known that doping of ZnO with Al or/and Al_2O_3 modified its structural, electrical and optical

properties. Hafnium, Zirconium and Aluminium oxide nanolaminates has been prepared by ALD with different thicknesses and deposition temperature [100]. AFM measurement on hafnium oxide and zirconium oxide shows a decrease in the surface roughness when the deposition temperature decreases from 250°C to 150°C. To avoid this roughness increases when the deposition temperature rises, nanolaminates of crystalline/amorphous materials has been used to stop the nucleation process or the crystals growths of the crystalline phase when the thickness and the deposition temperature increases. ($\text{Al}_2\text{O}_3/\text{ZrO}_2/\text{Al}_2\text{O}_3$) nanolaminates have been elaborated by ALD [101] then characterized using medium-energy ion scattering spectroscopy, and x-ray photoelectron spectroscopy. ($\text{Al}_2\text{O}_3/\text{ZrO}_2/\text{Al}_2\text{O}_3$) shows a thermal stability under vacuum up to 1000°C plasma nitridation. After a Pt deposition and photolithography and etching metal–oxide–semiconductor MOS devices has been achieved and characterized by capacitance–voltage (C–V), and current density–voltage (J –V) measurements and shows excellent electrical properties.

Compatibility problem between copper and TiN and W_xN as diffusion barrier has been solved by a nanolaminate structure of $\text{W}_x\text{N}/\text{TiN}$ and $\text{WN}_x\text{C}_y/\text{TiN}$ elaborated by ALD [102]. Those nanolaminate structures show a strong adhesion and no pitting on the copper surface. $\text{W}/\text{Al}_2\text{O}_3$ nanolaminates have been deposited by ALD as temperature barrier [103]. This study shows a decrease on the thermal conductivity with increasing the interface density that can achieve 0.6 watts per meter per kelvin. Despite this advantage a thermal stability at high temperature has been noted. Nanolaminate of aluminum oxide/hafnium oxide elaborated by ALD than annealed at 700°C [104] show a greater dielectric constant against amorphous Al_2O_3 and monoclinic or tetragonal HfO_2 .

5. ALD for energy applications

The development of new materials for applications in energy field is currently an area of intensive research. Nanostructured materials appear highly promising in this field because of their new properties combined to the device miniaturization. On the nanostructured materials synthesis, the ALD technique meets the requirement of such fields in the reproducibility and the conformal coating. The thickness control of the ALD layers combined to the conformal coating opens a new fields of nanostructured synthesis using nanopatterning by area selective ALD [105-107], porous[49, 108-112] and nanostructured templates[81, 113-

118], novel nanostructured materials can be elaborated by ALD. Those nanostructured materials have been used in different energy applications fields such as solar cells [62, 119-123], catalysis [124-126], photocatalysis[80, 127-135] and gas and liquid purification [127, 136-138].

5.1. ALD for solar cell applications

Based on the photovoltaic effect, solar cell converts the energy of light directly into electricity. The conversion efficiency and the cost of a solar cell is the challenge of the day in the solar cell research field. Due to the conformal coating of the ALD and the large number of metal oxides deposited using this technique, ALD can be widely used in the fabrication of new photo-electrodes. ZnO nanotube photo-anodes have been synthesized using the ZnO ALD coating on AAO membranes for use in dye-sensitized solar cells (DSSCs)[139]. Compared to similar ZnO-based devices, ZnO nanotube cells show high photovoltage and fill factors (FF), in addition to power efficiencies up to 1.6%. Concentric nanotubes of conducting and semiconducting materials have been elaborated using ALD. AAO has been coated subsequently by indium oxide (ITO) and TiO_2 and used as photoelectrodes[140]. Higher current density has been detected due to the radial collection of electrons. Low density templates with high surface area have been coated by ZnO ALD then incorporated into DSSCs displayed. Good light harvesting efficiency and excellent power efficiencies compared to other ZnO based DSSCs [141]. ZnO has been also deposited on CdSe nanocrystal to improve electron transfer between quantum dots [142]. Nanocrystallite aggregates of ZnO have been coated by TiO_2 ALD [143]. Higher power conversion efficiency (PCE) of 6.3% and an open circuit voltage of 709 mV has been obtained compared to 5.2% for the ZnO-based solar cell. TiO_2 nanotube array have been coated by In_2S_3 ALD as a semiconductor sensitizer, a low quantum efficiency of $\sim 10\%$ in $\text{Co}^{2+}/\text{Co}^{3+}$ electrolyte have been reported due to recombination losses and charge injection/collection processes. SnO_2 doped Al_2O_3 with different ratio have been investigated using ALD in order to increase the electrical resistivity of SnO_2 that can be used as a hole-blocking layers in solar cells[144]. Quantum dots of PbS ALD have been fabricated during the ALD nucleation stage[145]. The photoluminescence measurements on the quantum dot/nanowires composites show a blue shift when the number of ALD cycles is decreased, suggesting a route to fabricate unique three-dimensional nanostructured devices such as solar cells. TiO_2 coating on ZnO nanoparticles has been carried using the ALD in order to increase the temperature annealing of ZnO from 350°C to 450°C to enhance the efficiency of DSCs without any change in the

structured of the ZnO nano-crystallites. A 30% enhancement in the efficiency of DSCs has been reported [146].

5.2 ALD for catalysis applications

The development of heterogeneous catalysis materials is an important research topic due to the large application sectors such as pollution, hydrogen production and others. Nanostructured materials are very promoting on this field due to their high surface area. Thin layer deposited by ALD has been used as catalysis materials or protective coating [109, 147-163]. ALD coating of AAO before loading it with VO_x showed higher specificity toward the oxidative dehydrogenation of cyclohexane[74]. Nanoparticles of Au/TiO_2 have been covered by SiO_2 using ALD which covered TiO_2 particles totally and partially the gold particles. Despite the partial recovery of gold nanoparticles which blocks some active catalytic sites $\text{SiO}_2/\text{Au/TiO}_2$ showed an improved sintering resistance, maintaining a comparable activity toward CO oxidation upon thermal treatment [164]. Porous gold has been stabilized by Al_2O_3 and TiO_2 . The ALD/porous gold showed a three-fold improvement of CO oxidation activity due to a higher thermal stability and to the gold oxide interaction [165]. Pt nanocatalysts deposited by ALD on porous carbon aerogel enhance the catalytic activity even with 2 Pt ALD cycles [166]. Supported Ru-Pt bimetallic NPs on Al_2O_3 nanoparticles have been elaborated by ALD. Due to the conformal coating and the thickness control, the ratio of Ru/Pt can be controlled by the number of cycles of each one. Ru-Pt bimetallic NPs supported on Al_2O_3 show a higher methanol conversion compared to the pure metallic particles [163].

5.3. ALD for photocatalysis applications

Today Global warming, depletion of fossil fuels and pollution pushed the development of several research field based on the renewable nonpolluting energy. Hydrogen is one of the most important energy vectors for the future because of its high energy density and environmental friendliness. Among the different generation methods of hydrogen, photocatalytic semiconductor-based water splitting methods using solar energy has attracted wide attention. Due to his importance, semiconductor-based water splitting methods take a large place in the today research. Different nanostructures for photocatalytic applications have been elaborated by ALD then characterized and tested. $\text{TiO}_2/\text{TiSi}_2$ core/shell nanostructures have been elaborated using the ALD and CVD technique [167]. An efficiency of 16.7% under monochromatic UV illumination has been observed. ALD WO_3 has been deposited on ITO or

on TiSi_2 as catalyst to enhance the hole transfer from the semiconductor to the solution [168]. A thin ALD coating of Al-doped zinc oxide and titanium oxide has been deposited on cuprous oxide to prevent photocathodic decomposition in water then Pt nanoparticles has been electrodeposited in order to activate the nanostructure [169]. ALD of TiO_2 transparent well-aligned nanotube arrays have been performed on Glass using free-Standing porous anodic alumina template than functionalized by Pd sputtering than tested in the Photo-degradation of aqueous methylene blue (MB) solution and solid stearic acid (SA). The obtained materials show a photodegradation efficiency of 76% after 4 h of UV irradiation [170].

5.4. ALD for Batteries

Portable power system sources are one of the most needed energy system for different types of applications. Batteries are an electrochemical energy sources with an efficiency that can be increased by improving the electrodes properties in term of electron and ion conductivity and surface area. Despite that ions battery are a high performance rechargeable-battery there is a serious demand for higher storage capacity and density, faster charging and discharging rates and improved cycling stability which pushes the research to develop new electrode materials. Solid electrolyte interface (SEI) layer of Al_2O_3 to suppress the undesirable side reactions has been deposited by ALD on LiCoO_2 nanoparticles or directly on the electrode delivers a high discharge capacity and currents (250% improvement in reversible capacity compared to the bare nanoparticles)[171]. 3D hollow nano-ribbons of TiO_2 have been synthesized by coating a peptide assembly with TiO_2 by ALD. The well-connected network and the hollow structure of Nanoribbons ensure the effective transport of electrons and Li ions[172]. Nanotubular metal–insulator–metal capacitor arrays for energy storage has been made using a successive ALD layers of metal (TiN), insulator (Al_2O_3) and metal (also TiN) into an AAO nanopore templates[173]. These highly regular arrays have a capacitance per unit planar area of 10 mF cm^{-2} for 1 mm thick AAO and 100 mF cm^{-2} for 10mm thick AAO. Those values are largely higher than other reported elsewhere for metal–insulator–metal capacitors in porous templates. Al_2O_3 ALD coating has been performed on MoO_3 nanoparticles in order to increase the stability and the capacity retention [174].

5.5. ALD for thermoelectric materials application

In a temperature gradient, thermoelectric materials convert the thermal energy to an electrical energy. Those types of materials can also work as cooling system. If we deliver an electrical current to a thermoelectric material, a temperature gradient will be established. Electrochemical ALD has been used to synthesize PbSe/PbTe super-lattices with 4.2 nm and 7 nm sequences corresponding to 10 PbSe ALD-cycles and 100 PbTe ALD-cycles. A $\text{PbSe}_{0.44}\text{Te}_{0.56}$ has been formed using those sequences[175]. Thermoelectric misfit-layered oxide, $[\text{Ca}_2\text{CoO}_3]_{0.62}[\text{CoO}_2]$ has been synthesized using the ALD technique with $\text{Ca}(\text{thd})_2$, $\text{Co}(\text{thd})_2$, and O_3 as precursors [176]. The synthesized film has been treated under oxygen at 550°C to crystallize it. Then the film was treated under N_2 to decrease the oxygen content which result on an enhancement on the Seebeck coefficient.

6. ALD for sensor application

Gas sensors, UV sensors, biological sensors as well as other sensing applications require high surface detection area in order to enhance the sensor properties such as response time, recovery time, and others. Due to their unique properties nanomaterial's shows an interesting feedback on different sensing applications such as optical sensors[177], gas sensors[178], UV sensors [179] and others. Due to their ability for high aspect ratio deposition on different templates structures, ALD can be a promising technique for sensors application. Ultrathin tin oxide films were deposited on SiO_2 nanoparticles using atomic layer deposition (ALD) techniques with SnCl_4 and H_2O_2 as the reactants[180]. These SnO_x films were then exposed to O_2 and CO gas pressure at 300°C to measure and understand their ability to serve as CO gas sensors. O_2 pressure was observed to decrease the SnO_x film conductivity. The ultrathin SnO_x ALD films with a thickness of $\sim 10 \text{ \AA}$ were able to respond to O_2 within $\sim 100 \text{ s}$ and to CO within $\sim 10 \text{ s}$. ZnO nanotubes with a wall thickness on the order of nanometers were produced by utilizing an organic template and atomic layer deposition (ALD)[181]. The ZnO nanotube with a wall thickness of 10 nm was wholly depleted and thus highly responds to the adsorption of chemical species on its surface. Accurate control of the wall thickness of the ZnO nanotubes is crucial to make ZnO nanotube sensors with high response. Ivo Erkens *et al.*[182] report on the room temperature sensing performance of atomic layer deposition (ALD) prepared i-ZnO and Al-doped ZnO sensing devices. The sensitivity of these devices has been catalytically enhanced with ALD Pt nanoparticles (NPs). It was shown that the size distribution of the Pt NPs can be controlled by the number of Pt-ALD cycles. The

Pt-enhanced sensing devices showed a reversible, proportional change in current response at RT upon exposure to O₂ and CO. O₂ could be detected, diluted in N₂, down to 0.5%. CO could be detected, diluted in N₂ in the presence of O₂ and H₂O, down to 20 ppm. Reference devices without Pt NPs showed no response, indicating the importance of the Pt NPs for the sensing mechanism. Kim *et al.* [183] report on the fabrication of SnO₂ nanotube network by utilizing electrospinning and atomic layer deposition (ALD), and the network sensor is proven to exhibit excellent sensitivity to ethanol owing to its hollow and nanostructured character. Different publications reports on the promising sensing properties for the ALD fabricated sensors which make from this technique highly suitable for sensor applications.

7. ALD for membrane applications

The high efficiency and the low cost of membrane technologies make it a promising technology for different applications such as gas purification, water desalination, catalysis and environmental issues. One of the separation processes is the Molecular sieve mechanism. It is a size based mechanism that depends of the particles size and the pore diameter in porous membrane. Most of industrial porous membranes have a sub-nanometer up to micrometers pores diameter. However some separation process especially in gas separation process required an angstrom pore size range. From the different methods to control the pore diameter, ALD has attractive attention due to the conformal coating and the high thickness control offered by this technique.

Track etched polycarbonate membranes with a diameter and thickness of 25 mm and 6 μm respectively with 30 nm pores size has been reduced by Al₂O₃ ALD. SEM image shows the continuously pore reduction when we increase the number of ALD cycles from 10 to 300 cycles. TEM image after dissolving the polymers shows a uniform coating along the pores. The Al₂O₃ ALD inorganic coating improves the membrane hydrophilicity and enhanced the chemical stability to acids and organic solvents. A decrease in water flux and more protein retention has been detected when the pores size decreases [88]. In situ N₂ and Ar conductance measurements have been performed in Alumina Tubular Membranes during the Al₂O₃ ALD cycles demonstrated that the ALD can reduce the pore diameter to molecular size [184]. The same experiment has also performed on Alumina Tubular Membranes during SiO₂ and TiO₂ ALD cycles [185]. The N₂ conductance measurements shows a progressive reduction in pores

diameter during the SiO_2 and TiO_2 ALD cycles corresponding to 1.3 ± 0.1 Å per SiO_2 cycle and 3.1 ± 0.9 Å per SiO_2 cycle. Cross-sectional scanning electron microscopy (SEM) and electron probe microanalysis (EPMA) have been performed on anodic alumina membranes with Al_2O_3 ALD and shows a uniform coating using sufficient reactant exposure times [186]. EPMA measurement following ZnO ALD of anodic alumina membranes shows the infiltration of Zn into the nanopores when we increase the exposure times. Monte Carlo simulation of the Zn diffusion profile assuming a Knudsen diffusion mechanism. Meso-porous silica membranes have been tuned using catalyzed atomic layer deposition (C-ALD) of silicon dioxide and pyridine as catalyst to reduce the deposition temperature [187]. Gas separation measurement shows a transition from the Knudsen diffusion mechanism to a molecular sieving mechanism. A selectivity of 8.6 between CH_4 and H_2 has been measured at 473 K after the SiO_2 ALD deposition. In order to increase membrane selectivity, ALD has been used to enhance surface reaction between the membrane surface and the gas phases by activating the membrane surface with different functions.

ALD amino functionalization has been performed on silica membrane in order to enhance CO_2 transport. FTIR measurement shows that the amino modified membrane has positive CO_2 activation energy due to the higher mobility of chemisorbed CO_2 and to the pore reduction [188]. Track etched polycarbonate membranes have been also tuned by TiO_2 -ALD and then gas conductance measurements were performed to assure the tailoring pore sizes in PC membranes using the TiO_2 -ALD [189]. Diatom frustules have been coated by TiO_2 -ALD [190] to reduce the pores size from 40 nm to less than 5 nm in order to enhance the filtration properties of the membrane. High-density polyethylene (HDPE) particles (16 and 60 nm) have been coated with a thin layer of Al_2O_3 using a fluidized bed reactors [191] than a polymer/ceramic nanocomposite membranes were fabricated by extruding alumina coated HDPE particles. An inclusion of 7.29 vol.% alumina flakes leads to reduce of the diffusion coefficient to the half compared to the uncoated particles. Due to the voids formed during the extrusion process at the polymer/ceramic interface, an increase in the permeability of the membrane has been detected.

Electrofluidic applications or Electrical manipulation of charged species like ions, DNA, proteins, and nanoparticles have a high importance in solid state membrane fabrication. In such systems pore diameter and the surface chemistry (surface charge, hydrophobic, hydrophilic etc.) have attracted attention. Controlling such parameters can lead to the fabrication of electric circuit elements, such as diodes and transistors or to biological elements

for DNA or proteins sieving and sensing. ALD of TiO_2 has been performed on multipores of Si_3N_4 sandwiched between 2 TiN layers (TiN 30nm/ Si_3N_4 20 nm/TiN 30 nm) membrane after an E-beam lithography and reactive ion etching (RIE) processes to make the pores[192] and to reduce the pore diameter to sub 10nm. This membrane has been used as ionic field effect transistor (IFET) which is the Electrofluidic version of the semiconductor field effect transistor (FET) that works on ions instead of electrons. Nano-porous supported QI-phase LLC polymer membranes has been modified by Al_2O_3 ALD [193] to reduce the pore diameter to the angstrom range for gas separation application. 10 cycles of Al_2O_3 ALD has been enough to enhance the selectivity of H_2/N_2 from 12 to 65 with a decrease of 40% in the H_2 permeability.

The surface of nanoporous alumina membranes has been modified by ZnO-ALD for biological applications [194]. ZnO coating enhanced the antimicrobial activity of the alumina membrane against *Escherichia coli* and *Staphylococcus aureus* bacteria. A volatile organic compounds filter has been elaborated with 2 different structures: the first one is the TiO_2 ALD modification of an AAO membrane, and the second one is the TiO_2 ALD modification of a nanodiamond substrate [195]. Adsorption capacities test for toluene such VOC shows that the TiO_2 surface can allow adsorption of toluene. Ceramic microfiltration membranes with an average pore size of 50 nm has been tuned using Al_2O_3 ALD [196]. After the Al_2O_3 ALD deposition, the membranes show a decrease in water flux, and an increase in the retention of bovine serum albumin. After 600 ALD cycles water flux decrease from $1698 \text{ L (m}^2 \text{ h bar)}^{-1}$ to $118 \text{ L (m}^2 \text{ h bar)}^{-1}$, and BSA retention increases from 2.9% to 97.1%.

8. General conclusion

Atomic Layer deposition (ALD) is a vapor deposition method of ultrathin layers. It was known for his debut under the name of ALE (Atomic Layer Epitaxy). Atomic layer deposition technique is a thin film deposition technique based on 2 self limiting reaction limited at the surface of the substrate. The non presence of the gas phase reaction on ALD give this technique several advantages such as high aspect ratio deposition ability, high thickness control in the angstrom range, high deposition purity and others. Those advantages make from the ALD a suitable technique for different application on different field such as electronic field, optical field, optoelectronic, sensors, battery and others. We reported on this chapter the ALD deposition mechanism, the ALD deposition parameter that can affect the

deposition, the different types of ALD reactors and finally we reports on the different application for the ALD.

9. Thesis objectives

The aim of this PhDthesis is the synthesis of different nanostructured materials based on ALD oxide thin film (Al_2O_3 , ZnO and $\text{Al}_2\text{O}_3/\text{ZnO}$ nanolaminates) deposited on different types of substrates such as silicon substrate, glass, fibers, multipores membrane, monopore membrane, PET and gold coated nickel dogbones. ALD deposition was performed on those substrates with changing the film thickness (number of cycles), the deposition temperature, and the film composition (doping, multilayers...). After the ALD deposition chemical, structural, optical, electrical as well as mechanical characterization were performed on the ALD deposited layer in order to study the influence of the deposition parameters on the thin film properties. The deposited and characterized ALD films were investigated for different applications:

- Optical properties for solar cell applications (chapter 2)
- UV detection (Chapter3)
- Protective coating and gas barrier (chapter 4)
- Ionic transport, water desalination, Mass spectrometry, DNA sequencing and Gas purification (chapter 5)

References

1. Paciotti, G.F., D.G.I. Kingston, and L. Tamarkin, Colloidal gold nanoparticles: A novel nanoparticle platform for developing multifunctional tumor-targeted drug delivery vectors. *Drug Development Research*, 2006. 67(1): p. 47-54.
2. G. Binnig, H.R., *Angew. Chem., Int. Ed.*, 1987. 99: p. 622
3. Guozhong Cao, Y.W., nanostructures and nanomaterials synthesis properties and application. Vol. 2. 2011, usa.
4. Krebs, F.C., Fabrication and processing of polymer solar cells: A review of printing and coating techniques. *Solar Energy Materials and Solar Cells*, 2009. 93(4): p. 394-412.
5. Artur Goldschmidt, H.-J.S., *BASF Handbook on Basics of Coating Technology* 2003, germany.
6. Y.Ito, T.O.T.o., *Electrochemical Technology: Innovation and New Technologies* 1996, amsterdam.
7. Suntola, T., An Invited Talk at AVS Topical Conference on Atomic Layer Deposition, in *Thirty Years of ALD* 2004: University of Helsinki: Helsinki, Finland.
8. Puurunen, R.L., Surface chemistry of atomic layer deposition: A case study for the trimethylaluminum/water process. *Journal of Applied Physics*, 2005. 97(12).
9. George, S.M., Atomic Layer Deposition: An Overview. *Chemical Reviews*, 2010. 110(1): p. 111-131.
10. Suntola, T., Cost-effective processing by atomic layer epitaxy. *Thin Solid Films*, 1993. 225(1-2): p. 96-98.
11. Elam, J.W., M.D. Groner, and S.M. George, Viscous flow reactor with quartz crystal microbalance for thin film growth by atomic layer deposition. *Review of Scientific Instruments*, 2002. 73(8): p. 2981-2987.
12. Ott, A.W., et al., Al₂O₃ thin film growth on Si(100) using binary reaction sequence chemistry. *Thin Solid Films*, 1997. 292(1-2): p. 135-144.
13. Ritala, M. and J. Niinisto, Chapter 4 Atomic Layer Deposition, in *Chemical Vapour Deposition: Precursors* 2009, The Royal Society of Chemistry. p. 158-206.
14. D. H. Everett, P.A.C., 579 (1972),. Available from: [http://www.iupac.org/reports/2001/colloid/2001/-manual of s and t.pdf](http://www.iupac.org/reports/2001/colloid/2001/-manual%20of%20s%20and%20t.pdf).
15. Niinisto, L., et al., Advanced electronic and optoelectronic materials by Atomic Layer Deposition: An overview with special emphasis on recent progress in processing of high-k dielectrics and other oxide materials. *Physica Status Solidi a-Applied Research*, 2004. 201(7): p. 1443-1452.
16. Gordon, R., *ALD Precursors and Reaction Mechanisms*, Harvard University Center for Nanoscale Systems.
17. Kytokivi, A., et al., Surface characteristics and activity of chromia/alumina catalysts prepared by atomic layer epitaxy. *Journal of Catalysis*, 1996. 162(2): p. 190-197.
18. Puurunen, R.L., S.M.K. Airaksinen, and A.O.I. Krause, Chromium(III) supported on aluminum-nitride-surfaced alumina: characteristics and dehydrogenation activity. *Journal of Catalysis*, 2003. 213(2): p. 281-290.
19. Dolgushev, N.V., et al., Synthesis and characterization of nanosized titanium oxide films on the (0001) α -Al₂O₃ surface. *Thin Solid Films*, 1997. 293(1-2): p. 91-95.
20. Kim, H. and S.M. Rossmagel, Growth kinetics and initial stage growth during plasma-enhanced Ti atomic layer deposition. *Journal of Vacuum Science & Technology A*, 2002. 20(3): p. 802-808.
21. Besling, W.F.A., et al., Characterisation of ALCVD Al₂O₃-ZrO₂ nanolaminates, link between electrical and structural properties. *Journal of Non-Crystalline Solids*, 2002. 303(1): p. 123-133.
22. Nohira, H., et al., Characterization of ALCVD-Al₂O₃ and ZrO₂ layer using X-ray photoelectron spectroscopy. *Journal of Non-Crystalline Solids*, 2002. 303(1): p. 83-87.

23. Lim, J.W., H.S. Park, and S.W. Kang, Kinetic modeling of film growth rate in atomic layer deposition. *Journal of the Electrochemical Society*, 2001. 148(6): p. C403-C408.
24. Satta, A., et al., Growth mechanism and continuity of atomic layer deposited TiN films on thermal SiO₂. *Journal of Applied Physics*, 2002. 92(12): p. 7641-7646.
25. Puurunen, R.L. and W. Vandervorst, Island growth as a growth mode in atomic layer deposition: A phenomenological model. *Journal of Applied Physics*, 2004. 96(12): p. 7686-7695.
26. T. Suntola and J. Antson, 15 November 1977.
27. Suntola, T. and J. Hyvarinen, ATOMIC LAYER EPITAXY. *Annual Review of Materials Science*, 1985. 15: p. 177-195.
28. van Delft, J.A., D. Garcia-Alonso, and W.M.M. Kessels, Atomic layer deposition for photovoltaics: applications and prospects for solar cell manufacturing. *Semiconductor Science and Technology*, 2012. 27(7).
29. Beneq February 15, 2012 [cited February 15, 2012 Available from: <http://www.beneq.com>].
30. Granneman, E., et al., Batch ALD: Characteristics, comparison with single wafer ALD, and examples. *Surface and Coatings Technology*, 2007. 201(22–23): p. 8899-8907.
31. Poedt, P., et al., Spatial atomic layer deposition: A route towards further industrialization of atomic layer deposition. *Journal of Vacuum Science & Technology A*, 2012. 30(1): p. -.
32. Lee, S.W., et al., Atomic Layer Deposition of SrTiO₃ Thin Films with Highly Enhanced Growth Rate for Ultrahigh Density Capacitors. *Chemistry of Materials*, 2011. 23(8): p. 2227-2236.
33. Vehkamäki, M., et al., Growth of SrTiO₃ and BaTiO₃ thin films by atomic layer deposition. *Electrochemical and Solid State Letters*, 1999. 2(10): p. 504-506.
34. Mao, M., R. Bubber, and T. Schneider, ALD for Data Storage Applications. *ECS Transactions*, 2006. 1(10): p. 37-47.
35. Smith, S., et al., Physical and electrical characterization of ALCVD™ TiN and WN_xC_y used as a copper diffusion barrier in dual damascene backend structures (08.2). *Microelectronic Engineering*, 2002. 64(1–4): p. 247-253.
36. Chou, S., et al., ZnO:Al Thin Film Gas Sensor for Detection of Ethanol Vapor. *Sensors*, 2006. 6(10): p. 1420-1427.
37. Zhao, Z., et al., ZnO-Based Amperometric Enzyme Biosensors. *Sensors*, 2010. 10(2): p. 1216-1231.
38. Elias, J., et al., Urchin-inspired zinc oxide as building blocks for nanostructured solar cells. *Nano Energy*, 2012. 1(5): p. 696-705.
39. Elias, J., et al., Hollow Urchin-like ZnO thin Films by Electrochemical Deposition. *Advanced Materials*, 2010. 22(14): p. 1607-1612.
40. Su, P.-C., et al., Solid Oxide Fuel Cell with Corrugated Thin Film Electrolyte. *Nano Letters*, 2008. 8(8): p. 2289-2292.
41. Brahim, C., et al., Electrical properties of thin yttria-stabilized zirconia overlayers produced by atomic layer deposition for solid oxide fuel cell applications. *Applied Surface Science*, 2007. 253(8): p. 3962-3968.
42. Ballée, E., et al., Synthesis of a Thin-Layered Ionic Conductor, CeO₂-Y₂O₃, by Atomic Layer Deposition in View of Solid Oxide Fuel Cell Applications. *Chemistry of Materials*, 2009. 21(19): p. 4614-4619.
43. Holme, T.P., C. Lee, and F.B. Prinz, Atomic layer deposition of LSM cathodes for solid oxide fuel cells. *Solid State Ionics*, 2008. 179(27–32): p. 1540-1544.
44. Jiang, X., et al., Application of Atomic Layer Deposition of Platinum to Solid Oxide Fuel Cells. *Chemistry of Materials*, 2008. 20(12): p. 3897-3905.
45. Cheng, H.-E., C.-M. Hsu, and Y.-C. Chen, Substrate Materials and Deposition Temperature Dependent Growth Characteristics and Photocatalytic Properties of ALD TiO₂ Films. *Journal of the Electrochemical Society*, 2009. 156(8): p. D275-D278.
46. Kim, J.-S., J.-H. Yoon, and S.M. Gforce, Study on the Photocatalytic Reaction of TiO₂ALD-Coated Phosphor Particles. *Journal of the Korean Physical Society*, 2009. 54(3): p. 1082-1086.

47. Lee, C.-S., et al., Plasma-Enhanced ALD of TiO₂ Thin Films on SUS 304 Stainless Steel for Photocatalytic Application. *Journal of the Electrochemical Society*, 2009. 156(5): p. D188-D192.
48. Jeong, M.-G., et al., Toluene combustion over NiO nanoparticles on mesoporous SiO₂ prepared by atomic layer deposition. *Chemical Engineering Journal*, 2014. 237: p. 62-69.
49. Liang, X. and R.L. Patel, Porous titania microspheres with uniform wall thickness and high photoactivity. *Ceramics International*, 2014. 40(2): p. 3097-3103.
50. Wang, H., et al., Improvement of photocatalytic hydrogen generation from CdSe/CdS/TiO₂ nanotube-array coaxial heterogeneous structure. *International Journal of Hydrogen Energy*, 2014. 39(1): p. 90-99.
51. Bertrand, J.A. and S.M. George, Evaluating Al₂O₃ gas diffusion barriers grown directly on Ca films using atomic layer deposition techniques. *Journal of Vacuum Science & Technology A*, 2013. 31(1).
52. Carcia, P.F., et al., Effect of early stage growth on moisture permeation of thin-film Al₂O₃ grown by atomic layer deposition on polymers. *Journal of Vacuum Science & Technology A*, 2013. 31(6).
53. Hirvikorpi, T., et al., Barrier properties of plastic films coated with an Al₂O₃ layer by roll-to-roll atomic layer deposition. *Thin Solid Films*, 2014. 550: p. 164-169.
54. Illiberi, A., et al., On the environmental stability of ZnO thin films by spatial atomic layer deposition. *Journal of Vacuum Science & Technology A*, 2013. 31(6).
55. Lee, G.B., et al., Low-temperature atomic layer deposition of Al₂O₃ on blown polyethylene films with plasma-treated surfaces. *Journal of Vacuum Science & Technology A*, 2013. 31(1).
56. Lee, J.G., H.G. Kim, and S.S. Kim, Enhancement of barrier properties of aluminum oxide layer by optimization of plasma-enhanced atomic layer deposition process. *Thin Solid Films*, 2013. 534: p. 515-519.
57. Lee, U.S., et al., Formation of a Bilayer of ALD-SiO₂ and Sputtered Al₂O₃/ZrO₂ Films on Polyethylene Terephthalate Substrates as a Moisture Barrier. *Ecs Solid State Letters*, 2013. 2(6): p. R13-R15.
58. Maindron, T., et al., Investigation of Al₂O₃ barrier film properties made by atomic layer deposition onto fluorescent tris-(8-hydroxyquinoline) aluminium molecular films. *Thin Solid Films*, 2013. 548: p. 517-525.
59. Seo, S.-W., et al., FLEXIBLE ORGANIC/INORGANIC MOISTURE BARRIER USING PLASMA-POLYMERIZED LAYER. *Nano*, 2013. 8(4).
60. Kim, E., et al., Thin film encapsulation for organic light emitting diodes using a multi-barrier composed of MgO prepared by atomic layer deposition and hybrid materials. *Organic Electronics*, 2013. 14(7): p. 1737-1743.
61. Park, S.H.K., et al., Ultra thin film encapsulation of organic light emitting diode on a plastic substrate. *Etri Journal*, 2005. 27(5): p. 545-550.
62. Clark, M.D., et al., Ultra-thin alumina layer encapsulation of bulk heterojunction organic photovoltaics for enhanced device lifetime. *Organic Electronics*, 2014. 15(1): p. 1-8.
63. Han, D.-S., D.-K. Choi, and J.-W. Park, Al₂O₃/TiO₂ multilayer thin films grown by plasma enhanced atomic layer deposition for organic light-emitting diode passivation. *Thin Solid Films*, 2014. 552: p. 155-158.
64. Ferrari, S., et al., Atomic layer deposited Al₂O₃ as a capping layer for polymer based transistors. *Organic Electronics*, 2007. 8(4): p. 407-414.
65. Latella, B.A., G. Triani, and P.J. Evans, Toughness and adhesion of atomic layer deposited alumina films on polycarbonate substrates. *Scripta Materialia*, 2007. 56(6): p. 493-496.
66. Knez, M., K. Niesch, and L. Niinistö, Synthesis and surface engineering of complex nanostructures by atomic layer deposition. *Advanced Materials*, 2007. 19(21): p. 3425-3438.
67. Knez, M., et al., Atomic Layer Deposition on Biological Macromolecules: Metal Oxide Coating of Tobacco Mosaic Virus and Ferritin. *Nano Letters*, 2006. 6(6): p. 1172-1177.
68. Jangwoong, U. and J. Hyeongtag, TiN Diffusion Barrier Grown by Atomic Layer Deposition Method for Cu Metallization. *Japanese Journal of Applied Physics*, 2001. 40(7R): p. 4657.

69. Kyung In, C., et al. Characteristics of ALD-TaN thin films using a novel precursors for copper metallization. in Interconnect Technology Conference, 2003. Proceedings of the IEEE 2003 International. 2003.
70. Lim, B.S., A. Rahtu, and R.G. Gordon, Atomic layer deposition of transition metals. *Nat Mater*, 2003. 2(11): p. 749-754.
71. Kim, H., Atomic layer deposition of metal and nitride thin films: Current research efforts and applications for semiconductor device processing. *Journal of Vacuum Science & Technology B*, 2003. 21(6): p. 2231-2261.
72. Bae, C., H. Shin, and K. Nielsch, Surface modification and fabrication of 3D nanostructures by atomic layer deposition. *Mrs Bulletin*, 2011. 36(11): p. 887-897.
73. Chang, Y.-H., et al., The Effect of Geometric Structure on Photoluminescence Characteristics of 1-D TiO₂ Nanotubes and 2-D TiO₂ Films Fabricated by Atomic Layer Deposition. *Journal of the Electrochemical Society*, 2012. 159(7): p. D401-D405.
74. Feng, H., et al., Oxidative dehydrogenation of cyclohexane over alumina-supported vanadium oxide nanoliths. *Journal of Catalysis*, 2010. 269(2): p. 421-431.
75. Foong, T.R.B., et al., Template-Directed Liquid ALD Growth of TiO₂ Nanotube Arrays: Properties and Potential in Photovoltaic Devices. *Advanced Functional Materials*, 2010. 20(9): p. 1390-1396.
76. Gu, D., et al., Synthesis of Nested Coaxial Multiple-Walled Nanotubes by Atomic Layer Deposition. *Acs Nano*, 2010. 4(2): p. 753-758.
77. Ha, S., et al., Low temperature solid oxide fuel cells with proton-conducting Y:BaZrO₃ electrolyte on porous anodic aluminum oxide substrate. *Thin Solid Films*, 2013. 544: p. 125-128.
78. Kwon, C.-W., et al., High-Performance Micro-Solid Oxide Fuel Cells Fabricated on Nanoporous Anodic Aluminum Oxide Templates. *Advanced Functional Materials*, 2011. 21(6): p. 1154-1159.
79. Lee, J., et al., Atomic layer deposition of TiO₂ nanotubes and its improved electrostatic capacitance. *Electrochemistry Communications*, 2010. 12(2): p. 210-212.
80. Liang, Y.-C., et al., Photocatalysis of Ag-Loaded TiO₂ Nanotube Arrays Formed by Atomic Layer Deposition. *Journal of Physical Chemistry C*, 2011. 115(19): p. 9498-9502.
81. Meng, X., et al., Controllable atomic layer deposition of one-dimensional nanotubular TiO₂. *Applied Surface Science*, 2013. 266: p. 132-140.
82. Norek, M., et al., Plasmonic enhancement of blue emission from ZnO nanorods grown on the anodic aluminum oxide (AAO) template. *Applied Physics a-Materials Science & Processing*, 2013. 111(1): p. 265-271.
83. Pardon, G., et al., Pt-Al₂O₃ dual layer atomic layer deposition coating in high aspect ratio nanopores. *Nanotechnology*, 2013. 24(1).
84. Phillips, R., P. Hansen, and E. Eisenbraun, Atomic layer deposition fabricated substoichiometric TiO_x nanorods as fuel cell catalyst supports. *Journal of Vacuum Science & Technology A*, 2012. 30(1).
85. Romero, V., et al., Changes in Morphology and Ionic Transport Induced by ALD SiO₂ Coating of Nanoporous Alumina Membranes. *Acs Applied Materials & Interfaces*, 2013. 5(9): p. 3556-3564.
86. Tupala, J., et al., Preparation of regularly structured nanotubular TiO₂ thin films on ITO and their modification with thin ALD-grown layers. *Nanotechnology*, 2012. 23(12).
87. Wu, Z., et al., Preparation and magnetoviscosity of nanotube ferrofluids by viral scaffolding and ALD on porous templates. *Physica Status Solidi B-Basic Solid State Physics*, 2010. 247(10): p. 2412-2423.
88. Li, F., et al., Precise pore size tuning and surface modifications of polymeric membranes using the atomic layer deposition technique. *Journal of Membrane Science*, 2011. 385(1-2): p. 1-9.
89. Hakim, L.F., et al., Synthesis of oxidation-resistant metal nanoparticles via atomic layer deposition. *Nanotechnology*, 2007. 18(34).
90. Weimer, M.A., et al., Ultrafast metal-insulator varistors based on tunable Al₂O₃ tunnel junctions. *Applied Physics Letters*, 2008. 92(16): p. -.

91. King, D.M., et al., Atomic Layer Deposition of UV-Absorbing ZnO Films on SiO₂ and TiO₂ Nanoparticles Using a Fluidized Bed Reactor. *Advanced Functional Materials*, 2008. 18(4): p. 607-615.
92. Hakim, L.F., et al., Nanoparticle Coating for Advanced Optical, Mechanical and Rheological Properties. *Advanced Functional Materials*, 2007. 17(16): p. 3175-3181.
93. Wank, J.R., S.M. George, and A.W. Weimer, Nanocoating individual cohesive boron nitride particles in a fluidized bed by ALD. *Powder Technology*, 2004. 142(1): p. 59-69.
94. Zhang, H., et al., High permittivity thin film nanolaminates. *Journal of Applied Physics*, 2000. 87(4): p. 1921-1924.
95. Kil, D.-S., et al., Improvement of Leakage Current Property of TIT Capacitor with Compositionally Stepped HfxAl_yO_z Thin Films. *Electronic Materials Letters*, 2006. 2(1): p. 15-18.
96. Mitchell, D.R.G., et al., Atomic layer deposition of TiO₂ and Al₂O₃ thin films and nanolaminates. *Smart Materials & Structures*, 2006. 15(1): p. S57-S64.
97. Mitchell, D.R.G., et al., TEM anti ellipsometry studies of nanolaminate oxide films prepared using atomic layer deposition. *Applied Surface Science*, 2005. 243(1-4): p. 265-277.
98. Elam, J.W., Z.A. Sechrist, and S.M. George, ZnO/Al₂O₃ nanolaminates fabricated by atomic layer deposition: growth and surface roughness measurements. *Thin Solid Films*, 2002. 414(1): p. 43-55.
99. Jensen, J.M., et al., X-ray reflectivity characterization of ZnO/Al₂O₃ multilayers prepared by atomic layer deposition. *Chemistry of Materials*, 2002. 14(5): p. 2276-2282.
100. Hausmann, D.M. and R.G. Gordon, Surface morphology and crystallinity control in the atomic layer deposition (ALD) of hafnium and zirconium oxide thin films. *Journal of Crystal Growth*, 2003. 249(1-2): p. 251-261.
101. Chang, H.S., et al., Excellent thermal stability of Al₂O₃/ZrO₂/Al₂O₃ stack structure for metal-oxide-semiconductor gate dielectrics application. *Applied Physics Letters*, 2002. 80(18): p. 3385-3387.
102. Elers, K.E., et al., Atomic layer deposition of W_xN/TiN and WN_xC_y/TiN nanolaminates. *Thin Solid Films*, 2003. 434(1-2): p. 94-99.
103. Costescu, R.M., et al., Ultra-low thermal conductivity in W/Al₂O₃ nanolaminates. *Science*, 2004. 303(5660): p. 989-990.
104. Park, P.K., E.-S. Cha, and S.-W. Kang, Interface effect on dielectric constant of HfO₂/Al₂O₃ nanolaminate films deposited by plasma-enhanced atomic layer deposition. *Applied Physics Letters*, 2007. 90(23).
105. Mackus, A.J.M., et al., Nanopatterning by direct-write atomic layer deposition. *Nanoscale*, 2012. 4(15): p. 4477-4480.
106. Mackus, A.J.M., et al., Local deposition of high-purity Pt nanostructures by combining electron beam induced deposition and atomic layer deposition. *Journal of Applied Physics*, 2010. 107(11).
107. Mackus, A.J.M., et al., Direct-Write Atomic Layer Deposition of High-Quality Pt Nanostructures: Selective Growth Conditions and Seed Layer Requirements. *Journal of Physical Chemistry C*, 2013. 117(20): p. 10788-10798.
108. Dabbous, S., et al., Comparative study of Indium and Zinc doped WO₃ self-organized porous crystals in terms of nano-structural and opto-thermal patterns. *Materials Science in Semiconductor Processing*, 2014. 18: p. 171-177.
109. Gueder, F., et al., Engineered High Aspect Ratio Vertical Nanotubes as a Model System for the Investigation of Catalytic Methanol Synthesis Over Cu/ZnO. *Acs Applied Materials & Interfaces*, 2014. 6(3): p. 1576-1582.
110. Guo, S.-h., et al., Impact of interface roughness on the performance of broadband blackbody absorber based on dielectric-metal film multilayers. *Optics Express*, 2014. 22(2): p. 1953-1963.
111. Jiang, C. and X. Liang, Catalytic hydrogen transfer of ketones over atomic layer deposited highly-dispersed platinum nanoparticles supported on multi-walled carbon nanotubes. *Catalysis Communications*, 2014. 46: p. 41-45.

112. Yang, C., et al., Color-tuning method by filling porous alumina membrane using atomic layer deposition based on metal-dielectric-metal structure. *Applied Optics*, 2014. 53(4): p. A142-A147.
113. Gnerlich, M., et al., Solid flexible electrochemical supercapacitor using Tobacco mosaic virus nanostructures and ALD ruthenium oxide. *Journal of Micromechanics and Microengineering*, 2013. 23(11).
114. Gruenzel, T., et al., Preparation of electrochemically active silicon nanotubes in highly ordered arrays. *Beilstein Journal of Nanotechnology*, 2013. 4: p. 655-664.
115. Li, Y., et al., Physical processes-aided periodic micro/nanostructured arrays by colloidal template technique: fabrication and applications. *Chemical Society Reviews*, 2013. 42(8): p. 3614-3627.
116. Motoyama, M., et al., Nanotubular Array Solid Oxide Fuel Cell. *Acs Nano*, 2014. 8(1): p. 340-351.
117. Phillips, R., et al., Processing and functionalization of conductive substoichiometric TiO_2 catalyst supports for PEM fuel cell applications. *Journal of Materials Research*, 2013. 28(3): p. 461-467.
118. Sarkar, K., et al., Custom-Made Morphologies of ZnO Nanostructured Films Templated by a Poly(styrene-block-ethylene oxide) Diblock Copolymer Obtained by a Sol-Gel Technique. *Chemsuschem*, 2013. 6(8): p. 1414-1424.
119. Lee, D.-J., et al., Ultrasoother, High Electron Mobility Amorphous In-Zn-O Films Grown by Atomic Layer Deposition. *Journal of Physical Chemistry C*, 2014. 118(1): p. 408-415.
120. Noh, Y. and O. Song, Dye-Sensitized Solar Cells for Ruthenium Counter Electrodes Employing Polystyrene Beads and ZnO. *Korean Journal of Metals and Materials*, 2013. 51(12): p. 901-905.
121. Noh, Y. and O. Song, Formation of Ruthenium-Dots on Counter Electrodes for Dye Sensitized Solar Cells. *Electronic Materials Letters*, 2014. 10(1): p. 263-266.
122. Oh, S.-K., et al., Process Temperature Dependence of Al_2O_3 Film Deposited by Thermal ALD as a Passivation Layer for c-Si Solar Cells. *Journal of Semiconductor Technology and Science*, 2013. 13(6): p. 581-588.
123. Richter, A., et al., Reaction kinetics during the thermal activation of the silicon surface passivation with atomic layer deposited Al_2O_3 . *Applied Physics Letters*, 2014. 104(6).
124. Enterkin, J.A., K.R. Poeppelmeier, and L.D. Marks, Oriented Catalytic Platinum Nanoparticles on High Surface Area Strontium Titanate Nanocuboids. *Nano Letters*, 2011. 11(3): p. 993-997.
125. Pellin, M.J., et al., Mesoporous catalytic membranes: Synthetic control of pore size and wall composition. *Catalysis Letters*, 2005. 102(3-4): p. 127-130.
126. Kim, D., et al., TiO_2/Ni Inverse-Catalysts Prepared by Atomic Layer Deposition (ALD). *Catalysis Letters*, 2011. 141(6): p. 854-859.
127. Ahn, C., et al., Monolithic 3D titania with ultrathin nanoshell structures for enhanced photocatalytic activity and recyclability. *Nanoscale*, 2013. 5(21): p. 10384-10389.
128. Dey, N.K., et al., Adsorption and photocatalytic degradation of methylene blue over TiO_2 films on carbon fiber prepared by atomic layer deposition. *Journal of Molecular Catalysis a-Chemical*, 2011. 337(1-2): p. 33-38.
129. Kumar, M.K., et al., Field Effects in Plasmonic Photocatalyst by Precise SiO_2 Thickness Control Using Atomic Layer Deposition. *Acs Catalysis*, 2011. 1(4): p. 300-308.
130. Lee, C.-S., et al., Photocatalytic activities of TiO_2 thin films prepared on Galvanized Iron substrate by plasma-enhanced atomic layer deposition. *Thin Solid Films*, 2010. 518(17): p. 4757-4761.
131. Luo, Y., et al., Photocatalytic Decomposition of Toluene Vapor by Bare and TiO_2 -coated Carbon Fibers. *Bulletin of the Korean Chemical Society*, 2010. 31(6): p. 1661-1664.
132. Meng, X., et al., Heterostructural coaxial nanotubes of $\text{CNT}@\text{Fe}_2\text{O}_3$ via atomic layer deposition: effects of surface functionalization and nitrogen-doping. *Journal of Nanoparticle Research*, 2011. 13(3): p. 1207-1218.

133. Ngo, T.Q., et al., Atomic layer deposition of photoactive CoO/SrTiO_3 and CoO/TiO_2 on $\text{Si}(001)$ for visible light driven photoelectrochemical water oxidation. *Journal of Applied Physics*, 2013. 114(8).
134. Szilagyi, I.M., et al., Photocatalytic Properties of WO_3/TiO_2 Core/Shell Nanofibers prepared by Electrospinning and Atomic Layer Deposition. *Chemical Vapor Deposition*, 2013. 19(4-6): p. 149-155.
135. Zhou, Y., et al., Optimal preparation of Pt/TiO_2 photocatalysts using atomic layer deposition. *Applied Catalysis B-Environmental*, 2010. 101(1-2): p. 54-60.
136. Sanyal, O. and I. Lee, Recent Progress in the Applications of Layer-By-Layer Assembly to the Preparation of Nanostructured Ion-Rejecting Water Purification Membranes. *Journal of Nanoscience and Nanotechnology*, 2014. 14(3): p. 2178-2189.
137. Wang, H., et al., Graphene-based materials: Fabrication, characterization and application for the decontamination of wastewater and wastegas and hydrogen storage/generation. *Advances in Colloid and Interface Science*, 2013. 195: p. 19-40.
138. Xu, Q., et al., Atomic layer deposition of alumina on porous polytetrafluoroethylene membranes for enhanced hydrophilicity and separation performances. *Journal of Membrane Science*, 2012. 415: p. 435-443.
139. Martinson, A.B.F., et al., ZnO nanotube based dye-sensitized solar cells. *Nano Letters*, 2007. 7(8): p. 2183-2187.
140. Martinson, A.B.F., et al., Radial electron collection in dye-sensitized solar cells. *Nano Letters*, 2008. 8(9): p. 2862-2866.
141. Hamann, T.W., et al., Aerogel templated ZnO dye-sensitized solar cells. *Advanced Materials*, 2008. 20(8): p. 1560-+.
142. Pourret, A., P. Guyot-Sionnest, and J.W. Elam, Atomic Layer Deposition of ZnO in Quantum Dot Thin Films. *Advanced Materials*, 2009. 21(2): p. 232-+.
143. Park, K., et al., Effect of an Ultrathin TiO_2 Layer Coated on Submicrometer-Sized ZnO Nanocrystallite Aggregates by Atomic Layer Deposition on the Performance of Dye-Sensitized Solar Cells. *Advanced Materials*, 2010. 22(21): p. 2329-2332.
144. Heo, J., et al., $(\text{Sn,Al})\text{Ox}$ Films Grown by Atomic Layer Deposition. *The Journal of Physical Chemistry C*, 2011. 115(20): p. 10277-10283.
145. Dasgupta, N.P., et al., Atomic Layer Deposition of Lead Sulfide Quantum Dots on Nanowire Surfaces. *Nano Letters*, 2011. 11(3): p. 934-940.
146. Park, K., et al., Effect of Annealing Temperature on $\text{TiO}_2\text{-ZnO}$ Core-Shell Aggregate Photoelectrodes of Dye-Sensitized Solar Cells. *Journal of Physical Chemistry C*, 2011. 115(11): p. 4927-4934.
147. Biener, M.M., et al., ALD Functionalized Nanoporous Gold: Thermal Stability, Mechanical Properties, and Catalytic Activity. *Nano Letters*, 2011. 11(8): p. 3085-3090.
148. Christensen, S.T. and J.W. Elam, Atomic Layer Deposition of Ir-Pt Alloy Films. *Chemistry of Materials*, 2010. 22(8): p. 2517-2525.
149. Comstock, D.J., et al., Tuning the Composition and Nanostructure of Pt/Ir Films via Anodized Aluminum Oxide Templated Atomic Layer Deposition. *Advanced Functional Materials*, 2010. 20(18): p. 3099-3105.
150. Edelmann, F.T., Lanthanide amidinates and guanidates in catalysis and materials science: a continuing success story. *Chemical Society Reviews*, 2012. 41(23): p. 7657-7672.
151. Enterkin, J.A., et al., Propane Oxidation over Pt/SrTiO_3 Nanocuboids. *Acs Catalysis*, 2011. 1(6): p. 629-635.
152. Feng, H., et al., Subnanometer Palladium Particles Synthesized by Atomic Layer Deposition. *Acs Catalysis*, 2011. 1(6): p. 665-673.
153. Gould, T.D., et al., Synthesis of supported Ni catalysts by atomic layer deposition. *Journal of Catalysis*, 2013. 303: p. 9-15.
154. Hsueh, Y.-C., et al., Deposition of platinum on oxygen plasma treated carbon nanotubes by atomic layer deposition. *Nanotechnology*, 2012. 23(40).
155. Johansson, A.C., et al., Ru-decorated Pt nanoparticles on N-doped multi-walled carbon nanotubes by atomic layer deposition for direct methanol fuel cells. *International Journal of Hydrogen Energy*, 2013. 38(26): p. 11406-11414.

156. Liang, X., N.-H. Li, and A.W. Weimer, Template-directed synthesis of porous alumina particles with precise wall thickness control via atomic layer deposition. *Microporous and Mesoporous Materials*, 2012. 149(1): p. 106-110.
157. Marichy, C. and N. Pinna, Carbon-nanostructures coated/decorated by atomic layer deposition: Growth and applications. *Coordination Chemistry Reviews*, 2013. 257(23-24): p. 3232-3253.
158. Mondloch, J.E., et al., Vapor-Phase Metalation by Atomic Layer Deposition in a Metal-Organic Framework. *Journal of the American Chemical Society*, 2013. 135(28): p. 10294-10297.
159. Pagan-Torres, Y.J., et al., Synthesis of Highly Ordered Hydrothermally Stable Mesoporous Niobia Catalysts by Atomic Layer Deposition. *Acs Catalysis*, 2011. 1(10): p. 1234-1245.
160. Rauwel, E., et al., Oxide Coating of Alumina Nanoporous Structure Using ALD to Produce Highly Porous Spinel. *Chemical Vapor Deposition*, 2012. 18(10-12): p. 315-325.
161. Sereda, G., et al., Effect of Atomic Layer Deposition Support Thickness on Structural Properties and Oxidative Dehydrogenation of Propane on Alumina- and Titania-Supported Vanadia. *Catalysis Letters*, 2012. 142(4): p. 399-407.
162. Sun, S., et al., Single-atom Catalysis Using Pt/Graphene Achieved through Atomic Layer Deposition. *Scientific Reports*, 2013. 3.
163. Weber, M.J., et al., Supported Core/Shell Bimetallic Nanoparticles Synthesis by Atomic Layer Deposition. *Chemistry of Materials*, 2012. 24(15): p. 2973-2977.
164. Rashkeev, S.N., S. Dai, and S.H. Overbury, Modification of Au/TiO₂ Nanosystems by SiO₂ Monolayers: Toward the Control of the Catalyst Activity and Stability. *The Journal of Physical Chemistry C*, 2010. 114(7): p. 2996-3002.
165. Biener, M.M., et al., ALD Functionalized Nanoporous Gold: Thermal Stability, Mechanical Properties, and Catalytic Activity. *Nano Letters*, 2011. 11(8): p. 3085-3090.
166. King, J.S., et al., Ultralow Loading Pt Nanocatalysts Prepared by Atomic Layer Deposition on Carbon Aerogels. *Nano Letters*, 2008. 8(8): p. 2405-2409.
167. Lin, Y., et al., TiO₂/TiSi₂ Heterostructures for High-Efficiency Photoelectrochemical H₂O Splitting. *Journal of the American Chemical Society*, 2009. 131(8): p. 2772-+.
168. Liu, R., et al., Water Splitting by Tungsten Oxide Prepared by Atomic Layer Deposition and Decorated with an Oxygen-Evolving Catalyst. *Angewandte Chemie-International Edition*, 2011. 50(2): p. 499-502.
169. Paracchino, A., et al., Highly active oxide photocathode for photoelectrochemical water reduction. *Nature Materials*, 2011. 10(6): p. 456-461.
170. Tan, L.K., et al., Transparent, Well-Aligned TiO₂ Nanotube Arrays with Controllable Dimensions on Glass Substrates for Photocatalytic Applications. *Acs Applied Materials & Interfaces*, 2010. 2(2): p. 498-503.
171. Jung, Y.S., et al., Ultrathin Direct Atomic Layer Deposition on Composite Electrodes for Highly Durable and Safe Li-Ion Batteries. *Advanced Materials*, 2010. 22(19): p. 2172-+.
172. Kim, S.-W., et al., Fabrication and Electrochemical Characterization of TiO₂ Three-Dimensional Nanonetwork Based on Peptide Assembly. *Acs Nano*, 2009. 3(5): p. 1085-1090.
173. Banerjee, P., et al., Nanotubular metal-insulator-metal capacitor arrays for energy storage. *Nature Nanotechnology*, 2009. 4(5): p. 292-296.
174. Riley, L.A., et al., Conformal Surface Coatings to Enable High Volume Expansion Li-Ion Anode Materials. *Chemphyschem*, 2010. 11(10): p. 2124-2130.
175. Vaidyanathan, R., et al., Preliminary studies in the electrodeposition of PbSe/PbTe superlattice thin films via electrochemical atomic layer deposition (ALD). *Langmuir*, 2006. 22(25): p. 10590-10595.
176. Lybeck, J., et al., Thermoelectric Properties of Oxygen-Tuned ALD-Grown Ca₂CoO₃ (0.62) CoO₂ Thin Films. *Chemistry of Materials*, 2010. 22(21): p. 5900-5904.
177. Shi, J., et al., Recent developments in nanomaterial optical sensors. *TrAC Trends in Analytical Chemistry*, 2004. 23(5): p. 351-360.
178. Llobet, E., Gas sensors using carbon nanomaterials: A review. *Sensors and Actuators B: Chemical*, 2013. 179(0): p. 32-45.

179. Ding, B., et al., Electrospun nanomaterials for ultrasensitive sensors. *Materials Today*, 2010. 13(11): p. 16-27.
180. Du, X., Y. Du, and S.M. George, CO gas sensing by ultrathin tin oxide films grown by atomic layer deposition using transmission FTIR spectroscopy. *Journal of Physical Chemistry A*, 2008. 112(39): p. 9211-9219.
181. Cho, S., et al., Ethanol sensors based on ZnO nanotubes with controllable wall thickness via atomic layer deposition, an O₂ plasma process and an annealing process. *Sensors and Actuators B: Chemical*, 2012. 162(1): p. 300-306.
182. Erkens, I., et al., Room Temperature Sensing of O₂ and CO by Atomic Layer Deposition Prepared ZnO Films Coated with Pt Nanoparticles. *ECS Transactions*, 2013. 58(10): p. 203-214.
183. Kim, W.-S., et al., SnO₂ nanotubes fabricated using electrospinning and atomic layer deposition and their gas sensing performance. *Nanotechnology*, 2010. 21(24).
184. Berland, B.S., et al., In situ monitoring of atomic layer controlled pore reduction in alumina tubular membranes using sequential surface reactions. *Chemistry of Materials*, 1998. 10(12): p. 3941-3950.
185. Cameron, M.A., et al., Atomic layer deposition of SiO₂ and TiO₂ in alumina tubular membranes: Pore reduction and effect of surface species on gas transport. *Langmuir*, 2000. 16(19): p. 7435-7444.
186. Elam, J.W., et al., Conformal coating on ultrahigh-aspect-ratio nanopores of anodic alumina by atomic layer deposition. *Chemistry of Materials*, 2003. 15(18): p. 3507-3517.
187. McCool, B.A. and W.J. DeSisto, Synthesis and characterization of silica membranes prepared by pyridine-catalyzed atomic layer deposition. *Industrial & Engineering Chemistry Research*, 2004. 43(10): p. 2478-2484.
188. McCool, B.A. and W.J. DeSisto, Amino-functionalized silica membranes for enhanced carbon dioxide permeation. *Advanced Functional Materials*, 2005. 15(10): p. 1635-1640.
189. Triani, G., et al., Nanostructured TiO₂ membranes by atomic layer deposition. *Journal of Materials Chemistry*, 2006. 16(14): p. 1355-1359.
190. Losic, D., et al., Controlled pore structure modification of diatoms by atomic layer deposition of TiO₂. *Journal of Materials Chemistry*, 2006. 16(41): p. 4029-4034.
191. Liang, X., et al., Barrier properties of polymer/alumina nanocomposite membranes fabricated by atomic layer deposition. *Journal of Membrane Science*, 2008. 322(1): p. 105-112.
192. Nam, S.-W., et al., Ionic Field Effect Transistors with Sub-10 nm Multiple Nanopores. *Nano Letters*, 2009. 9(5): p. 2044-2048.
193. Liang, X., et al., Modification of nanoporous supported lyotropic liquid crystal polymer membranes by atomic layer deposition. *Journal of Membrane Science*, 2010. 349(1-2): p. 1-5.
194. Narayan, R.J., et al., Atomic layer deposition of nanoporous biomaterials. *Materials Today*, 2010. 13(3): p. 60-64.
195. Lee, H.J., et al., A high-performing nanostructured TiO₂ filter for volatile organic compounds using atomic layer deposition. *Chemical Communications*, 2011. 47(19): p. 5605-5607.
196. Li, F., et al., Modification of ceramic membranes for pore structure tailoring: The atomic layer deposition route. *Journal of Membrane Science*, 2012. 397: p. 17-23.

**Chapter2. Synthesis of ALD Zinc oxide thin
film and zinc oxide/Aluminium oxide
nanolaminates: studies of their structural and
optical properties.**

Synthesis of ALD Zinc oxide thin film and zinc oxide/Aluminium oxide nanolaminates: studies of their structural and optical properties.

1. Introduction.....	51
2. Bibliographic records of ZnO films, Al₂O₃ films and Al₂O₃ /ZnO nanolaminates.....	51
2.1.Zinc oxide.....	51
2.2.Aluminum oxide.....	52
2.3.Al ₂ O ₃ /ZnO Nanolaminates.....	53
3. Development of the Atomic layer deposition (ALD) set up.....	54
3.1.Atomic layer deposition of zinc oxide thin film.....	56
3.2. Atomic layer deposition of Aluminum oxide.....	59
4.Chemical and structural Characterization of ZnO ALD thin film.....	61
4.1.SEM cross section.....	61
4.2.Ellipsometry.....	62
4.3.Energy-dispersive X-ray spectroscopy (EDX).....	63
4.4.Grazing incidence X-Ray diffraction (GIXRD).....	64
4.5.Transmission Electron Microscopy (TEM).....	67
4.6.Atomic force microscopy.....	67
5. Optical Characterization of ZnO ALD thin films.....	68
5.1.Transmittance test.....	69
5.1.1.Band gap and Urbach energy calculation.....	69
5.2.Photoluminescence and absorption.....	72
5.2.1.ZnO band gap estimation based on Photoluminescence and absorption measurement.....	75
6.Correlation between optical and structural properties.....	76
7.Conclusion.....	78

8. Al₂O₃ ALD thin film.....	79
8.1. SEM observation.....	79
8.2. Ellipsometry.....	80
8.3. Energy-dispersive X-ray spectroscopy (EDX).....	81
9. ALD of Aluminum oxide/ Zinc Oxide nanolaminates.....	82
9.1. Chemical and structural characterization of Al ₂ O ₃ /ZnO nanolaminates.....	83
9.1.1. SEM observations.....	83
9.1.2. Energy-dispersive X-ray spectroscopy (EDX).....	84
9.1.3. Grazing Incidence X-ray Diffraction.....	85
9.1.4. Atomic force microscopy (AFM).....	87
9.2. Optical Characterization of Al ₂ O ₃ /ZnO nanolaminates.....	89
9.2.1. Transmittance measurement.....	89
9.2.2 Ellipsometry.....	92
9.2.3. Photoluminescence.....	97
9.3. Conclusion.....	100
10. General conclusion.....	101

1. Introduction

Thin film coating of semiconductors insulators and conductive materials has such importance in the electronic and optical field. Miniaturization of electronic devices to improve their properties and to reduce their cost motivates the researcher to the development of several new techniques for the elaboration of thin film materials and to improve their properties in term of high chemical purities, conformal coating, and high thickness control ability. As demonstrated in chapter 1, among all the deposition techniques used for thin film elaboration, Atomic Layer Deposition (ALD) meet all those request in term of chemical purities, conformal coating on high aspect ratio materials and high thickness control ability. Different types of materials have been elaborated by ALD for different applications (Chapter 1). In this chapter we will report on the synthesis of ZnO and Al_2O_3 /ZnO nanolaminates by ALD method with their structural and optical properties investigation using different characterization techniques. Different parameters have been calculated such as thickness, grain size, refractive index, extinction coefficient, Urbach energy and band gap. A correlation between the structural and the optical properties have been established in order to extract the structural behavior on the optical properties. ZnO and Al_2O_3 /ZnO nanolaminates show promising structural and optical properties that can be appealing for different applications.

2. Bibliographic records of ZnO films, Al_2O_3 films and Al_2O_3 /ZnO nanolaminates

2.1. Zinc oxide

Zinc oxide (ZnO) is an n-type transparent conductive oxide (TCO) with excellent optoelectronic properties, a wide band gap (3.36 eV), a high dielectric constant, a high exciton binding energy (60 meV), and a high thermal stability[1]. Hence it is an important material for different applications in devices such as gas sensors [2], biosensors [3], transducers [4], solar cells [5-7], electronic and optoelectronic instruments (*i.e.* ultraviolet photo-detectors) [8], surface acoustic wave (SAW) gadgets [9], and transparent electrodes[10]. ZnO crystals with a grain size in the range of 1–50 nm have demonstrated interesting optical properties, such as a UV shift of the absorption edge and

strong photoluminescence at room temperature caused by quantum confinement[11] and, an improvement of the photovoltaic and sensor performance due to a high surface area[12, 13]. ZnO nanostructures are obtained as nanoparticles [14], nano-tubes [15], nano-wires [5, 7], and ultra-thin films[16, 17]using different elaboration techniques. Ultra-thin ZnO films can be synthesized using different deposition techniques such as sol-gel [18], chemical vapor deposition[19],electro-deposition [5-7],RF sputtering,and atomic layer deposition (ALD) [16, 17].It is well known that the optoelectronic properties of zinc oxide thin film[20, 21] are strongly dependent on their structure [11, 22]. Crystallinity and stoichiometry of the film determine the concentration of point defects (zinc and oxygen vacancies, interstitial zinc and oxygen)[20]. The band gap of ZnO nanostructures decreases from 3.29 to 3.23 eV with an increase of the grain size [21]. The electrical conductivity of ZnO is affected by a defect concentration and diminishes at annealing in an oxygen environment (oxygen vacancy healing) [21]. One of the methods applied to analyze the crystalline structure and defect level in zinc oxide is photoluminescence. It has been shown that ZnO exhibits a narrow UV emission band in the 378–381 nm range and a broad emission band in the range of 480–620 nm [23-25]. The UV emission band in ZnO has been related to exciton emission, whereas the visible emission has been related to radiative transitions involving intrinsic defects point (O/Zn vacancies and O/Zn interstitials) [23, 24]. In this chapter we will discuss the evolution of the microstructure and related optical properties of ZnO grown by atomic layer deposition[25].

2.2. Aluminum oxide

Aluminum oxide (Al_2O_3) is an electrical insulator with low dielectric constant (approx. 9), a relatively high thermal conductivity of ($30\text{Wm}^{-1}\text{K}^{-1}$) and a large band gap. Hence Al_2O_3 is an important material for different applications in optical and electronic fields such as a dielectric films for non-volatile semiconductor memories (NVSM)[26], dynamic random-access memory (DRAM)capacitors[27],and metal-oxide-semiconductor field-effect transistor(MOS-FETs)[28]. It was also used as gas diffusion barrier on polymer substrate[29] and to tune the pore size of anodic aluminum membranes for different applications such as gas separation[30]. ALD of Al_2O_3 was the typical model of ALD, different studies and characterization for different applications have been achieved and reported [31-40].

2.3. Al₂O₃ /ZnO Nanolaminates

Composites materials with novel properties have attracted attention in different fields. One of those structures is nanolaminates: composite films formed by alternating layers of different materials, with an individual layer thickness on the nanometric scale [41-43]. These multilayered structures often demonstrate unique properties such as high dielectric constants and advanced mechanical, electrical and optical properties [17, 44, 45]. The latter depends on the constituent materials, forming the nanolaminates [41-43]. Fundamental properties of ZnO can be tailored by doping[1]. It is known that doping of ZnO with Al or/and Al₂O₃ modified its structural, electrical and optical properties [46-51].

ALD technique is a powerful method for the fabrication of superlattice materials. ALD deposited Al₂O₃: ZnO (1:x) nanolaminates with the number of deposition cycles, “x”, ranging from 5 to 30 have been studied [49, 52]. A Comparison of the XRD spectra of ZnO and Al₂O₃: ZnO(1:x) nanolaminates indicated the change of the ZnO growth direction and the deposition of ZnO parallel to the substrate surface when deposited on Al₂O₃ layer. Surface roughness of Al₂O₃:ZnO (1:x) nanostructures was lower than for the bare ZnO on glass. The roughness value decreased at the range of 2-10 % Al doping and then slightly increased in the range 12-24 %[52]. Investigation of optical properties of Al₂O₃/ZnO (1:x) showed the increase of the band gap versus Al doping concentrations from 3.28 to 3.7[49, 52]. Blue shift of band gap could be explained by Al doping of ZnO layers and high concentration of oxygen vacancies (Burstein-Moss effect) and quantum confinement effects [49, 52]. It was found that Al₂O₃ buffer layer led to an increase of near band edge (NBE) emission and a decrease of deep level emission (DLE) emission[53]. The ratio of NBE/DLE intensities was above 60. The decrease of the DLE of ZnO films with Al₂O₃ buffer layer was directly related to the decrease of oxygen vacancies concentration on the interfacial layer. The proposed model supposed the oxygen atoms to be removed from the amorphous Al₂O₃ layer and occupy the oxygen vacancies at the initial stage of the growth of ZnO films to improve its crystallization [41, 42]. Bi-layered ALD deposited Al₂O₃/ZnO nanolaminates have been investigated by Wang *et al*[53]. Quantum confinement effects in ZnO can appear in case of encapsulation into a dielectric core, changing electrical, dielectric and optical properties [54, 55]. Due to this, ZnO thin layers (thickness less than 50 nm) surrounded by dielectric media, formed by Al₂O₃ are expected to demonstrate quantum confinement effects. Despite

a high number of papers on nanolaminates fabrication and their structural and mechanical properties, optical properties of $\text{Al}_2\text{O}_3/\text{ZnO}$ nanolaminates are not investigated yet.

3. Development of the Atomic layer deposition (ALD) setup

Our ALD reactors (Figure 1) is a homemade reactor that combines a low-vacuum system based on a rotary vane pump, a circular vacuum chamber with 2 inch sample stage heated up to 230°C , three pneumatic three way valves and a two ways valves supplied by Swagelok fixed to the circular chamber using VCR connections. Those three pneumatic three way valves consist a double input valves that was used as precursor input (input1 related to the precursor bottles; input 2 related to the gas vector). Valves can be controlled manually to do some purge step before starting the deposition and after the precursor refilling. Manifold (input valves support) and exhaust channel can be heated up to 250°C . Beside this a heating option for two precursor bottles is available up to 120°C to enhance the vapor pressure of some precursors. ALD precursors were filled into a stainless bottle from Swagelok in a glove box under argon atmosphere due to the high precursor reactivity under oxygen and moisture atmosphere. A mass flow that can be controlled between 0 and 100 sccm, has been used to control the gas vector during the pulse and the purge steps. A Pirani gauge was coupled to the reactor with a manual valve to protect it during deposition. Five omicron temperature controllers have been used to control the chamber, exhaust, valves and precursors temperatures. The entire system can be controlled electronically by Labview. Our Labview program is based on 6 different functions reported in table 1.

Table 1. ALD function description

Function	Setup
Pulse precursor 1	Valve 1 open; Exhaust closed; Mass flow can be controlled between 0 and 100 sccm
Pulse precursor 2	Valve 2 open; Exhaust closed; Mass flow can be controlled between 0 and 100 sccm
Pulse precursor 3	Valve 3 open; exhaust closed; Mass flow can be controlled between 0 and 100 sccm
Exposure	All valves are closed; Mass flow is set to zero
Purge	Valves 1,2, and 3 are closed; Only exhaust valve is open; Mass flow can be set between 0 and 100 sccm
Evacuate	Valves 1,2, and 3 are closed; Only exhaust valve is open; Mass flow is set to 0 sccm

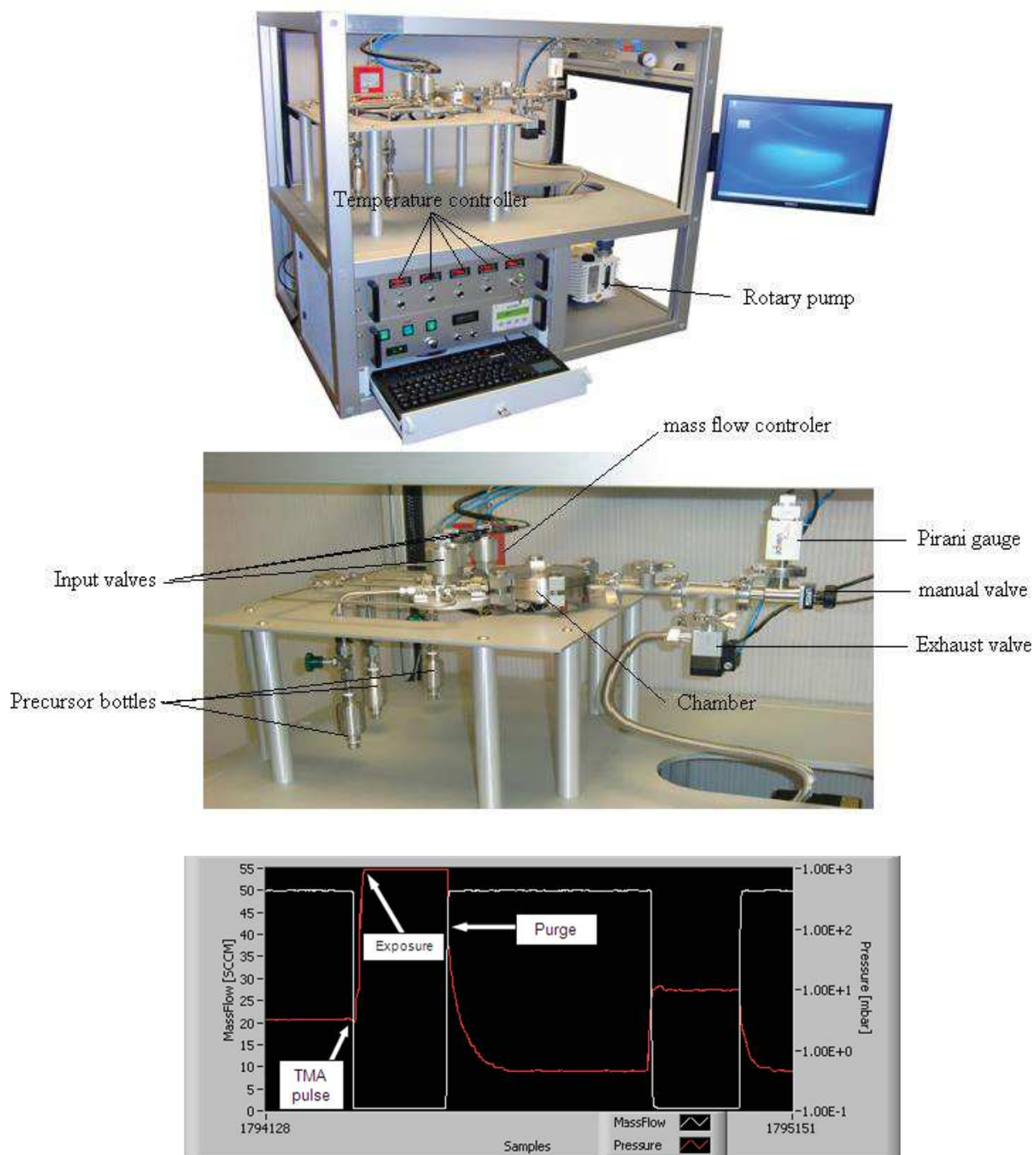


Figure 1. The homemade ALD reactor

We should note that the system has been coupled to an argon gas bottle (Ar) as gas vector beside an air generator compressor for pneumatic valves supplying. The air pressure was fixed at 6 bars for a proper valves operation.

3.1. Atomic layer deposition of zinc oxide thin film

ALD ZnO was performed using Diethyl zinc (DEZ) and water. Before loading the substrate into the reactor chamber, substrate was cleaned by ethanol then washed with distilled water and finally dried with a dry air flow. After loading, the ALD chamber was purged for 2 min under 100sccm argon flows than evacuated for 1 minute to reach the 10^{-2} mbar pressure. Due to their high vapor pressure at room temperature, both of precursors have been kept at room temperature. To avoid precursor condensation into the precursors input valves and the exhaust unit, manifold and exhaust unit have been heated at 20°C higher than the ALD reactor chamber.

Before starting the ALD deposition of Zinc oxide, many parameters should be fixed such as ALD windows, pulse time, exposure time and purge time for both of DEZ and H₂O to assure a good ALD process and to avoid precursor decompositions or CVD process. Different ZnO ALD windows were reported in the literature for DEZ such as 100-170°C[56] and 200-300°C [57]. Different parameters can be behind these different values such as precursor purity or temperature dispersion issues inside the reactor chamber due to different setup design. To avoid this mismatch we start to define our ZnO ALD window (Figure 2) matching our home made reactors. 250 cycles was performed in a temperature range between 50 and 230°C with the highest pulse exposure and evacuation times (Table 2) to assure a complete ALD reaction and to avoid CVD. Than those samples have been characterized by Elipsometry and SEM.

Table2. Setup used for ZnO deposition during the identification of the ZnO ALD window.

	DEZ Pulse	Exposure	purge	Water pulse	Exposure	Purge
Time/flow	2s/25sccm	60s/0sccm	60s/100sccm	4s/25sccm	60s/0sccm	60s/100sccm

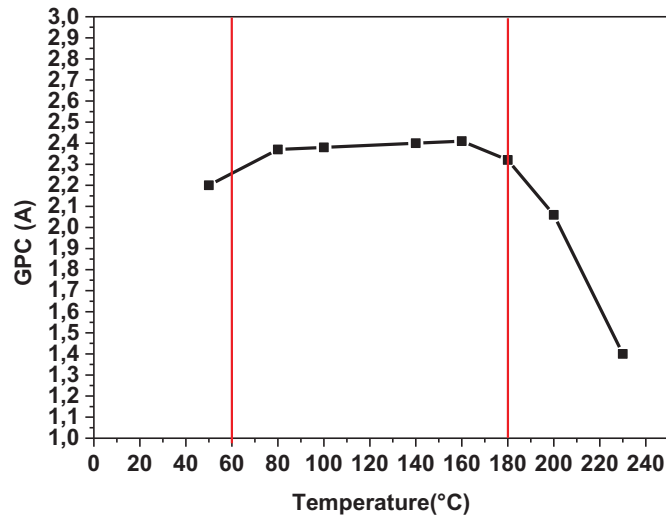


Figure 2. ALD windows du ZnO

Figure 2 shows a constant growth per cycle of 2.4 Å per cycle in the extended temperature range from 60 to 230°C. After the identification of the ZnO ALD Windows, all ZnO deposition has been performed between 60 and 180°C. Lim *et al.*[58] report the GPC of ZnO in a temperature range between 100 and 250°C, the growth rates increase with increasing temperatures at low growth temperature, reaching highest value of 2.0 Å/cycle at 175 °C. Above 175 °C, the growth rates decrease again to 1.12 Å/cycle at 250 °C. The same behavior was reported on our case: an increase of the GPC up to 160°C with a decrease at higher temperature. Tapily *et al.*[56] show the ALD window of ZnO to be between 100 and 170°C, with a growth rate of 0.2 nm per cycle. This difference between the GPC reported in our case and the corresponding value reported in the literature can be due to the different deposition parameters such as purge and exposure time. Moreover the reported study on the literature has been performed on others ALD reactors coupled with highest vacuum system capability.

After the identification of the ZnO ALD windows, pulse, exposure and purge time for DEZ and water was investigated (Table 3).

Table 3. Step times investigation of ZnO ALD

Step	Time interval (s)/Argon mass flow(Sccm)
Pulse DEZ	0.1-2/25
Exposure for DEZ	10-60/0
Purge of DEZ	10-60/100
Pulse water	0.1-4/25
Exposure to water	10-60/0
Purge of Water	10-60/100

250 cycles have been deposited at 100°C using those different parameter times. Unconformable coating was visually detected for exposure and purge time less than 40 seconds (figure3a) indicating inadequate exposure time and incomplete evacuation. Also a non-conformal coating was visually detected for DEZ pulse under 0.2 seconds and water pulse under 2 seconds (Figure3b) indicating an insufficient amount of precursor. Table 4 shows the optimized parameters used for the deposition of ZnO on flat substrates.

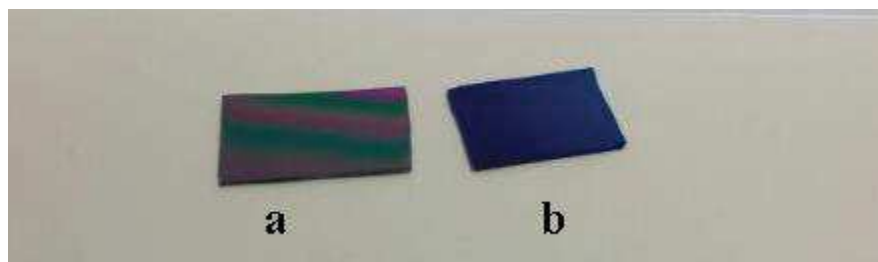


Figure 3. Unconformable ZnO ALD coating; due to inadequate exposure time and incomplete evacuation (a), due to insufficient amount of precursors (b)

Table 4. Setup used for ZnO deposition on flat substrate at 100 °C.

	DEZ Pulse	Exposure	purge	Water pulse	Exposure	Purge
Time/flow	0.2s/25sccm	30s/0sccm	40s/100sccm	2s/25sccm	30s/0sccm	40s/100sccm

By reducing the exposure and purge time from 60s to 30s and 40 s for both of DEZ and water precursors, the ALD process was become 50% faster.

3.2. Atomic layer deposition of Aluminum oxide

For the Al_2O_3 ALD deposition, trimethylaluminium (TMA) and water was used as precursors. The same cleaning and loading process were used as for ZnO. In order to define the Al_2O_3 ALD window, 250 cycles of Al_2O_3 was performed in a temperature range between 40 and 230°C using the following sequence (Table5), than characterized by SEM cross-section and ellipsometry to extract the growth rate per cycle.

Table5. Setup used for Al_2O_3 ALD deposition during the identification of the ALD window

	TMA Pulse	Exposure	Purge	Water pulse	Exposure	Purge
Time/flow	2s/25sccm	60s/0sccm	60s/100sccm	4s/25sccm	60s/0sccm	60s/100sccm

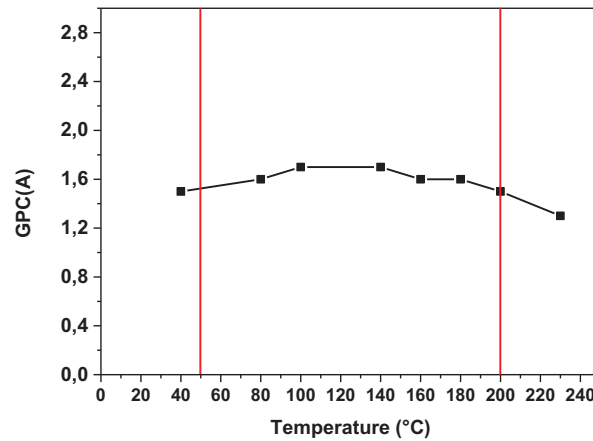


Figure 4. Al_2O_3 ALD Window

Figure 4 shows a constant growth per cycle of 1.7 Å per cycle in the extended temperature range from 50 to 200°C. Groner *et al.*[59] reports approximately the same Al_2O_3 ALD window with a growth rate per cycle that change between 1.1 and 1.24 Å per cycle when the deposition temperature go from 33°C to 175°C. After the identification of the Al_2O_3 ALD window, all Al_2O_3 deposition was

performed between 50 and 200°C. After the identification of the Al_2O_3 ALD window, pulse, exposure and purge time for TMA and water have been investigated (Table 6).

Table 6. Step times investigation of Al_2O_3 ALD.

Step	Time interval (s)/Argon mass flow(sccm)
Pulse TMA	0.1-2/25
Exposure for TMA	10-60/0
Purge of TMA	10-60/100
Pulse water	0.1-4/25
Exposure to water	10-60/0
Purge of water	10-60/100

250 cycles have been deposited at 100°C using those different parameter times. Unconformable coating was visually detected for exposure and purge time less than 40 seconds (Figure5a) indicating inadequate exposure time and incomplete evacuation. Also a non-conformal coating was visually detected for water pulse under 1 seconds (Figure5b) indicating an insufficient amount of precursors. TMA pulsed of 0.1 s was enough to fill up the entire reactor chamber due to the high vapor pressure of TMA. Table 7 shows the optimized parameters used for the deposition of Al_2O_3 on flat substrate.

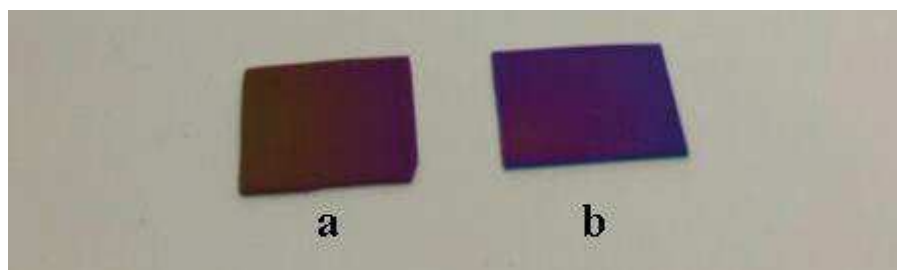


Figure 5. Unconformable Al_2O_3 ALD coating; due to inadequate exposure time and incomplete evacuation (a) due to insufficient amount of precursor (water) (b)

Table7.Setup used for Al_2O_3 deposition at 100 C.

	TMA Pulse	Exposure	purge	Water pulse	Exposure	Purge
Time/flow	0.1s/25sccm	30s/0Sccm	40s/100Sccm	2s/25Sccm	30s/0Sccm	40s/100Sccm

4. Chemical and structural Characterization of ZnO ALD thin film

Atomic layer deposition of ZnO thin films with different numbers of cycles between 100 and 1000 were elaborated using the setup mentioned in Table 3 at 100°C on silicon and glass substrates. Then it was characterized by SEM, EDX, DRX, TEM, GIXRD, and AFM. Optical characterization such as absorption, transmittance and photo-luminescence tests were also performed.

4.1 SEM cross section

SEM cross section was performed on the ZnO ALD films elaborated and mentioned above using an emission field Hitachi S-4800 microscope. Figure 6 shows the SEM cross-sections of 200, 500 and 1000 cycles of ZnO, due to its low thickness the 100 cycles sample was not observed by SEM.

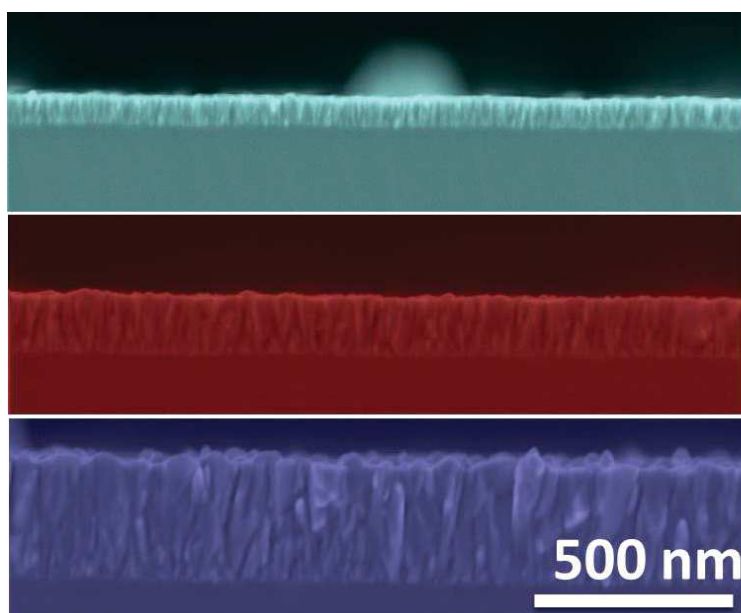


Figure 6. Cross-section SEM a) 200 cycles ZnO; b) 500 cycles ZnO and 1000 cycles ZnO

Chapter 2. Synthesis of ALD Zinc oxide thin film and zinc oxide/Aluminium oxide nanolaminates: studies of their structural and optical properties.

SEM cross-section images (Figure 5) show a conformal ZnO ALD coating with a columnar growth increasing with the layer thickness inducing an increase of surface roughness. Table8 reports the thickness measured by SEM and the extracted GPC.

Table 8. ZnO thickness of 100, 200, 500 and 1000 ALD cycle extracted from the SEM cross section measurement

Number of ZnO cycles	Thicknesses(nm) measured by SEM
100	-
200	45±5
500	120±5
1000	241±5
GPC	0.238±5

4.2. Ellipsometry

Ellipsometric measurement was performed on the same series deposited on Si substrate using a Semilab GES5E spectroscopic ellipsometer (of extended visible range: 1.23–5 eV) under conditions of a fixed incident angle of 75° close to the Brewster's angle of silicon substrate, and variable wavelength between 300 nm and 1 µm. Winelli II software was used to fit the experimental $\tan(\psi)$ and $\cos(\delta)$ data in the full wavelength range by using Cauchy dispersion law and a single layer ZnO adjusted model to obtain the film thickness. Table9 shows the thickness value extracted from the ellipsometry measurement with a correlation coefficient of 0.99.

Table 9. ZnO thickness of 100, 200, 500 and 1000 ALD cycle s extracted from the ellipsometric measurement.

Number of ZnO cycles	Thicknesses(nm) measured by ellipsometry
100	25
200	49.8
500	124
1000	250
GPC	0.249

SEM and ellipsometry thickness measurements show the same growth per cycle value about 0.24nm per cycle. A growth rate of 2 angstrom per cycle was calculated in the ALD process window[60]. As we discuss above in paragraph 3.1 this difference between the GPC reported in our case and the corresponding value reported in the literature can be due to the different deposition parameters such as purge and exposure time. Moreover the reported study in the literature has been performed on others ALD reactors coupled with higher vacuum system capability.

4.3. Energy-dispersive X-ray spectroscopy (EDX)

EDX measurement was also performed on the same samples in order to have a qualitative/quantitative representation of the chemical composition of the ALD ZnO Layers. EDX measurement was carried out using a Hitachi S-4500 microscope coupled with a Thermofisher EDX detector. EDX has been calibrated with commercial ZnO powder of known stoichiometry. Figure 7 presents the EDX measurement performed on 100,200,500 and 1000 cycles of ZnO ALD at 100°C. Table 10 reports the quantitative composition of the ZnO layers with the O/Zn Ratio.

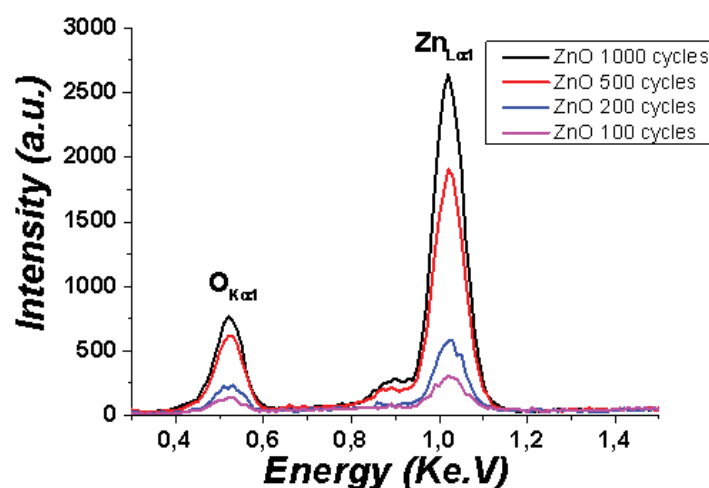


Figure 7. EDX measurement of 100, 200, 500 and 1000 ZnO ALD cycles

Table 10. Quantitative compositions of ZnO layers and the O/Zn Ratio for different ZnO ALD thicknesses.

ZnO number of cycles	O content (% at)	Zn content (% at)	O/Zn ratio
100	66	33	2
200	63	37	1.7
500	58	42	1.38
1000	56	44	1.27

A non-stoichiometric ratio between Zn and O (>1) indicates an Oxygen excess that can be due to residual OH⁻ and a partially hydroxylated phase ZnO (OH) due to the incomplete removal of excess H₂O at such a low temperature or to a fraction of unreacted hydroxyl groups observed earlier[61, 62]. As seen from Table 9, the O/Zn ratio decreases with increasing the thickness.

4.4. Grazing incidence X-Ray diffraction (GIXRD)

In order to identify the crystalline phases of the deposited ZnO layers, Grazing incidence X-Ray diffraction (GIXRD) was carried out on the same ALD ZnO samples using A Bruker D5000 instrument. GIXRD has been performed instead of normal XRD because it is more adapted method to characterize the crystallinity of thin layers (Figure 8).

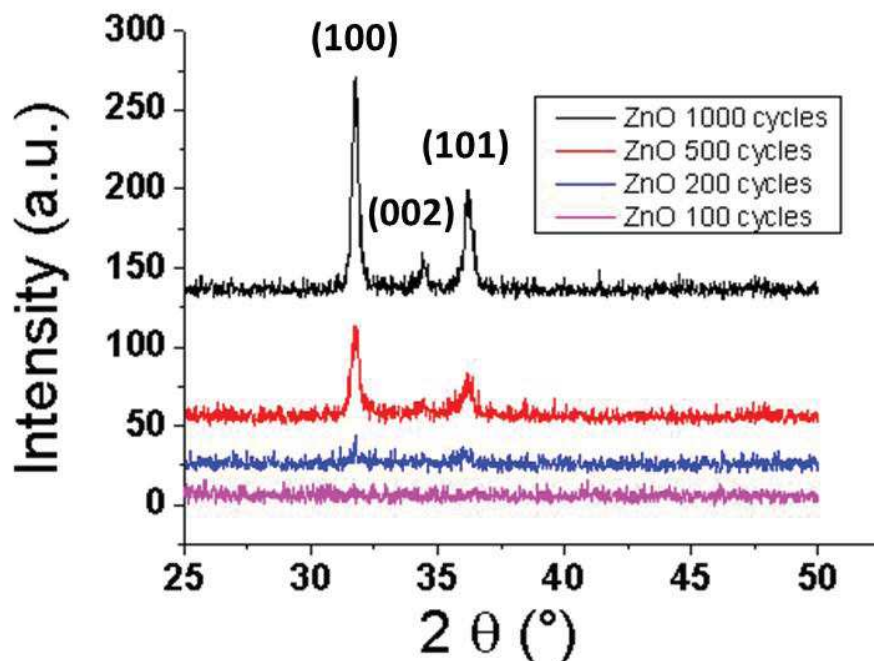


Figure9. GIXRD of 100,200, 500 and 1000 ZnO ALD cycles

GIXRD measurement reports a transition from an amorphous state to a crystalline state when the ZnO thickness increases. We note here that the used GIXRD machine has a limit for detecting the minimum size for nanocrystals of 4 nm. So an amorphous state at 25 nm can be due to a crystalline grain size less than 4 nm or to an amorphous structure. At 49.8nm ZnO thickness, two weak peaks appear at $2\theta = 31.74$ and 36.22° respectively corresponding to (100) and (101), those two peaks become more intense at 124 and 250 nm with an additionally peak at $2\theta = 34.42^\circ$. Using the GIXRD diagram, the warren averbach techniques with winfitsoftware, lattice constant, grain size and lattice strain were calculated. The Lattice constants calculated from GIXRD diagram of 49.8, 124, and 250 nm thick ZnO films are equal to $a = 0.325$ nm and $c = 0.52$ nm. No drastic changes of lattice parameters are observed with increasing the film thickness. The maximum values of the texture coefficients (TC) for 49.8, 124, and 250 nm thick ZnO films calculated according to Rivera *et al.* [63] (1.2, 1.66, 2.12, respectively) match the preferred growth in the (100) direction. Grain size and lattice strain evolution over the ZnO layer thicknesses are reported at Figure 10. An increase in the ZnO grain size with a decrease on the lattice strain extracted from the GIXRD measurements is observed on Figure 10.

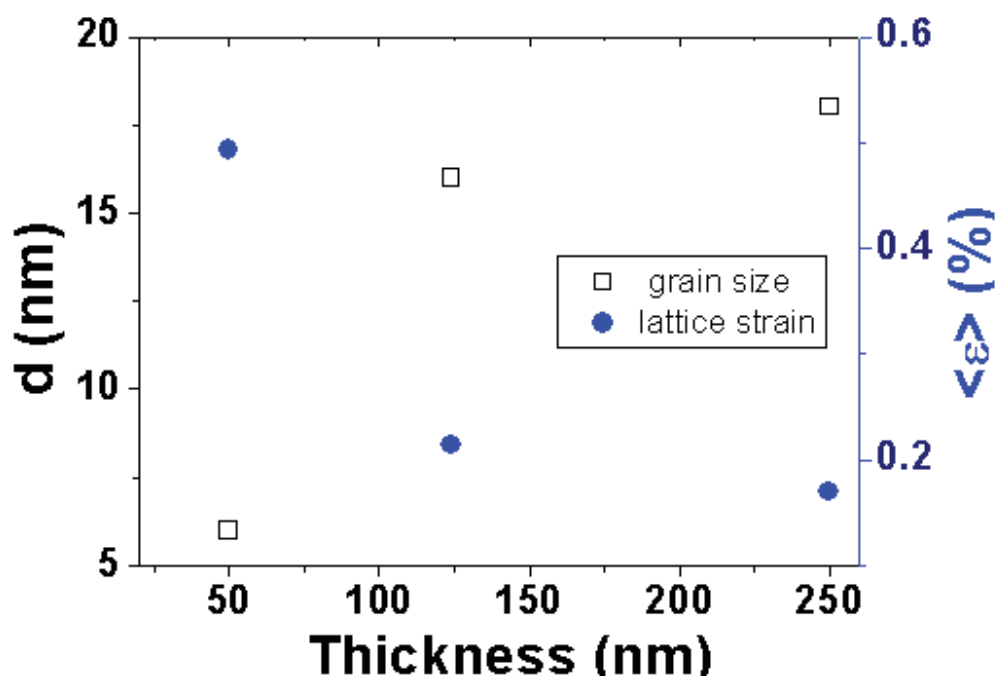


Figure10. Grain size and lattice strain in ZnO ALD films of different thickness.

4.5. Transmission Electron Microscopy (TEM)

TEM cross-section was performed at 1000 ZnO ALD cycle (Figure 11).

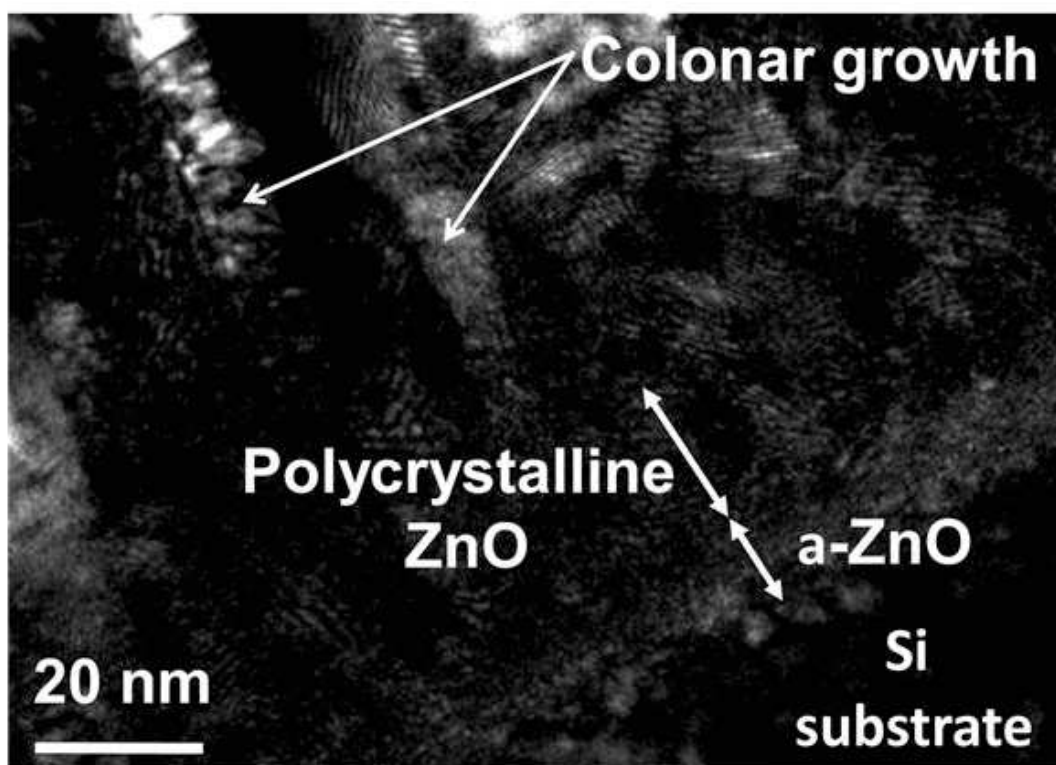


Figure 11. Cross section TEM image of a 1000cycles ZnO ALD film deposited on Si substrate.

TEM cross section shows an amorphous ZnO layer below 20 nm. Nanocrystalline grains randomly oriented in the ultrathin films are observed between 20 and 50 nm thick films. Finally a columnar growth for a thickness higher than 50 nm is observed. This result confirms the SEM observations and the GIXRD measurement.

4.6. Atomic force microscopy

Surface morphology of the samples was studied by atomic force microscopy in order to identify the relation between the layer thickness and the surface roughness (Figure12a).

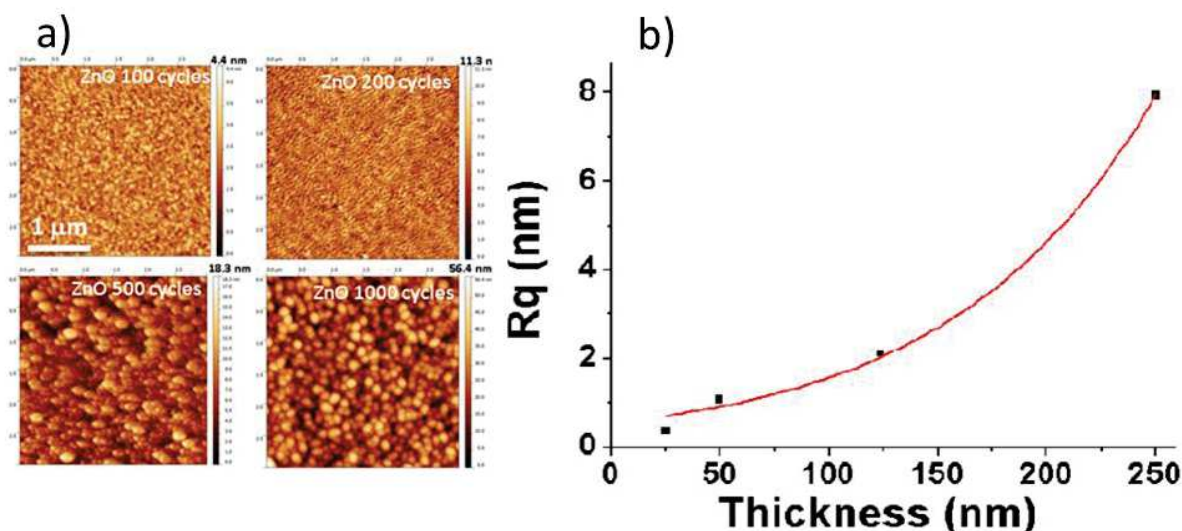


Figure 12. AFM measurement for the ALD ZnO films of different thicknesses: a) AFM photo for different ZnO thicknesses; b) the mean-square roughness R_q versus thickness.

AFM images show a smooth surface for ALD ZnO layer with the thickness less than 100nm. Well shaped 100-150 nm elevations are observed on the surfaces of thicker samples. The mean-square roughness (R_q), calculated from AFM data increases with the ZnO thickness (Figure 12b).

5. Optical characterization of ZnO ALD thin films

After the chemical and structural characterization of the ZnO ALD thin films series, optical characterizations have been performed on the same samples in order to study the evolution of optical properties when the ZnO thickness increases. Transmittance, absorbance and photoluminescence were performed. A Shimadzu UV-1700 spectrophotometer was used to study the optical properties of ZnO thin films by 1 nm step over the 300–1100 nm range, and photoluminescence in the 370–800 nm range. A solid state LCS-DTL-374QT Nd:YAG 355 nm

Chapter 2. Synthesis of ALD Zinc oxide thin film and zinc oxide/Aluminium oxide nanolaminates: studies of their structural and optical properties.

laser source (Russia) at the intensity of 19 mW/cm^2 was used to excite the luminescence. Emission spectra were registered by the experimental setup described elsewhere by Viter *et al.*[64].

5.1. Transmittance test

Transmittance tests were performed on the ALD ZnO films with different thicknesses (Figure 13).

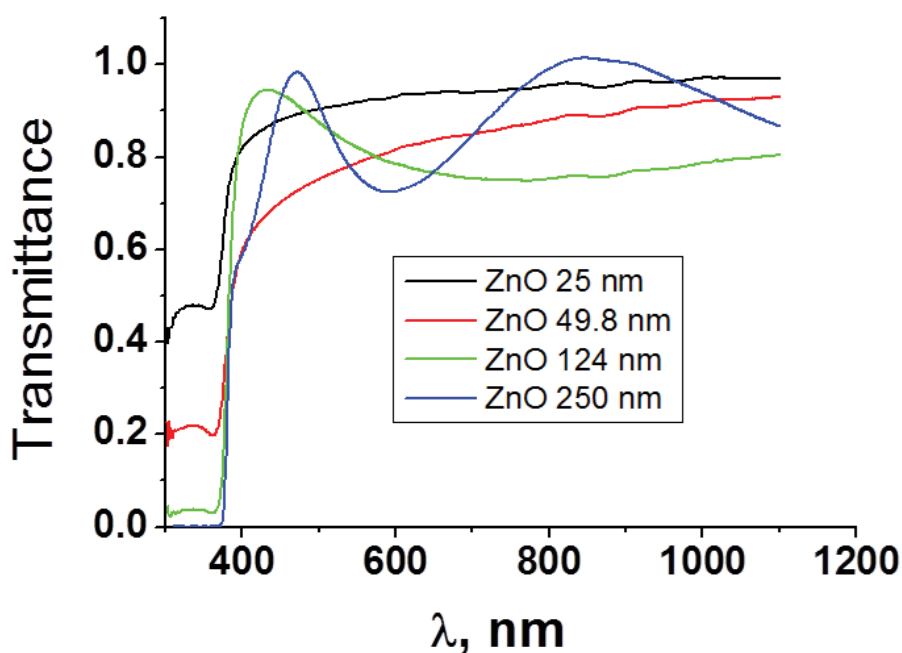


Figure 13. Transmittance spectra of the ZnO ALD films with different thicknesses.

As shown in Figure 13, ZnO layers with a thickness less than 100 nm are transparent in the 500-1100 nm range. ZnO layers with a thickness higher than 100 nm show a maximum and minimum transmittance in the same range.

5.1.1. Band gap and Urbach energy calculation

Based on the transmittance spectra and the n-Type proprieties of ZnO with the direct optical transitions, graphical estimation of the band gap (Figure 14) was performed using equation 1 and equation 2.

Chapter 2. Synthesis of ALD Zinc oxide thin film and zinc oxide/Aluminium oxide nanolaminates: studies of their structural and optical properties.

$$D = \ln\left(\frac{1}{T}\right) \quad (\text{Equation 1})$$

Where D is the optical density and T is the optical transmittance.

$$(D \cdot hv)^2 \sim (hv - E_g) \quad (\text{Equation 2})$$

Where hv is the photon energy and E_g is the band gap.

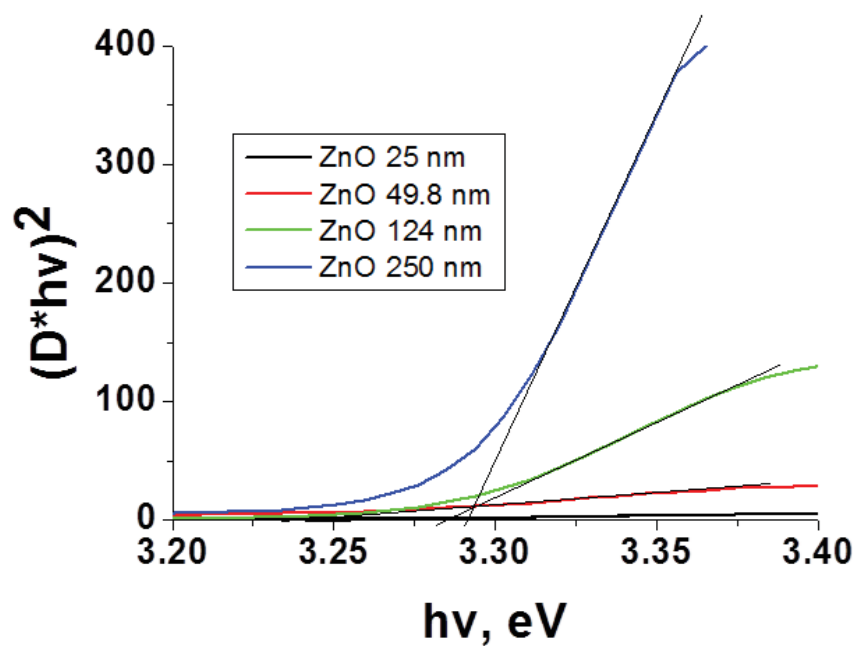


Figure 14. Band gap estimation of the ALD ZnO samples with different thicknesses

Band gap values corresponding to the different ZnO thicknesses extracted from the transmittance spectra are reported on Table 11.

Chapter 2. Synthesis of ALD Zinc oxide thin film and zinc oxide/Aluminium oxide nanolaminates: studies of their structural and optical properties.

Table 11. Band gap value calculated from the transmittance spectra for different ZnO thicknesses

ZnO thickness(nm)	Band gap (eV)
25	3.26
49.8	3.24
124	3.28
250	3.3

The Urbach energy E_0 has also been calculated using the Urbach law (Equation 3), and reported in Table 12.

$$D = D_0 \cdot \exp\left(\frac{h\nu}{E_0}\right) \quad (\text{Equation 3})$$

Table 12. Urbach energy E_0 calculated using the Urbach law for different ZnO ALD thicknesses

ZnO thickness(nm)	Urbach energy (eV)
25	0.16
49.8	0.18
124	0.075
250	0.056

The estimated Band gap and the calculated Urbach energy were reported against the ZnO thickness in Figure 15.

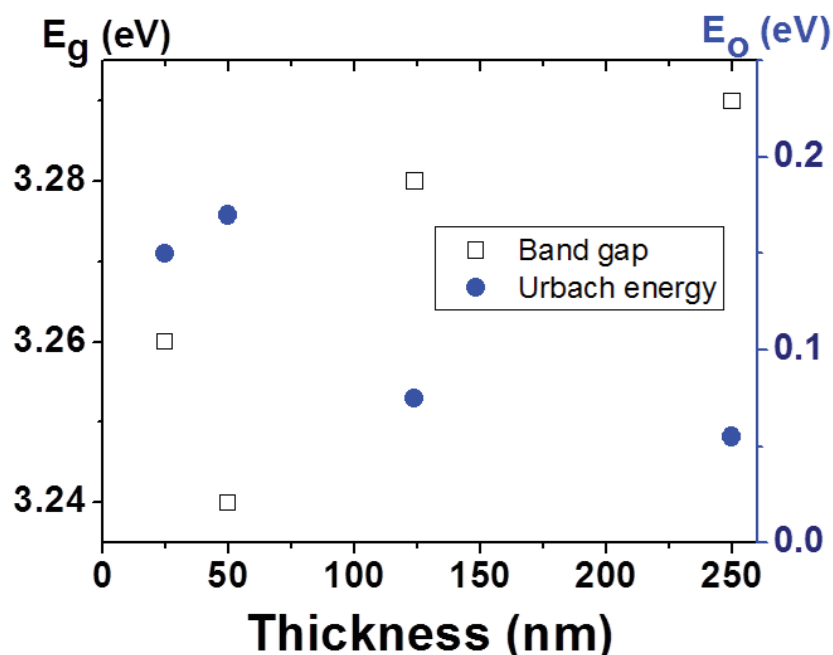


Figure 15. Band gap and Urbach energies of ZnO ALD films of different thicknesses

As shown in Figure 15, an uncharacteristic change of the band gap and the Urbach energy have been observed when the ZnO thickness increases.

5.2. Photoluminescence and absorption

Photoluminescence and absorption measurement was performed on the ALD ZnO films with different thicknesses and reported in Figure 16. According to the Beer–Lambert law, the penetration depth of the laser spot in the ALD deposited thin films is between 40 and 44 nm which mean the photoluminescence comes from the substrate and the ZnO film for the 25 nm thick layer. For the thicker layer the photoluminescence is limited to the ZnO layer.

Chapter 2. Synthesis of ALD Zinc oxide thin film and zinc oxide/Aluminium oxide nanolaminates: studies of their structural and optical properties.

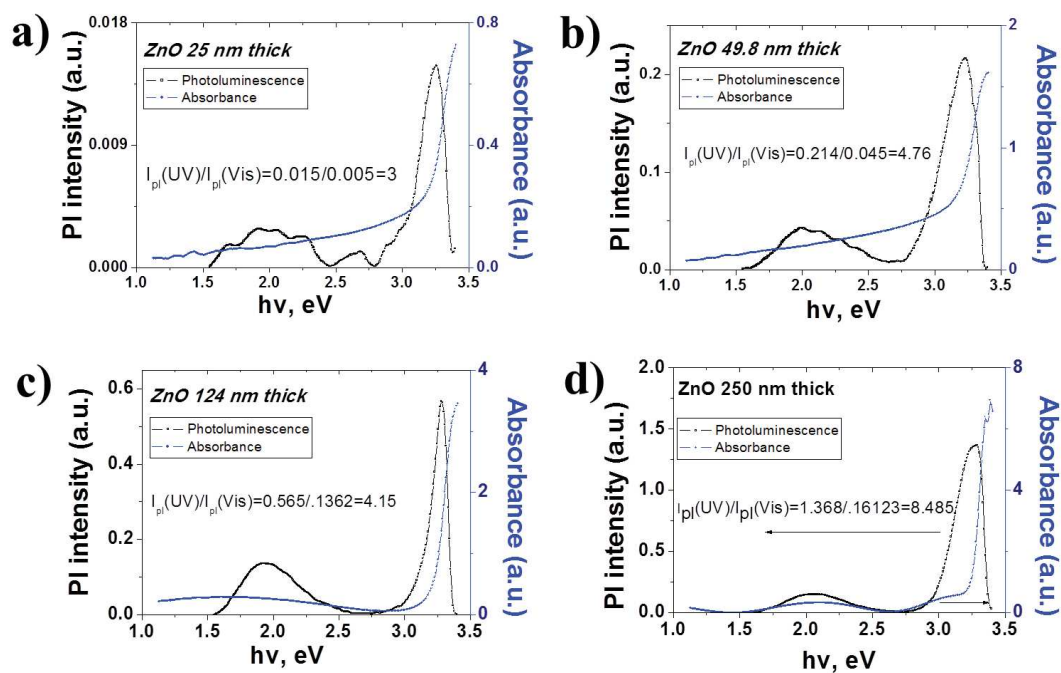


Figure 16. Photoluminescence and absorption spectra of 25 (a), 49.8 (b), 124 (c), and 250 nm (d) thick ZnO ALD films.

The shapes of the PL bands have been fitted to a Gaussian peak function by the Origin 7.0 software and presented in Figure 17.

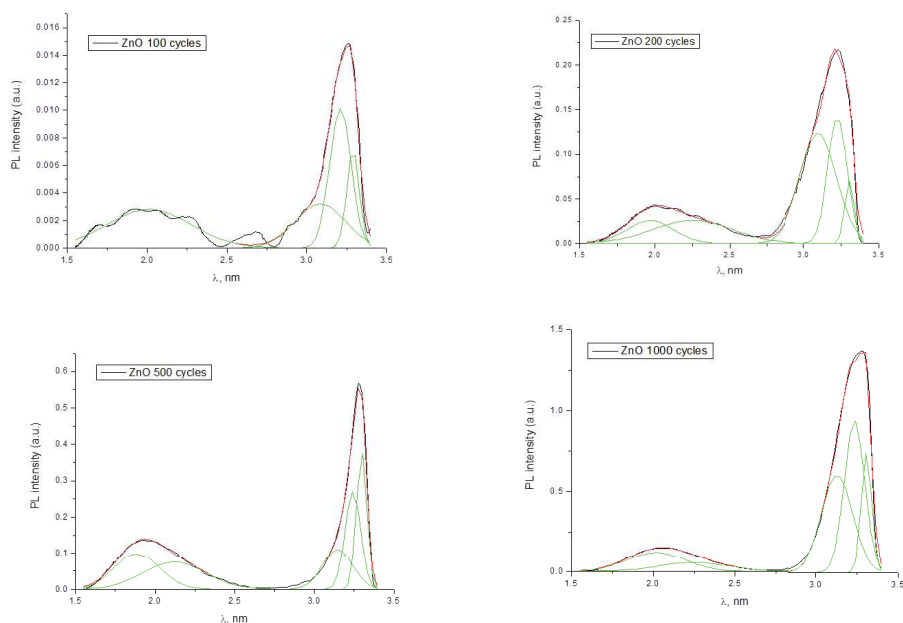


Figure 17. Gaussian fit of PL spectra for 25, 49.8, 124, and 250 nm thick ZnO ALD films.

PL spectra of ZnO films of different thicknesses show two emission bands at 3.08–3.30 eV (UV band) and 1.80–2.28 eV (VIS band). Peaks intensity increases when the ZnO thickness increases. Photoluminescence peaks position and absorption values are shown in Table 13. Cui *et al.*[65] attributed the 3.28–3.30 eV PL Peak in the Absorption edge region to the band–band transitions. Giriet *al.*[66] reported that the 3.21–3.24 eV peaks is related to a transition in the band-tail states of ZnO. Wanget *al.*[67] attributed the observed 3.21–3.24 eV emission to electron transitions from tail states of the conduction band to tail states of the valence band. According to Djurišić *et al.*[68] the 3.08–3.14 eV UV peaks correspond to defect states formed by neutral Zn vacancies ($V(Zn)^0$). Chen *et al.*[69] suggests that the visible emission is caused by defect points. The 2.21–2.25 eV peaks are attributed to oxygen interstitials (O_i). According to Wanget *al.*[18], Emission bands at 1.9–2.0 eV of ZnO ALD ultrathin films are due to doubly ionized oxygen vacancies ($V(O^{++})$) [70]. Absorption spectra have tails and peaks in the 3.2–1.78 eV range matching the optical transitions defect state–valence band and the defect state–conduction band.

Table13. Positions of absorption and PL peaks of ZnO thin films of different thicknesses.

Thickness (nm)	Peak positions			
	V(O ⁺⁺) (eV)	(Oi) (eV)	V(Zn ⁰) (eV)	Band tail states (eV)
25	2.01103		3.08374	3.21019
49.8	1.96819	2.24953	3.09573	3.22453
124	1.88601	2.12068	3.14621	3.24162
250	2.01575	2.24768	3.12942	3.2352

5.2.1. ZnO band gap estimation based on Photoluminescence and absorption measurement.

Equation 4 was used to estimate ZnO band gap(Table14) where E_x is the exciton emission energy, E_g is the band gap, E_b is the exciton binding energy($E_b=0.06\text{eV}$). \hbar , k , m_{ex} are respectively the Plank's constant, wave vector, and effective mass of the exciton.

$$E_x = E_g - E_b + \frac{\hbar^2 \cdot k^2}{2 \cdot m_{ex}} \quad \text{(Equation 4)}$$

Table14. Band gap estimation based on photoluminescence and absorption measurement.

Thickness (nm)	ZnO band gap estimation
25	3.34
49.8	3.31
124	3.35
250	3.36

Since ZnO is a direct band gap semiconductor, the wave vector $k=0$ and the value of the energy gap of the samples, according to Eq. 4, is around 3.35-3.36 eV. The difference between estimations and the experimental data are due to structural defects.

6. Correlation between optical and structural properties.

ALD ZnO Crystallinity, grain size, roughness and stoichiometric ratio have been tuned by the ZnO film thickness. A transition from an amorphous phase to a crystalline phase with an improvement on the crystallinity when the ALD ZnO film thickness increases was clearly observed by the GIXRD measurement. The quantitative composition of the ZnO film was measured by the EDX. A O/Zn ratio higher than 1 is observed. In addition it decreases when the ZnO film thickness increases. This non-stoichiometric oxygen-rich film can be due to Zn vacancies, oxygen interstitials and oxygen interstates[71]. Comparing to the GIXRD measurement with the AFM and EDX measurement, low ZnO ALD thickness correspond to low grain size, high grain boundaries surface, in other terms when the ZnO thickness increases the grain boundaries surface decreases and the oxygen/Zinc ratio decreases which can be due to an absorption oxygen layer localized on the grain boundaries forming a negative surface charge and depletion layer as well as to residual OH⁻ and a partially hydroxylated phase ZnO (OH). The electric field of the surface charge in the depletion layer would stimulate the dissociation of the excitons in ZnO.

PL spectra reported defect states at 3.08-3.14eV due to the neutral Zn vacancies. It shows also a peak at 2.21-2.25eV that identifies interstitial oxygen. Due to those 2 peaks, PL spectra shows oxygen-rich samples correlate well with the EDX results. Another peak at 1.9-2 eV related to double ionized oxygen vacancies are also found in the PL spectra related to the active role of the surface effect in the emission spectra. The band gap energy widening, the UV emission intensity increase, and the Urbach energy decrease are related to the enhancement of ZnO crystallinity due to thickness increase.

Increasing the ZnO film thickness leads to the decrease of the grain size inducing a decrease of the active surface area and affects negatively the concentration of oxygen adsorbed on the grain surface. This oxygen percentage decreases due to thickness increases, decreasing the Vis

PL peak related to the adsorbed oxygen on the grain surface leading to a growing of the UV/Vis intensity ratio in ZnO PL as reported on Figure 18.

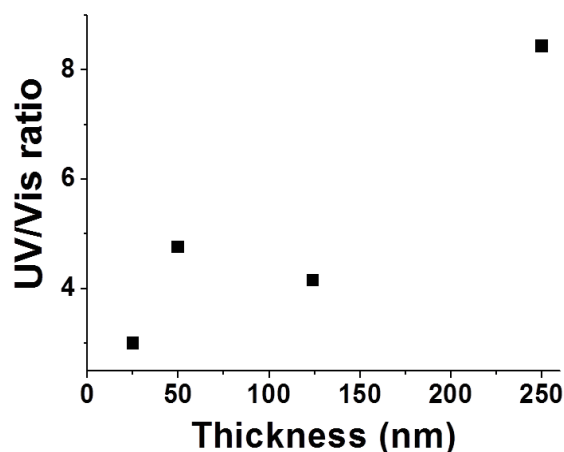


Figure 18. UV/Vis intensity ratio of ZnO ALD films of different thicknesses.

According to Liu *et al.* [72] and Reshchikov *et al.*[73], the photo-generated electrons and holes in the depletion region are known to be separated by a strong electric field. The negative charge at the surface and the band bending upward are primarily caused by the adsorbed species (oxygen, hydroxyl groups, etc.). According to Reshchikov *et al.*[73] under the steady-state conditions, the equilibrium is achieved between the flow of holes to the surface and the flow of electrons to the “bulk” region. The flow of holes reaching the surface reduces the surface charge and, therefore, the bending of the surface band. As result, the near-surface electric field and the width of the depletion region decrease when the intensity of the excitonic PL increases.

Liao *et al.*[70] and Wang *et al.* [18]reported that the decrease of the depletion layer in ZnO nanostructures being capable to stimulate transitions between neutral, single-charged, and doubly ionized oxygen vacancies assisted by a UV shift of the visible emission. The neutral oxygen vacancies are located in the bulk, whereas the doubly ionized vacancies are located in the depleted region.

However, in the present study neither the UV shift of the visible emission, nor emission peaks corresponding to neutral oxygen vacancies have been observed. By the UV/Vis ratio

completely depleted and partially depleted, ZnO grains can be distinguished[18,48]. The first is related to the case of the UV/Vis ratio being much less than 1, the latter is related to the UV/Vis ratio exceeding 1. Since the UV/Vis ratio exceeds 1 in all measured cases, the samples should contain partially depleted grains. Thus, the oxygen vacancies could be formed as point defects mostly in the surface region in an oxygen rich environment, the concentration in bulk of the grains being negligible. Therefore, the change of the width of the depleted layer should not affect the emission from oxygen vacancies.

7. Conclusion

Different thicknesses of ultra-thin ZnO films were grown using the atomic layer deposition technique (25 nm to 250 nm). A transition from amorphous to polycrystalline state was reported when the ZnO thickness increases. An increase of the crystalline grains size is accompanied by a decrease of lattice strain, a rise of the Zn/O ratio, and an uncharacteristic change of the energy gap due to a decrease of the defects point concentration and an improvement of the film crystallinity. Due to those structural defects, ZnO thin film band gap is lower than bulk ZnO crystals band gap. UV and Visible photoluminescence emissions peaks in ZnO thin films correspond to band-edge and defect-related transitions, respectively. Additional UV emissions are observed from band-tail states. The defects related to observed PL bands are identified as neutral Zn vacancies, interstitial oxygen, and doubly ionized oxygen vacancies. The optical properties correlate with the crystalline structure, the point defect concentration, the grain size, and the depleted layer. The Crystalline structure improvement when the ZnO thickness increases, was reflected in the photoluminescence spectra by an increasing on the UV emissions intensity. The oxygen excess is attributed to formation of Zn vacancies, oxygen interstitials and adsorbed molecular oxygen on the surface of grains.

8. Al_2O_3 ALD thin film

Al_2O_3 ALD films with a number of cycles varying between 100 and 1000 cycles were elaborated using the setup mentioned in Table 6 at 100°C on Silicon substrate. The samples were characterized by SEM, EDX and ellipsometry.

8.1. SEM observation

SEM cross section was performed on the Al_2O_3 ALD films elaborated and mentioned above using a high Resolution Scanning Electron Microscope (HRSEM), Hitachi S-4800 microscope. Due to their dielectrical properties, metallization have been realized before the SEM observation. Figure 19 shows the SEM cross-section of 1000 cycles of Al_2O_3 .

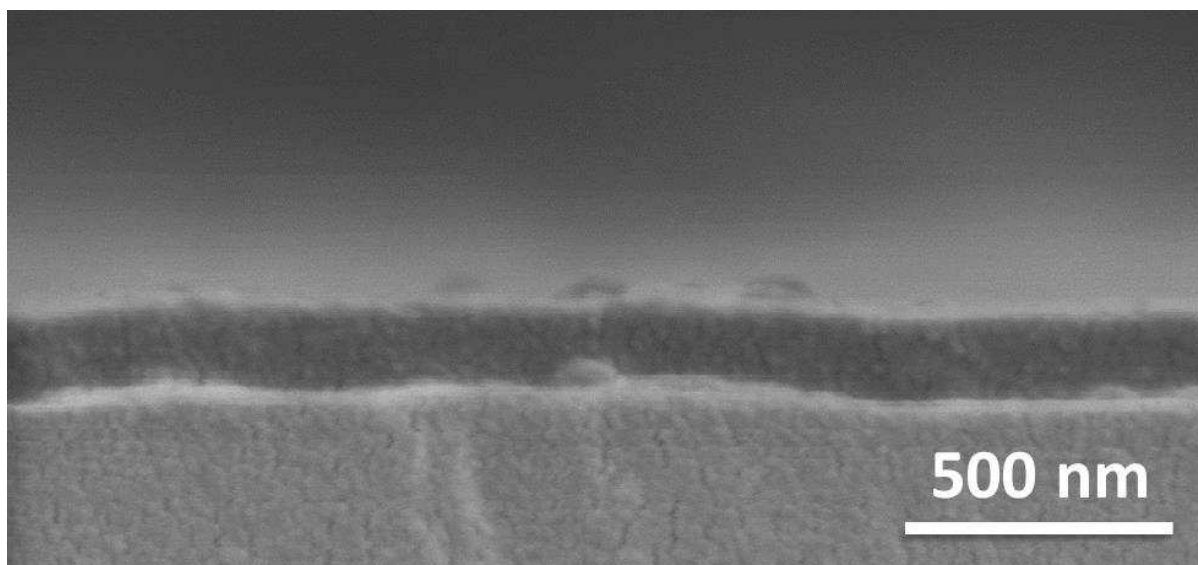


Figure 19. SEM cross-section of films deposited using 1000 Al_2O_3 ALD cycles.

SEM cross section image shows a conformal coating. Table 15 reports the Al_2O_3 thickness measured by SEM for films deposited using 200, 500 and 1000 Al_2O_3 ALD cycles and the extracted GPC. Due to the dielectric properties of aluminum oxide the thinnest layer corresponding to 100 cycles Al_2O_3 was difficult to be observed by SEM.

Table 15. Al_2O_3 thicknesses of 100, 200 and 500 ALD cycles extracted from the SEM cross section measurement.

Number of Al_2O_3 cycles	Thicknesses measured by SEM cross section
100	-
200	37.5
500	82
1000	170
GPC	0.17

The growth rate per cycle for Al_2O_3 ALD at 100°C extracted from the SEM cross-section measurement is about 0.17nm per cycle.

8.2. Ellipsometry

Ellipsometric measurement was performed on the same samples deposited on Si substrate using a Semilab GES5E spectroscopic ellipsometer (of extended visible range: 1.23–5 eV) under conditions of a fixed incident angle of 75° close to the Brewster's angle of silicon substrate, and variable wavelength between 300 nm and 1 μm . Winelli II software was used to fit the experimental $\tan(\psi)$ and $\cos(\delta)$ data in the full wavelength range by using Cauchy dispersion law and a single layer Al_2O_3 adjusted model to obtain the film thickness. Table 16 shows the thickness value extracted from the ellipsometric measurement with a correlation coefficient of 0.99.

Table 16. Al_2O_3 thicknesses of 100, 200, and 500 ALD cycle extracted from the ellipsometric measurement.

Number of Al_2O_3 cycles	Thicknesses (nm) measured by ellipsometry
100	19.9
200	36.5
500	80
GPC	0.17

A growth per cycle of 0.17 nm was extracted from the SEM cross-section observation and the ellipsometry measurements. The reported Al_2O_3 growth per cycle in the literature is about 0.11 and 0.12 nm per cycle [74, 75].

8.3. Energy-dispersive X-ray spectroscopy (EDX)

EDX measurement was also performed on 1000 cycles Al_2O_3 ALD layer deposited on silicon substrate. EDX measurement was carried out using a Hitachi S-4500 microscope coupled with a Thermofisher EDX detector. EDX has been calibrated with commercial Al_2O_3 powder of known stoichiometry. Figure 19 presents the EDX measurement performed on 1000 cycles of Al_2O_3 at 100°C.

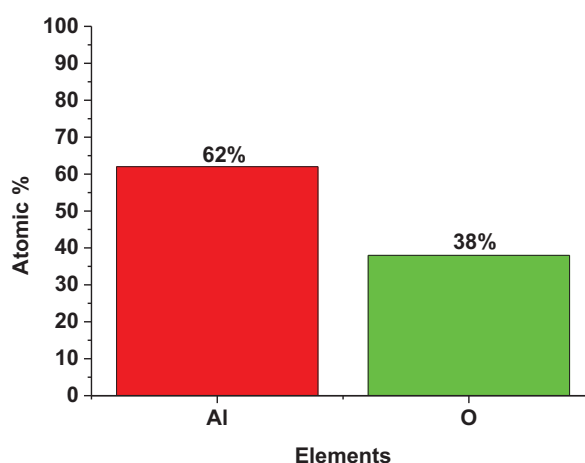


Figure 20. EDX measurements for 1000 cycle Al_2O_3 deposited at 100°C.

Figure 20 shows a stoichiometric ratio between Al(38%) and O(62%). Moreover the EDX measurement does not show any residual carbon which confirms a complete ALD reaction between trimethylaluminium (TMA) and water at 100°C. The stoichiometric ratio Al/O and the complete ALD reaction verified by the EDX measurement confirmed the sufficient purge time used in Table 6.

Since the Al_2O_3 elaborated by ALD present an amorphous structure[76], GIXRD was not done on the ALD Al_2O_3 samples. Growth rate per cycle and chemical characterization have been achieved in order to use the Al_2O_3 as a doping material for ZnO ALD layer and to investigate his effect on the structural and optical properties of $\text{Al}_2\text{O}_3/\text{ZnO}$ nanolaminates. A growth rate per cycle of 0.17 nm per cycle at 100°C has been extracted from the SEM and the ellipsometric measurements. Moreover the EDX measurements confirm the stoichiometric ratio and the complete ALD reaction between trimethylaluminium (TMA) and water at 100°C.

9. ALD of Aluminum oxide/ Zinc Oxide nanolaminates

In this study, three different $\text{Al}_2\text{O}_3/\text{ZnO}$ ALD nanolaminates sequences were elaborated by ALD(Table17) at 100°C using the ALD setup reported on Table 18. 1000 cycles of ZnO were also deposited in order to be used as reference during the characterization.

Table 17. Three nanolaminates sequences of $\text{Al}_2\text{O}_3/\text{ZnO}$.

Samples	Sequences Nbr of sequences*(number of Al_2O_3 cycle/number of ZnO cycles)
A1	1000 cycles ZnO
A2	2(250/250)
A3	10(50/50)
A4	50(10/10)

Table 18. Al₂O₃ and ZnO ALD deposition setup

	Al ₂ O ₃ setup P1=TMA; P2=H ₂ O	ZnO setup P1=DEZ; P2=H ₂ O
P1 Pulse time	0.1	0.2
Exposure to P1	30	30
Purge	30	30
P2 Pulse time	2	2
Exposure to P2	30	30
Purge	40	40

9.1. Chemical and structural characterization of Al₂O₃/ZnO nanolaminates

SEM cross section, EDX, GIXRD and AFM were performed on the nanolaminate with different sequences in order to study the chemical and structural properties of the obtained materials.

9.1.1. SEM observations

SEM cross section images have been realized on the ZnO and the nanolaminates structure in order to assure the ability to perform nanolaminates structures using the ALD technique with a conformal coating. Figure 21 shows the SEM cross-section images of A1,A2 and A3 samples.

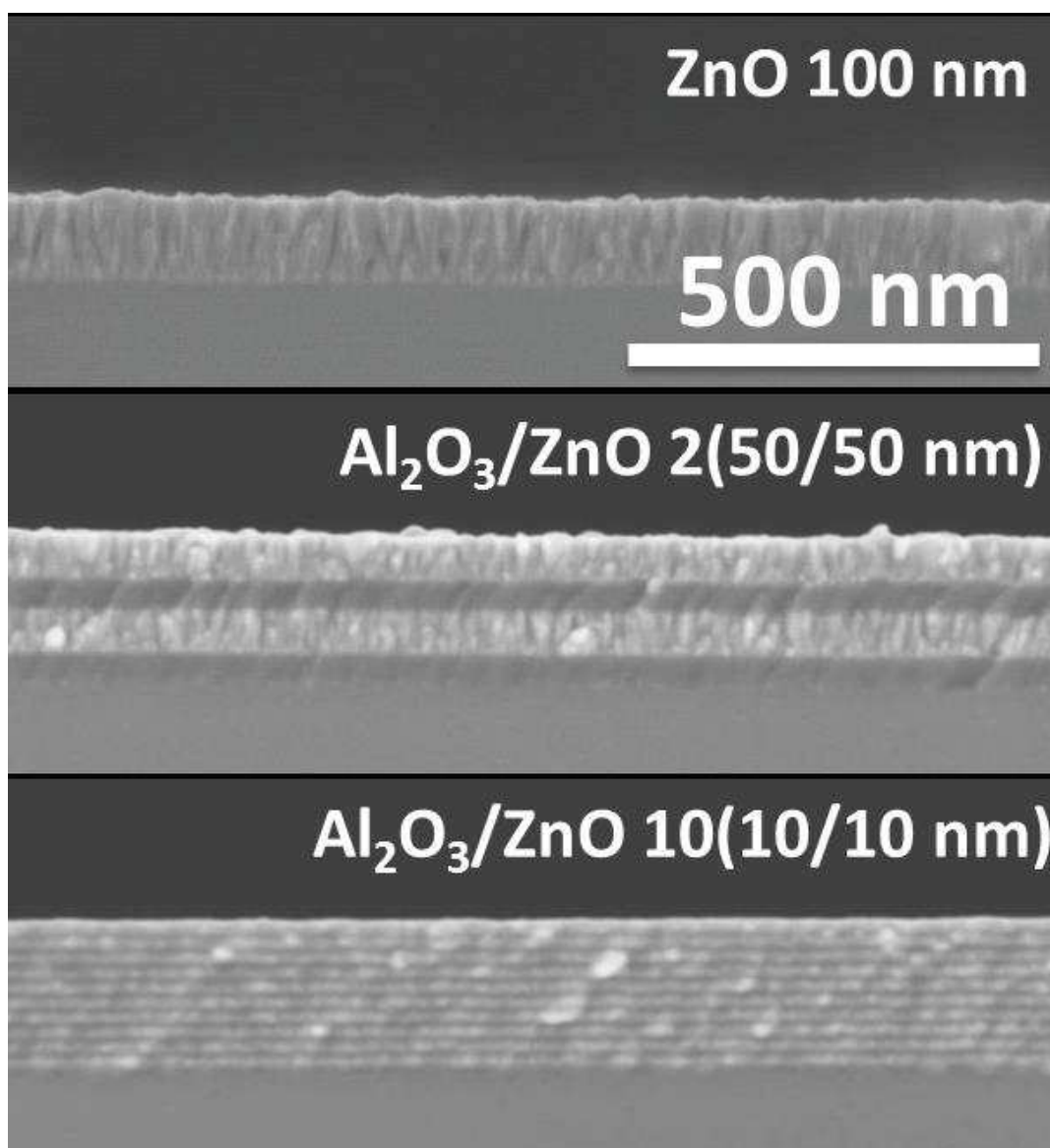


Figure 21. SEM cross section image of samples A2, and A3 samples.

SEM cross section shows a conformal coating with a well-defined nanolaminates structure for the thickest bilayer thicknesses (A2, A3). Due to her thinnest bilayer thickness (less than 3nm), the nanolaminates structures of the A4 sample was not observed by SEM. The growth rates per cycles of Al₂O₃ and ZnO in the nanolaminates vary between 1.4 to 2 Å per cycle and 1.8 to 2 Å per cycle respectively. Since the surface chemistry changes, the growth rate per cycle may evolve during deposition.

9.1.2. Energy-dispersive X-ray spectroscopy (EDX)

EDX measurement was also performed on the nanolaminates with different sequences deposited on silicon substrate. EDX measurement was carried out using a Hitachi S-4500 microscope coupled with a Thermofisher EDX detector. Figure 22 present the EDX spectra performed on the nanolaminates.

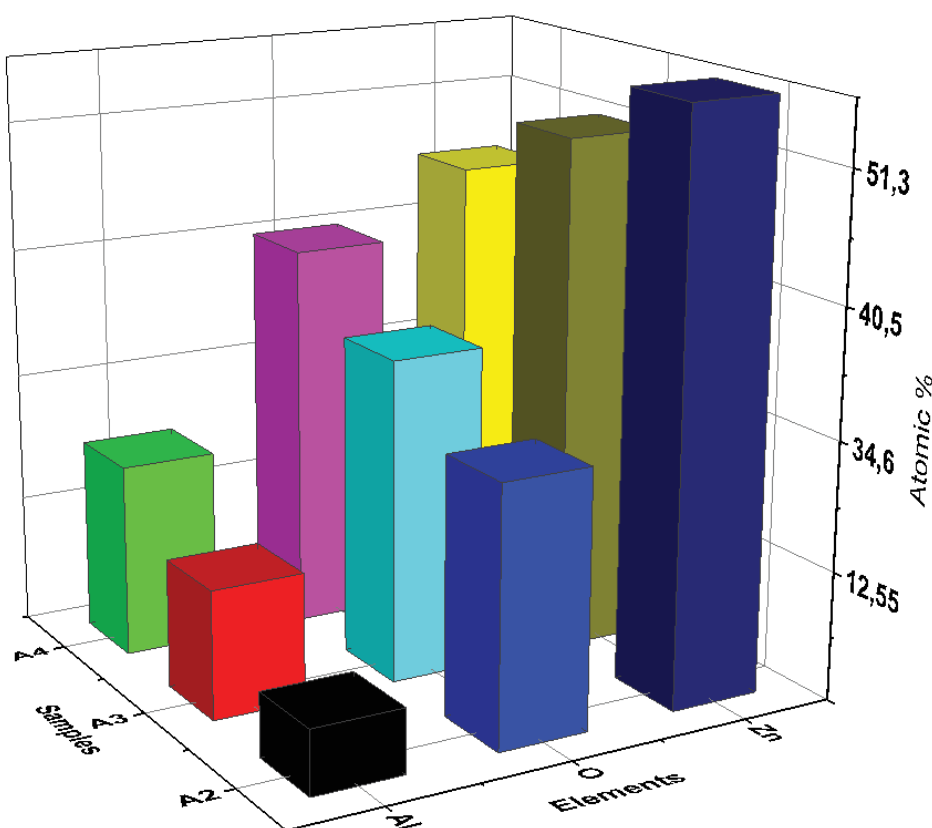


Figure 22. EDX measurement of A1,A2,A3, and A4 Samples

Figure22 reports the Al, Zn and O presence without any residual carbon confirming the ALD complete reaction at such temperature with the setup mentioned above in Table 18. As we can show in Figure 22, when the bilayer number increases the Al and O atomic percentage

increases and the Zn atomic percentage decreases. This Zn atomic percentage decreases when the bilayer number increases can be related to the ZnO etching by the $\text{Al}(\text{CH}_3)_3$ precursor during the Al_2O_3 ALD cycles as reported elsewhere at 177°C by Elam *et al.*[77]. The Al atomic percentage increases can be related as well to the increase of the Al_2O_3 density deposited on ZnO due to the residual OH^- and the partially hydroxylated phase $\text{ZnO}(\text{OH})$ on the surface of the ZnO grains as reported in paragraph 4.3.

9.1.3. Grazing Incidence X-ray Diffraction

Grazing Incidence X-ray Diffraction was performed in all the deposited samples mentioned in Table 17 in order to understand the Al_2O_3 interlayer effect on the ZnO growth(Figure 23).

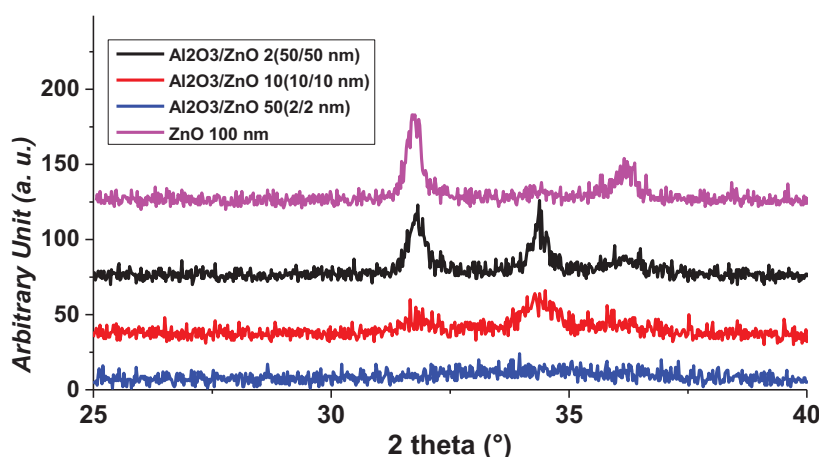


Figure 23. GIXRD spectra of A1, A2, A3 and A4 samples

Figure 23 shows a transition from amorphous state to crystalline state on the GIXRD spectra when the bilayer thickness increases. In addition, when we compare the nanolaminates to the ZnO monolayer, a change of the crystalline direction is observed. The thinnest bilayer thickness sample (A4) showed a weak broad X-ray diffraction peak at 34.26° that can be due to their amorphous structure or their crystalline size below 4nm. When the bilayer thickness increases three XRD peaks appear at $2\theta = 31.82^\circ$ and 34.35° and weak peak at $2\theta = 36.1^\circ$

corresponding to (100), (002) and (101) reflections of ZnO, respectively. For the thicker bilayer thickness, “A2”, strong peaks at $2\theta = 31.74^\circ$ and 34.35° have been observed with a low intensity peak at $36.1-36.2^\circ$. When we compare the thicker nanolaminate sample “A2” to the single ZnO film “A1”, a transition in the preferential growth orientation can be clearly seen. A strong (002) and a weak (101) XRD peaks is observed for A2 samples. A weak (002) and strong (101) XRD peaks is observed for the A1 sample. Table 19 reports the lattice constants, the d-spacing between the atomic planes, the texture coefficients (TC) and the grain size for ZnO single films and $\text{Al}_2\text{O}_3/\text{ZnO}$ nanolaminates with different sequences calculated using the XRD peaks.

Grain size calculation

Debye-Scherrer equation has been used to calculate the grain size (Equation 5):

$$D = \frac{0.9 \cdot \lambda}{\beta \cdot \cos(\theta)} \quad (\text{Equation 5})$$

Where λ , β and θ are X-ray wavelength, full width at half maximum (FWHM) and diffraction angle, respectively. Table 19 shows the grain size value calculated using the Debey-Scherrer equation. Since the particles are of unknown morphologies, the shape factor is set to 0.9.

Table 19. lattice constant, d-spacing, texture coefficient and grain size

	$\text{Al}_2\text{O}_3/\text{ZnO}$ 50 (2/2 nm) A4	$\text{Al}_2\text{O}_3/\text{ZnO}$ 10 (10/10 nm) A3	$\text{Al}_2\text{O}_3/\text{ZnO}$ 2 (50/50 nm) A2	ZnO (100 nm) A1
Lattice constant				
a(nm)	-	0.3244	0.3247	0.3253
c(nm)	0.523	0.5218	0.5215	0.5213
d-spacing				
d (100) (nm)		0.2809	0.2812	0.2849
d (002)(nm)	0.2615	0.2609	0.2607	0.2606

d (101) (nm)	-	0.2481	0.2485	0.2478
Texture coefficient				
[100]	-	0.66	1.28	1.66
[002]	-	2.07	1.52	0.237396
[101]	-	0.27	0.2	0.468436
Grain size	2	7	14	16

When the bilayer thickness increases the lattice constant (a) increases and the lattice constant (c) decreases. Nanolaminates lattice constant (a) for samples A2 and A3 is lower than ZnO lattice constant (a) "A1". Contrariwise nanolaminate lattice constant (c) for samples A2, A3 and A4 is higher than ZnO lattice constant (c) "A1". This increase on the lattice parameter (c) can be related to the interstitial Al incorporation in the interface between ZnO and Al₂O₃[48]. This Al doped ZnO interlayer can vary from 0.1 to 1 nm when the bilayer thickness increases from 4 nm to 100 nm. The d-spacing (100) is higher for ZnO single layer "A1" compared to that of Al₂O₃/ZnO 2 (50/50 nm) "A2" and Al₂O₃/ZnO 10 (10/10 nm) "A3". For the d-spacing (002), samples A2, A3 and A4, it is a bit higher than for ZnO single layer "A1". For the nanolaminate with higher bilayer thickness has higher d-spacing (101), contrariwise ZnO d-spacing (101) is lower than the nanolaminates d-spacing (101). Nanolaminates Texture coefficients (TC) calculation demonstrated that the (002) direction is the preferred growth orientation. In thicker bilayers (Al₂O₃/ZnO 2 (50/50 nm)), lateral growth in (100) direction was observed (TC = 1.28).

9.1.4. Atomic force microscopy (AFM)

The surface morphology was studied by AFM (Figure 24). AFM measurements were performed on an Asylum Research MFP-3D atomic force microscope, operating in tapping mode and equipped with a commercial silicon tip. The size of the AFM images was 3 μm \times 3 μm .

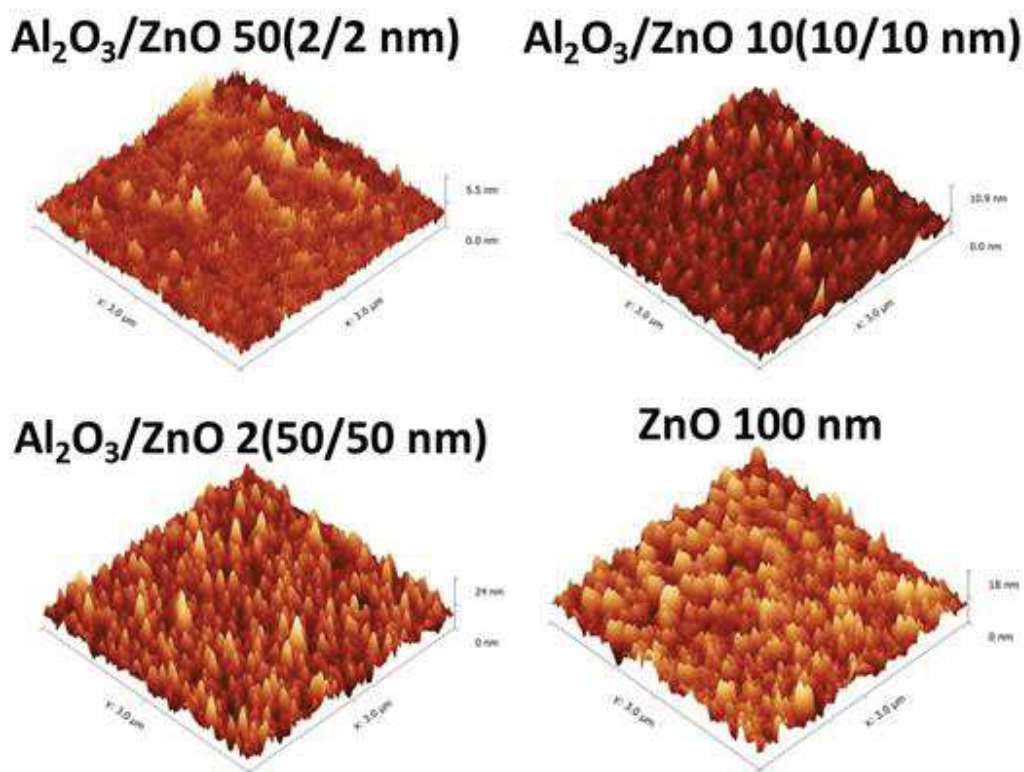


Figure 24. AFM measurement of different nanolaminate sequences and ZnO monolayer

The thinnest bilayers $\text{Al}_2\text{O}_3/\text{ZnO}$ 50 (2/2 nm) and $\text{Al}_2\text{O}_3/\text{ZnO}$ 10 (10/10 nm) showed smooth surface with low surface roughness. Well-shaped hill features with average lateral dimensions 50–100 nm has been observed on the $\text{Al}_2\text{O}_3/\text{ZnO}$ 2 (50/50 nm) sample surface. The mean square roughness, calculated from AFM data, showed linear behavior vs the increase of bilayer thickness (Figure 25). Amorphous Al_2O_3 inhibits the ZnO crystal growth and forces the ZnO to renucleate on the Al_2O_3 surface. We note that the surface roughness of nanolaminates was lower than the surface roughness of 200 nm thick ZnO mentioned before at paragraph 4.7 (Figure 25).

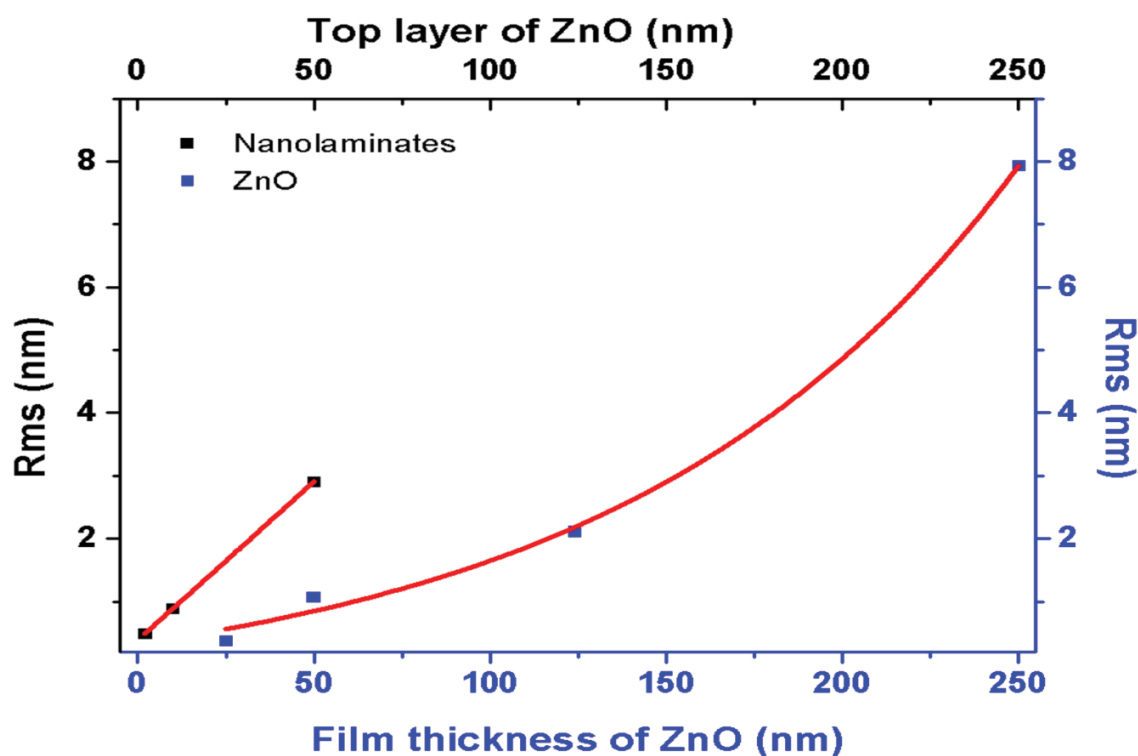


Figure 25. Blue Square: Roughness vs the film thickness of the single layer of ZnO; black square, Roughness vs the top layer of ZnO in the Al₂O₃/ZnO nanolaminates

9.2. Optical Characterization of Al₂O₃/ZnO nanolaminates

Optical properties of Al₂O₃/ZnO nanolaminates elaborated by ALD have been studied with UV–VIS transmittance (UV–VIS spectrophotometer Shimadzu UV-1700, spectral range 300–1100 nm, 1 nm step) and photoluminescence spectroscopy (spectral range 370–800nm). The excitation of luminescence was performed by a solid state laser source (Nd:YAG, LCS-DTL-374QT, Russia, 355 nm, 13 mW/cm²).

9.2.1. Transmittance measurement

The transmittance spectra of the Al₂O₃/ZnO nanolaminates with different bilayers thickness are reported on Figure 26.

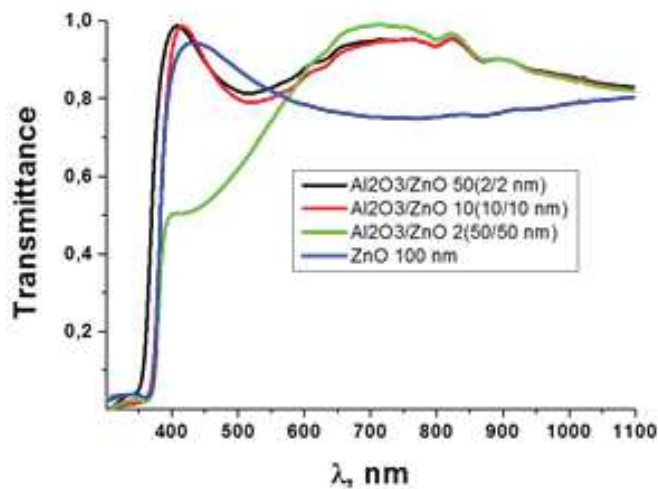


Figure 26. Transmittance spectra and of Al₂O₃/ZnO nanolaminates with different bilayer thicknesses and single ZnO thin film

Transmittance spectra show that all the nanolaminates samples were transparent in the range of 550-1100 nm. An absorption edge is observed in the 370-410nm range. A blue shift of the absorption edge is observed when the nanolaminates bilayers thickness decreases. Based on the transmittance spectra, we calculate the absorption coefficient α and then we estimate the band gap value of the Al₂O₃/ZnO nanolaminates.

Absorption coefficient α

Based on the transmittance spectra and the direct optical transitions properties of ZnO and by assuming that the Al₂O₃ is totally transparent and the observed absorption edge was related to ZnO layers, the absorption coefficient α has been calculated using Equation 6.

$$\alpha = \frac{(h\nu - E_g)^2}{h\nu} \quad \text{(Equation 6)}$$

Where $h\nu$ and E_g are a photon energy and a band gap values, respectively. The Absorption coefficient α is related to the transmittance of the sample T by the Equation 7:

Chapter 2. Synthesis of ALD Zinc oxide thin film and zinc oxide/Aluminium oxide nanolaminates: studies of their structural and optical properties.

$$\alpha \cdot d = \ln\left(\frac{1}{T}\right) \quad (\text{Equation 7})$$

Where d is a thickness of the sample.

Band gap estimation

Considering equation 6 and equation 7 and using the optical density $D = d \cdot \alpha$, we plot the $(D \times hv)^2$ vs hv in figure 27 then we calculated graphically the Band gap values E_g in the linear part of the absorption edge.

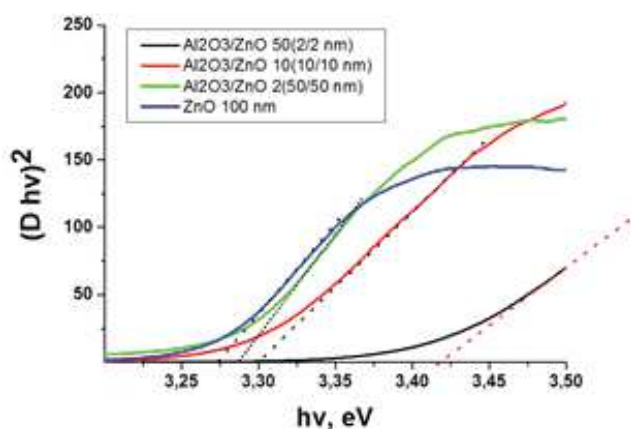


Figure 27. band gap estimation of $\text{Al}_2\text{O}_3/\text{ZnO}$ nanolaminates with different bilayer thickness and the single ZnO thin film

Table 20 reports the band gap value estimated graphically of the $\text{Al}_2\text{O}_3/\text{ZnO}$ nanolaminates with different bilayers thicknesses and the single ZnO thin film.

Table 20. Band gap value of $\text{Al}_2\text{O}_3/\text{ZnO}$ nanolaminates with different bilayer thicknesses and single ZnO thin film extracted from transmittance spectra

Samples	E_g (eV) from transmittance
$\text{Al}_2\text{O}_3/\text{ZnO}$ 50 (2/2 nm)	3.41
$\text{Al}_2\text{O}_3/\text{ZnO}$ 10 (10/10 nm)	3.3
$\text{Al}_2\text{O}_3/\text{ZnO}$ 2 (50/50 nm)	3.28
ZnO (50 nm)	3.24

As shown in Table 20 when the nanolaminates bilayers thickness increases, the band gap decreases. This band gap variation can be related to structural defects (interstitials, vacancies, etc.) and impurities. According to Wang *et al.*[78] and Charpentier *et al.*[79], the observed blue shift could be determined by three physical phenomena[80, 81]:

1. Quantum confinement effect of small nanograins
2. Doping of ZnO by Al
3. The improvement of crystalline quality of the single layer.

Quantum confinement due to small nanograins can only occur for nanolaminates with bilayer thickness of 4 nm. For other samples, the doping by Al and the improvement of the crystalline structure reported on the GIXRD spectra (Figure 22) are the most possible explanations for the observed blue shift.

9.2.2. Ellipsometry

Bilayers thickness, refractive index and extinction coefficients have been investigated using the ellipsometric measurements realized on the single ZnO and Al₂O₃ layers as well as on the nanolaminates (Figure 28).

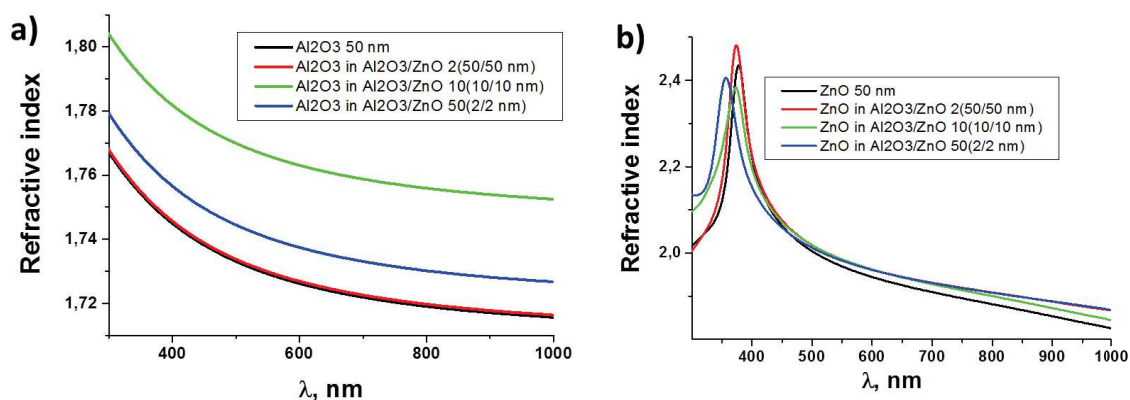


Figure 28. a) Refractive index of Al₂O₃ single thin film and Al₂O₃ in Al₂O₃/ZnO nanolaminates with different bilayer thicknesses. b) Refractive index of ZnO single thin film and ZnO in Al₂O₃/ZnO nanolaminates with different bilayer thicknesses.

Different models have been used to analyze the regression. ZnO layer was characterized using Psemi-MO and two Gaussian oscillators from 'Complete Ease' software. Al₂O₃ layers were characterized using Cauchy dispersion function that is commonly used for transparent materials as dielectrics and semiconductors. Starting by fixing the thickness value and fitting the dispersion function, optical constants and layer thickness of single Al₂O₃ and ZnO layers deposited on Si substrate were obtained. Cauchy constant used for Al₂O₃ characterization are $A = 1.716$, $B = 2.36 \times 10^{-2}$ and $C = 1.57 \times 10^{-3}$ and a thickness of layer ($d = 40.81 \text{ nm}$) were determined from regression analysis. This optical constant value is close to that reported by Barker *et al.* on α -Al₂O₃ lattice belongs to the trigonal crystal system[82]. The single layer of ZnO optical constants and the layer thickness ($d = 48.63 \text{ nm}$) was obtained from regression analysis with following Psemi-Mo oscillator values: $\text{Amp1} = 2.542$, $\text{Br1} = 0.0798$, $\text{Eo1} = 3.288$, $\text{WR1} = 2.2419$, $\text{PR1} = 0.631$, $\text{AR1} = 0.542$, $\text{O2R1} = -0.565$, Gaussians oscillator values were: $\text{Amp2} = 2.53$, $\text{Br2} = 2.53$, $\text{En2} = 6.47$, $\text{Amp3} = 0.265$, $\text{Br3} = 0.46$, $\text{En3} = 0.885$. The calculated optical constants of ZnO nanolayers obtained by ALD is in good agreement with ZnO having hexagonal crystals structure reported by Dai *et al.*[83].

In order to study the optical response of ellipsometric parameters of multilayer system (nanolaminates) composed of Al₂O₃ and ZnO layers deposited by ALD method during regression analysis, the thicknesses of layers were fixed parameters, meanwhile coefficients in optical dispersion functions were free fitting values. As noted above, the obtained optical constants for single Al₂O₃ and ZnO layers were used as a starting point for the regression analysis based on the evaluation of ZnO/Al₂O₃ nanolaminates.

For the Al₂O₃/ZnO 50 (2/2 nm) nanolaminate, the Bruggeman effective media approach was used for regression analysis. Firstly, the total thickness was obtained in a range from 400 nm to 1000 nm. After that the coefficients of optical constants functions were fitted in spectral range from 300 to 1000 nm to evaluate the peculiarity in UV range. Bruggemans effective media approximation model gives possibility to evaluate the percentage of materials from which the layer consists and usually is used for the evaluation of polycrystalline materials. After the fitting of percent's in effective media model, using 'Complete Ease' software, it was calculated that the part of Al₂O₃ takes 54.9 % and ZnO 45.1 % of total volume. We note here that due to the roughness of the interface between layers, the ultrathin (about 2 nm) layers

fluctuations can be of the same order as the thickness of this layer. It can be seen from XRD measurements that demonstrated the amorphous of layers having thickness below 2 nm. This means that such nanolaminates are more close to the dispersed system than to the regular one. Thus, the effective medium approach could be a good tool for the calculation of the effective refractive index. Since the exact shape of such fluctuations is unknown, the Bruggeman approach is most preferable because it is better to use it in the case of absence of any independent information about microstructure and describing film roughness and intermixed layer effects[84, 85]. However the investigation of nanolaminates using He-ion microscope reported elsewhere had demonstrated layered structure of the total film[17]. In order to estimate the error which could be generated due to this anisotropic structure, we used linear approach of effective medium and Hashin – Shtrikman limit[86] with known volume fractions of the components (55%/45%). This estimation showed that the difference between dielectric constants along and perpendicular to the nanolaminate structures is only 0.1%. This demonstrates that our choice of Bruggeman effective medium approach is able to give enough accurate results.

The main parameters of single ZnO and Al₂O₃ layers (refractive index n and extinction coefficient k) were calculated from ellipsometry measurements. It was found that Al₂O₃ was transparent in the whole UV and Vis range of the wavelength (Figure 28a). We note here that ellipsometry allows obtaining the optical constants n (real part of refractive index) and k (imaginary part of refractive index). This was used in the present work: n vs wavelength was plotted to analyze correlation with the structural properties. However, no drastic changes in n values were observed when we plot n , $\sqrt{n^2 - k^2}$ and $\sqrt{n^2 + k^2}$ in the UV-VIS range (Figure 29).

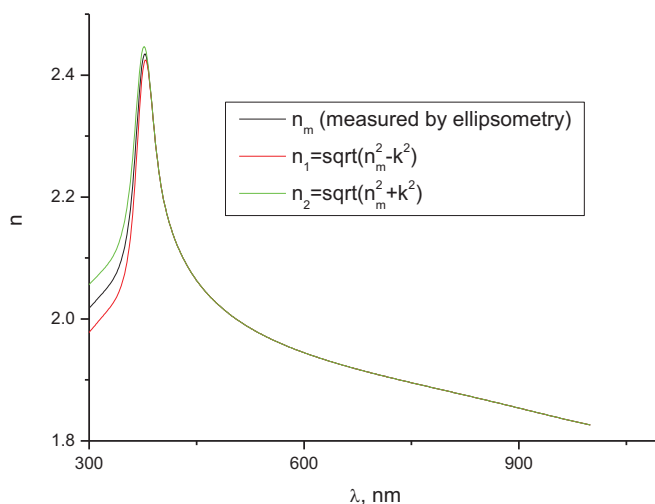


Figure29. Refractive index of ZnO single thin film of 50 nm

ZnO single layer demonstrated absorption peak in the range from 360 to 410 nm (Figure 28b). It is known that extinction coefficient k and absorption coefficient α are related as:[87]

$$\alpha = \frac{4 \cdot \pi \cdot k}{\lambda} \quad \text{(Equation 8)}$$

Where λ is a wavelength. Using equations 6and7, band gap values of ZnO single layer were calculated (Table 15).

Table 21. band gap value of Al₂O₃/ZnO nanolaminates with different bilayer thickness and single ZnO thin film extracted from the ellipsometric measurement

Samples	Eg (eV) from ellipsometry
Al ₂ O ₃ /ZnO 50 (2/2 nm)	3.45
Al ₂ O ₃ /ZnO 10 (10/10 nm)	3.36
Al ₂ O ₃ /ZnO 2 (50/50 nm)	3.31
ZnO (50 nm)	3.25

The calculated E_g values were similar to the ones, obtained by transmittance spectroscopy (see Table 20). It was found that average refractive index of ZnO single layer in nanolaminates was higher than that for the single ZnO films. No drastic changes in refractive index of ZnO in nanolaminates were observed in the range of 450 - 700 nm. The peak between 350 and 400 nm corresponds to the band gap transition of ZnO[88]. Blue shift of the peaks in dispersion curves ($n(\lambda)$) were observed with the decrease of the single ZnO layer thickness in nanolaminates due to grain size decrease, doping by Al or the improvement of the crystalline quality[88]. The observed blue shift peak is in good correlation with the calculated band gap values.

Doping of ZnO by Al resulted in changes of optical properties, such as band gap and refractive index[89, 90]. It was shown, that refractive index of ZnO doped by Al decreased with the concentration ratio of Al dopant [89, 90]. The observed results of refractive index of ZnO showed the increase of refractive index in comparison to single ZnO films. Recently we demonstrated that 50 nm ZnO film on Si was barely nanocrystalline with average grain size about 6 nm[25]. It was considered that shift of the refractive index is related to the packing density of the film:[89, 91, 92] as the packing density increases, the n value increases [89, 91, 92]. In fact the packaging density (density per volume) is related to the microstructure of the films. The higher the packing density the less moisture/voids are inside ZnO thin film. ZnO has a columnar microstructure and a columnar growth is proved. When we deposited ZnO on Al_2O_3 , lateral growth can take place. The deviation from the columnar growth can change then the microstructure and increase the packing density and the refractive index as reported by Krishna *et al.*[93]. According to the XRD analysis, the larger grain size in nanolaminates increased with the bilayers thickness. It might be considered that no significant doping occurred in ZnO single layers but the increase of refractive index of ZnO was based on improved crystalline properties. We suppose that the Al doping at the ZnO/ Al_2O_3 interface did not make an influence to the refractive index of ZnO layers.

The refractive index of Al_2O_3 single layer in nanolaminates increased in comparison to single layer of Al_2O_3 , deposited on Si (Figure 28b). This layer had amorphous structure [17]. In the present work Al_2O_3 also had amorphous nature as no XRD peaks, related to this material

were observed. This result is not fully understood yet, however, we could consider the improvement of the structure in amorphous Al_2O_3 , similar to ZnO, which resulted in the increase of the refractive index and/or the Zn incorporation at the $\text{ZnO}/\text{Al}_2\text{O}_3$ interface.

9.2.3. Photoluminescence

Photoluminescence tests were performed on the nanolaminates structures series. Figure 30 shows the photoluminescence spectra of different nanolaminates bilayer thickness.

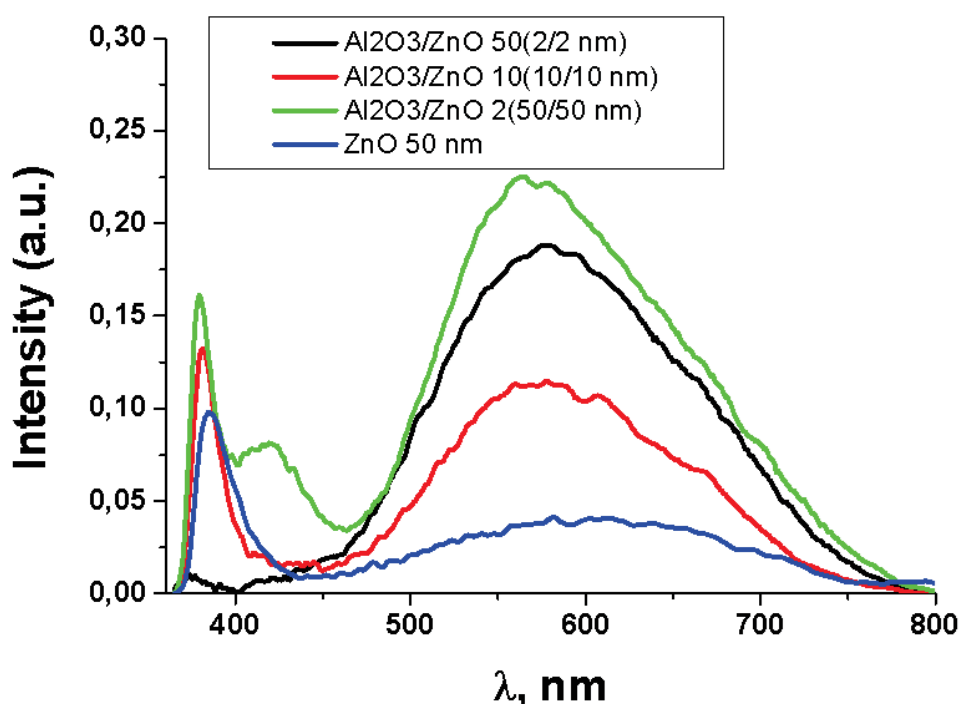


Figure 30. Photoluminescence spectra of 50 nm thick single ZnO film and $\text{Al}_2\text{O}_3/\text{ZnO}$ nanolaminates with different bilayer thicknesses.

Figure 30 reports a UV and Vis emission bands, usually observed in ZnO nanostructures. According to Wang *et al.*[13], the UV peak corresponds to free exciton emission and the Vis peak corresponds to defect level emission. Moreover an increase in the UV peak intensity with the increase of the bilayer thickness in the nanolaminates was reported by the

Chapter 2. Synthesis of ALD Zinc oxide thin film and zinc oxide/Aluminium oxide nanolaminates: studies of their structural and optical properties.

photoluminescence spectra. The intensity of the Vis peak does not follow the same tendency. According to Jinet *al.*[20] and Zandiet *al.*[80] the ratio of UV/Vis emission could be a parameter of the crystalline structure quality of ZnO inside the nanolaminates.

The high surface/volume ratio of the $\text{Al}_2\text{O}_3/\text{ZnO}$ 50 (2/2 nm) combined with the low crystalline properties can be behind the low intensity of the UV peak. Origine 7 software has been used to analyze the PL spectra of the nanolaminates by splitting the spectra on separate peaks with the Gaussian fitting (Figure 31). The obtained data is presented in the Table 22.

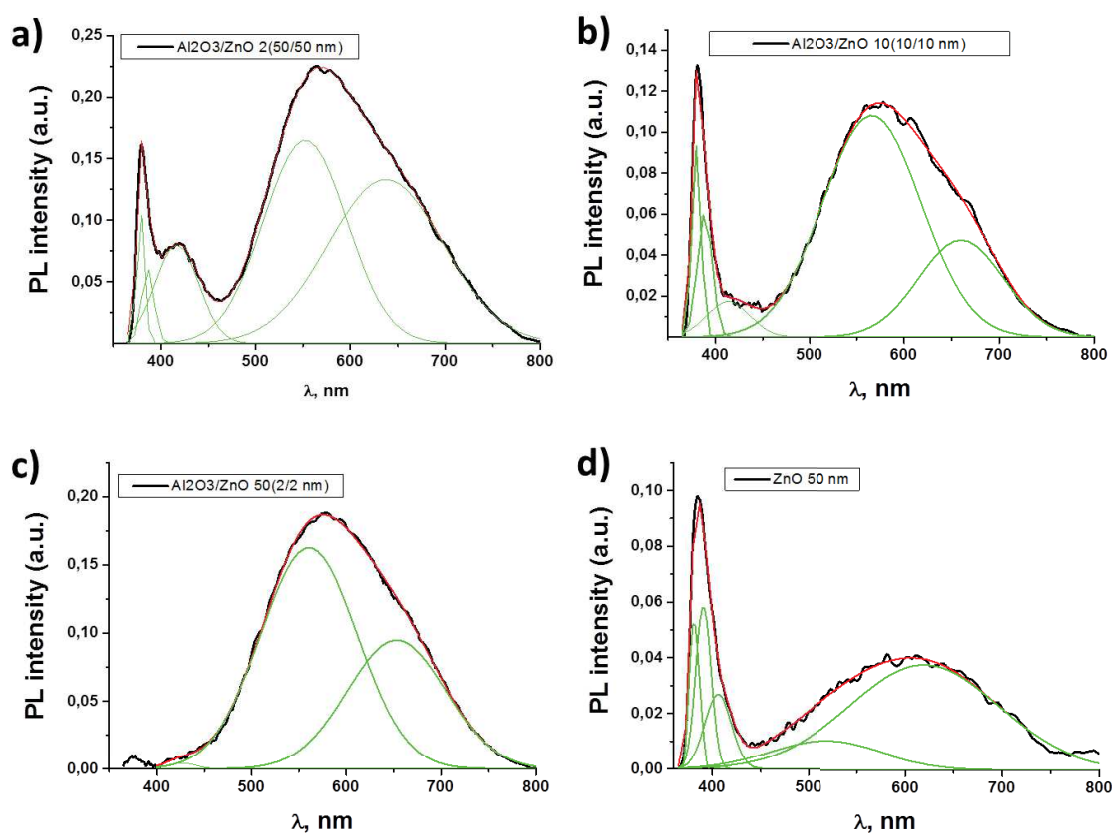


Figure 31. Photoluminescence spectra of ZnO single thin film of 50 nm thick and $\text{Al}_2\text{O}_3/\text{ZnO}$ nanolaminates with different bilayer thicknesses

Table 22. Peak positions of ZnO single thin film and Al₂O₃/ZnO nanolaminates with different bilayer thicknesses

Al ₂ O ₃ /ZnO 50 (2/2 nm)	Al ₂ O ₃ /ZnO 10 (10/10 nm)	Al ₂ O ₃ /ZnO 2 (50/50 nm)	ZnO (50 nm)
425.3	380	378	382
560.5	389	386	391
653.1	414	417	406
-	566	552	518
-	600	637	619

Excitonic peaks at 377-378 nm and phonon replicas at 386-388 nm fit with the previously published results [65, 66, 94, 95]. Peaks at 413-425 nm could be induced by neutral Zn vacancies and/or surface defects [65, 66, 94, 95]. Peaks at 536-565 nm and 635-656 nm correspond to oxygen vacancies and the interstitial oxygen[96].

Photoluminescence spectra show that UV/Vis intensity of nanolaminates did not increase monotonically with the increase of the single layer thickness (Figure 29). It could be affected by structural changes during the layer growth and/or doping by Al. According to Yogamalar *et al.*[97], the Al³⁺ ions could substitute Zn²⁺ and therefore Zn vacancies are formed, which are increasing the visible PL band. Yogamalar *et al.*[97] mentioned also that the Al doping results in the increase of electron concentration what could stimulate the defect-based luminescence and the formation of surface defects, which could be a luminescence centers as well.

A strong peak at 413 nm (Figure 29) confirms additional defects at Al₂O₃/ZnO interface. According to Willander *et al.*[96] and Liang *et al.*[98] the peaks at 413-426 were related to neutral Zn vacancies or/and Zn interstitials. Based on the ellipsometry and XRD measurements, that does not approve any Al doping. The increase of the peak intensity could be the result of higher concentration of Zn vacancies/Zn interstitials at Al₂O₃/ZnO interface.

9.3. Conclusion

Optical and structural properties of $\text{Al}_2\text{O}_3/\text{ZnO}$ nanolaminates elaborated by ALD have been investigated. Nanolaminates structures allow the tailoring of structural and optical parameters. Single layer thickness, grain size, band gap and PL have been calculated. From the analysis of optical and structural properties, it was determined that Al diffused into the interface of $\text{ZnO}/\text{Al}_2\text{O}_3$ bilayer, forming defect states which increased the visible peak of photoluminescence spectra. The improvement on the ZnO crystalline quality leads to a blue shift of band gap and excitonic peak position of ZnO single layers and was explained by the quantum confinement.

10. General Conclusion

This first experimental chapter was devoted to the optical and structural study of zinc oxide, aluminum oxide and $\text{Al}_2\text{O}_3/\text{ZnO}$ nanolaminates in order to investigate the behavior of the deposition parameter on the structural and optical properties. Before starting this study, view that the reactor used on this thesis is a homemade reactor, several established experiments were necessary before starting the ALD deposition such as homogenizing the temperature, solve the software problem, optimizing the deposition parameter such as precursor pulse time, exposure time, purge time, and others. After that, the setup of the ALD window was studied between 50 and 230°C. Based on the SEM and ellipsometric measurement, the ALD window was found to be between 50 and 200°C for the Al_2O_3 with a growth rate per cycle of 0.17 nm per cycle and between 60 and 180°C for the ZnO with a growth rate of 0.24 nm per cycle. Those results were matching the literature data.

After the identification of the ALD window and the growth per cycle, ZnO layers with different thicknesses between 25 and 250 nm have been deposited at 100°C in silicon and glass substrates and then characterized by SEM, GIXRD, TEM, EDX, AFM, transmittance test and photoluminescence. SEM cross section shows a conformal coating with a columnar growth when the ZnO thickness increase leading to a rough surface. GIXRD measurements shows a transition from an amorphous to polycrystalline state when the ZnO thickness increases. Moreover GIXRD shows an increase of the crystalline grains size with increasing the ZnO thickness. TEM shows an amorphous ZnO layer below 20 nm, nano-crystalline grains randomly

oriented in the ultrathin films observed between 20 and 50 nm thick films and a columnar growth for thickness higher than 50 nm which confirms the SEM and the GIXRD measurements. AFM images shows an increase on the mean-square roughness (R_q) extracted from the AFM images when the ZnO thickness increases which match the SEM observation. EDX measurements report a non-stoichiometric ratio between Zn and O (>1) indicate Oxygen excess that can be due to residual OH- and a partially hydroxylated phase ZnO(OH) on the surface of the ZnO grains. Moreover the O/Zn ratio decreases with increasing the thickness. Transmittance tests show a transparent behavior on the 500-1100nm range for ZnO layers with a thickness less than 100nm contrary to the ZnO layers with a thickness higher than 100 nm that shows a maximum and minimum transmittance in the same range.

Based on the transmittance spectra the band gap energy and the urbach energy were calculated. An uncharacteristic change of the band gap and the urbach energy have been reported when the ZnO thickness increases. PL spectra of ZnO films with different thicknesses reported a defect states at 3.08-3.14eV due to the neutral Zn vacancies. It shows also a peak at 2.21-2.25eV that identifies interstitials oxygen. Due to those 2 peaks PL spectra shows an oxygen-rich samples correlate well with the EDX results. Band gap was also calculated based on the photoluminescence and the absorption measurements. In summary an increase of the crystalline grains size is accompanied by a decrease of lattice strain, a rise of the Zn/O ratio, and an uncharacteristic change of the energy gap due to a decrease of the defects point concentration and an improvement of the film crystallinity.

Due to those structural defect ZnO thin film band gap is lower than bulk ZnO crystals band gap. UV and Visible photoluminescence emissions peaks in ZnO thin films correspond to band-edge and defect-related transitions, respectively. Additional UV emissions are observed from band-tail states. The defects related to observed PL bands are identified as neutral Zn vacancies, interstitial oxygen, and doubly ionized oxygen vacancies. The optical properties correlate with the crystalline structure, the point defect concentration, the grain size, and the depleted layer. The Crystalline structure improvement when the ZnO thickness increase was reflected in the photoluminescence spectra by an increasing on the UV emissions intensity. The oxygen excess is attributed to formation of Zn vacancies, oxygen interstitials and adsorbed molecular oxygen on the surface of grains.

After this optical and structural study on ZnO films with different thicknesses, optical and structural properties of Al₂O₃/ZnO nanolaminates elaborated by ALD have been as well investigated. Three different nanolaminates sequences have been elaborated and characterized:

- 2 x (250 cycles Al₂O₃/250 cycles ZnO)
- 10 x (50 cycles Al₂O₃/50 cycles ZnO)
- 50 x (10 cycles Al₂O₃/10 cycles ZnO)
- A monolayer of 1000 cycles ZnO as reference.

SEM, GIXRD, AFM, Ellipsometry, transmittance tests and photoluminescence characterization have been performed on different nanolaminates sequences. SEM cross section images show a conformal coating with well-defined nanolaminates structures. GIXRD reports a transition in the preferential growth orientation on the thicker bilayers sequences and a transition to an amorphous state for the thinnest one. Moreover when the bilayer thickness increases the grain size increases, the lattice constant (a) increases and the lattice constant (c) decreases. AFM images show a decrease on the mean square roughness when the bilayer thickness decreases.

Transmittance spectra show that all the nanolaminates samples were transparent in the range of 550-1100 nm. An absorption edge is observed in the 370-410nm range. A blue shift of the absorption edge is observed when the nanolaminate bilayer thickness decreases. The extracted band gap from the transmittance spectra reports a decrease behavior when the nanolaminates bilayers thicknesses increase. Ellipsometric measurements report a band gap values close to the ones obtained by transmittance spectroscopy. Moreover it was found that average refractive index of ZnO single layer in nanolaminates was higher than that for the single ZnO films. Photoluminescence spectra show an increase in the UV peak intensity with the increase of the bilayer thickness in the nanolaminates. The intensity of the Vis peak does not follow the same tendency. In summary nanolaminates structures allow the tailoring of structural and optical parameters. Single layer thickness, grain size, band gap and PL have been calculated. From the analysis of optical and structural properties, it was determined that Al diffused into the interface of ZnO/Al₂O₃ bilayer, forming defect states which increased the visible peak of photoluminescence spectra. The improvement on the ZnO crystalline quality

Chapter 2. Synthesis of ALD Zinc oxide thin film and zinc oxide/Aluminium oxide nanolaminates: studies of their structural and optical properties.

leads to a blue shift of band gap and excitonic peak position of ZnO single layers and was explained by the quantum confinement.

Coupling the ability to modify optical properties and active surface with the biocompatibility properties of the deposited films, our materials show a good capacity for the development of different applications such electrical, optical sensors and biosensors, photocatalytic, membrane etc. It will be shown in the following chapters.

References

1. Ozgur, U., et al., A comprehensive review of ZnO materials and devices. *Journal of Applied Physics*, 2005. 98(4).
2. Chou, S.M., et al., ZnO : Al thin film gas sensor for detection of ethanol vapor. *Sensors*, 2006. 6(10): p. 1420-1427.
3. Zhao, Z., et al., ZnO-Based Amperometric Enzyme Biosensors. *Sensors*, 2010. 10(2): p. 1216-1231.
4. Srivastava, J.K., L. Agarwal, and A.B. Bhattacharyya, ELECTRICAL CHARACTERISTICS OF LITHIUM-DOPED ZNO FILMS. *Journal of the Electrochemical Society*, 1989. 136(11): p. 3414-3417.
5. Elias, J., et al., Hollow Urchin-like ZnO thin Films by Electrochemical Deposition. *Advanced Materials*, 2010. 22(14): p. 1607-+.
6. Elias, J., et al., Well ordered Hollow Urchin-like ZnO by Electrodeposition, in *Electroless Deposition Principles, Activation, and Applications*, S. Djokic and J.L. Stickney, Editors. 2011. p. 67-73.
7. Elias, J., et al., Urchin-inspired zinc oxide as building blocks for nanostructured solar cells. *Nano Energy*, 2012. 1(5): p. 696-705.
8. Bae, H.S. and S. Im, Ultraviolet detecting properties of ZnO-based thin film transistors. *Thin Solid Films*, 2004. 469-470(0): p. 75-79.
9. Muthukumar, S., et al., Control of morphology and orientation of ZnO thin films grown on SiO₂/Si substrates. *Journal of Crystal Growth*, 2001. 225(2-4): p. 197-201.
10. Assunção, V., et al., Influence of the deposition pressure on the properties of transparent and conductive ZnO:Ga thin-film produced by r.f. sputtering at room temperature. *Thin Solid Films*, 2003. 427(1-2): p. 401-405.
11. Sun, C.Q., Size dependence of nanostructures: Impact of bond order deficiency. *Progress in Solid State Chemistry*, 2007. 35(1): p. 1-159.
12. Prajapati, C.S. and P.P. Sahay, Alcohol-sensing characteristics of spray deposited ZnO nanoparticle thin films. *Sensors and Actuators B-Chemical*, 2011. 160(1): p. 1043-1049.
13. Flickyngerova, S., V. Tvarozek, and P. Gaspierik, ZINC OXIDE - A UNIQUE MATERIAL FOR ADVANCED PHOTOVOLTAIC SOLAR CELLS. *Journal of Electrical Engineering-Elektrotechnicky Casopis*, 2010. 61(5): p. 291-295.
14. Bechelany, M., et al., Preparation of ZnO nanoparticles localized on SiC@SiO₂ nanocables by a physical templating method. *Journal of the European Ceramic Society*, 2009. 29(5): p. 863-867.
15. Bechelany, M., et al., ZnO nanotubes by template-assisted sol-gel route. *Journal of Nanoparticle Research*, 2012. 14(8).
16. Marichy, C., M. Bechelany, and N. Pinna, Atomic Layer Deposition of Nanostructured Materials for Energy and Environmental Applications. *Advanced Materials*, 2012. 24(8): p. 1017-1032.
17. Raghavan, R., et al., Nanocrystalline-to-amorphous transition in nanolaminates grown by low temperature atomic layer deposition and related mechanical properties. *Applied Physics Letters*, 2012. 100(19).
18. Wang, D. and N. Reynolds, Photoluminescence of Zinc Oxide Nanowires: The Effect of Surface Band Bending. *ISRN Condensed Matter Physics*, 2012. 2012: p. 6.
19. Fay, S. and A. Shah, Zinc Oxide Grown by CVD Process as Transparent Contact for Thin Film Solar Cell Applications, in *Transparent Conductive Zinc Oxide*, K. Ellmer, A. Klein, and B. Rech, Editors. 2008, Springer Berlin Heidelberg. p. 235-302.
20. Jin, B.J., et al., Relationship between photoluminescence and electrical properties of ZnO thin films grown by pulsed laser deposition. *Applied Surface Science*, 2001. 169: p. 521-524.

21. Zandi, S., et al., Microstructure and optical properties of ZnO nanoparticles prepared by a simple method. *Physica B-Condensed Matter*, 2011. 406(17): p. 3215-3218.
22. Armelao, L., et al., The Origin and Dynamics of Soft X-Ray-Excited Optical Luminescence of ZnO. *ChemPhysChem*, 2010. 11(17): p. 3625-3631.
23. Bethke, S., H. Pan, and B.W. Wessels, LUMINESCENCE OF HETEROEPITAXIAL ZINC-OXIDE. *Applied Physics Letters*, 1988. 52(2): p. 138-140.
24. Egelhaaf, H.J. and D. Oelkrug, Luminescence and nonradiative deactivation of excited states involving oxygen defect centers in polycrystalline ZnO. *Journal of Crystal Growth*, 1996. 161(1-4): p. 190-194.
25. Abou Chaaya, A., et al., Evolution of microstructure and related optical properties of ZnO grown by atomic layer deposition. *Beilstein Journal of Nanotechnology*, 2013. 4: p. 690-698.
26. Mroczynski, R., et al., Double gate dielectric stacks with Gd₂O₃ layer for application in NVSM devices. *Microelectronic Engineering*, 2014. 115: p. 61-65.
27. Cho, H.J., et al., New TIT capacitor with ZrO₂/Al₂O₃/ZrO₂ dielectrics for 60 nm and below DRAMs. *Solid-State Electronics*, 2007. 51(11-12): p. 1529-1533.
28. Zhang, C. and X. Li, Planar GaAs nanowire tri-gate MOSFETs by vapor-liquid-solid growth. *Solid-State Electronics*, 2014. 93: p. 40-42.
29. Groner, M.D., et al., Gas diffusion barriers on polymers using Al₂O₃ atomic layer deposition. *Applied Physics Letters*, 2006. 88(5).
30. Ott, A.W., et al., Modification of porous alumina membranes using Al₂O₃ atomic layer controlled deposition. *Chemistry of Materials*, 1997. 9(3): p. 707-714.
31. Zhang, Y., et al., Direct growth of high-quality Al₂O₃ dielectric on graphene layers by low-temperature H₂O-based ALD. *Journal of Physics D-Applied Physics*, 2014. 47(5).
32. Zhang, X., et al., Structural and Electrochemical Study of Al₂O₃ and TiO₂ Coated Li_{1.2}Ni_{0.13}Mn_{0.54}Co_{0.13}O₂ Cathode Material Using ALD. *Advanced Energy Materials*, 2013. 3(10): p. 1299-1307.
33. Spahr, H., et al., Regimes of leakage current in ALD-processed Al₂O₃ thin-film layers. *Journal of Physics D-Applied Physics*, 2013. 46(15).
34. Rafi, J.M., et al., 2 MeV electron irradiation effects on the electrical characteristics of MOS capacitors with ALD Al₂O₃ dielectrics of different thickness. *Microelectronics Reliability*, 2013. 53(9-11): p. 1333-1337.
35. Oh, S.-K., et al., Process Temperature Dependence of Al₂O₃ Film Deposited by Thermal ALD as a Passivation Layer for c-Si Solar Cells. *Journal of Semiconductor Technology and Science*, 2013. 13(6): p. 581-588.
36. Na, H., et al., Growth of n-type organic semiconductor for low-voltage transistors based on an ALD grown Al₂O₃ gate dielectric. *Synthetic Metals*, 2013. 185: p. 103-108.
37. Meunier, R., et al., AlGaN/GaN MIS-HEMT gate structure improvement using Al₂O₃ deposited by plasma-enhanced ALD. *Microelectronic Engineering*, 2013. 109: p. 378-380.
38. Lotfabad, E.M., et al., Si nanotubes ALD coated with TiO₂, TiN or Al₂O₃ as high performance lithium ion battery anodes. *Journal of Materials Chemistry A*, 2014. 2(8): p. 2504-2516.
39. Cappella, A., et al., High Temperature Thermal Conductivity of Amorphous Al₂O₃ Thin Films Grown by Low Temperature ALD. *Advanced Engineering Materials*, 2013. 15(11): p. 1046-1050.
40. Blaho, M., et al., Ni/Au-Al₂O₃ gate stack prepared by low-temperature ALD and lift-off for MOS HEMTs. *Microelectronic Engineering*, 2013. 112: p. 204-207.
41. Seo, S.-W., et al., Optimization of Al₂O₃/ZrO₂ nanolaminate structure for thin-film encapsulation of OLEDs. *Organic Electronics*, 2012. 13(11): p. 2436-2441.
42. Rowlette, P.C. and C.A. Wolden, Pulsed plasma-enhanced chemical vapor deposition of Al₂O₃-TiO₂ nanolaminates. *Thin Solid Films*, 2010. 518(12): p. 3337-3341.

43. Freyman, C.A. and Y.-W. Chung, Synthesis and characterization of hardness-enhanced multilayer oxide films for high-temperature applications. *Surface and Coatings Technology*, 2008. 202(19): p. 4702-4708.
44. Cabello-Aguilar, S., et al., Slow translocation of polynucleotides and their discrimination by alpha-hemolysin inside a single track-etched nanopore designed by atomic layer deposition. *Nanoscale*, 2013. 5(20): p. 9582-9586.
45. Abou Chaaya, A., et al., Enhanced Ionic Transport Mechanism by Gramicidin A Confined Inside Nanopores Tuned by Atomic Layer Deposition. *Journal of Physical Chemistry C*, 2013. 117(29): p. 15306-15315.
46. Hu, Y.M., C.W. Lin, and J.C.A. Huang, Dependences of the Al thickness and annealing temperature on the structural, optical and electrical properties in ZnO/Al multilayers. *Thin Solid Films*, 2006. 497(1-2): p. 130-134.
47. Geng, Y., et al., Influence of Al Doping on the Properties of ZnO Thin Films Grown by Atomic Layer Deposition. *The Journal of Physical Chemistry C*, 2011. 115(25): p. 12317-12321.
48. Dasgupta, N.P., et al., Atomic Layer Deposition of Al-doped ZnO Films: Effect of Grain Orientation on Conductivity. *Chemistry of Materials*, 2010. 22(16): p. 4769-4775.
49. Cheun, H., et al., Oriented Growth of Al₂O₃:ZnO Nanolaminates for Use as Electron-Selective Electrodes in Inverted Polymer Solar Cells. *Advanced Functional Materials*, 2012. 22(7): p. 1531-1538.
50. Banerjee, P., et al., Structural, electrical, and optical properties of atomic layer deposition Al-doped ZnO films. *Journal of Applied Physics*, 2010. 108(4).
51. Baji, Z., et al., Structure and morphology of aluminium doped Zinc-oxide layers prepared by atomic layer deposition. *Thin Solid Films*, 2012. 520(14): p. 4703-4706.
52. Banerjee, P., et al., Structural, electrical, and optical properties of atomic layer deposition Al-doped ZnO films. *Journal of Applied Physics*, 2010. 108(4).
53. Wang, T., et al., Growth, optical, and electrical properties of nonpolar m-plane ZnO on p-Si substrates with Al₂O₃ buffer layers. *Applied Physics Letters*, 2012. 100(1): p. -.
54. Dallali, L., et al., Energy of excitons and acceptor–exciton complexes to explain the origin of ultraviolet photoluminescence in ZnO quantum dots embedded in a SiO₂ matrix. *Solid State Communications*, 2011. 151(11): p. 822-825.
55. Dallali, L., et al., Optical properties of exciton confinement in spherical ZnO quantum dots embedded in SiO₂ matrix. *Superlattices and Microstructures*, 2009. 46(6): p. 907-916.
56. Tapily, K., D. Gu, and H. Baumgart, Growth Mechanism of ALD ZnO Films Investigated by Physical Characterization. *Atomic Layer Deposition Applications* 6, 2010. 33(2): p. 355-363.
57. Min, Y.-S., et al., Growth and Characterization of Conducting ZnO Thin Films by Atomic Layer Deposition. *Bulletin of the Korean Chemical Society*, 2010. 31(9): p. 2503-2508.
58. Lim, S.J., S. Kwon, and H. Kim, ZnO thin films prepared by atomic layer deposition and rf sputtering as an active layer for thin film transistor. *Thin Solid Films*, 2008. 516(7): p. 1523-1528.
59. Groner, M.D., et al., Low-temperature Al₂O₃ atomic layer deposition. *Chemistry of Materials*, 2004. 16(4): p. 639-645.
60. Tapily, K., et al., Mechanical and structural characterization of atomic layer deposition-based ZnO films. *Semiconductor Science and Technology*, 2011. 26(11).
61. Huby, N., et al., Electrical behavior of zinc oxide layers grown by low temperature atomic layer deposition. *Applied Physics Letters*, 2008. 92(2).
62. Kim, S.K., et al., Comparison between ZnO films grown by atomic layer deposition using H₂O or O⁻³ as oxidant. *Thin Solid Films*, 2005. 478(1-2): p. 103-108.
63. Rivera Marquez, J.A., et al., Effect of Surface Morphology of ZnO Electrodeposited on Photocatalytic Oxidation of Methylene Blue Dye Part I: Analytical Study. *International Journal of Electrochemical Science*, 2011. 6(9): p. 4059-4069.

64. Viter, R., et al., Immune Biosensor Based on Silica Nanotube Hydrogels for Rapid Biochemical Diagnostics of Bovine Retroviral Leukemia. *Procedia Engineering*, 2011. 25(0): p. 948-951.
65. Cui, L., et al., Effect of film thickness and annealing temperature on the structural and optical properties of ZnO thin films deposited on sapphire (0001) substrates by sol-gel. *Ceramics International*, 2013. 39(3): p. 3261-3268.
66. Giri, P.K., et al., High-Yield Chemical Synthesis of Hexagonal ZnO Nanoparticles and Nanorods with Excellent Optical Properties. *Journal of Nanoscience and Nanotechnology*, 2012. 12(1): p. 201-206.
67. Wang, Q.P., et al., Violet luminescence emitted from ZnO films deposited on Si substrate by rf magnetron sputtering. *Applied Surface Science*, 2002. 201(1-4): p. 123-128.
68. Djurišić, A.B. and Y.H. Leung, Optical Properties of ZnO Nanostructures. *Small*, 2006. 2(8-9): p. 944-961.
69. Chen, C.-Y., et al., Surface effects on optical and electrical properties of ZnO nanostructures. *Pure and Applied Chemistry*, 2010. 82(11): p. 2055-2073.
70. Liao, Z.-M., et al., Surface effects on photoluminescence of single ZnO nanowires. *Physics Letters A*, 2008. 372(24): p. 4505-4509.
71. Liu, X., et al., Growth mechanism and properties of ZnO nanorods synthesized by plasma-enhanced chemical vapor deposition. *Journal of Applied Physics*, 2004. 95(6): p. 3141-3147.
72. Liu, K.W., et al., Photoluminescence characteristics of high quality ZnO nanowires and its enhancement by polymer covering. *Applied Physics Letters*, 2010. 96(2).
73. Reshchikov, M.A., et al., Photoluminescence from ZnO nanowires. *Journal of Vacuum Science & Technology B*, 2009. 27(3): p. 1688-1692.
74. Elam, J.W., M.D. Groner, and S.M. George, Viscous flow reactor with quartz crystal microbalance for thin film growth by atomic layer deposition. *Review of Scientific Instruments*, 2002. 73(8): p. 2981-2987.
75. Ott, A.W., et al., Al₂O₃ thin film growth on Si(100) using binary reaction sequence chemistry. *Thin Solid Films*, 1997. 292(1-2): p. 135-144.
76. Ghiraldelli, E., et al., ALD growth, thermal treatments and characterisation of Al₂O₃ layers. *Thin Solid Films*, 2008. 517(1): p. 434-436.
77. Elam, J.W. and S.M. George, Growth of ZnO/Al₂O₃ Alloy Films Using Atomic Layer Deposition Techniques. *Chemistry of Materials*, 2003. 15(4): p. 1020-1028.
78. Wang, N.W., Y.H. Yang, and G.W. Yang, Great blue-shift of luminescence of ZnO nanoparticle array constructed from ZnO quantum dots. *Nanoscale Research Letters*, 2011. 6.
79. Charpentier, C., P. Prod'homme, and P.R.I. Cabarrocas, Microstructural, optical and electrical properties of annealed ZnO:Al thin films. *Thin Solid Films*, 2013. 531: p. 424-429.
80. Zandi, S., et al., Microstructure and optical properties of ZnO nanoparticles prepared by a simple method. *Physica B: Condensed Matter*, 2011. 406(17): p. 3215-3218.
81. Jin, B.J., et al., Relationship between photoluminescence and electrical properties of ZnO thin films grown by pulsed laser deposition. *Applied Surface Science*, 2001. 169-170(0): p. 521-524.
82. Barker, A.S., Infrared Lattice Vibrations and Dielectric Dispersion in Corundum. *Physical Review*, 1963. 132(4): p. 1474-1481.
83. DAI, et al., Optical Properties of Zinc-oxide Films Determined Using Spectroscopic Ellipsometry with Various Dispersion Models. Vol. 55. 2009, Seoul, COREE, REPUBLIQUE DE: Korean Physical Society. 6.
84. Nguyen, H.V., I. An, and R.W. Collins, Evolution of the optical functions of thin-film aluminum: A real-time spectroscopic ellipsometry study. *Physical Review B*, 1993. 47(7): p. 3947-3965.
85. Leng, J.M., et al., Characterization of titanium nitride (TiN) films on various substrates using spectrophotometry, beam profile reflectometry, beam profile ellipsometry and spectroscopic beam profile ellipsometry. *Thin Solid Films*, 1998. 313-314(0): p. 308-313.

86. Talbot, D.R.S., J.R. Willis, and V. Nesi, ON IMPROVING THE HASHIN-SHTRIKMAN BOUNDS FOR THE EFFECTIVE PROPERTIES OF 3-PHASE COMPOSITE MEDIA. *Ima Journal of Applied Mathematics*, 1995. 54(1): p. 97-107.
87. YAKUPHANOGLU, et al., The determination of the optical band and optical constants of non-crystalline and crystalline ZnO thin films deposited by spray pyrolysis. Vol. 9. 2007, Bucuresti: INOE 2000. 6.
88. Miao, L., et al., Ellipsometric studies of optical properties of Er-doped ZnO thin films synthesized by sol-gel method. *Thin Solid Films*, 2013. 543(0): p. 125-129.
89. Benzarouk, H., et al., Effect of different dopant elements (Al, Mg and Ni) on microstructural, optical and electrochemical properties of ZnO thin films deposited by spray pyrolysis (SP). *Superlattices and Microstructures*, 2012. 52(3): p. 594-604.
90. Xue, S.W., et al., Effects of Al doping concentration on optical parameters of ZnO : Al thin films by sol-gel technique. *Physica B-Condensed Matter*, 2006. 381(1-2): p. 209-213.
91. Cho, E.N., S. Park, and I. Yun, Spectroscopic ellipsometry modeling of ZnO thin films with various O₂ partial pressures. *Current Applied Physics*, 2012. 12(6): p. 1606-1610.
92. Fang, Z.B., et al., Influence of post-annealing treatment on the structure properties of ZnO films. *Applied Surface Science*, 2005. 241(3-4): p. 303-308.
93. Krishna, M.G., K.N. Rao, and S. Mohan, Optical properties of ion assisted deposited zirconia thin films. *Journal of Vacuum Science & Technology A: Vacuum, Surfaces, and Films*, 1992. 10(6): p. 3451-3455.
94. Wang, Q.P., et al., Violet luminescence emitted from ZnO films deposited on Si substrate by rf magnetron sputtering. *Applied Surface Science*, 2002. 201(1-4): p. 123-128.
95. Djuricic, A.B. and Y.H. Leung, Optical properties of ZnO nanostructures. *Small*, 2006. 2(8-9): p. 944-961.
96. Willander, M., et al., Luminescence from Zinc Oxide Nanostructures and Polymers and their Hybrid Devices. *Materials*, 2010. 3(4): p. 2643-2667.
97. Yogamalar, N.R. and A. Chandra Bose, Absorption-emission study of hydrothermally grown Al:ZnO nanostructures. *Journal of Alloys and Compounds*, 2011. 509(34): p. 8493-8500.
98. Liang, Z., et al., Novel blue-violet photoluminescence from sputtered ZnO thin films. *Journal of Alloys and Compounds*, 2011. 509(17): p. 5437-5440.

Chapter 2. Synthesis of ALD Zinc oxide thin film and zinc oxide/Aluminium oxide nanolaminates: studies of their structural and optical properties.

Chapter 3: Atomic layer deposition on nanostructured materials for sensor applications

Atomic layer deposition on nanostructured materials for sensor applications

1.Introduction	113
2.Bibliographical introduction on UV Photodetector.....	113
3.Semiconductor based UV photodetectors	114
3.1.Group-III nitrides based photodetectors	114
3.2.SiC based photo-detectors.....	115
3.3.Diamond based photodetectors	115
3.4.ZnO based photo-detectors	116
3.4.1.Design of ZnO photoconductors	116
3.4.2.Metal-Semiconductor-Metal (MSM)Photodiodes	118
3.4.3.Schottky Photodiodes.....	119
3.4.4.p-n Junction Photodiodes	120
4.One dimensional nanostructured UVPhotodetectors.....	121
5.Elaboration of ZnO 1D nanostructures for UV Photodetection	123
5.1.Electrospinning	123
5.2.Synthesis of polyacrilonitrile nanofibers	124
5.3.Atomic layer deposition of zinc oxide	125
6. Chemical and structural characterizations	126
6.1.X-Ray diffraction (XRD)	126
6.2.Scanning electron microscopy (SEM)	128
7.UV characterization	130
7.1.UV characterization of Different ZnO thicknesses deposited on PAN nanofibers	131
7.1.1.Cyclic Voltammetry	132
7.1.2.Chronoamperometry	133
7.2.UV characterization of different electrospinning times	136

Chapter3. Atomic layer deposition on nanostructured materials for sensor applications

7.2.1.Cyclic Voltammetry	136
7.2.2.Chronoamperometry	138
7.3.UV characterization of ZnO ALD deposited at different temperatures	141
7.3.1.Cyclic voltammetry	141
7.3.2.Chronoamperometry	142
8.Different ohmic contact distance	146
9.Device stability	147
10.Conclusion and perspectives.....	148

1. Introduction

Due to their large application fields (civil and military applications) such as secure space-to-space communications, pollution monitoring, water sterilization, and flame sensing [1], UV photodetectors have attracted attention for the research. After the structural and optical studies performed on ZnO deposited by ALD in chapter 2, this chapter will be devoted to the design of ZnO 1D nanostructures and their investigations as UV photodetectors. Polyacrylonitrile fibers synthesized by electrospinning will be used as a template for ZnO ALD deposition in order to enhance the specific surface of the ZnO based UV Photodetectors. Structural, chemical and UV photoresponse properties of the obtained materials will be investigated. We should note here that ALD ZnO UV detection was not extensively studied in the literature. Shan *et al.*[1] performed a short study on ZnO ALD films deposited on glass substrates for UV Photodetection. They show a photoresponse current of ZnO based photodetectors (0.7 A/W at 5V bias) without the investigation of other parameters such as recovery time, response time and device stability. The design of high surface electrode based ALD deposition and the investigation of ALD conditions such as temperature, thickness and others parameters have not been addressed yet.

2. Bibliographical introduction on UV photodetector

UV photodetection has been widely studied in the last few years [2-11]. The semiconductor based UV photodetectors process is a simple physical phenomenon based on electron-hole generation into a semiconductor under photon shelling. Those pairs of electron-hole are collected before any recombination process (Figure1). When a photon with energy larger than the band-gap energy of semiconductor is absorbed, an electron-hole pair would be produced, there by changing the electrical conductivity of the semiconductor.

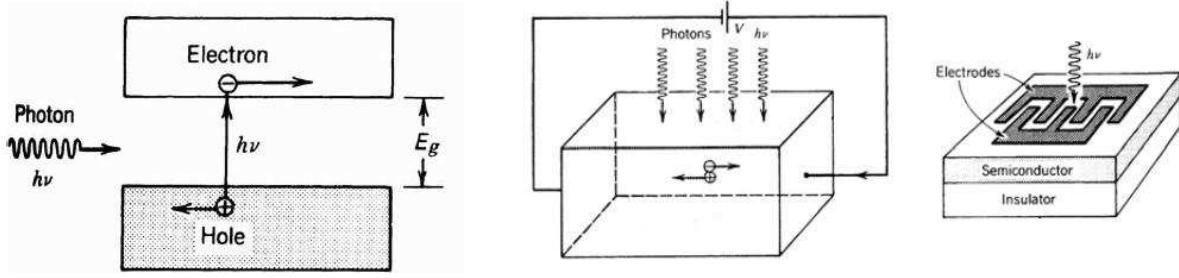


Figure1. Electron-hole generation under photon shelling collected before any recombination process.

UV range can be divided to four spectral regions [12, 13]:

- UV-A ($320 \text{ nm} < \lambda < 400 \text{ nm}$)
- UV-B ($280 \text{ nm} < \lambda < 320 \text{ nm}$)
- UV-C ($200 \text{ nm} < \lambda < 280 \text{ nm}$)
- Far UV ($10 \text{ nm} < \lambda < 200 \text{ nm}$)

Solar radiations cover all the UV spectra. The UV-C and Far UV emitted from the solar radiation are absorbed by the atmospheric ozone layer and the UV-A and UV-B reach the Earth. UV photodetectors with high sensitivity on the UV-A, UV-B, UV-C regions and far UV and with a low sensitivity for the visible range (400-700nm) are called Visible-blind photodetectors. UV photo-detectors with high sensitivity on the UV-C and far UV regions compared to the UV-A, UV-B regions are called Solar-blind [14]. A high-performance photo-detector should satisfy the 5S requirements of high sensitivity, high signal-to-noise ratio, high spectral selectivity, high speed and high stability[15].

3. Semiconductor based UV photodetectors

Low band gap energy semiconductor has been widely used for UV photodetection especially the Si-based photodetectors ($E_g = 1.1 \text{ eV}$). Despite their high sensitivity and quick response advantages, low E_g UV photodetectors are sensible to low energy photon such as visible and IR light which requires the insertion of protection filters to avoid signal noise related to those low electron energy. Moreover an ultra high vacuum and a very high voltage supply were

required [16]. Those entire disadvantages of the low E_g based photodetectors disappear for the high band gap semiconductors. Moreover, wide-band gap materials are chemically and thermally more stable which reflects an advantage for devices operating in harsh environments [17-19]. In the following part we will introduce the different types of high band gap semiconductors used for UV photodetection applications.

3.1. Group-III nitrides based photodetectors

Different types of thin film semiconductors have been elaborated using different techniques for UV photodetection applications. Group-III nitrides semiconductors such as AlN, GaN, InN, $Al_xGa_{1-x}N$, and $In_{0.1}Ga_{0.9}N$ have been widely used on the UV photodetection field due to their advantages such as the ideal spectral selectivity with wide direct band-gap, high breakdown field, high thermal stability, radiation hardness and expected high responsivity [20]. $Al_xGa_{1-x}N$ and $In_xGa_{1-x}N$ provide the full UV region photodetection[21, 22]. With Al percentage higher than 40, $Al_xGa_{1-x}N$ presents solar-blind detection properties. Nevertheless achieving this high Al percentage presents a big challenge due to the crack formation and the high density defect on the $Al_xGa_{1-x}N$ layer. Using the interlayer technique, a percentage of 30% was achieved without any cracks formation [23].

3.2. SiC based photo-detectors

Due to its high chemical and thermal stability with wide band-gap ($2.0 \text{ eV} \leq E_g \leq 7.0 \text{ eV}$), SiC has been widely used for flame detectors (UV-C range). p-type and n-type SiC can be realized by doping with Al and N respectively. Due to the little Fermi-level pinning, the SiC Schottky barrier height highly depends on the work function of the contact metal. Razeghi *et al.*[24] and Kosyachenko *et al.*[25] report a 6H-SiC Schottky photodiodes based on n-type or p-type, working in the 200–400 nm spectral range. Anikinet *et al.*[26] reported the high-quality Schottky junction on n-type SiC with the Schottky barrier height of 1.4–1.63 eV using Au. 4H-SiC-based Metal/Semiconductor/Metal (MSM) photo-detector has been widely reported on the literature [27, 28]. p-i-n SiC based junction presents a low-noise and high-speed response with an insensibility to the visible and IR photon [29]. The 6H-SiC UV p-i-n photodiodes had already been fabricated and commercially available [29]. Biondo *et al.* [30] reports a 4H-SiC p-n junction,

UV-photo-detector with a spectral responsivity of 0.03 A/W at 280 nm. Liu *et al.*[31] reported a 4H-SiC p-i-n avalanche photodiodes (APD) with dark current density of 63 nA /cm², and quantum efficiency of ~40%.

3.3. Diamond based photodetectors

Single crystal diamond based UV-Photodetectors meet the 5S requirement due to his wide band gap of 5.5 eV with extreme properties such as a high thermal conductivity, high carrier saturation velocity and mobility[15]. S-doped diamond shows high sensitivity, high speed, and relative blindness to visible radiation that can be due to defects generated due to the doping [32, 33]. Smith *et al.* [34] reports a p-type conductive diamond using boron. n-type doped diamond is difficult to achieve because of the close packing and rigidity of the diamond lattice. However Koizumi *et al.*[35] and Sakaguchiet *al.*[36] report n-type diamond that can only achieved by phosphor incorporation on (111) oriented surfaces. Interdigitated-finger MSM photoconductor, MSM photodiode, and Schottky photodiode based on diamonds were also reported [17, 37-40].

3.4. ZnO based photo-detectors

Among the high band gap semiconductors category, ZnO was one of the most semiconductors used for UV photo-detection due to its high chemical stability, low cost, and large band gap of 3.37 eV at room temperature. Mollowet *al.* reports in 1940 the first UV photoresponse in ZnO films[41]. Since then, many complex ZnO-based photodetectors with high performance were reported, such as p-n junction, p-i-n junction and Schottky junction [4, 42-49]. Different types of ZnO based UV detectors has been reported such as photoconductors types [50-62], metal-semiconductor-metal (MSM) [4, 63-65], Schottky photodiodes [66-68] and p-n junction photodiodes[69-73].

3.4.1. Design of ZnO photoconductors

A photoconductor is a radiation-sensitive resistor with two Ohmic contacts coupled with a load resistance[24]. The load resistance should be much smaller than the device resistance (Figure 2). Due to their high internal gain at room temperature, photoconductors can operate without any amplifying equipment. Despite this advantage photoconductors device present a low discrimination ratio between UV and visible light and persistent photoconductivity effects. ZnO based photoconductors device has been elaborated and tested using different techniques. Different electrode types have been as well used for ohmic contact (electrodes) such as Au, Al, Pt, Al/Au, Ni/Au, and ITO [50, 52-54, 58, 61, 62, 74-78]. Table 1 adapted from the review of Liu *et al.*[79] shows the different ZnO photoconductors devices elaborated by different techniques and their performance.

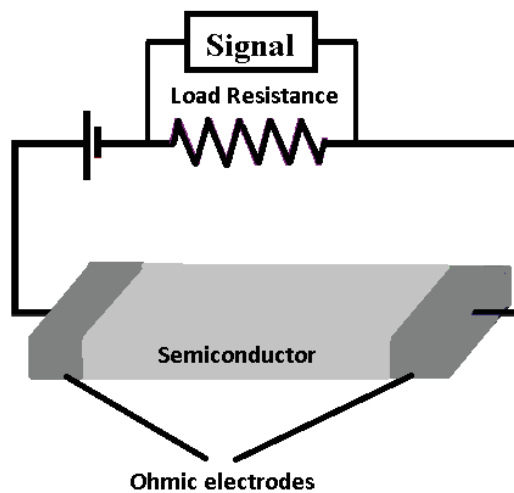


Figure2. Schematic structure of photoconductors

Table1. Different fabrication methods of ZnO photoconductors and their performance : Adapted from the review of Liu *et al.*[79]

Fabrication Method	Electrodes	Doping or treating	Dark current	Responsivity	Response time	Ref
PLD	Al	-	0.2mA/5V	-	50s(rise time) 120s(fall time)	[4]
MOCVD	Al	N-doping	450nA/5V	400A/W At 5v bias	1 μ s (rise time) 1.5 μ s(fall time)	[14]
RF-Sputtering	Al	-	38 μ A/5V	18A/W At 5V bias	100ns(rise time) 1.5 μ s(fall time)	[15]
RF-Sputtering	Au	-	250nA/3V	30A/W at3V	20ns(rise time) 10 μ s(fall time)	[16]
RF-Sputtering	Al, ITO	-	640 μ A/5V	1616A/W at 5V	71.2ns(rise time) 377 μ s(fall time)	[17]
RF-Sputtering	Al	Oxygen Plasma treatment	400pA/3V	1-10A/W	50 μ s(fall time)	[18]
MBE	Ni/Au		38 mA/ (100V/cm)	<0.05A/W	0.556ms(falltime)	[19]
MBE		HCl treatment	0.1-0.2 mA/4V	0.141A/W at 10V bias	-	[19]
P-MBE	Al/Ti	Ga-doping	10mA/5V	1.68A/W At 20V bias	95s(rise time) 2068s(fall time)	[23]
Sol-gel	Au	-	-8mA/5V	-0.03A/W at 5V bias	160s (drop to 50% of its maximum value)	[24]
RF-Sputtering	Al	Ga-doping	-	2.6A/W at 10V bias	10ns(rise time) 960ns(fall time)	[27]

Different post treatments have been used to enhance the ZnO photoconductors performance [53, 76, 80]. According to Liu *et al.*[53], oxygen plasma treatment enhances the UV detection properties of ZnO, reduces the decay time constant (to below 50 μ s) and increasing the on/off ratio of photocurrent (to over 1,000) with a high UV responsivity (1–10 A/W). The reason for this result may be that oxygen plasma treatment can effectively suppress the chemisorption effect and the oxygen vacancy in ZnO films. Chang *et al.*[54] reports a photoresponse increases of ZnO photoconductor after a HCl treatment. Li *et al.*[80] reports the same effect after a SiO₂ covering, but they also report an increase on the dark current due to the damage of ZnO films generated during the SiO₂ covering. Sun *et al.*[60] reports a Ga-doped ZnO film on quartz by RF sputtering that offers higher performance from the n-type doped ZnO in term of rise time (10ns)

and fall time (960s). This fast response can be attributed to the enhancement of tunnel recombination across the potential barriers generated by surface and defects in ZnO:Ga sample. Similar behavior has been reported by Monroy *et al.* [13] in Si-doped $\text{Al}_x\text{Ga}_{1-x}\text{N}$ photoconductive detectors.

3.4.2. Metal-Semiconductor-Metal (MSM) Photodiodes.

A MSM photodiode is a semiconductor with two integrated Schottky contact on the top of the Semiconductor (Figure 3).

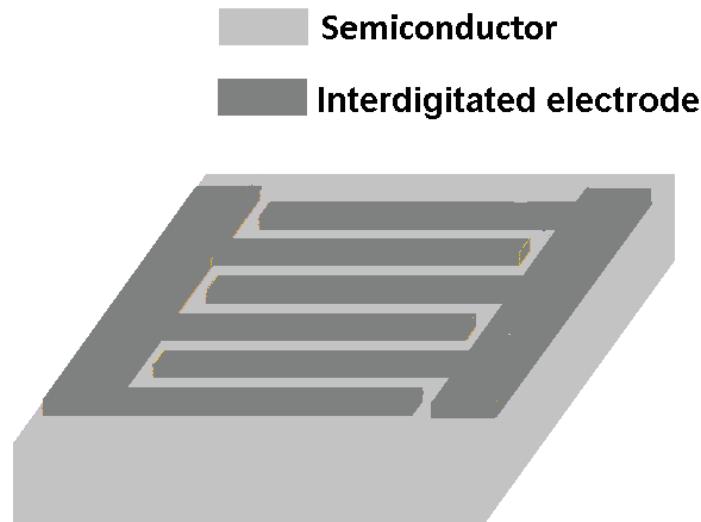


Figure3. Schematic structure of MSM Photodiodes

MSM photodiodes have faster recovery time due to their low capacitance per unit area. Despite this advantage, the metallization shadow on the semiconductors decreases the photoreponse current. This device cannot operate at a zero bias. ZnO MSM photodiodes has been elaborated using different deposition techniques such as MOCVD [68, 81], laser assisted molecular beam deposition (LAMBD)[82], radio frequency (RF) magnetron sputtering [83-85], atomic-layer deposition (ALD) [86] and molecular beam epitaxy (MBE)[87, 88]. Different

electrode types such as Au, Ag, Pt, Ni, Pd, Cr, Al, and Ru have been elaborated and investigated in term of performance. According to Li *et al.*[82], large Schottky barrier height at metal–semiconductor interface leads to increase of the on/off ratio of photocurrent (small leakage current and high breakdown voltage). An increase on the Schottky barrier height can be achieved using metals with high work functions [89]. The Schottky barrier height at the Ru/ZnO, Ag/ZnO, Pd/ZnO and Ni/ZnO was evaluated to be 0.76, 0.736, 0.701 and 0.613 eV, respectively [87, 88].

3.4.3. Schottky Photodiodes

Schottky photodiodes device is a semiconductor sandwiched between an Ohmic contact and a schottky electrode. Figure 4 shows the schematic representation of the Schottky photodiodes device.

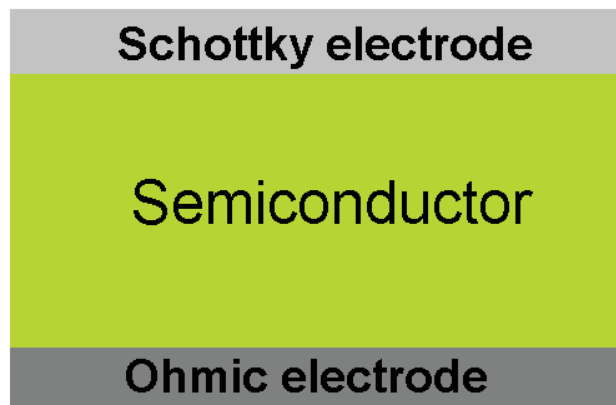


Figure4. The schematic structure of the Schottky photodiodes device

This device has many advantages such as high quantum efficiency, high response speed, low dark current, high UV/visible contrast, and possible zero-bias operation [24, 90]. The first ZnO based Schottky photodiodes device has been reported by Fabricius *et al.* [91] on 1986 with a rise time around 20 μ s and a decay time of 30 μ s. Since then, different publications have reported on this type of device using different substrates, different ZnO deposition techniques, and different types of metal electrodes. Kim *et al.* reports a highly sensitive ZnO Nanowires ultraviolet photodetectors based on mechanical schottky contact [67]. The high conducting

nanowire-based photodetector concurrently achieved a high photocurrent signal, fast response, and fast recovery time, compared with high conducting films and low conducting nanowires photodetectors.

3.4.4. p-n Junction Photodiodes.

This device is simply a p-n or p-i-n diodes, light transparent. Figure 5 shows the schematic structure of this device. This device has many advantages such as fast responding speed, low dark current, and working without applied bias (suitable for space applications).

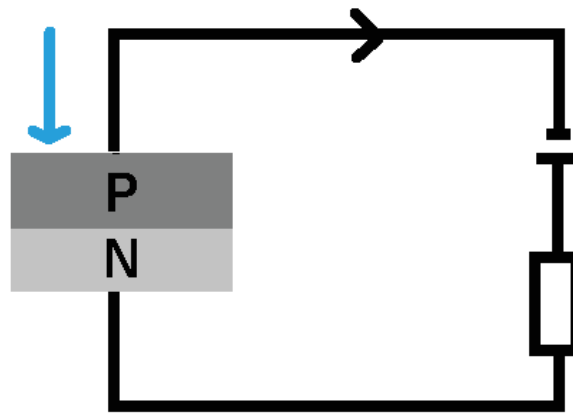


Figure5. Schematic structure of p-n Junction Photodiodes

Different mono and hetero junction ZnO based photodiodes has been reported on the literature. Purnima *et al.* [92] reports a ZnO/Si heterojunction diodes fabricated by ALD technique without using a buffer layer. A contrast ratio of ~ 1115 and responsivity of ~ 0.075 A/W at 2 V reverse bias voltage was detected. Alkiset *et al.* [93] also reports a UV/Vis range photodetectors based on thin film ALD grown ZnO/Si heterojunction diodes.

Different ZnO based UV photodetectors have been studied using different elaboration techniques and different photodetection setups such as Photoconductors, Metal-Semiconductor-Metal (MSM) photodiodes, Schottky photodiodes and p-n junction photodiodes.

Nanostructured ZnO for UV detection was also investigated and shows promising results in term of photoresponse current rise time and fall time [94-103].

4. One dimensional nanostructured UV Photodetectors.

Due to their small size, low fabrication cost, low operation cost, high active surface area combined with the large ability of structural and chemical tuning, one dimensional nanostructured UV photodetectors have attracted attention in the last decade. Different works have been reported on this field on nanostructured UV detectors based on ZnO or GaN. Due to the high relation between these nanostructures form in term of physical shape, structural state, chemical composition and its optical and electrical properties, ZnO is an important candidate for UV detection.

Wang *et al.* [94] reports the photoconduction mechanism in a single ZnO nanowire (Figure 6). Under UV illumination electron-hole pair will be generated. Holes migrate to the surface and recombined with the O₂ species adsorbed on the surface, the unpaired electrons are collected at the anode under an applied voltage, which leads to the increasing of the nanowire conductivity.

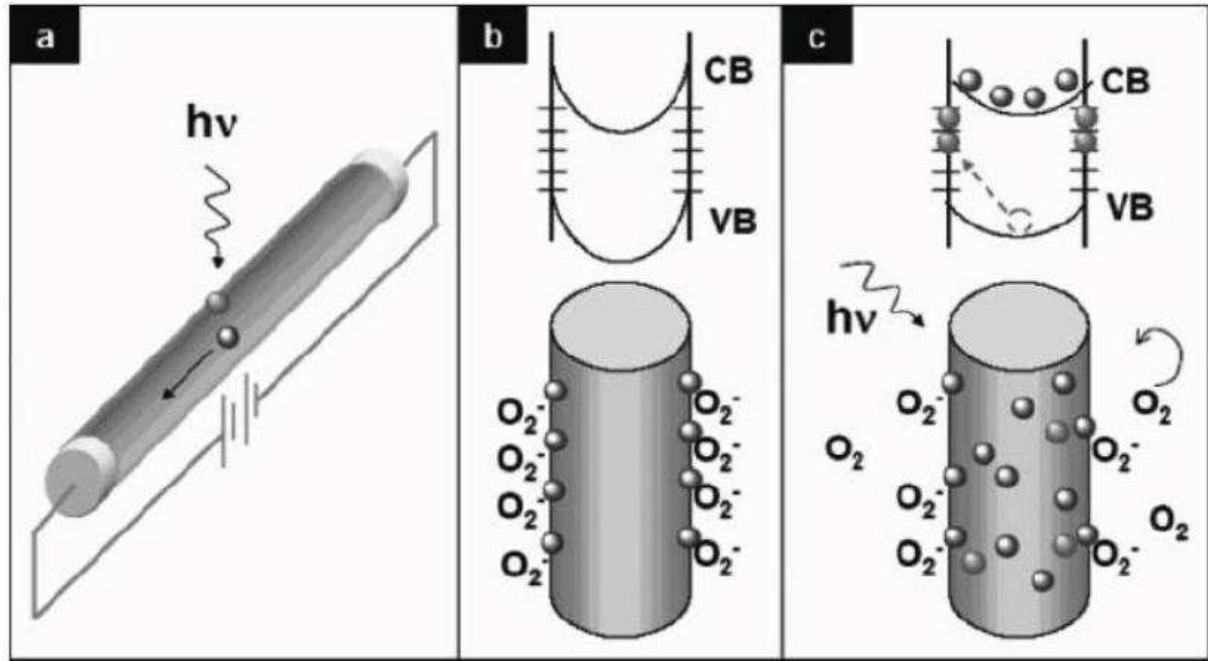


Figure 6. Photoconduction mechanism in a ZnO nanowire: Reproduced from Kind *et al.*[95]

According to Kind *et al.* [95], a transition from a fast photoreponse under oxygen to a slow photoreponse under vacuum assures the oxygen roles. Huang *et al.* [96] reports a three order enhancement on the UV photoreponse of ZnO nanowire due to a polystyrene coating. Lao *et al.* [97] reports a five order magnitudes enhancement on the UV photoreponse of ZnO nanobelt due to a surface functionalization with a high UV absorption ability polymer. UV photoreponse was also enhanced by Ag-ZnO nanowire Schottky contact[98]. Aluminium-doped ZnO nanorods arrays were also developed for UV photodetection[99]. According to Suobai *et al.*[100] the photoreponse current increases linearly with the number of NWs connected in parallel. A significant improvement on term of fast response and recovery times was also reported. Pt has been deposited by focused-ion-beam (FIB) technique[101]. Contact resistance measurements by the transmission line method reports that Pt deposited by the FIB technique reduces the contact resistance. Prades *et al.* [102] suggests to diminish the distance between the electrical contacts or increasing the width of the photoactive area, or improving the electrical mobility of the nanomaterials to enhance ZnO nanowires responses. Lin *et al.* reported a Zinc Oxide ALD on multiwalled carbon nanotubes for UV photodetector applications [103].

Al-doped ZnO nanorods arrays were also reported by Mamat *et al.* [99] for UV photodetection. Lin *et al.* [104] reported on a photoconductor device that was sensitive to illumination with below-gap light by electrospinning of a single Al doped-ZnO (AZO) nanowires followed by a calcination process at 550°C for 3h to obtain well-aligned polycrystalline AZO nanowires. Al-doped ZnO nanowires show higher conductivity than ZnO nanowire. The highest conductivity was reported at 5% Al doped ZnO. Alumina acts as a cationic dopant in the ZnO lattice, that is, the trivalent Al^{3+} ions occupies the divalent Zn^{2+} sites allowing electrons to move to the conduction band easily.

In this chapter ZnO 1D nanostructures based photodetectors will be elaborated using the atomic layer deposition technique combined with the electrospinning techniques. PAN/ZnO core/shell nanostructures were elaborated and characterized for UV photodetection.

5. Elaboration of ZnO 1D nanostructures for UV Photodetection

5.1. Electrospinning

Starting from a polymer solution, sub-micron nanofibers can be synthesized using the electrospinning techniques. The electrostatic field applied between a syringe and a disk collector provides the transformation of the droplet to a Taylor cone. The droplet is stretched under electrostatic field to form a sub-micron fiber after the evaporation of the solvent [105]. Figure 7 shows our electrospinning homemade setup. A 60 Kv high voltage power supply from ISEG, a Kd Scientific syringe pump, an aluminum collector disk and a glove box was used to build up the setup.



Figure7. Homemade electrospinning setup

5.2. Synthesis of polyacrylonitrile nanofibers

Electrospinning solution was prepared by dissolving 10 wt. % of Polyacrylonitrile (150000 (Typical)) in Dimethylformamide. The solution was maintained under agitation for 1 hour then heated at 80°C in an oil bath for 20 min. The polymer solution was electrospun at room temperature in ambient atmosphere under an applied voltage of 25kV with a flow rate of 1 ml/h using a 0.7 mm diameter syringe related to the positive output of the generator. The aluminum disk placed on 15 cm from the tip of the syringe was related to the negative output of the generator. 10*20 mm glass substrate was fixed on the aluminum disk using carbon tape. Silver glue was used as ohmic contact on the glass substrate separated by 5 mm distance as shown on Figure 8. Supported PAN nanofibers have been elaborated with different electrospinning time: 30, 60, 120, 240 and 600 s in order to increase the specific surface.

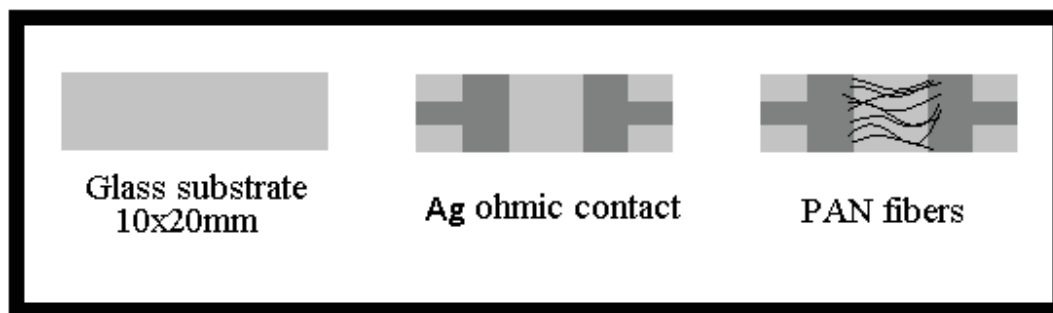


Figure8. PAN fibers supported on glass substrate with Ag Ohmic contact

5.3. Atomic layer deposition of zinc oxide

ZnO ALD was performed using Diethyl Zinc (DEZ) ($\text{Zn}(\text{CH}_2\text{CH}_3)_2$, 52% purity) and water. Due to the high surface area created by the electrospun PAN fibers, the ALD deposition setup has been modified in order to assure a conformal coating. Pulse and purge times have been raised. Table 2 reports the ALD setup used for the ZnO deposition on PAN nanofibers.

Table2. ALD setup for ZnO deposition on PAN nanofibers

	Pulse DEZ	Exposure	Purge	Pulse water	Exposure	purge
Time(s)	1.5s/25sccm	30s/0sccm	60s/100sccm	3s/25sccm	30s/0sccm	60s/100sccm

ZnO has been elaborated using different number of cycles 250, 500, 750 and 1000 cycles. ALD deposition temperature was also varied between 50 and 100 °C. All ALD /PAN nanofibers sensors were characterized using SEM, EDX and XRD.

6. Chemical and structural characterizations

Before starting the UV photo-response characterization for the ZnO nanofibers, structural and chemical characterizations were performed in order to extract the evolution of the structural properties when the ZnO thicknesses increase and the deposition temperature changes. All ZnO ALD samples were characterized by SEM, EDX and XRD.

6.1. X-Ray diffraction (XRD)

XRD measurement was performed on 2 batches of samples. As noted in chapter 2 the used XRD machine has a limit for detecting the minimum size for nanocrystals of 4 nm. The first one is a 50 nm ZnO deposited at different temperatures between 50 and 130°C (Figure9). The second one is 250, 500, 750 and 1000 cycles of ZnO deposited at 100°C (Figure10).

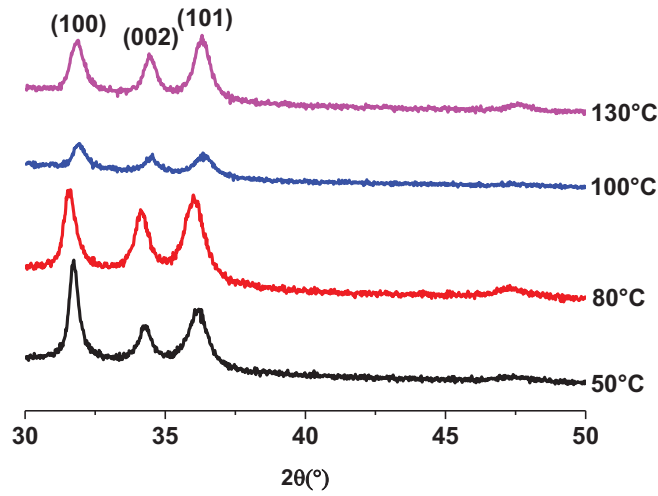


Figure 9. X-Ray diffraction spectra of 250 cycles ZnO elaborated at different temperatures between 50 and 130°C

As shown in Figure 9, XRD spectra at different temperatures 50, 80, 100 and 130°C shows three different peaks at $2\theta = 31.74^\circ$, 34.42° and 36.22° respectively corresponding to (100), (002) and (101) matching the ZnO growth orientation reported on chapter 2. A change in the preferential growth orientation is observed when the deposition temperature increases from 50°C to 130°C. The preferred growth orientation go from (100) to (101).

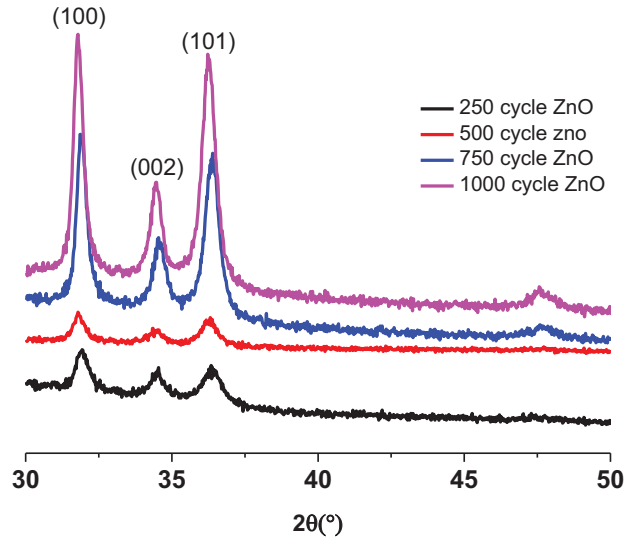


Figure10. X-Ray diffraction spectra of 250, 500, 750 and 1000 cycles of ZnO deposited at 100°C

At 250 cycles ZnO, three weak peaks appear at $2\theta = 31.74^\circ, 34.42^\circ$ and 36.22° respectively corresponding to (100), (002) and (101), those three peaks become more intense at 750 and 1000 cycles ZnO. We can clearly notice that X-ray pics on PAN nanofiber are more intense than the X-ray pics on ZnO thin films deposited on silicon substrate [106] (chapter 2, Figure 9) due to the high amount of ZnO materials deposited on the high surface area of the PAN fibers. Moreover the XRD measurements report a preferred growth in the (100) direction. This preferred growth direction match the one reported for ZnO deposited on silicon substrate [106].

Debye-Scherrer equation was used to calculate the grain size (equation1):

$$D = \frac{0.9 \cdot \lambda}{\beta \cdot \cos(\theta)} \quad \text{(Equation1)}$$

Table 3 shows respectively the grain size of 50 nm ZnO elaborated at 50, 80, 100 and 130°C. Table 4 reported the grain size of ALD ZnO elaborated at 100°C with 250, 500, 750, and 1000 cycles.

Table 3. Grain size values of 50 nm ALD ZnO elaborated at 50, 80, 100 and 130°C

ALD Temperature(°C)	50	80	100	130
Grain size(nm)	26.287	23.064	18.34	17.042

Table 3 shows a decrease of the grain size when the ALD deposition temperature increases. This decrease on the grain size with the deposition temperature increment leads to a higher specific surface. This unexpected finding could be explained by the different ZnO nucleation behaviour on PAN nanofibers as the function of the temperature involving different mechanism of precursor diffusion into the polymer [107-108].

Table 4. Grain size calculation of ALD ZnO elaborated at 100°C with 250, 500, 750, and 1000 cycles

Number of ALD cycles	250	500	750	1000
Grain size (nm)	18.3	23.009	25.052	25.9

As shown in table 4, the grain size increases from 18.3 nm to 25.9 nm when the number of ALD cycles increases from 250 to 1000. The same tendency was reported on chapter 2 for different number of ZnO cycles deposited on silicon substrate. This behavior was attributed to the columnar growth of the ZnO deposited by ALD. This increment on the grain size leads to a decrease in the specific surface.

6.2. Scanning electron microscopy (SEM)

SEM images were performed on PAN nanofibers obtained with different spinning times 30, 60, 120, 240, 600s coated with 250 cycles of ALD ZnO at 100°C using an emission field Hitachi S-4800 microscope (Figure11).

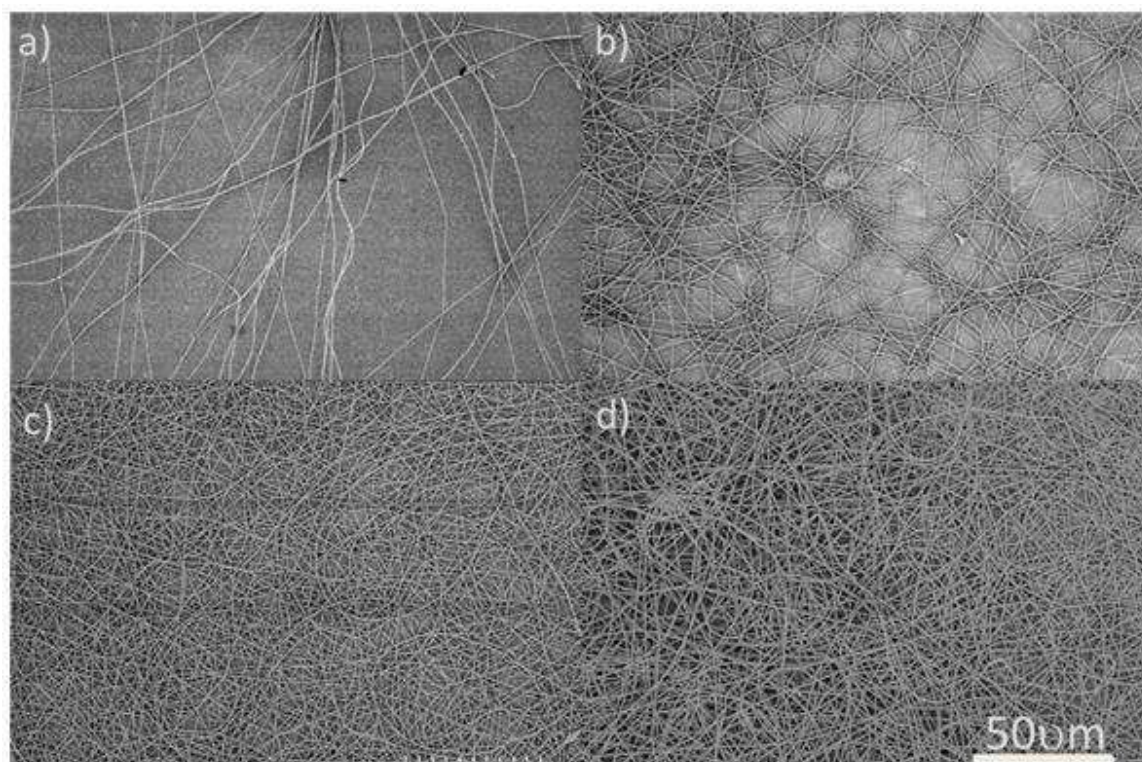


Figure 11. SEM images of PAN nanofibers obtained with different spinning times 30 (a), 60 (b), 240 (c), 600s (d) coated with 250 cycles ALD ZnO at 100°C

As shown by the SEM images (Figure 11) the fiber density increases when the spinning time increases. At higher magnification (Figure 12), a rough morphology is observed on the surface of the nanofibers inducing a higher specific area of the sensor nanomaterials.

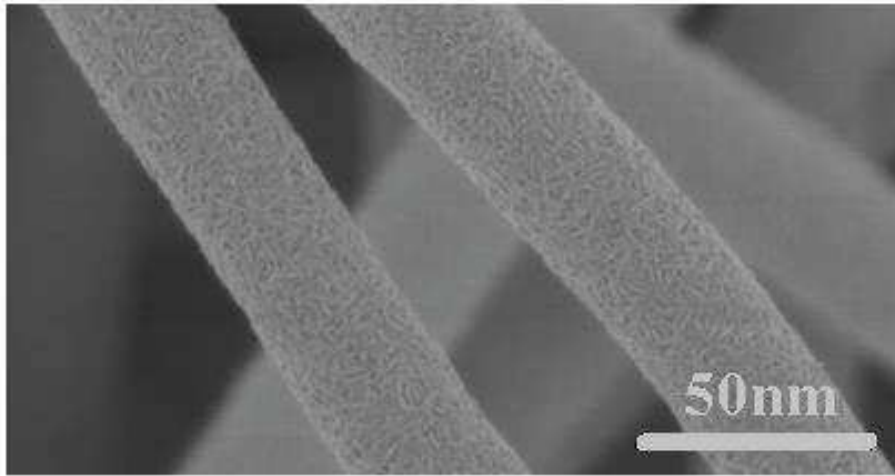


Figure 12. SEM image of 250 cycles ALD ZnO deposited at 100°C on PAN fibers with 600 s spinning time

7. UV characterization

Characterizations of electrical conductivity of ZnO samples deposited under different conditions were performed on dark and under UV illumination in order to study the behavior of ZnO 1D nanostructures based photodetectors. Cyclic voltammetry between -3V and 3V with a scan speed of 50 mV/sec was realized. Chronoamperometry measurement was also performed with On/Off UV illumination in order to extract the photoresponse current and the recovery time. UV detection cell is a homemade cell made from a black box, a UV (365 nm), 4W source from Roth, France and a 265A potentiostat from EG&G instruments (Figure 13). During the electrical measurement the UV cell was covered with a black box to assure a perfect light isolation. After that, $I(V)$ and $I(t)$ data was plotted using origin 9.0 software.

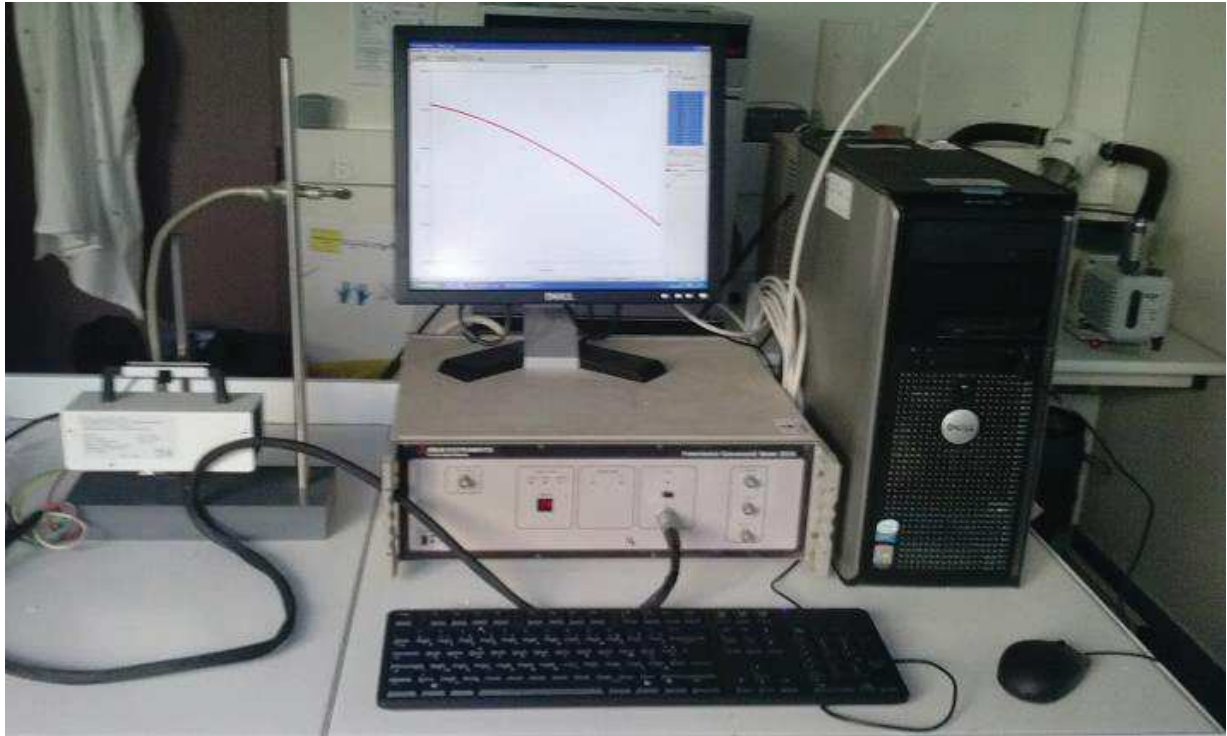


Figure13. UV detection cell

7.1. UV characterization of Different ZnO thicknesses deposited on PAN nanofibers.

Supported PAN nanofibers with 240 seconds of electrospinning time have been used for this part of this study in order to investigate the effect of the ZnO thickness on the UV detection properties. Four different samples of ZnO with different numbers of ALD cycles were deposited on the PAN fibers: 250, 500, 750 and 1000 cycles which correspond to 50, 100, 150 and 200 nm thick ZnO respectively. All those samples were performed at 100°C using the experimental conditions mentioned above in Table 2.

7.1.1. Cyclic Voltammetry

A cyclic voltammetry scan between -3 and 3 V with 50 mV/s scan rate has been performed on the different ALD ZnO thicknesses. Figure 14 shows the cyclic voltammetry of the 50, 100, 150, 200 nm ZnO deposited by ALD on supported electrospun PAN fibers (240 s time) in Dark and UV (365 nm).

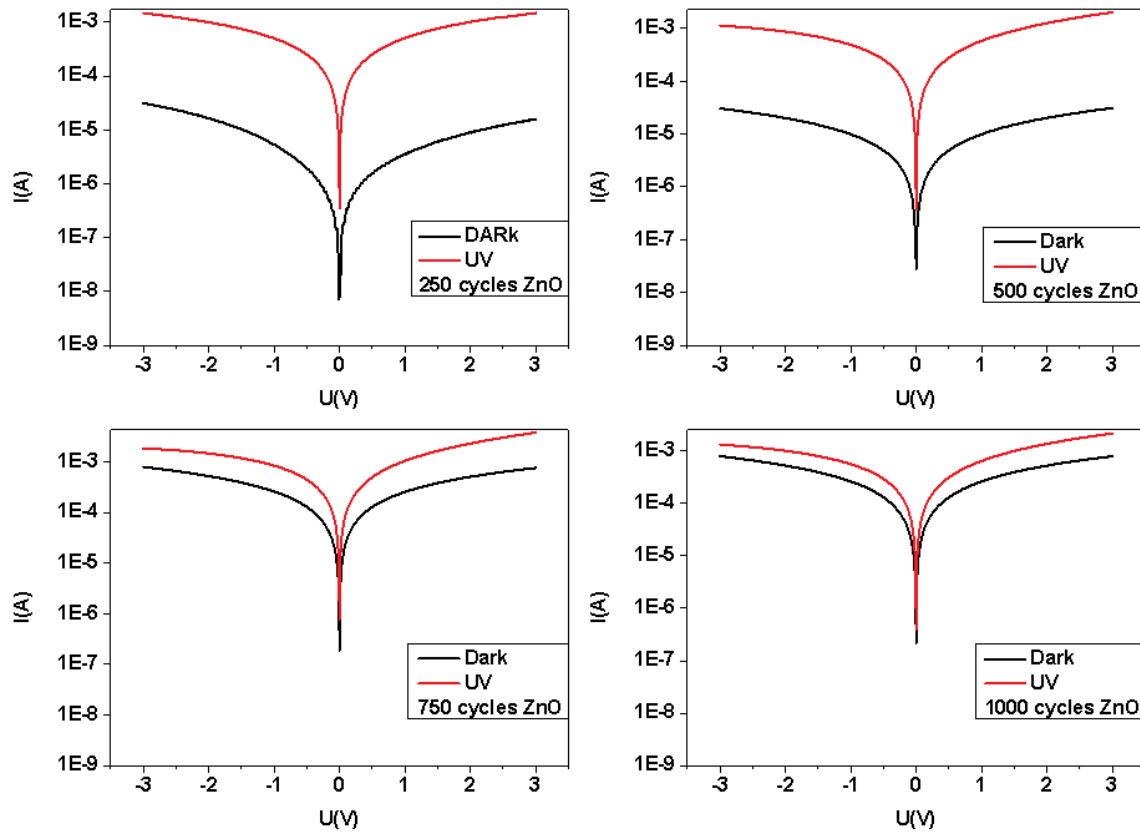


Figure 14. Cyclic voltammetry of 250, 500, 750, and 1000 cycles ZnO ALD thick deposited on PAN NFs, in Dark and UV 365nm.

The cyclic voltammetry of all ZnO sensors confirm an ohmic contact between the ZnO nano-fibers and the Ag contact. Table 5 reports the UV and dark current of different ZnO thicknesses with the UV/Dark current ratio at -1V bias.

Table5. UV and dark current of different ZnO thicknesses with the UV/Dark current ratio at -1V bias

Number of ZnO cycles	Dark current (A)	UV current (A)	UV/Dark ratio
250	5.33×10^{-6}	5.04×10^{-4}	94.5
500	9.9×10^{-6}	5.34×10^{-4}	53.9
750	2.6×10^{-4}	8.41×10^{-4}	3.23
1000	2.62×10^{-4}	5.6×10^{-4}	2.13

As shown on table 5, the UV current of different ZnO thicknesses stay in the range of 10^{-4} A when the number of cycles increases (ZnO thickness increases). On the contrary the dark current increases (resistivity decreases) when the number of cycles rises. Due to this Dark current increment, the UV/Dark ratio decreases from 94.5 to 2.13 when the number of ALD cycles goes from 250 to 1000. This resistivity decreasing when the ZnO ALD cycles increases was reported by Tapilyet *al.*[109]. The conductivity increases (resistivity decreases) can be attributed to the change of the amount of OH group in the ZnO ALD films. The OH group decreases when the thickness increases (as shown by the EDX results: chapter 2; paragraph 4.3). The influence of the OH groups on the free carrier concentration was reported by Guziewicz *et al.*[110]. They demonstrate that the low fraction of OH group on the ALD ZnO layer leads to high free carrier concentration.

7.1.2. Chronoamperometry

Chronoamperometry measurement at -1V has been performed on the same samples for 3000 seconds in order to extract the UV photoresponse current (ΔI) defined as: $\Delta I = I - I_0$ (where I_0 is the dark current and I is the photoresponse current under UV illumination) and the recovery time (τ), defined as the time for the photoresponse current to drop to $1/e$ (37%) of the maximum photoresponse current [100]. Table 6 shows the UV on/off setup used for this measurement.

Table6. UV on/off setup

Time interval (s)	0-100	100-200	200-3000
UV	off	on	Off

Figure 15 shows the Chronoamperometry measurement for samples with different ZnO ALD thicknesses 50, 100, 150, and 200 nm deposited on 240s supported PAN nanofibers. The UV photoresponse and the recovery time are reported on table 7.

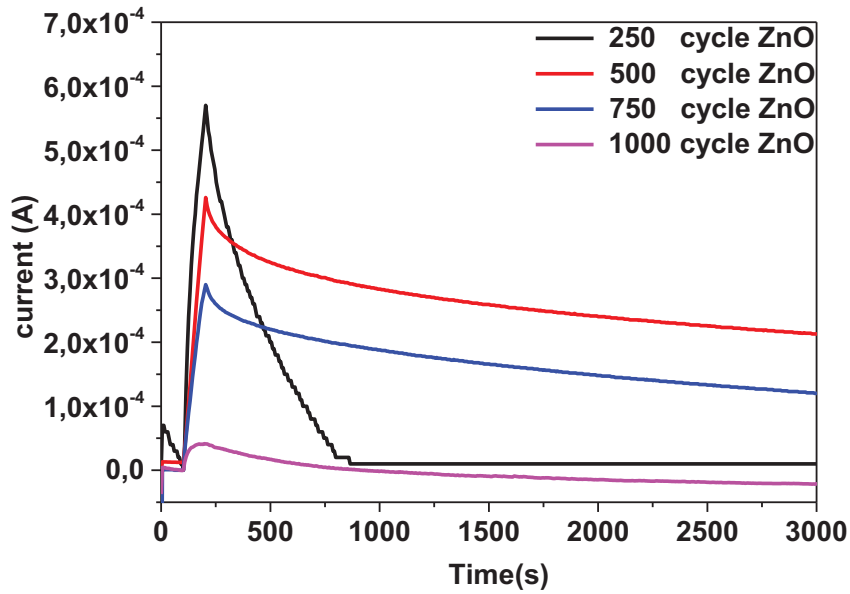


Figure 15. Chronoamperometry measurement for samples with different ZnO ALD thicknesses 50, 100, 150, and 200 nm deposited on PAN nanofibers with UV illumination (365 nm) ‘on’ between 100 and 200 s.

Table 7. UV photoresponse current and the recovery time for the samples with different ZnO ALD thicknesses: 50, 100, 150, and 200 nm deposited on PAN nanofibers.

ZnO thickness (nm)	ΔI (A)	T (s)
50	5.7×10^{-4}	144
100	4.14×10^{-4}	985
150	2.9×10^{-4}	763
200	4.11×10^{-5}	162

In order to understand the influence of ZnO thickness on the UV photoresponse properties, the UV photoresponse current and the recovery time has been plotted against the ZnO ALD layer thicknesses on Figure 16.

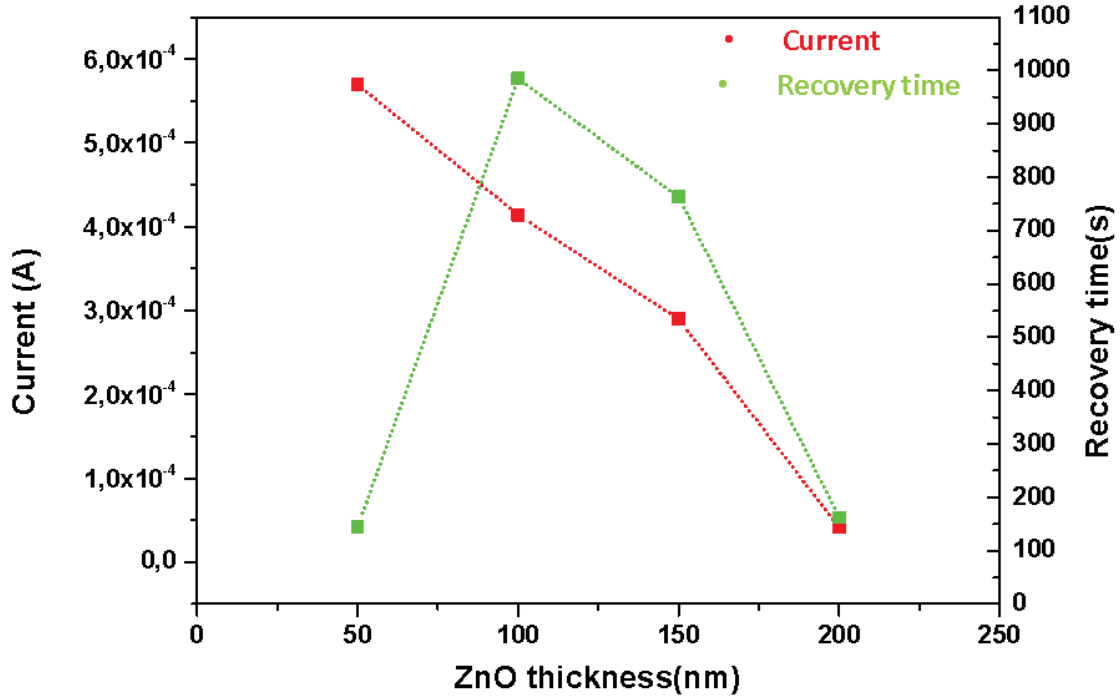


Figure16. UV photo-response current and recovery time versus ZnO ALD layer thicknesses

As shown on Figure 16, the UV photoresponse current ΔI decreases when the ZnO thickness increases due to the dark current increment which can be due to the decrease on the amount of OH groups [110]. Liu *et al.*[53] demonstrates that a O_2 plasma treatment for ZnO can enhance the UV photoresponse due to the oxygen vacancies filling at the ZnO surface. This observation confirms the oxygen role on the UV photoresponse. This UV response ΔI decreases behavior can also be related to the increment on the grain size when the ZnO thickness increases. That leads to a decrease on the specific surface of the ZnO sensor [106]. Despite the linear behavior of the photoresponse current, the recovery time shows too different performances: it rises with the thickness increases between 50 and 100 nm than decrease between 100 and 200

nm. These uncharacteristic changes on the recovery time can be due to the non-reproducible PAN nanofiber structure by the electrospinning technique that lead to an uncharacteristic change on the contact point between the nanofibers. Aligned fibers spinning on a rotatory collector can be an interesting perspective for reproducible PAN nanofiber structure. The ZnO film with 50 nm has been used to carry on the next part of this study due to her highest photoresponse current combined with the low recovery time.

7.2. UV characterization of different electrospinning times

The sensors specific surface area can be controlled by the PAN electrospinning times. In order to investigate the influence of active surface on the UV photoresponse, five samples with different electrospinning times between 30 and 600 s were elaborated. A glass sample without PAN nanofibers deposition has been used as reference. 50 nm of ALD ZnO was deposited at 100°C using the experimental conditions reported in table 2.

7.2.1. Cyclic Voltammetry

A cyclic voltammetry scan between -3 and 3 V with 50 mv/s scan rate has been performed on the sensor samples with different PAN electrospinning times. Figure 13 shows the cyclic voltammetry of sensors with different electrospinning times 0, 30, 60, 120, 240, and 600s in Dark and under UV illumination (365 nm).

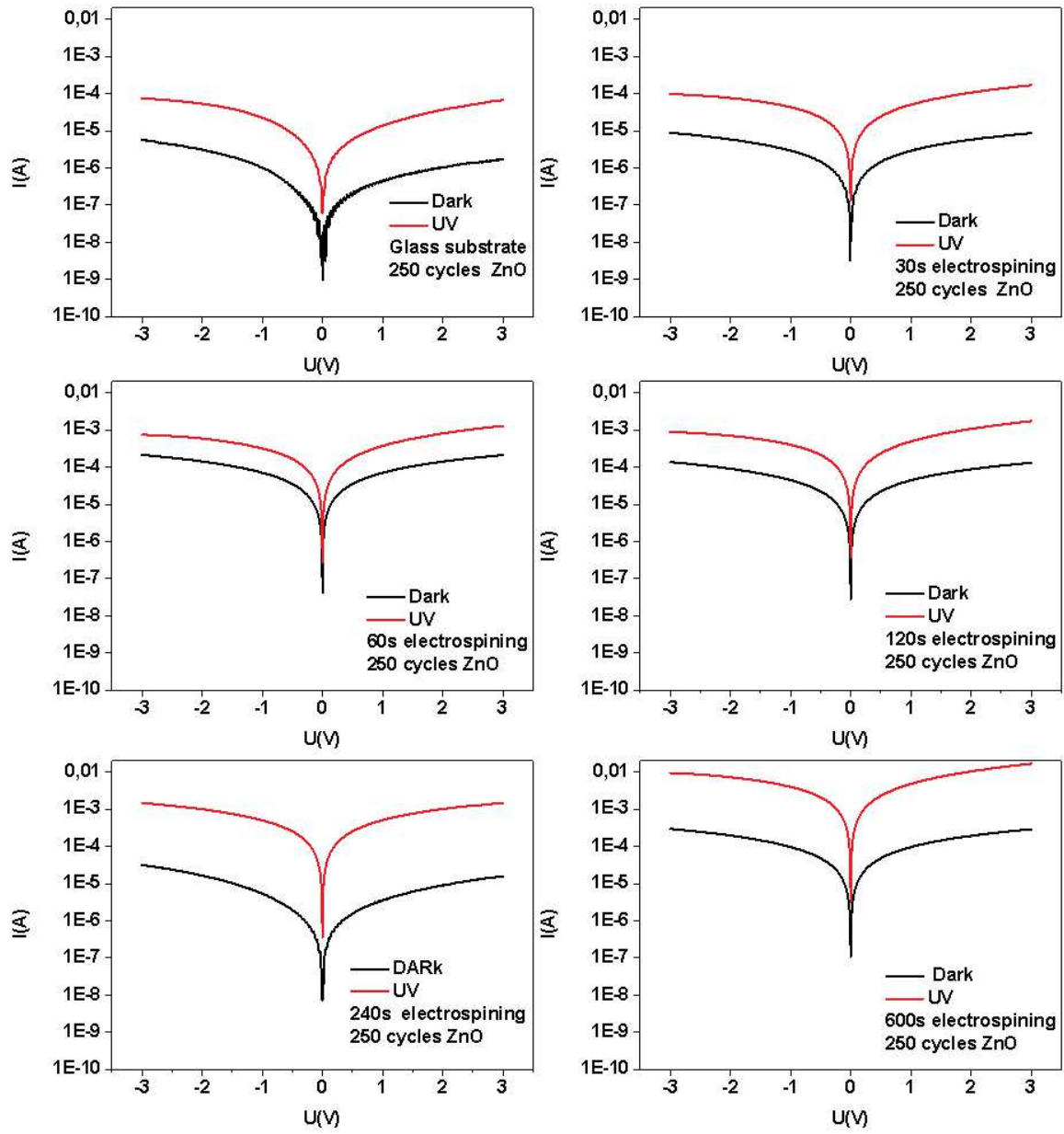


Figure 17. Cyclic voltammetry of sensors with different electrospinning times 0, 30, 60, 120, 240, and 600 s in Dark and under UV (365 nm)

The cyclic voltammetry measurement of all sensors confirms an ohmic contact between the ZnO nanofibers and the silver glue. Table 8 shows the UV and dark current with UV

photoresponse current at -1V bias of different electrospinning times PAN fibers covered with 250 cycles of ALD ZnO.

Table8. UV and dark current with UV photoresponse current at -1V bias of different electrospinning time PAN fibers covered with 250 cycles of ALD ZnO.

Electrospinning time (s)	Dark current	UV current	ΔI
0	1.01×10^{-6}	2.26×10^{-5}	2.15×10^{-5}
30	2.91×10^{-6}	4.31×10^{-5}	4.09×10^{-5}
60	7.09×10^{-5}	3.19×10^{-4}	2.48×10^{-4}
120	4.48×10^{-5}	4.02×10^{-4}	3.55×10^{-4}
240	5.33×10^{-6}	5.04×10^{-4}	4.98×10^{-4}
600	9.88×10^{-5}	4.01×10^{-3}	3.91×10^{-3}

As we shown in table 8, when the electrospinning time increases the dark current stay in the range 10^{-5} - 10^{-6} A. In the contrary, the UV current increases from 2.26×10^{-6} to 4.01×10^{-3} . This UV reponse increment was expected due to the enhancement on the specific area of ZnO fiber exposed to UV light when the spinning time increases. This UV current increment leads to the increase the ZnO detectors ΔI photoresponse from 2.15×10^{-5} to 3.91×10^{-3} when the electrospinning time increases from 0 s to 600 s.

7.2.2. Chronoamperometry

Chronoamperometry measurement at -1V was performed on the same series for 3000 seconds. Table 3 report the UV on/off setup used for this measurement. Figure 18 shows the Chronoamperometry measurement with UV (365 nm) illumination between 100 and 200s of different PAN spinning times based photodetectors.

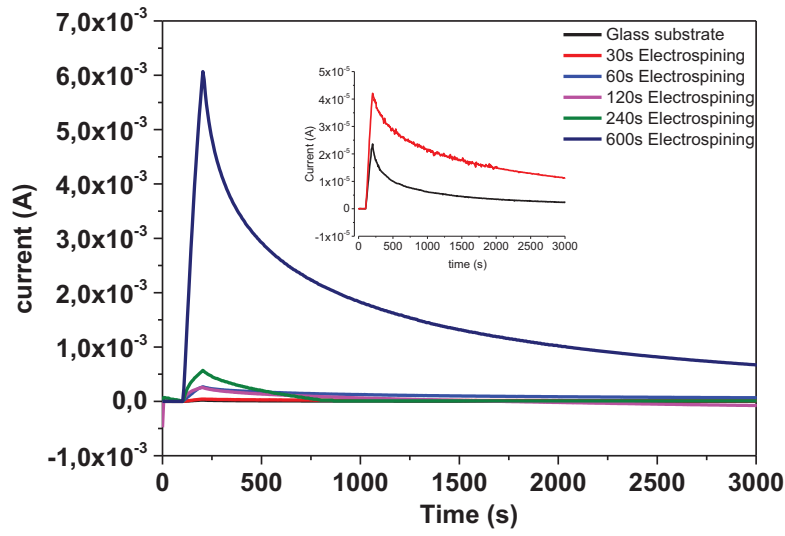


Figure 18. Chronoamperometry measurements of sensors with different electrospinning times 0, 30, 60, 120, 240, and 600 s with UV (365 nm) illumination between 100 and 200s

The UV photo-response current (ΔI) and the recovery time (τ) was extracted from Figure 14 and reported on table 9, then plotted in figure 19 versus the PAN electrospinning times. It allows illustrating the relation between the PAN electrospinning time and the UV photo-response properties.

Table9. UV photoresponse current (ΔI) and recovery time (τ) of sensors with different electrospinning times 0, 30, 60, 120, 240, and 600 s

Samples	ΔI (A)	T (s)
0 s PAN	2.36×10^{-5}	99
30 s PAN	4.207×10^{-5}	378
60 s PAN	2.7×10^{-4}	312
120 s PAN	2.53×10^{-4}	192

240 s PAN	5.7×10^{-4}	144
600 s PAN	6.068×10^{-3}	132

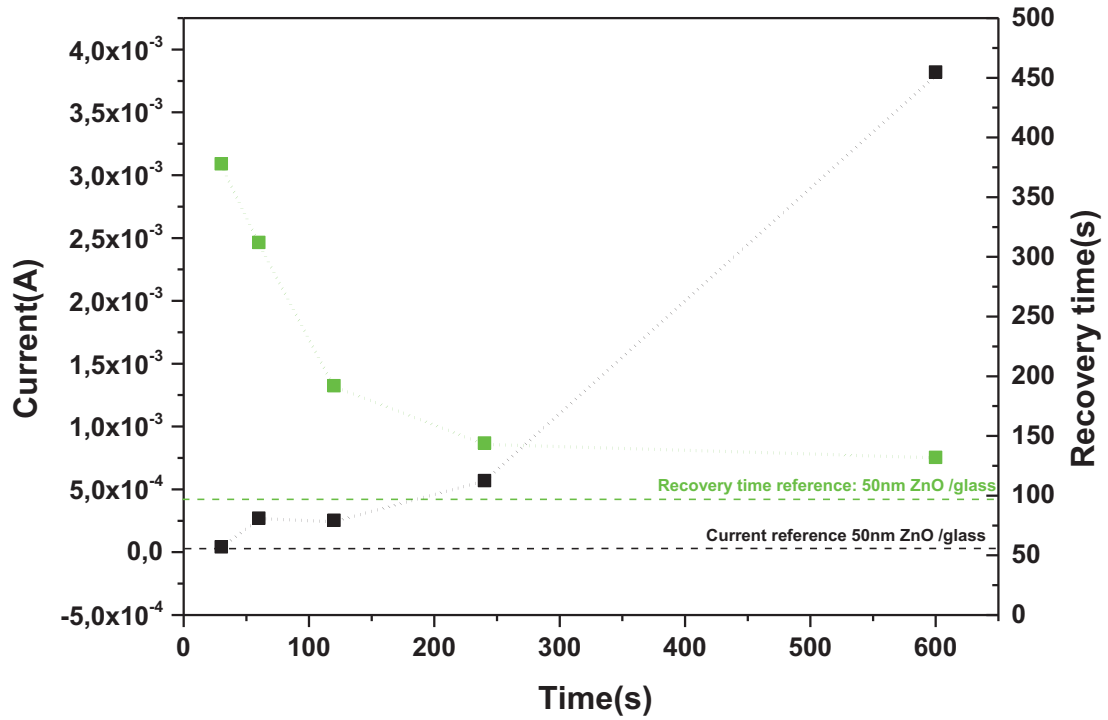


Figure 19. UV photo-response current and recovery time versus PAN electrospinning time

As shown in figure 19, the UV photoresponse current increases when the PAN electrospinning time increases which confirm the cyclic voltammetry tests. This behavior is related to the active surface enhancement. This behavior was also reported by Suobaiet *al.* [100]. The photoreponse current increases when the number of NWs connected in parallel increases. Moreover the recovery time decreases when the PAN electrospinning time increases due to more contact points between the nanofibers when their amount increases. Increasing the PAN electrospinning time enhances the UV photoresponse on both UV photoresponse current and recovery time properties. We should note that the UV photoresponse current has been enhanced by a factor of 250 when the PAN electrospinning time go from 0 to 600 s. An increase by a factor

of 1.3 of the recovery time has been observed which is negligible versus the huge amount of current enhancement.

7.3. UV characterization of ZnO ALD deposited at different temperatures

ZnO ALD deposition temperature effect was also investigated. Four different samples with ZnO ALD deposited at different temperatures between 50 and 130°C were investigated on 600s PAN electrospinning time substrate. The thickness of the deposited ALD layer was about 50 nm. The ZnO ALD thickness and the electrospinning time have been set according to their best performance reported in section 7.2.

7.3.1. Cyclic voltammetry

A cyclic voltammetry scan between -3 and 3 V with 50 mv/s scan rate has been performed on the different ALD deposition temperature photodetectors. Figure 20 shows the cyclic voltammetry of 50, 80, 100 and 130 °C ZnO ALD UV photodetectors in Dark and under UV illumination (365 nm).

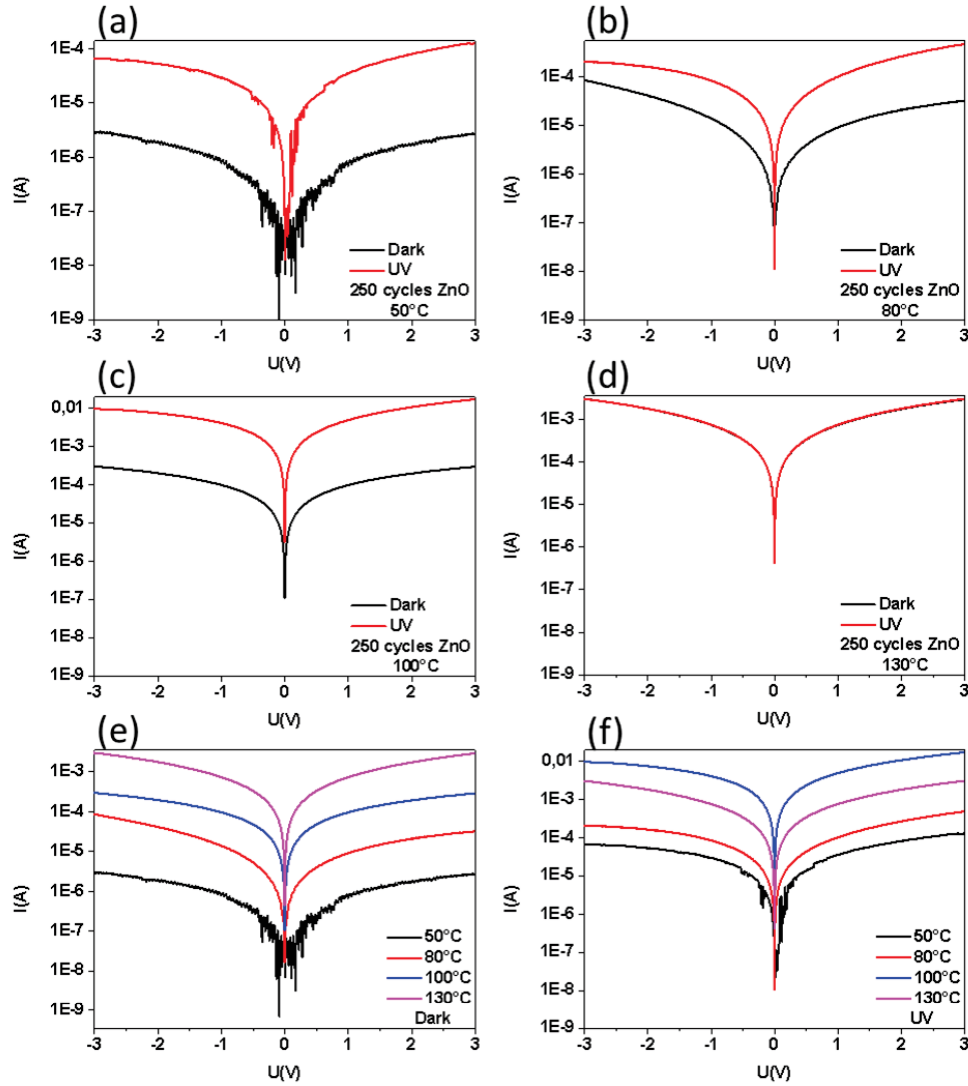


Figure 20. Cyclic voltammetry of sensors with different deposition temperature; 50°C (a), 80°C (b), 100°C (c), and 130°C (d). Cyclic voltammetry with different deposition temperatures in dark (e), cyclic voltammetry with different deposition temperatures under UV (f)

Based on the cyclic voltammetry measurement Figure 20 (a), (b), (c) and (d), it is clear that for the ZnO deposited between 50°C and 100°C, the UV illumination leads to a shift on the I(V) curve. The ZnO deposited at 130°C does not show any shift under UV (figure 20d).

Moreover Figure 20(e) shows an increase in the dark current when the deposition temperature increases from 50 to 130°C. This dark current increment can be due to the OH group decreases when the deposition temperature increases which lead to higher free career charge [110]. This results also match Hubyet *al.*[111] observations that report an increase on the conductivity when the deposition temperature increases. This dark current increment when the deposition temperature increases lead to a negative behavior on the UV photoresponse. In addition, when increasing the deposition temperature we decrease the grain size as reported on table 3. This grain size decreases when the deposition temperature increases lead to a higher UV current as reported on figure 20(f). The interference of those two opposite behavior on the UV photoresponse when the temperature increases lead to the high UV photoresponse for the ZnO deposited at 100°C.

7.3.2. Chronoamperometry

Chronoamperometry measurement at -1V was performed on the same samples for 3000 seconds. Table 3 reports the UV on/off setup used for this measurement. Figure 21 shows the chronoamperometry measurement with UV (365 nm) illumination between 100 and 200s for four different ZnO based photodetectors (600 s spinning time, 250 cycles ZnO) at 50, 80, 100 and 130°C.

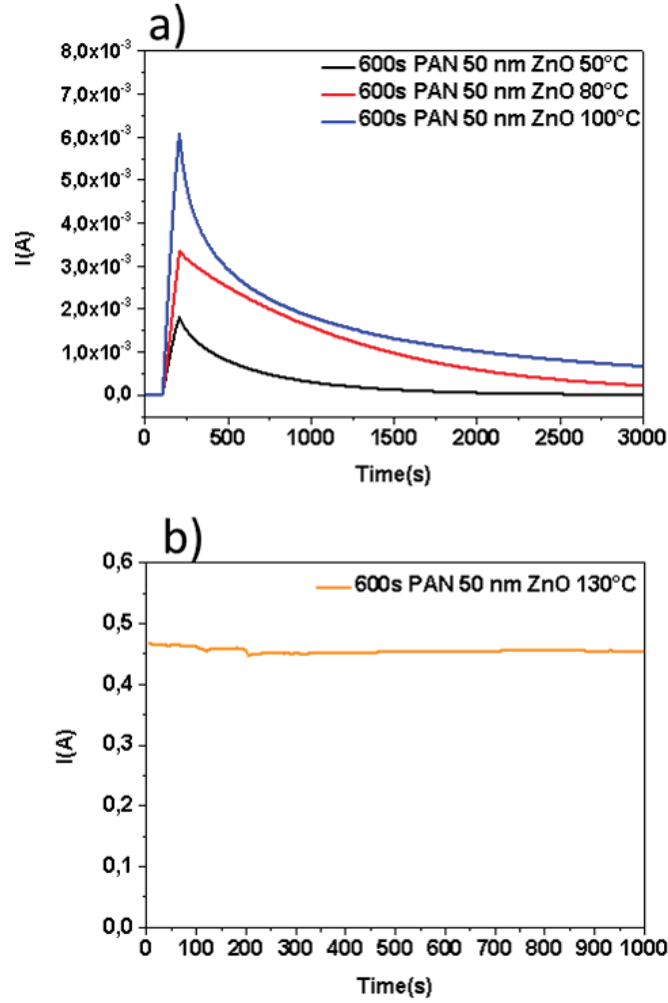
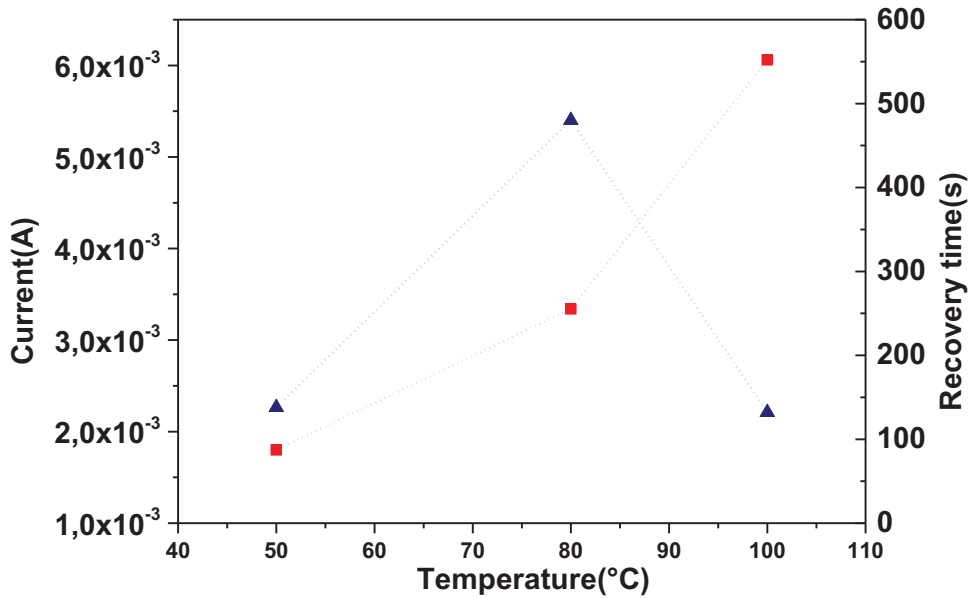


Figure 21. Chronoamperometry measurement of PAN/ZnO ALD with different temperatures 50, 80, 100 (a) and 130°C (b) with UV (365 nm) illumination between 100 and 200s.

The UV photoresponse current (ΔI) and the recovery time (τ) was extracted from Figure 20 and reported on table 6. The data were plotted in Figure 22 versus the ALD deposition temperatures to investigate the relation between the ALD deposition temperature and the UV photoresponse properties.

Table6. UV photoresponse current (ΔI) and recovery time (τ) of PAN/ZnO ALD with different temperatures 50, 80, 100 and 130°C.

ZnO ALD temperature (°C)	$\Delta I(A)$	T(s)
50	1.8×10^{-3}	138
80	3.34×10^{-3}	480
100	6.06×10^{-3}	132
130	-	-

**Figure22. UV photo-response current and recovery time versus ZnO ALD deposition temperatures**

As shown in figure 22, the UV photoresponse current increases when the ZnO ALD deposition temperature increases between 50 and 100°C. This behavior can be due to the overcome of the surface area increment (positive effect) on the dark current increment (negative effect). Contrary for the ZnO deposited at 130°C the dark current increment (negative effect) overcome the active surface increment (positive effect) to lead to a zero photoresponse. Moreover an uncharacteristic change on the recovery time is observed. This behavior is not well understood for the moment. More experiments are in progress to better illustrate this phenomena. Aligned fibers spinning on a rotatory collector can be an interesting perspective to better illustrate this

phenomena. Another perspective of this study will be to study the deposition temperature effect on the recovery time using flat substrate such as glass substrates.

8. Different ohmic contact distances

Sample with 600s PAN electrospinning time and 50 nm ALD ZnO (250 cycles) at 100°C show the higher photo-response and the lower recovery time (6.06×10^{-3} A; 132s). In order to study the effect of the distance between the electrodes, UV photoresponse test was performed on the same type of sensor on larger substrate (16.5 mm) with nearest electrodes distance (3 mm) in order to keep the same working area (Figure 23).

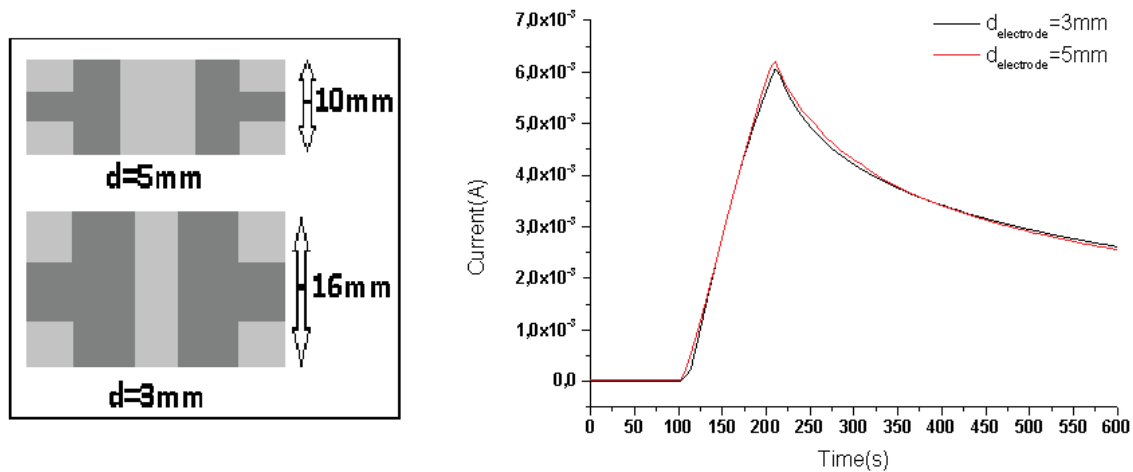


Figure23. PAN/ALD ZnO sensor with different electrode distances

Due to the nearest electrodes distance with the same illuminating area, the UV photoresponse current was approximately the same (6.17×10^{-3} A). In addition, the recovery time decreases from 132 to 108s due a lower electron path between the electrodes that leads to faster discharge. This results was reported elsewhere by Pradeset *al.*[102]. Shotcky contact can lead to lower recovery time due to the lower electron path between the electrodes. However, this type of contact cannot be achieved on the PAN nanofiber structure due to the high PAN nanofiber layer thickness.

9. Device stability

The 600 s electrospinning time photodetectors with 3 mm electrodes distance coated with 50 nm ALD ZnO (250 cycles) at 100°C shows the higher photoresponse and the lower recovery time (6.17×10^{-3} A; 108s). Figure 24 shows the device stability test performed on this sensor.

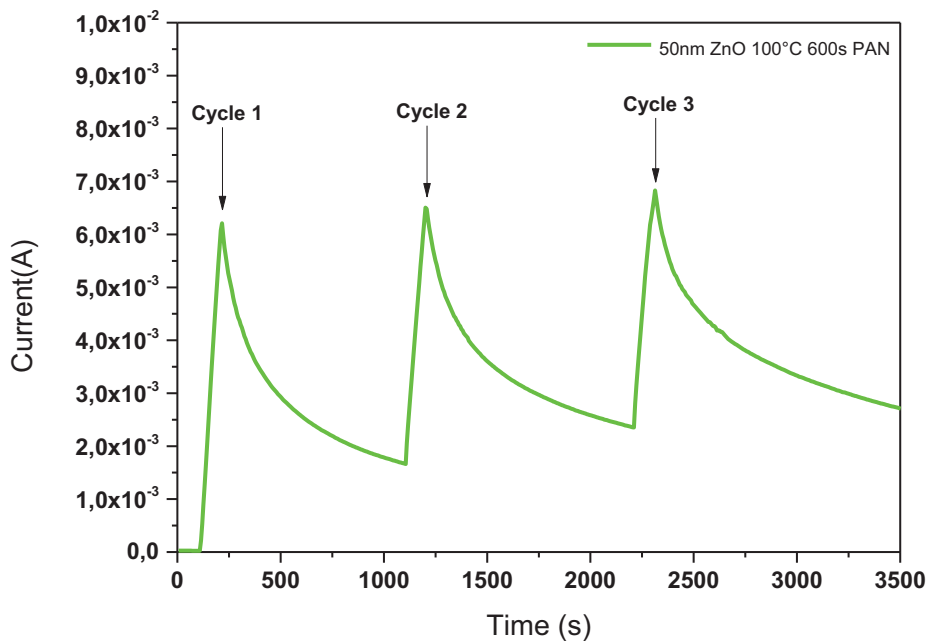


Figure24. Device stability test on 600 s PAN electrospinning with 250 cycles ZnO at 100°C

The UV photo-response current and the recovery time was extracted from Figure 24 and reported on table 7. Then it was plotted against the number of cycles on Figure 25.

Table7. UV photoresponse current and recovery time of cycle 1, 2 and 3

Cycle number	UV photoresponse current(A)	recovery time(s)
1	6.17×10^{-3}	108s
2	4.85×10^{-3}	108s
3	4.47×10^{-3}	108s

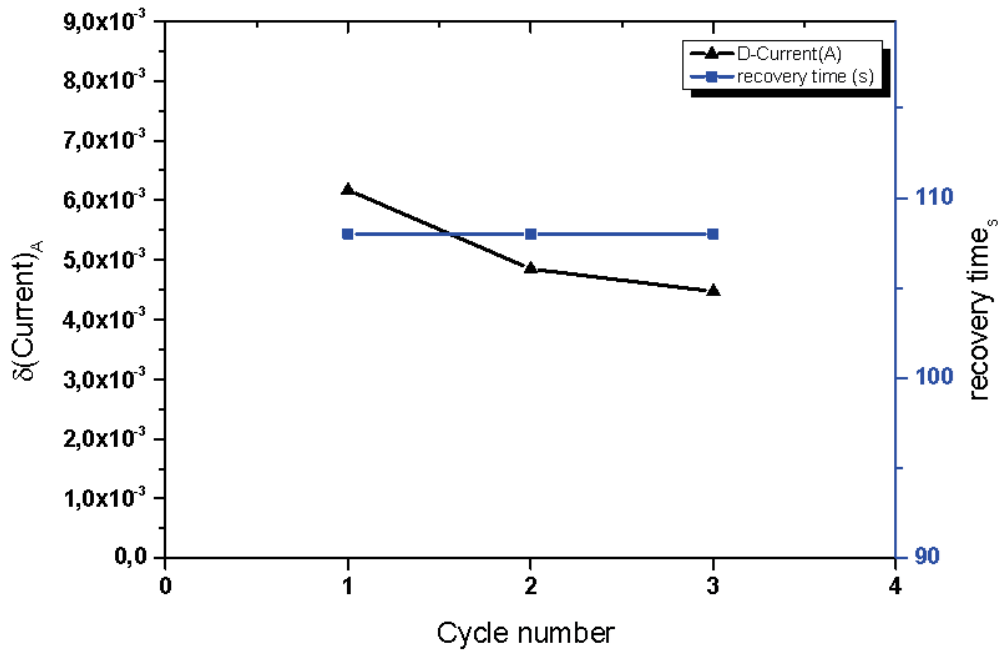


Figure25. UV photo-response current and the recovery time against the number of cycles

As shown in table 7 and Figure 25, the UV photoresponse decreases from 6.17×10^{-3} to 4.47×10^{-3} mA. This finding can be related to the non total recovery of the dark current due to the insufficient time between the cycles (Figure20). However, the recovery time remains constant for the 3 cycles.

10. Conclusion and perspectives

Combining the electrospinning technique and the atomic layer deposition, ZnO 1D nanostructures have been synthesized. Different parameters have been investigated such as the electrospinning time, the ZnO thickness and the deposition temperature. XRD and SEM measurements have been done on those samples. SEM observations on different electrospinning time show an increase of the PAN fibers thickness and that lead to high specific area. XRD measurements for the ZnO with different thicknesses show three structural peaks corresponding to the (100), (002) and (101) direction. A preferred growth in the (100) direction have been reported for the different ZnO thicknesses. Moreover the XRD measurement shows an increase on the grain size when the ZnO layer thickness increases.

XRD measurements have been also performed on 250 cycles ALD ZnO deposited at different temperatures. A change in the preferential growth orientation is observed when the deposition temperature increases from 50°C to 130°C. The preferred growth orientation goes from (100) to (101). Moreover the grain size decreases when the deposition temperature increases. This grain size decreases lead to an enhancement on the specific area. Cyclic voltametry and chronoamperometry measurements have been done on the different ZnO based photodetectors samples. Increasing the PAN fiber density shows an increase on the UV photoresponse and a decrease on the recovery time. This behavior has been linked to the increment of the specific surface and the contact point between the ZnO fibers. Moreover tests performed on different ZnO thicknesses report an increase on the UV photoresponse when the ZnO ALD layer thickness increases. Cyclic voltametry measurement reports an increase on the dark current when the ZnO thickness increases due to the decrease of OH group which lead to higher conductivity.

UV photoresponse tests have been also realized at different temperatures. An increase of the UV photoresponse has been reported between 50 and 100°C due to the increment of the specific area reported by the XRD measurement. A decrease of the grain size is observed when the deposition temperature increases. We should note that the same tendency was not observed for the 130°C deposition temperatures due to the high dark current measured on this sample. In order to decrease the recovery time, we decrease the electrodes distance. A decrease of 24 s for

the recovery time has been reported between 5 and 3 mm electrodes distances. Finally the device stability was tested. Device stability tests show a small decrease on the UV photoresponse current with a constant recovery time after 3 UV on/off cycles. Due to the promising results showed by this study, different studies are in progress in our group on ZnO doped Al_2O_3 , SnO_2 and TiO_2 for UV detection applications.

References

1. Shan, C.X., et al., Ultraviolet photodetector fabricated from atomic-layer-deposited ZnO films. *Journal of Vacuum Science & Technology B*, 2009. 27(3): p. 1765-1768.
2. Gu, X., et al., Photovoltaic Properties of $Zr_xTi_{1-x}O_2$ Solid Solution Nanowire Arrays. *Journal of Nanoscience and Nanotechnology*, 2014. 14(5): p. 3731-3734.
3. Huang, H., et al., Growth and fabrication of sputtered TiO_2 based ultraviolet detectors. *Applied Surface Science*, 2014. 293: p. 248-254.
4. Inamdar, S.I. and K.Y. Rajpure, High-performance metal-semiconductor-metal UV photodetector based on spray deposited ZnO thin films. *Journal of Alloys and Compounds*, 2014. 595: p. 55-59.
5. Jin, Z., et al., High-performance flexible ultraviolet photoconductors based on solution-processed ultrathin ZnO/Au nanoparticle composite films. *Scientific Reports*, 2014. 4.
6. Kim, D.Y., et al., Air-Stable, Solution-Processed Oxide p-n Heterojunction Ultraviolet Photodetector. *ACS applied materials & interfaces*, 2014. 6(3): p. 1370-4.
7. Rostami, A., et al., High-responsivity AlGaIn-GaN multi-quantum well UV photodetector. *International Journal of Numerical Modelling-Electronic Networks Devices and Fields*, 2014. 27(2): p. 309-317.
8. Tsay, C.-Y. and S.-H. Yu, Optoelectronic characteristics of UV photodetectors based on sol-gel synthesized GZO semiconductor thin films. *Journal of Alloys and Compounds*, 2014. 596: p. 145-150.
9. van Schalkwyk, L., et al., Implementation of an AlGaIn-based solar-blind UV four-quadrant detector. *Physica B-Condensed Matter*, 2014. 439: p. 93-96.
10. Xie, Y., et al., High-performance self-powered UV photodetectors based on TiO_2 nano-branched arrays. *Nanotechnology*, 2014. 25(7).
11. Zhang, M., et al., Solar-Blind Photodetector Based on $LaAlO_3$ with Low Dark Current. *Journal of Nanoscience and Nanotechnology*, 2014. 14(5): p. 3827-3830.
12. Lin, C.-H. and C.W. Liu, Metal-Insulator-Semiconductor Photodetectors. *Sensors*, 2010. 10(10): p. 8797-8826.
13. Monroy, E., F. Omnes, and F. Calle, Wide-bandgap semiconductor ultraviolet photodetectors. *Semiconductor Science and Technology*, 2003. 18(4): p. R33-R51.
14. Sang, L., M. Liao, and M. Sumiya, A Comprehensive Review of Semiconductor Ultraviolet Photodetectors: From Thin Film to One-Dimensional Nanostructures. *Sensors*, 2013. 13(8): p. 10482-10518.
15. Liao, M., et al., Comprehensive Investigation of Single Crystal Diamond Deep-Ultraviolet Detectors. *Japanese Journal of Applied Physics*, 2012. 51(9).
16. Munoz, E., et al., III nitrides and UV detection. *Journal of Physics-Condensed Matter*, 2001. 13(32): p. 7115-7137.
17. Liao, M.Y., Y. Koide, and J. Alvarez, Thermally stable visible-blind diamond photodiode using tungsten carbide Schottky contact. *Applied Physics Letters*, 2005. 87(2).
18. Munoz, E., (Al,In,Ga)N-based photodetectors. Some materials issues. *Physica Status Solidi B-Basic Solid State Physics*, 2007. 244(8): p. 2859-2877.
19. Toda, T., et al., Operation at 700 degrees C of 6H-SiC UV sensor fabricated using N+ implantation. *Japanese Journal of Applied Physics Part 2-Letters*, 2004. 43(1A-B): p. L27-L29.

20. Jain, S.C., et al., III-nitrides: Growth, characterization, and properties. *Journal of Applied Physics*, 2000. 87(3): p. 965-1006.
21. Nanishi, Y., Y. Saito, and T. Yamaguchi, RF-molecular beam epitaxy growth and properties of InN and related alloys. *Japanese Journal of Applied Physics Part 1-Regular Papers Short Notes & Review Papers*, 2003. 42(5A): p. 2549-2559.
22. Wu, J., et al., Unusual properties of the fundamental band gap of InN. *Applied Physics Letters*, 2002. 80(21): p. 3967-3969.
23. Jung, Y.R., et al., Pt/AlGaN metal semiconductor ultra-violet photodiodes on crack-free AlGaN layers. *Japanese Journal of Applied Physics Part 1-Regular Papers Short Notes & Review Papers*, 2003. 42(4B): p. 2349-2351.
24. Razeghi, M. and A. Rogalski, Semiconductor ultraviolet detectors. *Journal of Applied Physics*, 1996. 79(10): p. 7433-7473.
25. Kosyachenko, L.A., V.M. Sklyarchuk, and Y.F. Sklyarchuk, Electrical and photoelectric properties of Au-SiC Schottky barrier diodes. *Solid-State Electronics*, 1998. 42(1): p. 145-151.
26. Anikin, M.M., et al., UV PHOTODETECTORS IN 6H-SiC. *Sensors and Actuators a-Physical*, 1992. 33(1-2): p. 91-93.
27. Su, Y.K., et al., 4H-SiC metal-semiconductor-metal ultraviolet photodetectors with Ni/ITO electrodes. *Solid-State Electronics*, 2002. 46(12): p. 2237-2240.
28. Zhang, Y.G., A.Z. Li, and A.G. Milnes, Metal-semiconductor-metal ultraviolet photodetectors using 6H-SiC. *Ieee Photonics Technology Letters*, 1997. 9(3): p. 363-364.
29. Edmond, J., et al., 6H-Silicon carbide light emitting diodes and UV photodiodes. *Physica Status Solidi a-Applied Research*, 1997. 162(1): p. 481-491.
30. Biondo, S., et al., 4H-silicon carbide thin junction based ultraviolet photodetectors. *Thin Solid Films*, 2012. 522: p. 17-19.
31. Liu, H., et al., 4H-SiC PIN Recessed-Window Avalanche Photodiode With High Quantum Efficiency. *Ieee Photonics Technology Letters*, 2008. 20(17-20): p. 1551-1553.
32. Abdel-Rahman, M.A.E., A. Lohstroh, and P.J. Sellin, The effect of annealing on the X-ray induced photocurrent characteristics of CVD diamond radiation detectors with different electrical contacts. *Physica Status Solidi a-Applications and Materials Science*, 2011. 208(9): p. 2079-2086.
33. Mendoza, F., et al., Ultraviolet photosensitivity of sulfur-doped micro- and nano-crystalline diamond. *Journal of Applied Physics*, 2011. 109(11).
34. Smith, S.D. and W. Taylor, OPTICAL PHONON EFFECTS IN INFRA-RED SPECTRUM OF ACCEPTOR CENTRES IN SEMICONDUCTING DIAMOND. *Proceedings of the Physical Society of London*, 1962. 79(512): p. 1142-&.
35. Koizumi, S., et al., Growth and characterization of phosphorus doped n-type diamond thin films. *Diamond and Related Materials*, 1998. 7(2-5): p. 540-544.
36. Sakaguchi, I., et al., Sulfur: A donor dopant for n-type diamond semiconductors. *Physical Review B*, 1999. 60(4): p. R2139-R2141.
37. Adivarahan, V., et al., SiO₂-passivated lateral-geometry GaN transparent Schottky-barrier detectors. *Applied Physics Letters*, 2000. 77(6): p. 863-865.
38. Blank, T.V., et al., Temperature dependence of the photoelectric conversion quantum efficiency of 4H-SiC Schottky UV photodetectors. *Semiconductor Science and Technology*, 2005. 20(8): p. 710-715.
39. Bouhdada, A., et al., Electrical and optical proprieties of photodiodes based on ZnSe material. *Applied Physics Letters*, 2003. 83(1): p. 171-173.

40. Looi, H.J., M.D. Whitfield, and R.B. Jackman, Metal-semiconductor-metal photodiodes fabricated from thin-film diamond. *Applied Physics Letters*, 1999. 74(22): p. 3332-3334.
41. Mollow, E. in *Photoconductivity Conference*. 1954. New York, NY, USA,: Wiley,1954; .
42. Ali, G.M., et al., Effect of Embedded Pd Microstructures on the Flat-Band-Voltage Operation of Room Temperature ZnO-Based Liquid Petroleum Gas Sensors. *Sensors*, 2013. 13(12): p. 16801-16815.
43. Al-Salman, H.S. and M.J. Abdullah, Fabrication and Characterization of Undoped and Cobalt-doped ZnO Based UV Photodetector Prepared by RF-sputtering. *Journal of Materials Science & Technology*, 2013. 29(12): p. 1139-1145.
44. Hu, Z.-S., et al., Recovery of thermal-degraded ZnO photodetector by embedding nano silver oxide nanoparticles. *Applied Surface Science*, 2013. 279: p. 31-35.
45. Lee, S., et al., Impact of transparent electrode on photoresponse of ZnO-based phototransistor. *Applied Physics Letters*, 2013. 103(25).
46. Li, D., et al., Low-Frequency Noise Characteristics of Zinc-Oxide-Film-Based Photoconductive Detectors. *Japanese Journal of Applied Physics*, 2013. 52(8).
47. Moore, J.C. and C.V. Thompson, A Phenomenological Model for the Photocurrent Transient Relaxation Observed in ZnO-Based Photodetector Devices. *Sensors*, 2013. 13(8): p. 9921-9940.
48. Yu, J., et al., ZnO-based ultraviolet avalanche photodetectors. *Journal of Physics D-Applied Physics*, 2013. 46(30).
49. Li, G., et al., ZnO based UV detectors with Surface Plasmon Polariton enhancement on responsivity. *Solid-State Electronics*, 2014. 92: p. 47-51.
50. Liu, Y., et al., Ultraviolet detectors based on epitaxial ZnO films grown by MOCVD. *Journal of Electronic Materials*, 2000. 29(1): p. 69-74.
51. Liu, K.W., et al., Ultraviolet photoconductive detector with high visible rejection and fast photoresponse based on ZnO thin film. *Solid-State Electronics*, 2007. 51(5): p. 757-761.
52. Xu, Q.A., et al., ZnO thin film photoconductive ultraviolet detector with fast photoresponse. *Journal of Crystal Growth*, 2006. 289(1): p. 44-47.
53. Liu, M.J. and H.K. Kim, Ultraviolet detection with ultrathin ZnO epitaxial films treated with oxygen plasma. *Applied Physics Letters*, 2004. 84(2): p. 173-175.
54. Chang, S.P., et al., Surface HCl treatment in ZnO photoconductive sensors. *Thin Solid Films*, 2009. 517(17): p. 5050-5053.
55. He, Y., et al., Study of the photoconductive ZnO UV detector based on the electrically floated nanowire array. *Sensors and Actuators a-Physical*, 2012. 181: p. 6-12.
56. Bi, Z., et al., A high-performance ultraviolet photoconductive detector based on a ZnO film grown by RF sputtering. *Journal of Electronic Materials*, 2008. 37(5): p. 760-763.
57. Bian, X., et al., Fast-response photoconductive metal-semiconductor-metal ultraviolet detector based on ZnO film grown by radio-frequency magnetron sputtering. *Optical Engineering*, 2008. 47(6).
58. Mandalapu, L.J., et al., Ultraviolet photoconductive detectors based on Ga-doped ZnO films grown by molecular-beam epitaxy. *Solid-State Electronics*, 2007. 51(7): p. 1014-1017.
59. Sun, J., et al., The ultraviolet photoconductive detector based on Al-doped ZnO thin film with fast response. *Science China-Physics Mechanics & Astronomy*, 2011. 54(1): p. 102-105.

60. Sun, J., et al., Fast response ultraviolet photoconductive detectors based on Ga-doped ZnO films grown by radio-frequency magnetron sputtering. *Applied Surface Science*, 2010. 257(3): p. 921-924.
61. Xu, Z.-Q., et al., Ultraviolet photoconductive detector based on Al doped ZnO films prepared by sol-gel method. *Applied Surface Science*, 2006. 253(2): p. 476-479.
62. Zheng, X.G., et al., Photoconductive ultraviolet detectors based on ZnO films. *Applied Surface Science*, 2006. 253(4): p. 2264-2267.
63. Tian, C., et al., Performance Enhancement of ZnO UV Photodetectors by Surface Plasmons. *ACS applied materials & interfaces*, 2014. 6(3): p. 2162-2166.
64. Wang, P., et al., Dark current suppression of MgZnO metal-semiconductor-metal solar-blind ultraviolet photodetector by asymmetric electrode structures. *Optics Letters*, 2014. 39(2): p. 375-378.
65. Xu, Q., et al., A metal-semiconductor-metal detector based on ZnO nanowires grown on a graphene layer. *Nanotechnology*, 2014. 25(5).
66. Cheng, G., et al., ZnO nanowire Schottky barrier ultraviolet photodetector with high sensitivity and fast recovery speed. *Applied Physics Letters*, 2011. 99(20).
67. Kim, D.C., et al., Highly Sensible ZnO Nanowire Ultraviolet Photodetectors Based on Mechanical Schottky Contact. *Journal of the Electrochemical Society*, 2012. 159(1): p. K10-K14.
68. Liang, S., et al., ZnO Schottky ultraviolet photodetectors. *Journal of Crystal Growth*, 2001. 225(2-4): p. 110-113.
69. Fallert, J., et al., Surface-state related luminescence in ZnO nanocrystals. *Journal of Applied Physics*, 2007. 101(7).
70. Ryu, Y.R., et al., ZnO devices: Photodiodes and p-type field-effect transistors. *Applied Physics Letters*, 2005. 87(15).
71. Lopatiuk-Tirpak, O., et al., Influence of electron injection on the temporal response of ZnO homojunction photodiodes. *Applied Physics Letters*, 2007. 91(4).
72. Ohta, H., et al., Fabrication and photoresponse of a pn-heterojunction diode composed of transparent oxide semiconductors, p-NiO and n-ZnO. *Applied Physics Letters*, 2003. 83(5): p. 1029-1031.
73. Ohta, H., et al., UV-detector based on pn-heterojunction diode composed of transparent oxide semiconductors, p-NiO/n-ZnO. *Thin Solid Films*, 2003. 445(2): p. 317-321.
74. Basak, D., et al., Photoconductive UV detectors on sol-gel-synthesized ZnO films. *Journal of Crystal Growth*, 2003. 256(1-2): p. 73-77.
75. Bi, Z., et al., A Back-Illuminated Vertical-Structure Ultraviolet Photodetector Based on an RF-Sputtered ZnO Film. *Journal of Electronic Materials*, 2009. 38(4): p. 609-612.
76. Chang, S.P., et al., ZnO photoconductive sensors epitaxially grown on sapphire substrates. *Sensors and Actuators a-Physical*, 2007. 140(1): p. 60-64.
77. Liu, K.W., et al., Zn_{0.8}Mg_{0.2}O-based metal-semiconductor-metal photodiodes on quartz for visible-blind ultraviolet detection. *Journal of Physics D-Applied Physics*, 2007. 40(9): p. 2765-2768.
78. Zhang, D.H. and D.E. Brodie, PHOTORESPONSE OF POLYCRYSTALLINE ZNO FILMS DEPOSITED BY RF BIAS SPUTTERING. *Thin Solid Films*, 1995. 261(1-2): p. 334-339.
79. Liu, K., M. Sakurai, and M. Aono, ZnO-Based Ultraviolet Photodetectors. *Sensors*, 2010. 10(9): p. 8604-8634.

80. Li, Y.F., S.W.; Sun, J.Y.; Xie, X.S.; Yang, J.; Zhang, Y.Z.; Lu, Y.C. . and p. 947-949. The Study of ZnO

Photoconductive UV Detector. in 8th International Conference Solid-State and

Integrated Circuit Technology Shanghai, China, October 23-26, 2006;.

81. Liu, C.Y., et al., Fabrication and characterization of ZnO film based UV photodetector. Journal of Materials Science-Materials in Electronics, 2009. 20(3): p. 197-201.
82. Li, M., et al., Laser annealing of laser assisted molecular beam deposited ZnO thin films with application to metal-semiconductor-metal photodetectors. Journal of Applied Physics, 2006. 100(5).
83. Ji, L.-W., et al., Characteristic Improvements of ZnO-Based Metal-Semiconductor-Metal Photodetector on Flexible Substrate with ZnO Cap Layer. Japanese Journal of Applied Physics, 2010. 49(5).
84. Jiang, D., et al., Ultraviolet Schottky detector based on epitaxial ZnO thin film. Solid-State Electronics, 2008. 52(5): p. 679-682.
85. Li, M., et al., Radio frequency sputtered zinc oxide thin films with application to metal-semiconductor-metal photodetectors. Thin Solid Films, 2007. 515(18): p. 7357-7363.
86. Shan, C.X., et al., Ultraviolet photodetector fabricated from atomic-layer-deposited ZnO films. Journal of Vacuum Science & Technology B, 2009. 27(3): p. 1765-1768.
87. Lin, T.K., et al., ZnO MSM photodetectors with Ru contact electrodes. Journal of Crystal Growth, 2005. 281(2-4): p. 513-517.
88. Young, S.J., et al., ZnO metal-semiconductor-metal ultraviolet sensors with various contact electrodes. Journal of Crystal Growth, 2006. 293(1): p. 43-47.
89. Aurret, F.D., et al., Electrical characterization of 1.8 MeV proton-bombarded ZnO. Applied Physics Letters, 2001. 79(19): p. 3074-3076.
90. Nakano, M., et al., Schottky contact on a ZnO (0001) single crystal with conducting polymer. Applied Physics Letters, 2007. 91(14).
91. Fabricius, H., T. Skettrup, and P. Bisgaard, ULTRAVIOLET DETECTORS IN THIN SPUTTERED ZNO FILMS. Applied Optics, 1986. 25(16): p. 2764-2767.
92. Purnima Hazral, S.K.S., and S. Jitl*, Ultraviolet Photodetection Properties of ZnO/Si Heterojunction Diodes Fabricated by ALD Technique Without Using a Buffer Layer. JOURNAL OF SEMICONDUCTOR TECHNOLOGY AND SCIENCE, 2014. 14: p. 117-123.
93. Alkis, S., et al., UV/vis range photodetectors based on thin film ALD grown ZnO/Si heterojunction diodes. Journal of Optics, 2013. 15(10).
94. Wang, Z.L., ZnO nanowire and nanobelt platform for nanotechnology. Materials Science & Engineering R-Reports, 2009. 64(3-4): p. 33-71.
95. Kind, H., et al., Nanowire ultraviolet photodetectors and optical switches. Advanced Materials, 2002. 14(2): p. 158-+.
96. Huang, J.-H., et al., Enhancing ultraviolet photoresponse of ZnO nanowire device by surface functionalization. Acta Physica Sinica, 2008. 57(12): p. 7855-7859.
97. Lao, C.S., et al., Giant enhancement in UV response of ZnO nanobelts by polymer surface-functionalization. Journal of the American Chemical Society, 2007. 129(40): p. 12096-+.

98. Tzeng, S.-K., M.-H. Hon, and I.-C. Leu, Improving the Performance of a Zinc Oxide Nanowire Ultraviolet Photodetector by Adding Silver Nanoparticles. *Journal of the Electrochemical Society*, 2012. 159(4): p. H440-H443.
99. Mamat, M.H.K., Z.; Zahidi, M.M.; Mahmood, M.R., Performance of an ultraviolet photoconductive sensor using well-aligned aluminium-doped zinc-oxide nanorod annealed in an air and oxygen environment. *J. Appl. Phys.*, 2011. 6.
100. Bai, S., et al., High-Performance Integrated ZnO Nanowire UV Sensors on Rigid and Flexible Substrates. *Advanced Functional Materials*, 2011. 21(23): p. 4464-4469.
101. He, J.H., et al., Electrical and optoelectronic characterization of a ZnO nanowire contacted by focused-ion-beam-deposited Pt. *Nanotechnology*, 2009. 20(13).
102. Prades, J.D., et al., The effects of electron-hole separation on the photoconductivity of individual metal oxide nanowires. *Nanotechnology*, 2008. 19(46).
103. Lin, Y.H., et al., Atomic Layer Deposition of Zinc Oxide on Multiwalled Carbon Nanotubes for UV Photodetector Applications. *Journal of the Electrochemical Society*, 2011. 158(2): p. K24-K27.
104. Lin, D.D., H. Wu, and W. Pan, Photoswitches and Memories Assembled by Electrospinning Aluminum-Doped Zinc Oxide Single Nanowires. *Advanced Materials*, 2007. 19(22): p. 3968-3972.
105. Huang, Z.-M., et al., A review on polymer nanofibers by electrospinning and their applications in nanocomposites. *Composites Science and Technology*, 2003. 63(15): p. 2223-2253.
106. Abou Chaaya, A., et al., Evolution of microstructure and related optical properties of ZnO grown by atomic layer deposition. *Beilstein Journal of Nanotechnology*, 2013. 4: p. 690-698.
107. Elias, J., et al., Electrochemical growth of ZnO nanowires on atomic layer deposition coated polystyrene sphere templates. *Electrochimica Acta*, 2013. 110: p. 387-392.
108. Gong, B., Q. Peng, and G.N. Parsons, Conformal Organic - Inorganic Hybrid Network Polymer Thin Films by Molecular Layer Deposition using Trimethylaluminum and Glycidol. *Journal of Physical Chemistry B*, 2011. 115(19): p. 5930-5938.
109. Tapily, K., et al., Electrical Characterization of ALD ZnO and HfO₂ Thin Films, in *Physics and Technology of High-K Materials 8*, S. Kar, et al., Editors. 2010, Electrochemical Soc Inc: Pennington. p. 281-287.
110. Guziewicz, E., et al., Extra-Low Temperature Growth of ZnO Thin Films by Atomic Layer Deposition. *Journal of the Korean Physical Society*, 2008. 53(5): p. 2880-2883.
111. Huby, N., et al., Electrical behavior of zinc oxide layers grown by low temperature atomic layer deposition. *Applied Physics Letters*, 2008. 92(2): p. -.

Chapter4. Mechanical properties of **Al₂O₃/ZnO nanolaminates**

Mechanical properties of Al₂O₃/ZnO nanolaminates

1.Introduction.....	160
2.Mechanical properties of ALD thin films.....	161
3.Atomic layer deposition of Al₂O₃/ZnO nanolaminate structure.....	162
4.Structural characterization of Al₂O₃/ZnO nanolaminates.....	164
4.1.SEM cross-section.....	164
4.2.Energy-dispersive X-ray spectroscopy (EDX).....	165
4.3.X ray reflectometry.....	167
4.4.Grazing incident X-Ray diffraction.....	169
5.Mechanical characterization.....	172
5.1. Stress-strain curve.....	172
5.2. Crack formation.....	174
5.3.Mechanical test setups.....	175
5.3.1.UTS tensile stage.....	175
5.3.2.SEM-integrated EMPA microtensile stage.....	177
6.Al₂O₃/ZnO nanolaminates tensile tests.....	180
7.Conclusion and perspectives.....	187

1. Introduction

Understanding the relation between microstructure and mechanical properties has always been one of the primary goals of materials science. A large amount of research was developed in order to understand the microscopic processes responsible for the mechanical behavior of materials and nanomaterials. In recent years, more and more attention has been devoted to the investigation of the mechanical properties of nanomaterials such as nanotubes, [1-7] nanowires, [8-16] and thin films [17-40].

Thin films coating was widely used on the last few years due to their large application fields on micro-electronic, optoelectronic, gas barrier, surface modification and surface protection against mechanical stress (e.g. wear) or chemical reaction (e.g. corrosion, oxidation). Thin films present promising properties in terms of mechanical, electrical, optical and structural properties which give them an advantage over bulk materials. Due to their wide range of applications, thin films are subject to different mechanical stresses. Thin films incorporated in an electronic device for instance can be subject to thermal stress caused by the operating temperature of the device and the difference in the thermal expansion (DTE) between the film and the substrate. We should note that thin films can be subject to thermal stress during and after the deposition process. Thin film coatings as mechanical and chemical protection are also a subject to mechanical stress during their applications.

Different setups were used for the investigation of the thin film mechanical properties such as tensile tests [41-53] and nanoindentation [21, 27, 54-68]. Various mechanical parameters can be extracted from those tests such as Yield strength, Young's modulus, or ultimate tensile strength, hardness, saturation crack density, critical strain, and critical bending radius.

In this chapter we will investigate the mechanical properties of thin film deposited by ALD and their mechanical properties in comparison to other deposition techniques. We will focus mainly on the $\text{Al}_2\text{O}_3/\text{ZnO}$ nanolaminates.

2. Mechanical properties of ALD thin films

The mechanical properties of films grown using atomic layer deposition (ALD) were not widely studied. Jian *et al.* [69] studied by nanoindentation a ZnO thin film of 200 nm deposited by ALD. They reported that the fracture toughness of ALD-derived ZnO/Si(111) thin films is about 3.1 MPa m^{1/2}. Jen *et al.* [70] reports the critical strains of Al₂O₃ ALD film for both tensile and compressive strains. The results showed that the critical tensile strain is higher for thinner thicknesses of the Al₂O₃ ALD film on heat-stabilized polyethylene naphthalate (HSPEN) substrates. A low critical tensile strain of 0.52% was measured for a film thickness of 80 nm. The critical tensile strain increased to 2.4% at a film thickness of 5 nm. The fracture toughness for cracking, K_{IC}, of the Al₂O₃ ALD film was also determined to be K_{IC}=2.30 MPa m^{1/2}. Trippet *al.* studies [71] the Al₂O₃ ALD films by nanoindentation and show an elastic modulus E of 168–182 GPa. Tapilyet *al.* [72] reports the study of ALD HfO₂ and Al₂O₃ by nanoindentation as well. ALD HfO₂ thin films show hardness of 9.5±2 GPa and a modulus of 220±40 GPa, whereas the ALD Al₂O₃ thin films have a hardness of 10.5±2 GPa and a modulus of 220±40 GPa. Miller *et al.* [73] shows measurements of crack density versus applied tensile strain coupled with a fracture mechanics model of alumina and alucone films deposited on polyethylene naphthalate substrates. From measurements of crack density versus applied tensile strain coupled with a fracture mechanics model, the mode I fracture toughness of alumina and alucone films was determined to be K_(IC) = 1.89 +/- 0.10 and 0.17 +/- 0.02 MPa m^(0.5), respectively. From measurements of the saturated crack density, the critical interfacial shear stress was estimated to be tau(c) = 39.5 +/- 8.3 and 66.6 +/- 6.1 MPa, respectively. Latella *et al.* [74] studied toughness and adhesion of atomic layer deposited alumina films on polycarbonate substrates. The strength and toughness of the alumina film was determined to be 140 MPa and 0.23 MPa m^{1/2}, respectively. Adhesion of the alumina films was improved for substrates pre-treated with water-plasma.

Raghavan *et al.* [75] shows the influence of the Nanocrystalline-to-amorphous transition in Al₂O₃/ZnO nanolaminates on the mechanical properties by nanoindentation. The softer and more compliant response of the multilayers as compared to the single layers of Al₂O₃ and ZnO was attributed to the structural change from nanocrystalline to amorphous at smaller bilayer thicknesses. Herrmann *et al.* [76] investigates the mechanical properties of Al₂O₃, ZnO and Al₂O₃/ZnO nanolaminates. Pure Al₂O₃ ALD was determined to have a modulus between 150 and

155 GPa and a hardness of 8 GPa, while the results for pure ZnO ALD indicated a modulus between 120 and 140 GPa and a hardness of similar to 5 GPa. An Al₂O₃/ZnO ALD alloy displayed a modulus of 140 - 145 GPa, which falls between the two pure films, and a hardness of 8 GPa, which is similar to the pure Al₂O₃ film. We should note that tensile test on Al₂O₃/ZnO deposited by ALD was not reported yet.

In this chapter Al₂O₃/ZnO nanolaminates will be deposited using the atomic layer deposition technique on PET dogbones, gold coated nickel dogbones and silicon wafer. Nanolaminates deposited on silicon will be characterized in order to have an idea about the chemical and crystalline structure evolution with the bilayer thickness using SEM, XRR and GIXRD. PET and gold coated nickel dogbones will be submitted to a tensile test and micro tensile test under SEM respectively.

3. Atomic layer deposition of Al₂O₃/ZnO nanolaminate structure.

Atomic layer deposition of Al₂O₃ and ZnO was performed using trimethylaluminium, diethyl zinc and water at 90°C using the experimental conditions reported below in Table 1. Precursor pulse was coupled with 25 sccm Ar flow and the purge step was also coupled with 100 sccm Ar flow as a gas vector.

Table 1. ALD experimental conditions for the deposition of Al₂O₃ and ZnO

	Pulse(P1)	Exposure	Purge	Pulse(P2)	Exposure	Purge
Al ₂ O ₃	0.1	30	40	2	30	40
ZnO	0.2	30	40	2	30	40

The ALD deposition was performed on different types of substrates: on Si wafer (for structural and chemical characterizations), on PET dogbones and gold coated nickel dogbones (for mechanical properties study).

Table 2 shows 8 different sequences of Al₂O₃/ZnO nanolaminates deposited by ALD with different bilayer sequences. The total number of cycles was fixed at 1000 cycles. 1000 cycles of ZnO and 1000 cycles of Al₂O₃ were also deposited and characterized to be used as references.

Table 2. ALD deposition sequences of Al₂O₃/ZnO nanolaminates structures

Samples	Number of Al ₂ O ₃ cycles	Number of ZnO cycles	Number of bilayers
PMS1	0	1000	1
PMS2	1000	0	1
PMS3	500	500	1
PMS4	250	250	2
PMS5	125	125	4
PMS6	50	50	10
PMS7	25	25	20
PMS8	10	10	50
PMS9	5	5	100
PMS10	3	3	200

Based on the growth per cycle extracted from the SEM cross section and the ellipsometric measurement of Al₂O₃(0.17 nm per cycle) and ZnO (0.24 nm per cycle) calculated on chapter 2, we report on table 3 the expected estimated bilayer thicknesses and the total film thicknesses of those layers.

Table3. Estimated bilayer thickness and total thickness

Sample	bilayer thickness(nm)	Total thickness(nm)
PMS1		240
PMS2		170
PMS3	205	205
PMS4	102.5	205
PMS5	51.25	205
PMS6	20.5	205
PMS7	10.25	205
PMS8	4.1	205
PMS9	2.05	205
PMS10	1.025	205

4. Structural characterization of Al₂O₃/ZnO nanolaminates

The ALD nanolaminates sequences performed on silicon substrates were characterized using scanning electron microscopy, Grazing incident X-Ray diffraction and X-ray reflectometry in order to study the structural evolution of the nanolaminates when the bilayer thicknesses change.

4.1. SEM observation

SEM cross section was performed using an emission field Hitachi S-4800 microscope. Figure 1 shows the SEM cross section image of the PMS3, PMS4, PMS5 and PMS6. Samples with lower bilayer thicknesses were difficult to observe by SEM.

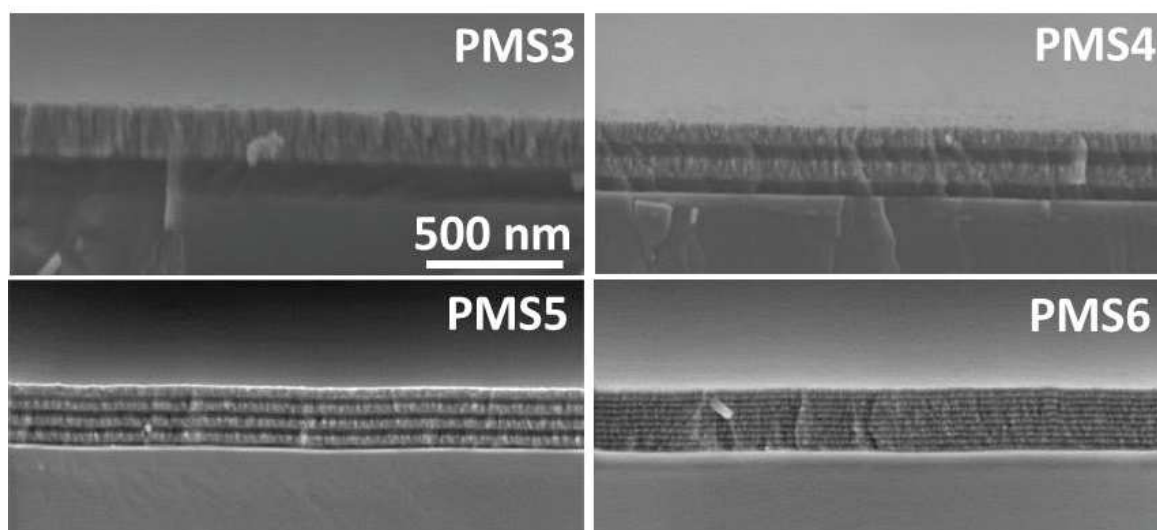


Figure 1. SEM cross-section of PMS3,PMS4,PMS5 and PMS6 samples

SEM cross-section observations confirm the nanolaminates structure of the ALD deposited layers. The SEM images indicate a conformal coating by ALD of the Si substrate. The SEM cross section proves as well that the sequence of alternating Al₂O₃ and ZnO interlayers was achieved throughout the total film thickness of the nanolaminates. In all nanolaminates, the first layer on Si substrate was Al₂O₃, and the top layer of the nanolaminates was ZnO. Thickness estimation was not possible by SEM cross section images due to the shift during observations.

4.2. Energy-dispersive X-ray spectroscopy (EDX)

EDX measurement was also performed on the nanolaminates with different sequences deposited on silicon substrate. EDX measurement was carried out using a Zeiss EVO ED15 microscope coupled with a Oxford X-Max^N EDX detector. As noted in chapter 2, the EDX has been calibrated with ZnO and Al_2O_3 powders of known stoichiometry. Figure 2 present the EDX spectra performed on the nanolaminates samples PMS4, PMS6, PMS8 and PMS10.

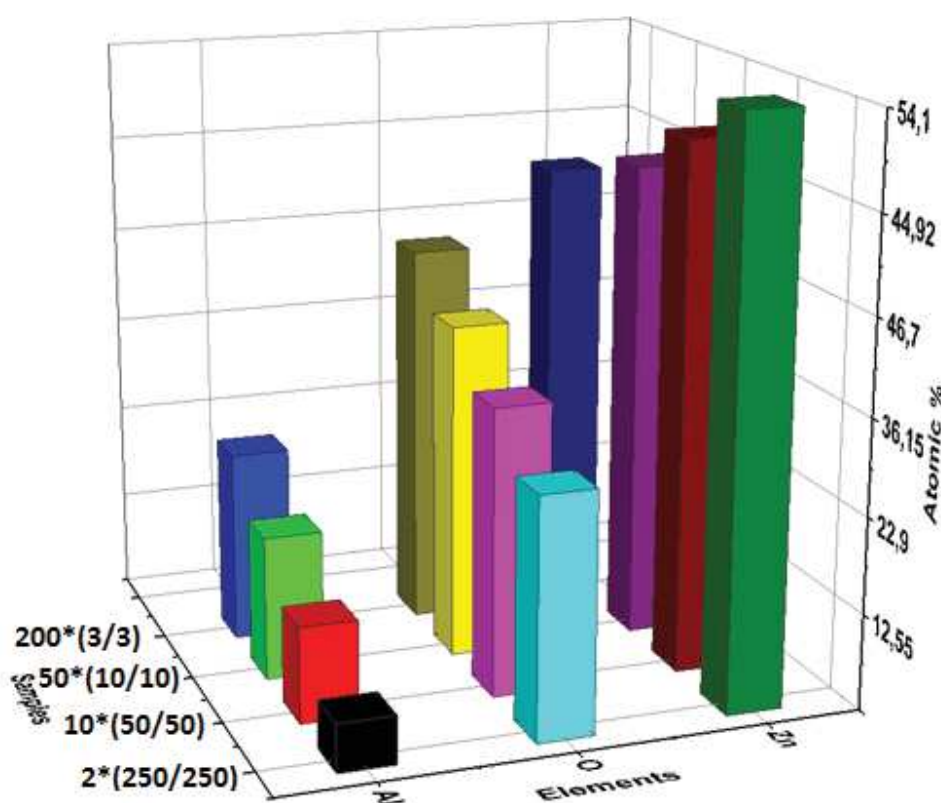


Figure 2. EDX measurement of nanolaminates samples: PMS4, PMS6, PMS8 and PMS10

Figure2 report the Al, Zn and O presence without any residual carbon confirming the ALD complete reaction at such temperature with the setup mentioned above in Table 1. As shown in Figure 2, when the bilayer number increases, the Al and O atomic percentage increases and the Zn atomic percentage decreases. This Zn atomic percentage decreases when the bilayer number increases can be related to the ZnO etching by the $\text{Al}(\text{CH}_3)_3$ precursor during the Al_2O_3 ALD cycles as reported elsewhere at 177°C by Elam et al.[77]. The Al atomic percentage

increases can be related as well to the increase of the Al₂O₃ density grown on ZnO due to the residual OH- and the partially hydroxylated phase ZnO (OH) on the surface of the ZnO grains as reported in chapter 2 paragraph 4.3. Figure 3 shows the evolution of the Al/Zn molar ratio when the bilayer number increases.

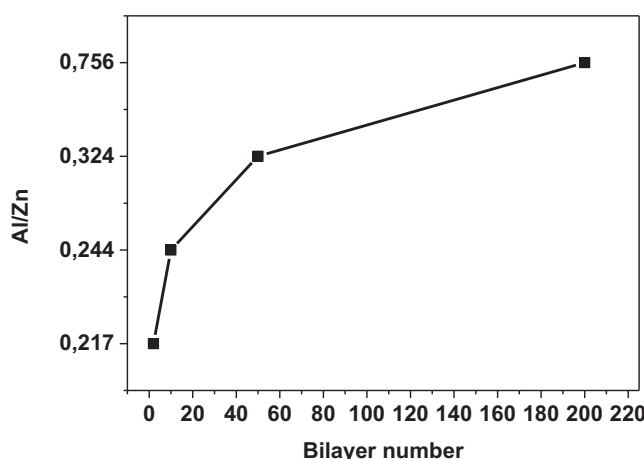


Figure 3. Al/Zn ratio evolution with the bilayer numbers

As shown in Figure 3, the Al/Zn ratio increases when the bilayer number increases. This Al/Zn ratio increases when the bilayer number increases can be related to the ZnO etching by the Al(CH₃)₃ precursor during the Al₂O₃ ALD cycles as reported elsewhere by Elam *et al.* for nanolaminates grown at 177°C [77]. This finding could be related as well to the Al₂O₃ GPC activation by the ZnO layer or the Al₂O₃ density increases due to the ZnO layer rich in OH group as demonstrated in chapter 2. The Al/Zn ratio lower than 1 can be obtained due to the change in the density of Al₂O₃ and ZnO films. Al₂O₃ ALD film densities of 3.0 g/cm³ at 177 °C and 2.5 g/cm³ at 33 °C are reported by Groner *et al.* [78]. ZnO ALD film density of 5.6 g/cm³ is reported by Elam *et al.* [77].

4.3. X ray reflectometry.

X-ray Reflectometry (Bruker AXS, D8 Discover) measurements were performed by using $\text{CuK}\alpha$ ($\lambda=1.5418 \text{ \AA}$) radiation to characterize the coatings. The excitation voltage and current were set at 40 kV and 40 mA, respectively. The step size and the scan range used were 0.005 degree and from 0.2 to 5 degree, respectively. Lptos 7.7 software provided by Bruker AXS was used to fit the XRR measurements. Figure 4 shows an example of the XRR measurements performed on the PMS3 sample and the theoretical fitting. Black curve represents the original data and the blue curve represents the simulated one. The XRR measurement was performed at EMPA (Switzerland).

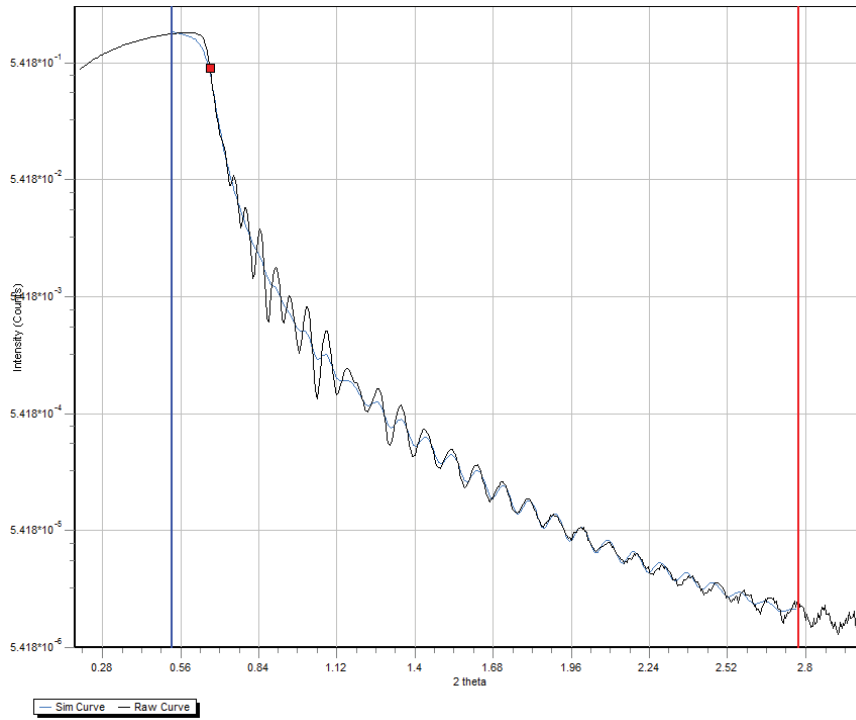


Figure 4. PMS3 XRR measurement curve (black) and simulated curve (blue)

ALD deposition thickness and bilayer thickness can be extracted from the simulated models. The simulation models have been done on EVA software. Based on the SEM image and the estimated layer thickness, we suggest a superlattice model then we fit on the layer thickness to

obtain the maximum correlation between the experimental data and the simulated one. Table 4 shows the estimated bilayer thickness and the total film thickness extracted from the XRR fit.

Table 4. Bilayer thicknesses and the total film thickness extracted from the XRR fit

Samples	Number of Al_2O_3 cycles	Thickness of Al_2O_3 layer by XRR	Al_2O_3 Growth per cycle	Number of ZnO cycles	Thickness of ZnO layer by XRR	ZnO Growth per cycle	Number of bilayers	Total thickness by XRR
PMS1	0	0	-	1000	212	0.212	1	212
PMS2	1000	181	0.181	0	0	-	1	181
PMS3	500	90	0.180	500	107	0.214	1	197
PMS4	250	-	-	250	-	-	2	-
PMS5	125	22.9	0.183	125	28.4	0.2272	4	205
PMS6	50	-	-	50	-	-	10	-
PMS7	25	-	-	25	-	-	20	-
PMS8	10	-	-	10	-	-	50	215
PMS9	5	-	-	5	-	-	100	217
PMS10	3	-	-	3	-	-	200	243

PMS1 and PMS2 XRR measurement shows a growth per cycle of 0.18 nm for the Al_2O_3 ALD and 0.21 nm for the ZnO which correlate the GPC extracted from the SEM measurements on chapter 2 paragraph 3.1 and 8.1. As shown in Table 4, it was not possible to perform the theoretical fitting on all samples and specially on the thinner ones due to the complicated theoretical models for bilayer number higher than 10. Those results confirm the SEM cross-section measurement and the ellipsometric measurement performed in chapter 2. Figure 5 shows the total thickness extracted from the XRR measurement versus the number of bilayer.

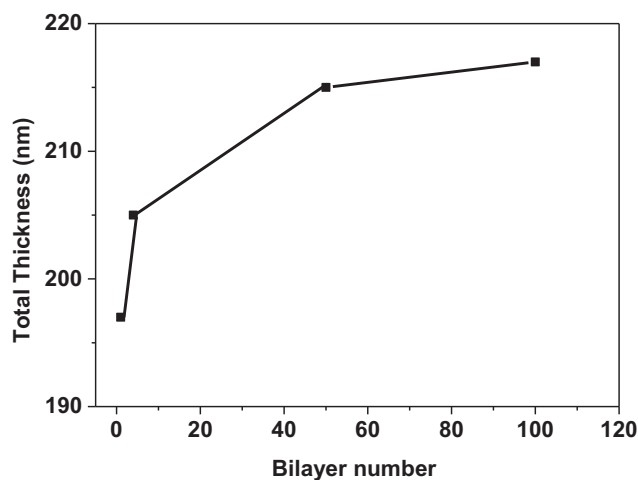


Figure 5. Total thickness evolution versus the number of bilayer

As shown on Figure 5, when the bilayer number increases (the number of $\text{Al}_2\text{O}_3/\text{ZnO}$ interface increases) and the total thickness increases. The thickness increases coupled with the EDX measurements that report an increase on the Al/Zn ratio when the bilayer number increases, with the constant GPC for Al_2O_3 , allow concluding that the Al_2O_3 density increases due the ZnO layer rich in OH group as demonstrated in chapter 2. Moreover the thickness increases coupled with the GPC increases of ZnO (0.212 for PMS1; 0.214 for PMS3; 0.227 for PMS5) proves that at such low temperature (90°C) we did not observe the ZnO etching by the TMA precursor during the Al_2O_3 ALD cycles as reported elsewhere by Elam *et al.* at 177°C [77]. So we can conclude that at such low temperature, the Al_2O_3 deposition was activated by the ZnO layer.

4.4. Grazing incident X-Ray diffraction.

Grazing incidence X-ray diffraction (Bruker AXS, D8 Discover) measurements were achieved by using $\text{CuK}\alpha$ ($\lambda=1.5418 \text{ \AA}$) radiation to characterize the coatings. The excitation voltage and the current were set at 40 kV and 40 mA, respectively. The angle of incidence was kept constant at 0.5 degree. The step size and the scan range used were 0.02 degree and from 25

to 50 degree, respectively. Figure 6 shows the GIXRD spectra performed on the nanolaminates samples. The GIXRD measurements have been performed as at EMPA (Switzerland).

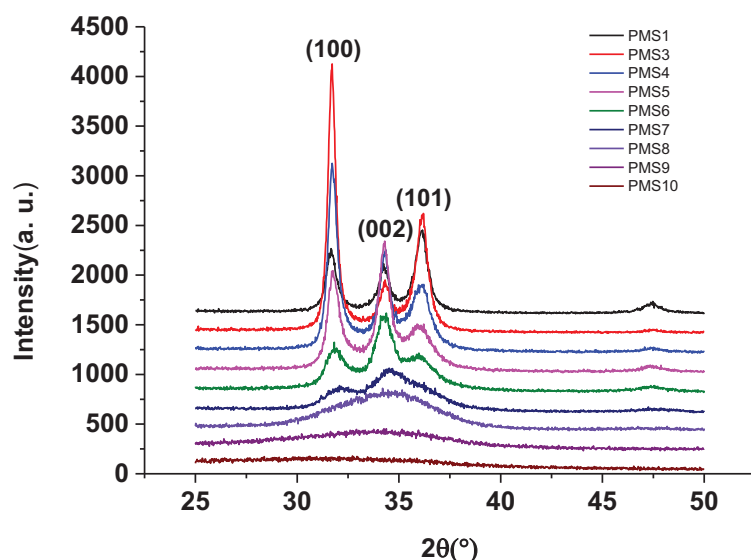


Figure 6. GIXRD spectra performed on the nanolaminates samples

As shown from the Figure 6, a transition from an amorphous to a crystalline state occurs when the bilayer thickness increases. This transition was reported elsewhere by Raghavan *et al.*[75] and AbouChaaya *et al.*[79]. PMS10, PMS9 and PMS8 nanolaminates with the thinnest bilayer thickness showed weak broad X-ray diffraction peak at 34.26° which can result from their amorphous structure or their crystalline size below 2 nm as reported by Elias *et al.*[80]. Thicker samples PMS3, PMS4, PMS5 and PMS6 demonstrate 3 structural peaks at $2\theta = 31.82^\circ$, 34.35° and 36.1° corresponding to (100), (002), and (101) reflections of ZnO, respectively. ZnO monolayer PMS1 shows the same structural peaks corresponding to (100), (002), and (101). A change in the preferential growth orientation is observed when comparing samples PMS5, PMS6 and PMS7 (strong (002) and negligible (101) XRD peaks) to sample PMS4 (strong (100) and negligible (101) XRD peaks) and sample PMS3 (strong (100) and negligible (002) XRD peaks) and sample PMS1 (strong (101) and negligible (002) XRD peaks). The preferential growth

orientation of Al₂O₃/ZnO nanolaminates goes from (002) to (100) when the bilayer thickness increases from 3.25 to 185 nm. Moreover the preferred growth orientation for ZnO monolayer PMS1 is (101) matching the results reported elsewhere for ZnO of 200 nm thickness[79].

Grain size was estimated from Debay-Scherer equation[81]:

$$D = \frac{0.9 \cdot \lambda}{\beta \cdot \cos(\theta)} \quad (\text{Equation 1})$$

Where λ , β and θ are X-ray wavelength, full width at half maximum (FWHM) and diffraction angle, respectively. Since the particles are of unknown morphologies, the shape factor is set to 0.9. The obtained grain size values were reported on table 5 then plotted versus the bilayer thickness in Figure 7.

Table 5. Grain size calculation of nanolaminates

Sample	PMS1	PMS2	PMS3	PMS4	PMS5	PMS6	PMS7	PMS8	PMS9	PMS10
Grain size	13.94	-	20.859	18.612	15.894	11.196	5.420	-	-	-

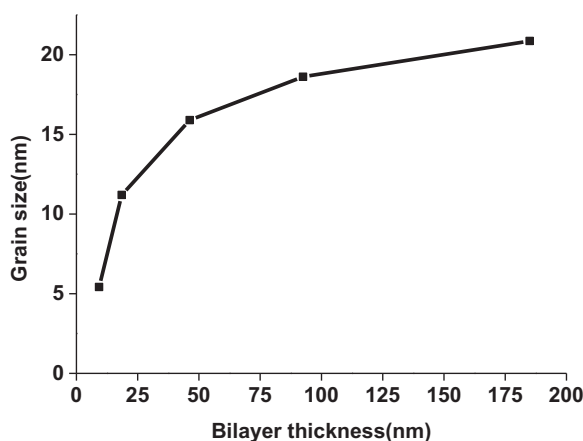


Figure 7. Nanolaminates grain size versus the bilayer thickness

As shown in Figure 7, the ZnO grain size increases with the bilayers thickness increment. This result matches our previous work on nanolaminates on chapter 2 performed at 100°C.

5. Mechanical characterization

Before starting the studies related on the mechanical properties of Al₂O₃/ZnO nanolaminates, we will describe first the mechanical tests techniques used in this work and the theory related to mechanical properties: stress strain curve and crack formation.

5.1. Stress-strain curve

Yield strength, Young's modulus, or ultimate tensile strength can be extracted from the uniaxial tensile testing. In this test, a sample of certain geometry is subjected to a slowly but permanently increasing load until failure. During the test, both, the applied load and the elongation of the sample are being measured and plotted into a load-displacement-diagram.

By knowing the initial cross sectional area A_0 and the gauge length of the sample l_0 , the measured load F and elongation Δl can be transformed to engineering stress σ (normalized to initial area A_0) and engineering strain ε (normalized to the initial length l_0) by applying the following equations [82]:

$$\sigma = \frac{F}{A_0} \quad \text{(Equation 2)}$$

$$\varepsilon = \frac{\Delta l}{l_0} \quad \text{(Equation 3)}$$

Plotting engineering stress vs. engineering strain leads to the so called engineering stress-strain-curve for which an example (ductile metal) [82] is shown in Figure 8.

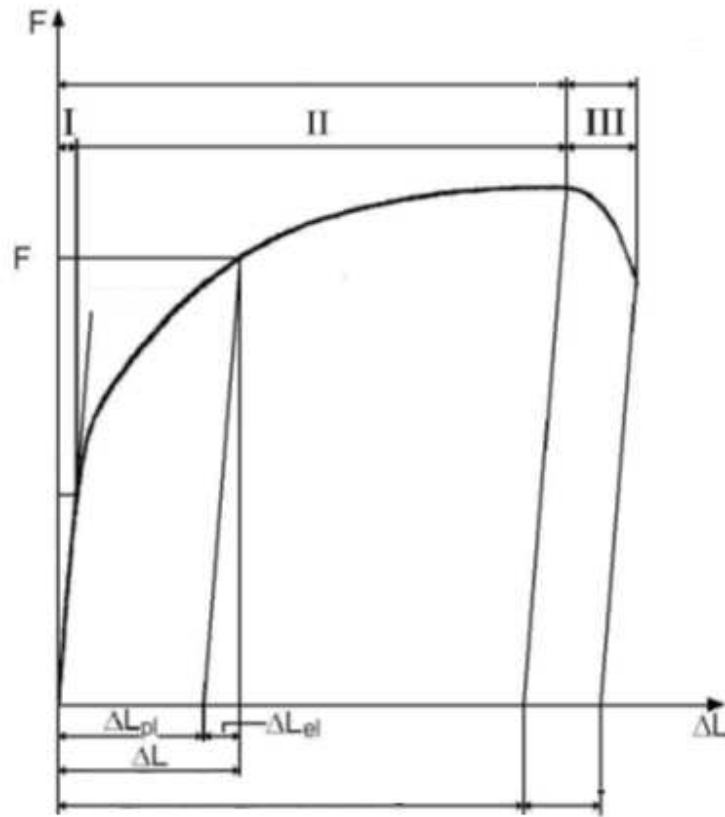


Figure 8. Stress-strain curve example of a ductile metal: For section I, II and III, see text. ΔL is the elongation at the given force F . ΔL contains ΔL_{pl} , the elongation from the plastic deformation and ΔL_{el} , the elongation from the elastic part.

The curve can be divided in three parts:

(I) the linear portion of the curve is due to proportionality between the applied stress and the measured strain which is described by Hook's law:

$$\sigma = E\varepsilon \quad \text{(Equation 4)}$$

The Young's Modulus (E) is a material constant, defined by the strength of the atomic bonding. It can be determined from the slope of the elastic portion. In the elastic regime of the

sample, no plastic deformation occurs in this part which means that if the load is released at one point in this regime the sample would retract to its initial length.

(II) The yield point (σ_y) defines the end of the elastic regime of the sample. Beyond this point, plastic deformation occurs. The slope of the curve decreases slightly but the stress increases further due to strain hardening behavior. In this regime, the sample's surface increases uniformly all over the sample without any change in cross sectional area (Poisson's contraction).

(III) The maximum stress of the sample allows without changes in cross sectional area is called ultimate tensile strength. Beyond this point, defects in the material like flaws, scratches or cracks lead to high local stresses and the sample laterally starts to neck where the local stress concentration is highest. This part ends by the rupture of the sample.

Even if the sample undergoes a plastic deformation, the elastic part remains reversible. This means that after releasing the load, either on purpose in the regimes II and III or by rupture, the sample will retract for the amount of elastic deformation. Only the irreversible plastic deformation remains [82].

5.2. Crack formation

When a coated substrate goes under a tensile stress, at some point, the first cracks appear. The corresponding strain is called the critical tensile strain. The cracks are perpendicular to the tensile stress. An interesting plot is the evolution of the crack density versus the tensile strain. The crack density is the amount of cracks on a certain length of substrate surface. Cracks with the same direction as the tensile stress may develop due to the Poisson contraction at large tensile deformations. The $(1/h)^{1/2}$ (where h is the film thickness) dependence for the critical tensile strain for cracking can be derived analytically using a shear lag model from Laws and Dvorak. The critical tensile strain ϵ_c is easily related to the critical tensile stress σ_c by Equation 5:

$$\epsilon_c = \frac{\sigma_c}{E_f} \quad \text{(Equation 5)}$$

Where E_f is the elastic modulus of the film coating. An equation derived from the Equation 5.

$$\epsilon_c \sim \left(\frac{h_s}{h^*(h_s + h)} \right)^{1/2} \quad (\text{Equation 6})$$

Where h is the film thickness and h_s the substrate thickness. Since $h_s \gg h$, the critical strain can be simplified to the right hand term in Equation 6. With the critical tensile strain for cracking, the critical bending radius R can be derived, see Equation 7. The critical bending radius is the minimum radius that a coated substrate can be bent before the coating layer start to crack.

$$\epsilon_c = \frac{h + h_s}{2R} \quad (\text{Equation 7})$$

The crack density saturates for increasing tensile strain. For the relation between the saturation crack density cd_{sat} and the film thickness, a generic relation of $cd_{sat} \sim h^{-1/m}$ was found theoretically. m was found experimentally to be around 2 and the relation which gives the Equation 8:

$$cd_{sat} = \left(\frac{1}{h} \right)^{1/2} \quad (\text{Equation 8})$$

5.3. Mechanical test setups

5.3.1. UTS tensile stage

UTS tensile stage is a tensile test setup installed at EMPA laboratory (Switzerland) (Figure 9). This setup was designed to test large scale samples. Two sample holders consisted of the UTS tensile stage: The first one is fixed to the chassis and the second one is a movable holder, speed controlled, with a speed range between 1 $\mu\text{m/s}$ and 20 cm/min . The tensile test stage measures the force as well as the displacement of the sample holder. The maximum load is 5 kN. The UTS tensile stage was coupled to a Keyence VH-Z100R camera.

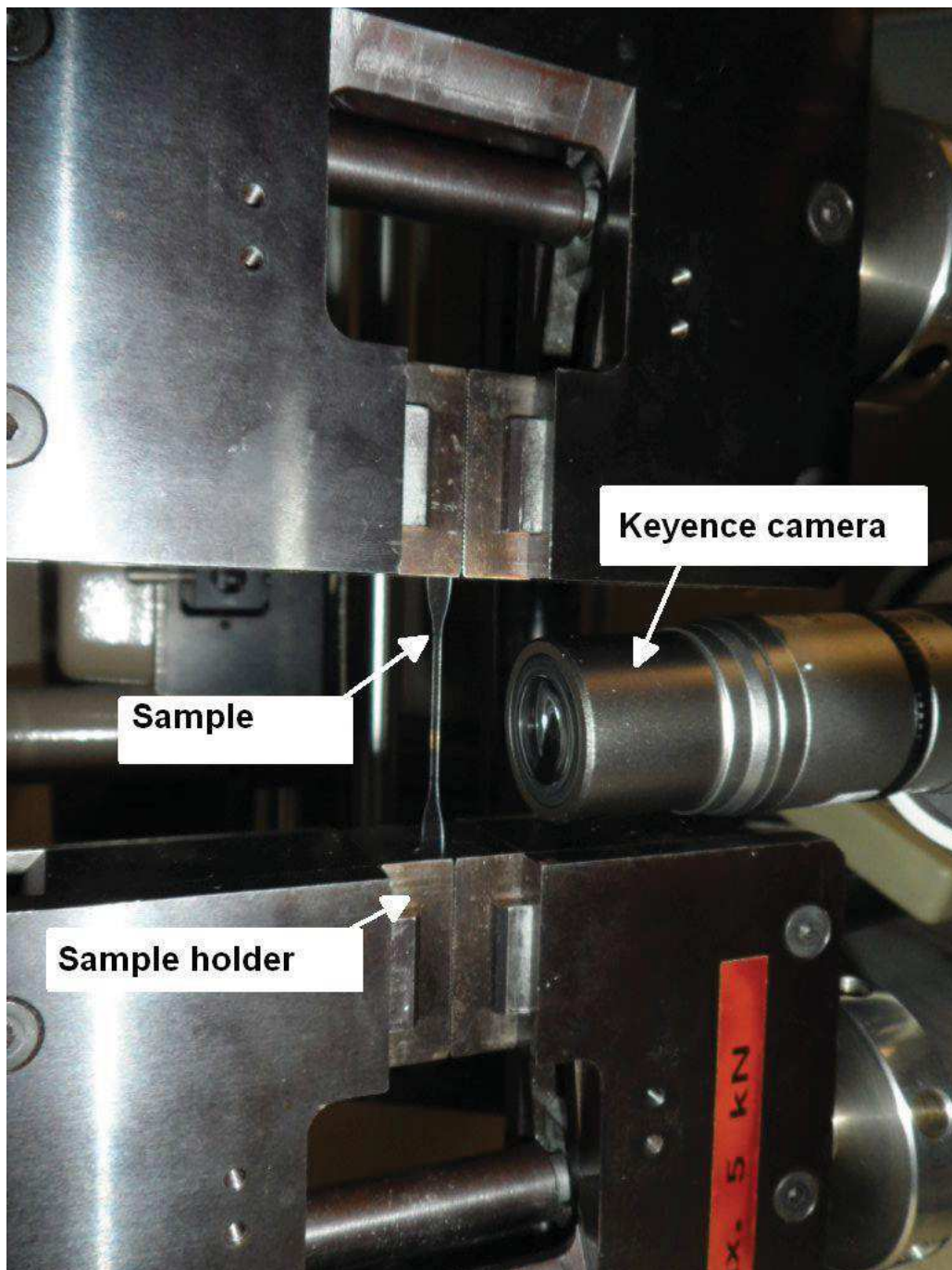


Figure 9. UTS tensile stage setup at EMPA laboratory (Switzerland)

5.3.2. SEM-integrated EMPA micro tensile stage

EMPA laboratory developed as well a Micro tensile stage (Figure 10) to be integrated into a SEM for micro samples testing with high resolution. This set up has been used as well for mechanical properties measurement. The maximum force for the load-cell is 2.5 kN.

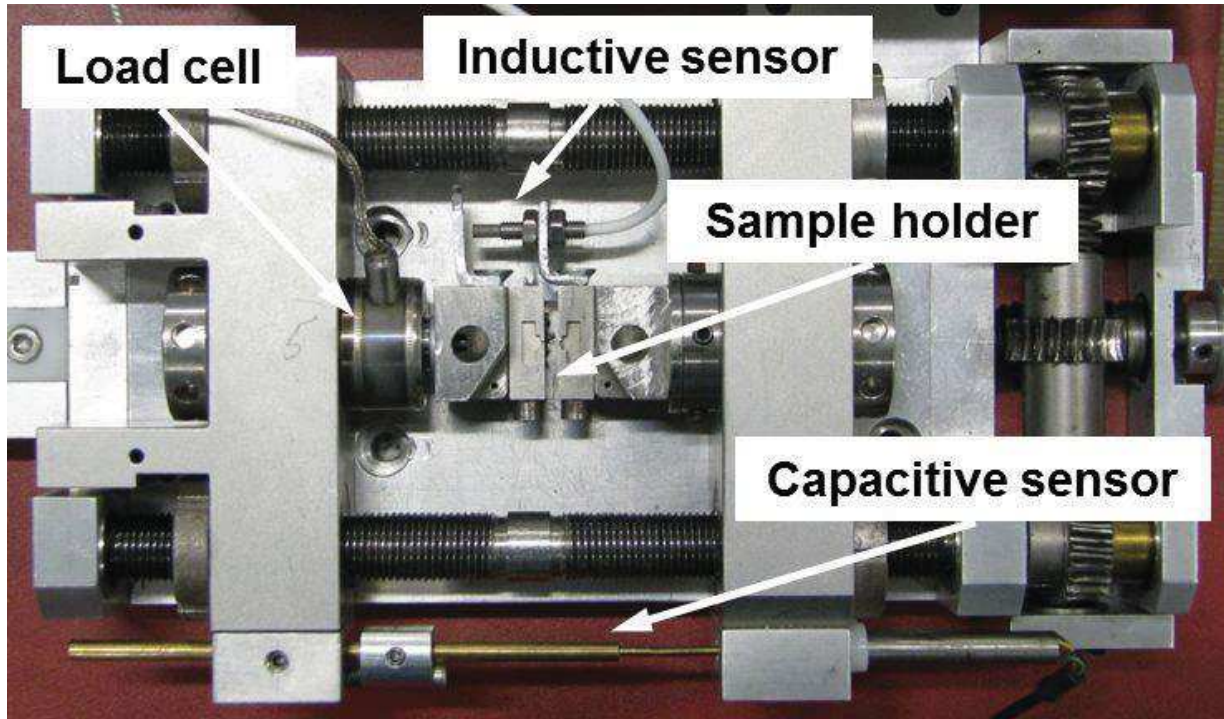


Figure 8. EMPA micro tensile stage for in-situ measurement

The resolution of an optical microscope is restricted by the wavelength of the visible light. In a light microscope, the wavelength is between 400 nm for the purple light and 800 nm for the red light. The resolution is roughly equal to the used wavelength. The Rayleigh criterion defines lateral optical resolution r as,

$$r = \frac{1.22\lambda}{2n\sin(\theta)} = \frac{0.61\lambda}{NA} \text{ (Equation 9)}$$

With n the refractive index of the medium between objective lens and sample (mostly air with $n=1$), λ the wavelength of light and θ the half angle of the light that enters into the objective lens.

With typical values of $n=1$, $\lambda=500\text{nm}$ (average), and $NA=0.73$ (Keyence camera), a resolution of $r=418\text{ nm}$ was obtained in theoretical measurement setup. In order to increase the resolution, a mini tensile test stage (Figure 8) was coupled to the Zeiss DSM 962 SEM. The cell was integrated into the SEM. The operation conditions of the SEM were set to:

- work distance (distance between sample and pole piece (objective)): 22 mm
- spot size: medium, 13
- acceleration voltage: 5 kV
- emission current: 3 A

In order to have an idea about the SEM resolution, we should note that the wavelength of the electron in the SEM is directly related to the acceleration voltage by the equation 12. The wavelength λ is related to the frequency f and the speed of light c (Equation 10). The energy E is directly proportional to the frequency f (Equation 11) and the energy E of an electron is given by the tension U (Equation 12). h is the Planck constant and e the elementary charge of the electron. Equation 13 is the combined form.

$$\lambda = c * f \quad \text{(Equation10)}$$

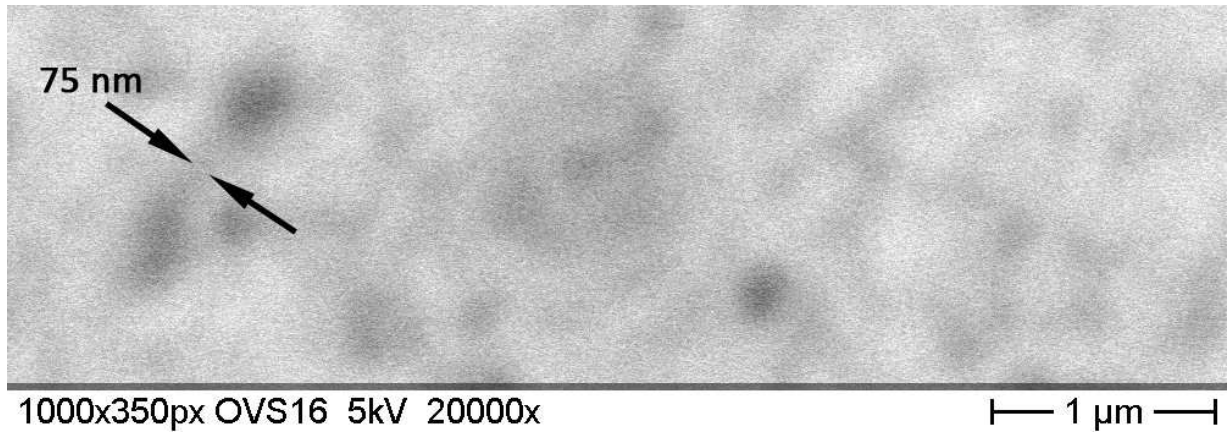
$$E = h * f \quad \text{(Equation11)}$$

$$E = e * U \quad \text{(Equation12)}$$

$$\lambda = c * h / e * U \quad \text{(Equation13)}$$

For the 5kV acceleration voltage used in the SEM integrated tensile measurements, Equation 5 results in $\lambda= 0.25\text{ nm}$ which gives a lateral resolution of $r=0.21\text{ nm}$ according to Equation 2. The electron beam size (focus) in a SEM is also dependent on lens aberrations which lead to a much larger beam size than given by the Rayleigh criterion and must be measured by calibration samples, see Figure 11 below.

a)



b)

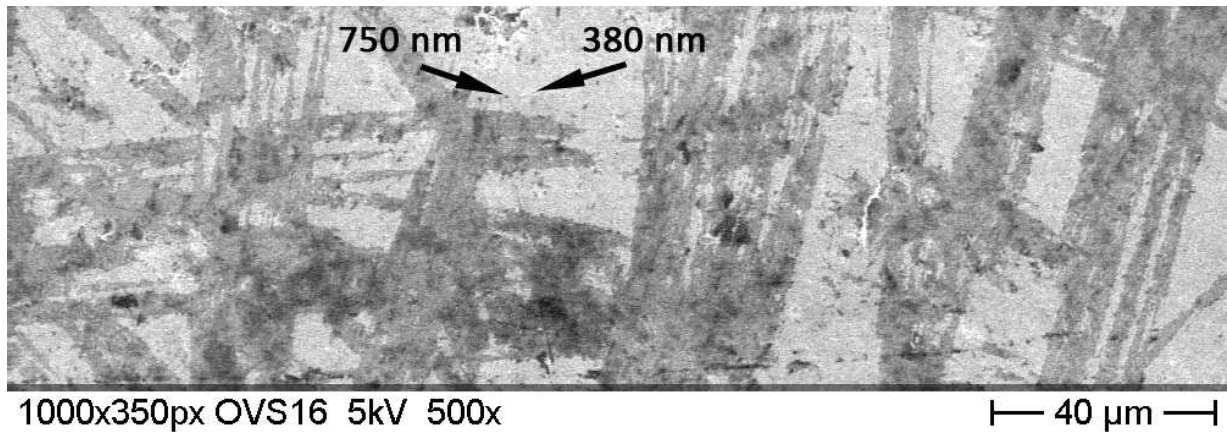


Figure 11. SEM images of a calibration sample (gold grains on carbon) at the conditions: 5keV, 22 mm working distance, medium spot size 13. (a) Image taken at 20kx magnification which gives a lateral resolution of 75 nm indicated by arrows. (b) Image taken at 500x magnification and one second per frame corresponding to the videos of tensile strain experiments. The pixel resolution is in this case 210 nm x 210 nm. The smallest features seen correspond to 380 nm. Well visible are features of 750 nm corresponding to roughly 3-4 image pixels[82].

From Figure 11 follows that the SEM has a lateral resolution of 75 nm under the described conditions. This corresponds to approximately 100 nm full width at half maximum (FWHM) of the electron beam. For the video, a representative area of the sample needed to be monitored within one second (one video frame) and a low magnification was used. In these

conditions, the pixel size became $214\text{nm} \times 217\text{nm}$ and the lateral resolution limit was measured to be 380 nm . This means that the resolution is pixel limited. 2-3 pixels are needed to see a contrast change with confidence at $500 \times$ magnifications[82].

6. $\text{Al}_2\text{O}_3/\text{ZnO}$ nanolaminates tensile tests

The $\text{Al}_2\text{O}_3/\text{ZnO}$ nanolaminates deposited on PET dogbones substrates were tested using the UTS Test stage at EMPA. Tensile speed was fixed to $0.1\text{ }\mu\text{m}/\text{second}$. Before starting the test, two pictures at $500\times$ and $1000\times$ magnification were taken as references. After the apparition of first crack, photos were taken every $10\mu\text{m}$ displacement (100seconds) at $1000\times$ magnification. Two points were fixed on the pictures and tracked along the measurement in order to calculate the strain. Crack densities extracted from photos were plotted against the applied strain. Figure 12 shows an example of the tensile tests done on the PMS3 sample.

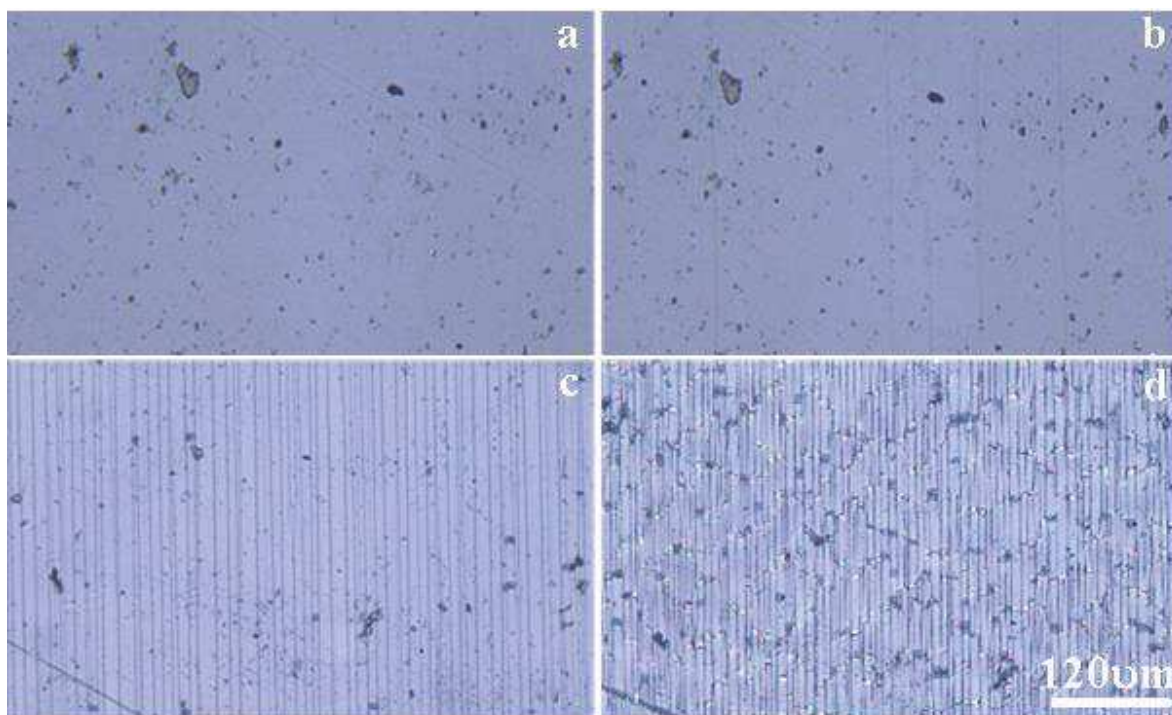


Figure 12. PMS3 tensile test a) at $S=0\%$, $1000\times$ b) first crack apparition at $s=1\%$, $1000\times$ c) at $S=5.6\%$, $500\times$ and d) at $S=16.66\%$ $500\times$ (saturated crack density).

As shown in Figure 12, cracks were formed perpendicularly to the applied strain. After the apparition of the first crack, crack density starts to increase with the strain increases to achieve a maximum called saturated crack density. After the crack saturation established, the delamination process occurs. Figure 13 represents the Crack density extracted from photos plotted against the applied strain for the samples PMS1 to PMS10.

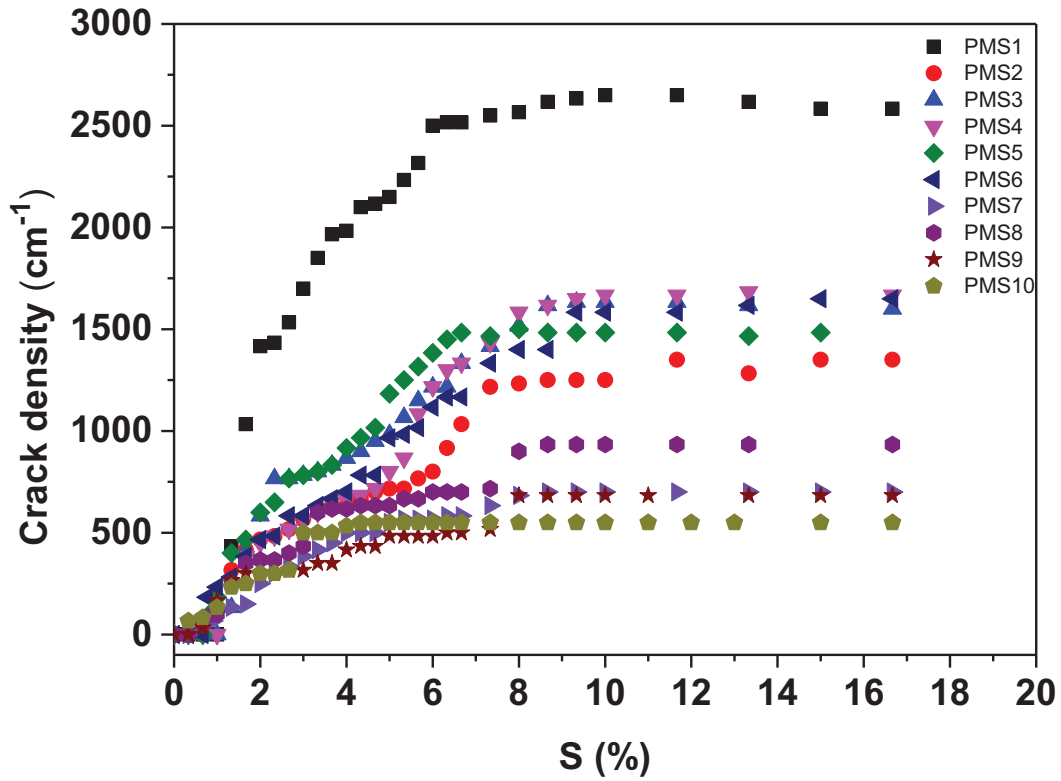


Figure 13. Crack density evolution during tensile tests for samples PMS1 to PMS10

Figure 13 reports the evolution of the crack density when the applied strain increases from 0 to 18%. As observed in this figure, crack density increases when the applied strain increases and then a maximum will be achieved indicating the saturation of those cracks. It is clearly shown in Figure 13 that when the bilayer thickness decreases, the saturated crack density decreases also. In order to evaluate the bilayer thickness effect on the saturated crack density, we plot in Figure 14 the saturated crack density versus the bilayer thickness.

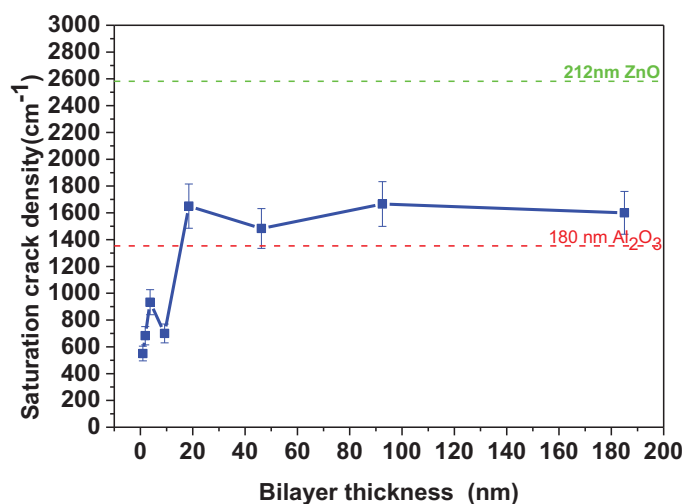


Figure 14. Saturation crack density versus the bilayer thickness

As observed in Figure 14, when the bilayer thicknesses decrease from 185 (PMS3) to 0.92nm (PMS10) the saturation crack density decreases from 1600 cracks/cm to 550 cracks/cm with a saturation crack density of 2583 cracks/cm for ZnO monolayer PMS1 and 1350 cracks/cm for the Al₂O₃ monolayer PMS2. This behavior was linked to the bilayers delamination during the tensile test that leads to less cracks formation. Figure 15 shows photos taken at S=10 %, 500x magnification for PMS1 to PMS10 samples.

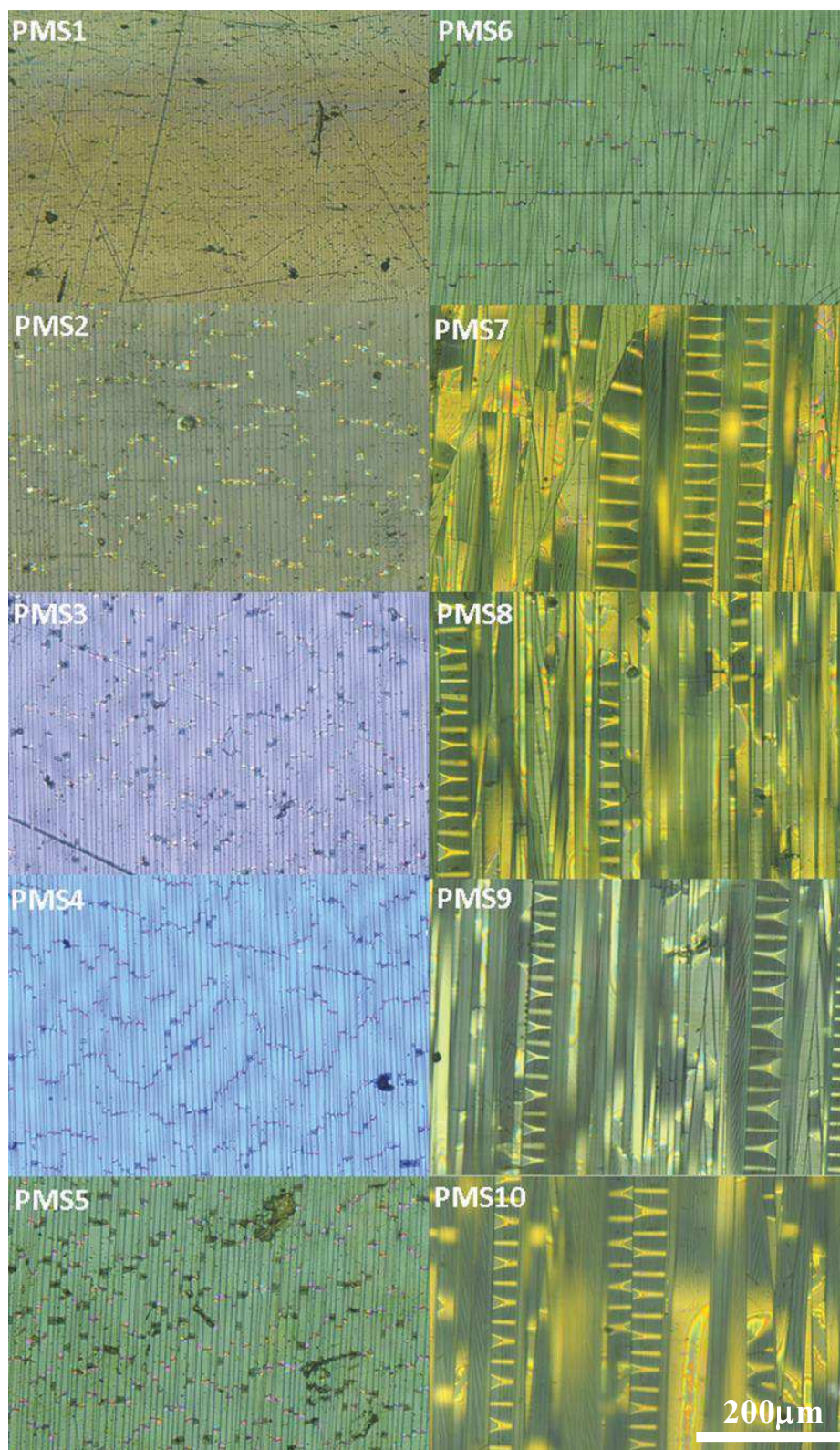


Figure 15. Photos of PMS1 to PMS10 samples at $s=10\%$ with 500x magnification

As shown in Figure 15, when the bilayer thickness decreases the delamination process increases which leads to the decrease of the saturation crack density. PMS7, PMS8, PMS9 and PMS10 show higher delamination behavior due to their lower bilayers thicknesses. Figure 16 shows the delamination starting strain versus the bilayer thicknesses.

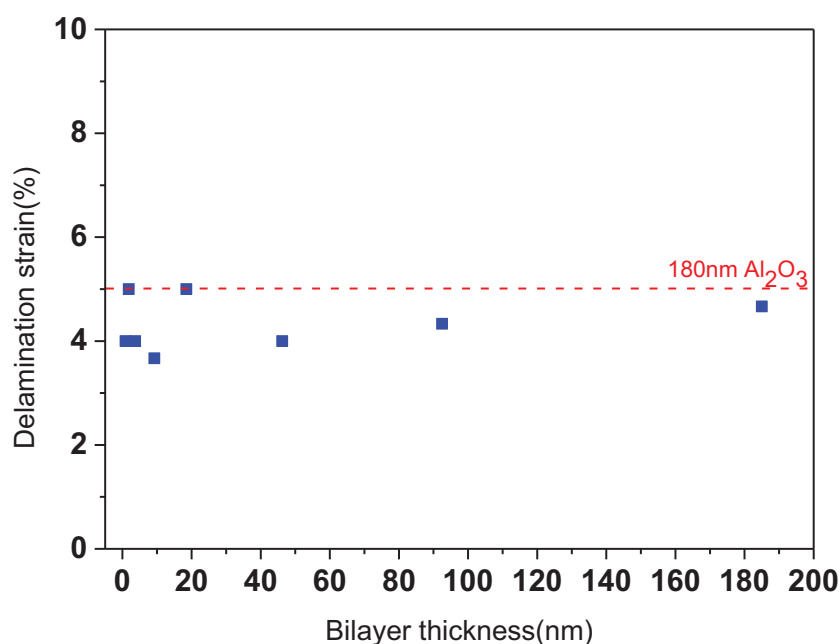


Figure 16. The delamination starting strain versus the bilayer thicknesses

From Figure 16, we can observe that the delamination starting strain of the Al₂O₃/ZnO nanolaminates are lower than the corresponding value for the Al₂O₃ which consists of the first layer (interface polymer/nanolaminates). So we can conclude from Figure 16 that the delamination process is limited to the delamination of the Al₂O₃ which consist of the first layer. Coupling the suggestion with Figure 15, which reports the non delamination of ZnO layers, we can have as perspective to start the nanolaminates structure with ZnO layers to enhance the adhesion.

Critical tensile strain was also plotted versus the bilayer thickness see figure 17.

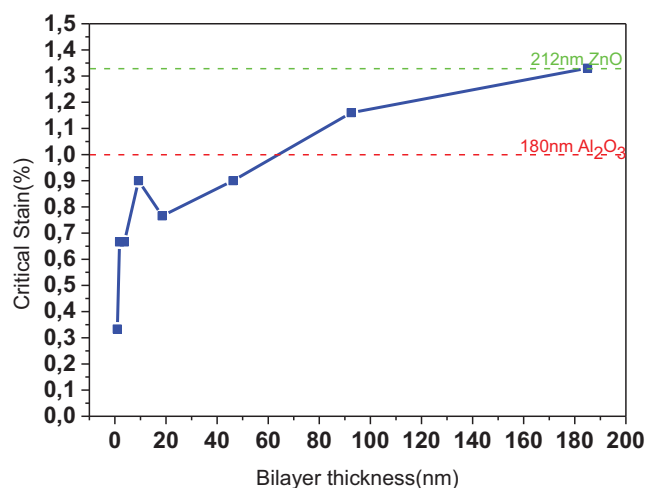


Figure 17. Critical Strain versus the Bilayer thickness

As shown in Figure 17, the critical strain of Al₂O₃/ZnO nanolaminates increases when the bilayer thickness increases. The maximum of the critical strain for the nanolaminates series was given for the PMS3 sample (1 bilayer of 500 cycles Al₂O₃/500 cycles ZnO) which shows the same value of the PMS1 sample (1000 cycles ZnO). None of the nanolaminates demonstrates a critical strain higher than the ZnO monolayer sample.

Using Equation 7 we can calculate the critical bending radius which is the minimum radius that a coated substrate can be bent before the coating suffers from cracking. R values were reported on table 6 then plotted against the bilayer thickness (Figure 18).

Table 6. Critical bending radius of Al₂O₃/ZnO nanolaminates samples (PMS1 to PMS10)

Samples	Bilayer thickness (nm)	R(μ m)
PMS1	180 nm ZnO	65.86
PMS2	212 nm Al ₂ O ₃	87.5
PMS3	185	65.85
PMS4	92.55	75.47
PMS5	46.25	97.24
PMS6	18.51	114.24
PMS7	9.25	97.22
PMS8	3.70	131.38
PMS9	1.85	131.38
PMS10	0.92	262.52

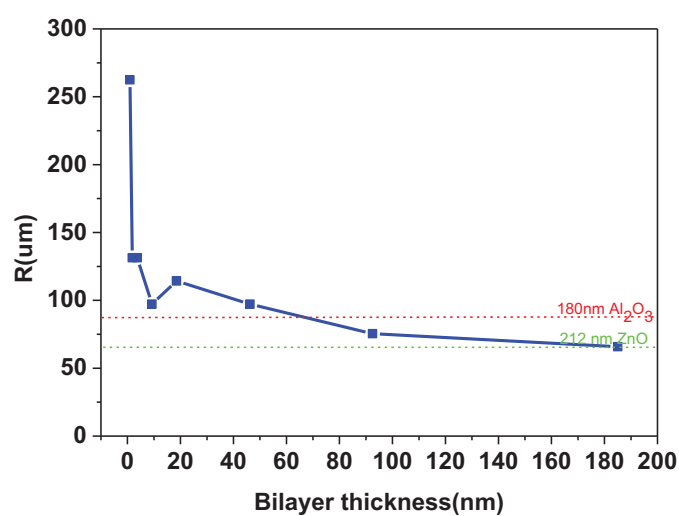
**Figure 18. Critical bending radius of the nanolaminates samples**

Figure 18 shows the critical bending radius decreasing when the bilayer thickness increases. None of the nanolaminates reports a critical bending radius less than the ZnO layers.

7. Conclusion and perspectives

$\text{Al}_2\text{O}_3/\text{ZnO}$ nanolaminates were deposited by the atomic layer deposition technique at 90°C with different bilayer thicknesses (conserving the total number of ALD cycles at 1000 cycles). Nanolaminates were deposited on silicon substrate to be characterized by SEM, XRR and XRD and on PET and nickel coated dogbones to be tested mechanically using the tensile tests stage at EMPA laboratory Switzerland. SEM image confirm the ability of the nanolaminates deposition using the ALD technique with a conformal coating and a well define nanolaminates structures. XRR measurement has been performed in order to extract the bilayer thickness and to assure the non presence of ZnO etching at such low temperature. GIXRD performed on the 10 samples shows a transition from an amorphous state to a crystalline state when the bilayer thickness increases. A change in the preferential growth orientation from (002) to (100) is observed when increasing the bilayer thickness from 9.25 nm to 185 nm.

Tensile tests measurement shows a decrease on the saturation crack density from 1600 cracks/cm to 550 cracks/cm when the bilayer thickness decreases from 185 to 0.92 nm with a saturation crack density of 2583 cracks/cm for ZnO monolayers and 1350 crack/cm for Al_2O_3 monolayer. This behavior was linked to the bilayers delamination during the tensile test that leads to less cracks formation. This behavior can also be due to the nanolaminates transition from a crystalline state to an amorphous state. We can also note that the delamination starting strain for the $\text{Al}_2\text{O}_3/\text{ZnO}$ nanolaminates are lower then the corresponding value for the Al_2O_3 which consist of the first layer (interface polymer/nanolaminates). The critical strain of $\text{Al}_2\text{O}_3/\text{ZnO}$ nanolaminates decreases when the bilayer thickness decreases, which can be due to the nanolaminates transition from a crystalline state to an amorphous state. In order to go dipper on this study we suggest solving the delamination process using three different approaches:

1. PET surface treatment using Oxygen plasma in order to increase the active sites on the PET film
2. NaOH surface treatment under UV in order to increase as well the active site on the PET film.
3. Another suggestion will be to deposit nanolaminates with ZnO as first layer due to the non delamination of the PMS1 sample (ZnO layer).

Micro tensile tests performed under SEM on the gold coated nickel dogbones reports the same tendency as the tensile tests performed on PET dogbones. The results were not reported on this chapter due to the initial load calibration for the micro tensile stage.

References

1. Bauerhenne, B., et al., Mechanical properties of boron-nitride nanotubes after intense femtosecond-laser excitation. *Nanotechnology*, 2014. 25(14).
2. Dulinska-Molak, I., et al., Variation of Mechanical Property of Single-Walled Carbon Nanotubes-Treated Cells Explored by Atomic Force Microscopy. *Journal of Biomedical Nanotechnology*, 2014. 10(4): p. 651-659.
3. Hemmatian, H., A. Fereidoon, and M. Rajabpour, Mechanical Properties Investigation of Defected, Twisted, Elliptic, Bended and Hetero-junction Carbon Nanotubes Based on FEM. *Fullerenes Nanotubes and Carbon Nanostructures*, 2014. 22(6): p. 528-544.
4. Li, C.D., et al., Effect of solidification on microstructures and mechanical properties of carbon nanotubes reinforced magnesium matrix composite. *Materials & Design*, 2014. 58: p. 204-208.
5. Li, K.-z., et al., Electrophoretic deposition of carbon nanotubes onto carbon fiber felt for production of carbon/carbon composites with improved mechanical and thermal properties. *Vacuum*, 2014. 104: p. 105-110.
6. Xu, S., et al., Interfacial intermetallic growth and mechanical properties of carbon nanotubes reinforced $\text{Sn}_{3.5}\text{Ag}_{0.5}\text{Cu}$ solder joint under current stressing. *Journal of Alloys and Compounds*, 2014. 595: p. 92-102.
7. Zanjanijam, A.R., M. Hajian, and G.A. Koohmarch, Fabrication of Single Wall Carbon Nanotubes-Based Poly(vinyl butyral) Nanocomposites with Enhanced Mechanical and Thermal Properties. *Journal of Macromolecular Science Part a-Pure and Applied Chemistry*, 2014. 51(4): p. 369-377.
8. Cheng, G., et al., Mechanical Properties of Silicon Carbide Nanowires: Effect of Size-Dependent Defect Density. *Nano Letters*, 2014. 14(2): p. 754-758.
9. Fu, B., et al., Size and temperature dependence of the tensile mechanical properties of zinc blende CdSe nanowires. *Physics Letters A*, 2013. 377(38): p. 2681-2686.
10. Fujii, T., et al., Focused Ion Beam Induced Surface Damage Effect on the Mechanical Properties of Silicon Nanowires. *Journal of Engineering Materials and Technology-Transactions of the Asme*, 2013. 135(4).
11. Georgakaki, D., O.G. Ziogos, and H.M. Polatoglou, Vibrational and mechanical properties of Si/Ge nanowires as resonators: A molecular dynamics study. *Physica Status Solidi a-Applications and Materials Science*, 2014. 211(2): p. 267-276.
12. Huskic, M., et al., The effect of $\text{Mo}_6\text{S}_3\text{I}_6$ nanowires on the thermal and mechanical properties of polyamide 12. *Composites Part B-Engineering*, 2014. 56: p. 62-67.
13. Li, X., et al., Mechanical properties of individual InAs nanowires studied by tensile tests. *Applied Physics Letters*, 2014. 104(10).
14. Lin, K.-H., et al., Mechanical properties and thermal stability of ultrathin tungsten nanowires. *Rsc Advances*, 2014. 4(14): p. 6985-6990.
15. Wang, W.-d., C.-l. Yi, and K.-q. Fan, Molecular dynamics study on temperature and strain rate dependences of mechanical tensile properties of ultrathin nickel nanowires. *Transactions of Nonferrous Metals Society of China*, 2013. 23(11): p. 3353-3361.
16. Zhang, J. and C. Wang, Effect of the electric field on the mechanical properties of gallium nitride nanowires. *Epl*, 2014. 105(2).
17. Amri, A., et al., Tailoring the physicochemical and mechanical properties of optical copper-cobalt oxide thin films through annealing treatment. *Surface & Coatings Technology*, 2014. 239: p. 212-221.
18. Ben-Nissan, B., A.H. Choi, and A. Bendavid, Mechanical properties of inorganic biomedical thin films and their corresponding testing methods. *Surface & Coatings Technology*, 2013. 233: p. 39-48.

19. Callisti, M., et al., Effects of Cu on the microstructural and mechanical properties of sputter deposited Ni-Ti thin films. *Surface & Coatings Technology*, 2013. 237: p. 261-268.
20. Chen, X., et al., Microstructure, Mechanical, and Tribological Properties of CN_x Thin Films Prepared by Reactive Magnetron Sputtering. *Acta Metallurgica Sinica-English Letters*, 2014. 27(1): p. 31-36.
21. Cherneva, S., et al., Nanoindentation investigation of mechanical properties of ZrO₂, ZrO₂-Y₂O₃, Al₂O₃ and TiO₂ thin films deposited on stainless steel OC 404 substrate by spray pyrolysis. *Materials Science and Engineering B-Advanced Functional Solid-State Materials*, 2014. 183: p. 12-16.
22. Dwivedi, N., et al., Influence of consumed power on structural and nano-mechanical properties of nano-structured diamond-like carbon thin films. *Applied Surface Science*, 2014. 300: p. 141-148.
23. Gao, Q., et al., Improved mechanical properties of SnO₂T thin film by structural modification. *Ceramics International*, 2014. 40(2): p. 2557-2564.
24. Goupy, J., et al., Structure, electrical conductivity, critical superconducting temperature and mechanical properties of TiN_xO_y thin films. *Surface & Coatings Technology*, 2013. 237: p. 196-204.
25. Hsiao, T.-P., et al., The microstructure and mechanical properties of nitrogen and boron contained ZrCuAlNi thin film metallic glass composites. *Surface & Coatings Technology*, 2013. 237: p. 276-283.
26. Huang, S., et al., Mechanical Properties of Nanoporous GaN and Its Application for Separation and Transfer of GaN Thin Films. *Acs Applied Materials & Interfaces*, 2013. 5(21): p. 11074-11079.
27. Jian, S.-R., G.-J. Chen, and W.-M. Hsu, Mechanical Properties of Cu₂O Thin Films by Nanoindentation. *Materials*, 2013. 6(10): p. 4505-4513.
28. Kim, I., T.-M. Lee, and J. Kim, A study on the electrical and mechanical properties of printed Ag thin films for flexible device application. *Journal of Alloys and Compounds*, 2014. 596: p. 158-163.
29. King, S.W., et al., Influence of network bond percolation on the thermal, mechanical, electrical and optical properties of high and low-k a-SiC:H thin films. *Journal of Non-Crystalline Solids*, 2013. 379: p. 67-79.
30. Li, X., et al., Effects of niobium content on electrical and mechanical properties of (Na_{0.85}K_{0.15})_{0.5}Bi_{0.5}Ti_(1-x)Nb_xO₃ thin films. *Journal of Materials Science-Materials in Electronics*, 2014. 25(3): p. 1416-1422.
31. Longun, J., G. Walker, and J.O. Iroh, Surface and mechanical properties of grapheneclay/polyimide composites and thin films. *Carbon*, 2013. 63: p. 9-22.
32. Mhaisagar, Y.S., B.N. Joshi, and A.M. Mahajan, Mechanical properties of surface modified silica low-k thin films. *Microelectronic Engineering*, 2014. 114: p. 112-116.
33. Mouro, J., et al., Microstructure factor and mechanical and electronic properties of hydrogenated amorphous and nanocrystalline silicon thin-films for microelectromechanical systems applications. *Journal of Applied Physics*, 2013. 114(18).
34. Pagon, A.M., E.D. Doyle, and D.G. McCulloch, The microstructure and mechanical properties of TiN-Ni nanocomposite thin films. *Surface & Coatings Technology*, 2013. 235: p. 394-400.
35. Tien, C.-L., et al., Temperature-dependent optical and mechanical properties of obliquely deposited MgF₂ thin films. *Indian Journal of Pure & Applied Physics*, 2014. 52(2): p. 117-123.
36. Tsau, C.-H. and Y.-H. Chang, Microstructures and Mechanical Properties of TiCrZrNbN_x Alloy Nitride Thin Films. *Entropy*, 2013. 15(11): p. 5012-5021.
37. Umar, Z.A., et al., Mechanical properties of Al/a-C nanocomposite thin films synthesized using a plasma focus device. *Chinese Physics B*, 2014. 23(2).
38. Van-Vinh, L., N. Thi-Trang, and S.-K. Kim, The influence of nitrogen pressure and substrate temperature on the structure and mechanical properties of CrAlBN thin films. *Thin Solid Films*, 2013. 548: p. 377-384.

39. Xing, Y.Y., et al., Enhancement of high-temperature oxidation resistance and mechanical properties of Ni₃Al thin films by inserting ultrathin Cr layers. *Vacuum*, 2014. 101: p. 107-112.
40. Zalnezhad, E., et al., Mechanical Property Enhancement of Ti-6Al-4V by Multilayer Thin Solid Film Ti/TiO₂ Nanotubular Array Coating for Biomedical Application. *Metallurgical and Materials Transactions a-Physical Metallurgy and Materials Science*, 2014. 45A(2): p. 785-797.
41. Ando, T., et al., FRACTURE TOUGHNESS OF SI THIN FILM AT VERY LOW TEMPERATURES BY TENSILE TEST, in 2011 Ieee 24th International Conference on Micro Electro Mechanical Systems2011. p. 436-439.
42. Chen, X., et al., Tensile testing of thin films supported on compliant substrates. *Mechanics of Materials*, 2009. 41(7): p. 839-848.
43. Dameron, A.A., et al., Tensile strain and water vapor transport testing of flexible, conductive and transparent indium-zinc-oxide/silver/indium-zinc-oxide thin films. *Thin Solid Films*, 2011. 519(10): p. 3177-3184.
44. Ignat, M., et al., Micro Tensile Tests on Aluminium Thin Films: Tensile Device and In-Situ Observations, in *Microelectromechanical Systems - Materials and Devices II*, S. Vengallatore, et al., Editors. 2009. p. 217-223.
45. Lee, S.J., et al., Electromechanical Characterization of Au Thin Films using Micro-tensile Testing. *Experimental Mechanics*, 2010. 50(5): p. 643-649.
46. Namazu, T., et al., Design and Development of a Biaxial Tensile Test Device for a Thin Film Specimen. *Journal of Engineering Materials and Technology-Transactions of the Asme*, 2012. 134(1).
47. Obara, Y., et al., Tensile Test of Diamond-Like Carbon Thin Films by Nanomaterials Testing System. *Journal of the Japan Institute of Metals*, 2012. 76(5): p. 327-331.
48. Oh, H.-J., et al., Mechanical characterization of sub-100-nm-thick Au thin films by electrostatically actuated tensile testing with several strain rates. *Japanese Journal of Applied Physics*, 2014. 53(2).
49. Park, J.H., et al., Tensile test of lead zirconate titanate (PZT)/Platinum (Pt) thin film. *Materialwissenschaft Und Werkstofftechnik*, 2011. 42(5): p. 478-484.
50. Park, J.-H., et al., Tensile and high cycle fatigue tests of NiCo thin films. 11th International Conference on the Mechanical Behavior of Materials (Icm11), 2011. 10: p. 1303-1308.
51. Park, J.-H., M.S. Myung, and Y.-J. Kim, Tensile and high cycle fatigue test of Al-3% Ti thin films. *Sensors and Actuators a-Physical*, 2008. 147(2): p. 561-569.
52. Smolka, M., et al., Novel temperature dependent tensile test of freestanding copper thin film structures. *Review of Scientific Instruments*, 2012. 83(6).
53. Zhang, X. and S. Zhang, A Microbridge Method in Tensile Testing of Substrate for Fracture Toughness of Thin Films. *Nanoscience and Nanotechnology Letters*, 2011. 3(6): p. 735-743.
54. Chen, Y.-T., Nanoindentation and Adhesion Properties of Ta Thin Films. *Journal of Nanomaterials*, 2013.
55. Chen, Z., et al., Nanoindentation of porous bulk and thin films of La_{0.6}Sr_{0.4}Co_{0.2}Fe_{0.8}O₃-delta. *Acta Materialia*, 2013. 61(15): p. 5720-5734.
56. de Knoop, L. and M. Legros, Absorption of crystal/amorphous interfacial dislocations during in situ TEM nanoindentation of an Al thin film on Si. *Scripta Materialia*, 2014. 74: p. 44-47.
57. Huang, C.-Y., et al., Nanoindentation of Mg-doped AlGaN thin films. *Journal of Alloys and Compounds*, 2014. 593: p. 220-223.
58. Jian, S.-R. and J.-Y. Juang, Nanoindentation-Induced Pop-In Effects in GaN Thin Films. *Ieee Transactions on Nanotechnology*, 2013. 12(3): p. 304-308.
59. Jian, S.-R. and Y.-H. Lee, Nanoindentation-induced interfacial fracture of ZnO thin films deposited on Si(111) substrates by atomic layer deposition. *Journal of Alloys and Compounds*, 2014. 587: p. 313-317.
60. Jian, S.-R. and Y.-C. Tseng, Nanomechanical Characteristics and Deformation Behaviors of ZnSe Thin Films by Nanoindentation. *Science of Advanced Materials*, 2014. 6(3): p. 617-622.

61. Jian, S.-R., et al., Dislocation Energetics and Pop-Ins in AlN Thin Films by Berkovich Nanoindentation. *Materials*, 2013. 6(9): p. 4259-4267.
62. Jimenez-Pique, E., et al., Nanoindentation of nanocolumnar TiO_2 thin films with single and stacked zig-zag layers. *Thin Solid Films*, 2014. 550: p. 444-449.
63. Lin, S., et al., Tuning heterogeneous poly(dopamine) structures and mechanics: in silico covalent cross-linking and thin film nanoindentation. *Soft matter*, 2013. 10(3): p. 457-64.
64. Nunes, J. and A.P. Piedade, Nanoindentation of functionally graded hybrid polymer/metal thin films. *Applied Surface Science*, 2013. 284: p. 792-797.
65. Ramos-Cano, J., et al., Characterization of Nanomechanical, Ferroelectric, and Piezoelectric Properties by Nanoindentation and Piezoresponse Force Microscopy of PbTiO_3 Thin Films. *Industrial & Engineering Chemistry Research*, 2013. 52(40): p. 14328-14334.
66. Sun, K., W. Shen, and L. Ma, The influence of residual stress on incipient plasticity in single-crystal copper thin film under nanoindentation. *Computational Materials Science*, 2014. 81: p. 226-232.
67. Wymyslowski, A. and L. Dowhan, Application of nanoindentation technique for investigation of elasto-plastic properties of the selected thin film materials. *Microelectronics Reliability*, 2013. 53(3): p. 443-451.
68. Zhang, C., et al., Extracting the elastic moduli of the constituent layers of a multilayered thin film from nanoindentation tests. *Journal of Materials Research*, 2013. 28(18): p. 2570-2576.
69. Jian, S.-R. and Y.-H. Lee, Nanoindentation-induced interfacial fracture of ZnO thin films deposited on $\text{Si}(1 \times 1)$ substrates by atomic layer deposition. *Journal of Alloys and Compounds*, 2014. 587(0): p. 313-317.
70. Jen, S.-H., J.A. Bertrand, and S.M. George, Critical tensile and compressive strains for cracking of Al_2O_3 films grown by atomic layer deposition. *Journal of Applied Physics*, 2011. 109(8).
71. Tripp, M.K., et al., The mechanical properties of atomic layer deposited alumina for use in micro- and nano-electromechanical systems. *Sensors and Actuators a-Physical*, 2006. 130: p. 419-429.
72. Tapily, K., et al., Nanoindentation Investigation of HfO_2 and Al_2O_3 Films Grown by Atomic Layer Deposition. *Journal of The Electrochemical Society*, 2008. 155(7): p. H545-H551.
73. Miller, D.C., et al., The mechanical robustness of atomic-layer- and molecular-layer-deposited coatings on polymer substrates. *Journal of Applied Physics*, 2009. 105(9).
74. Latella, B.A., G. Triani, and P.J. Evans, Toughness and adhesion of atomic layer deposited alumina films on polycarbonate substrates. *Scripta Materialia*, 2007. 56(6): p. 493-496.
75. Raghavan, R., et al., Nanocrystalline-to-amorphous transition in nanolaminates grown by low temperature atomic layer deposition and related mechanical properties. *Applied Physics Letters*, 2012. 100(19).
76. Herrmann, C.F., et al., Properties of atomic layer deposited $\text{Al}_2\text{O}_3/\text{ZnO}$ dielectric films grown at low temperature for RF MEMS, in *Micromachining and Microfabrication Process Technology X*, M.A. Maher and H.D. Stewart, Editors. 2005, Spie-Int Soc Optical Engineering: Bellingham. p. 159-166.
77. Elam, J.W. and S.M. George, Growth of $\text{ZnO}/\text{Al}_2\text{O}_3$ alloy films using atomic layer deposition techniques. *Chemistry of Materials*, 2003. 15(4): p. 1020-1028.
78. Groner, M.D., et al., Low-temperature Al_2O_3 atomic layer deposition. *Chemistry of Materials*, 2004. 16(4): p. 639-645.
79. Abou Chaaya, A., et al., Evolution of microstructure and related optical properties of ZnO grown by atomic layer deposition. *Beilstein Journal of Nanotechnology*, 2013. 4: p. 690-698.
80. Elias, J., et al., Electrochemical growth of ZnO nanowires on atomic layer deposition coated polystyrene sphere templates. *Electrochimica Acta*, 2013. 110: p. 387-392.
81. Reddy, A.J., et al., Combustion synthesis, characterization and Raman studies of ZnO nanopowders. *Spectrochimica Acta Part a-Molecular and Biomolecular Spectroscopy*, 2011. 81(1): p. 53-58.

82. Schär, T., Tensile Stress Investigations of ALD Al_2O_3 Films, 2013, EMPA: Thun Switzerland. p. 53.

Chapter 5. ALD modified PET and PC membranes for different applications

ALD modified PET and PC membranes for different applications

1.Introduction.....	197
2.Membrane types.....	198
2.1. Symmetrical membranes.....	198
2.2. Asymmetric membranes.....	199
3.ALD for membrane applications.....	200
4.Enhanced Ionic Transport Mechanism by Gramicidin A Confined Inside Nanopores Tuned by Atomic Layer Deposition.....	201
4.1.Track etching technique.....	203
4.2.Pores diameter estimation of PET track etched membrane.....	203
4.3.Tuning the Nanopore Diameter Using ALD.....	205
4.4.Structural and chemical characterization.....	206
4.4.1.Energy dispersive X ray.....	206
4.4.2. SAXS measurements.....	207
4.4.3.Transmission electron microscopy measurement.....	209
4.4.4.AFM measurement.....	209
4.4.5.XPS measurements.....	210
4.4.6.Contact angle measurements.....	211
4.4.7.Conductance measurements on ALD modified PET Membranes.....	213
4.5.Gramicidin A confinement.....	214
4.5.1.Sodium chloride transfer through the membrane by diffusion under a concentration gradient.....	215
4.5.2.Sodium chloride transfer through the membrane by diffusion under an applied voltage.....	217
4.6.Molecular Dynamic simulation.....	222
4.7.Conclusion on gA confinement inside tuned ALD nanopores.....	225

5.Experimental and simulation studies of unusual current blockade induced by translocation of small oxidized PEG through a single nanopore.....	226
5.1.Nanopores synthesis and tuning.....	227
5.2.Ionic current recordings.....	228
5.3.Conductance measurements.....	228
5.4.PEG detection.....	230
5.4.1.Neutral PEG detection.....	230
5.4.2.PEG-Carboxylate detection.....	231
5.5.Conclusion on PEG translocation.....	233
6.Polycarbonate porous membrane for gas purification.....	233
6.1.Membrane preparation.....	235
6.2.Gas separation setup.....	235
6.3 First results and discussion.....	237
6.4 Conclusion and perspectives.....	239
7.General conclusion.....	240

1. Introduction

Membranes technology has attractive attention in industrial and laboratory applications due their needs in different fields such as water and gas purification, catalysis, bio-sensor, and ion transport. The first membrane study can be attributed to Abb'eNolet in 1748 who described water permeation through a diaphragm[1]. Membranes technology found their first industrial application in the filtration of drinking water at the end of World War II[1]. Since 1960, membranes technology has grown from laboratory study to industrial applications after the seminal discovery of Loeb-Sourirajan of making a defect free high flux, asymmetric reverse osmosis membrane which consist of an ultrathin, selective surface film on a microporous support, which provides the mechanical strength[2]. In 1980, membranes technology entered the industrial gas separation and purification fields [1]. Polymeric membranes remain the most viable commercial choice and substantial research works on the design of polymers with improved separation performance and physicochemical properties are in progress. Most of industrial porous membranes have a sub-nanometer up to micrometers pores diameter. However some separation process especially gas separation process requires an angstrom pore size range. A variety of techniques have been employed to modify the pore size and surface properties of porous membranes such as chemical vapor deposition[3], sol gel procedure[4], and atomic layer deposition (ALD)[5]. From the different methods to control the pore diameter, ALD have attractive attention due to the conformal coating and the high thickness control offered by this technique.

In the first part of this chapter, we will introduce the different types of membrane and their elaboration methods. In the second part we will focus on multipores PET membrane synthesized by the track etching technique then tuned by the atomic layer deposition technique in order to obtain a sub 10 nm pores diameter. Biological function has been added to the multipores PET membrane using Gramicidin confinement into the pores. Membranes were characterized and tested for ionic transport application [6]. In the third part of this chapter we will report a 5 nm single nanopore PET membrane with high length/diameter ratio, synthesised by the track etching technique and tailored by the atomic layer deposition of $\text{Al}_2\text{O}_3/\text{ZnO}$ nanolaminates. After the nanopore design, Sebastien balme's team (European institute of membranes) investigated the PEG translocation throw the nanopore. The translocation of neutral Polyethylene glycol (PEG)

and charged Polyethylene glycol-carboxylate (PEG- carboxylate) molecules of low molar mass (200 and 600 g.mol⁻¹) through this nanodevice was studied. Finally we will present our first results and our perspectives on polycarbonate track etched porous membrane tuned by ALD for gas purification applications.

2. Membrane types

Excluding biological membranes, membranes can be divided to two categories: Symmetrical and asymmetrical membranes [1] (Figure 1).

2.1. Symmetrical membranes

Symmetrical membranes can be divided to three categories:

- Isotropic microporous membranes: this is a conventional filter with high density interconnected pores (Figure 1a). Pore diameter can be in the range of 0.01 up to 100 μm . Particles with diameters larger from the pore size are rejected. Only molecules with significant diameter difference can be separated by this membrane type. Microporous membrane are generally characterized by the average pore diameter d , the membrane porosity ϵ (the total porous fraction of the membrane) and the membrane tortuosity τ which is the ratio between pore length and membrane thickness (membranes with straight pores, $T=1$). Isotropic microporous membrane are generally prepared by solution precipitation technique, irradiation of dense membrane (track etching membrane) and the expanded film technique based on a crystalline transition of crystalline polymers after a rapid dropdown temperature which leads to voids appearance between crystallites.
- Nonporous dense membrane: it is a dense film pinhole free membrane (Figure 1b). Diffusion mechanism occurs under external forces (pressure, concentration or electrical potential gradient). Membrane selectivity is directly related to the transport rate within the membrane for each element which is relative to their diffusivity and solubility in the membrane material. Molecule size is not a separation parameter for this membrane type. This type of membrane is generally prepared by solution casting or by melt pressing.

- Electrically charged membranes: this membrane type can be porous or dense but generally it is a microporous membrane with the pore walls electrically charged by negative or positive ions (Figure1c). Based on Coulomb law, a positive charged membrane blocks the cations and lets the anions pass through the pores, it is an anion-exchange membrane. A negative charged membrane blocks the anions and lets the cations pass through the pore, it is a cation-exchange membrane. Separation mechanism on an electrically charged membrane is directly related to wall charge, ion charge and ions concentration in the solution.

2.2. Asymmetric membranes

Asymmetric membranes consist of a thin layer supported on a porous structure which functioned as a mechanical support only. The selective layer is the thin film deposited on the porous support that can be porous with smaller pores size than the support (Figure1d) or it can be dense (Figure1e). Membrane permeability is inversely proportional to the membrane thickness which reflects a higher permeability for thinner selective layer excluding the support thickness. High permeability is an advantage for this type of membrane.

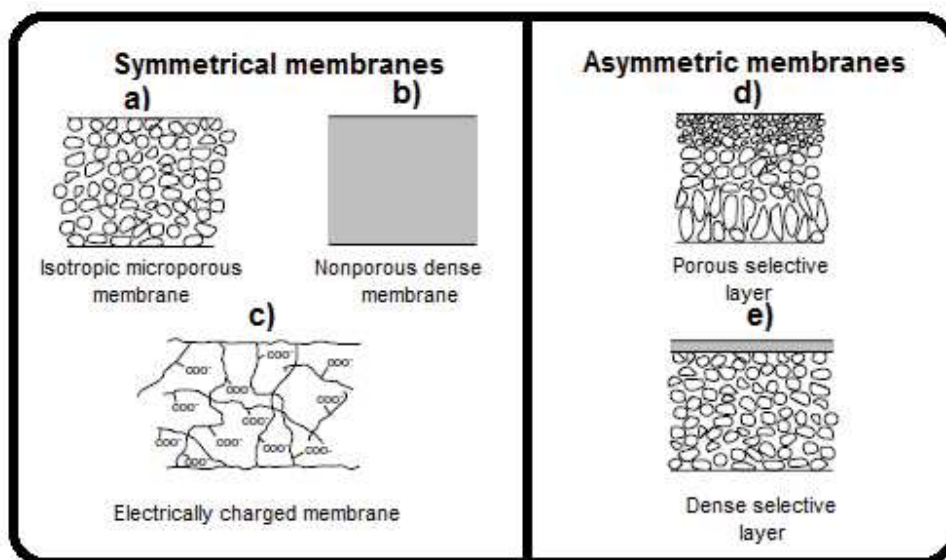


Figure 1: Symmetrical and Asymmetric membranes types

3. ALD for membrane applications

Since many years, porous materials such as polycarbonate membrane, alumina membrane (AAO) or mesoporous silica have been coated by ALD. An early work reported the AAO pore tuning by Al_2O_3 ALD[7]. H_2 and N_2 gas diffusion measurements were consistent with the pore size reduction as a function of the number of ALD cycles. Moreover, no increase of the pore size distribution was observed with the increase of the cycles, highlighting the high conformality of the ALD coating. Later on, SiO_2 and TiO_2 ALD were successfully applied to the coating of asymmetric microporous tubular membranes[8]. The conductance measurements reveal that gas transport through microscopic pores is determined by pore diameters and the effect of the surface functional groups. Surface properties and diameter tuning of Si_3N_4 membranes were achieved by Al_2O_3 ALD[9]. Such a membrane was used for the capture of DNA and other negative polyelectrolytes. Starting with large pores of any shape, correspondingly shaped single-nanometer sized high aspect ratio channels can be produced by ALD. Alternatively, starting with an already small ion beam sculpted nanopore of known diameter in a thin membrane, a short, molecularly sized nanopore can be fashioned with atomic precision without the need for final TEM verification.

In this chapter, we will focus on symmetrical isotropic microporous membrane elaborated by the track etching technique then modified using the atomic layer deposition with the vapor exposure process for surface modification. Membrane will be characterized before ALD then it will be tuned by ALD deposition of $\text{Al}_2\text{O}_3/\text{ZnO}$ nanolaminates. After this step, a vapor exposure surface treatment is applied. Multipores membrane with sub 10 nm pores diameter will be impregnated with gramicidin A and tested as ionic transport membrane (section 3 of this chapter). In the same time, single pore membrane with 5 nm pore diameter will be tested as molecular PEG (Polyethylene glycol) sensor (section 4 of this chapter). Other applications have been done on the porous PET membrane controlled by ALD such as gas purification, DNA sequencing and gas barrier. Those results are in progress and will not be presented on this thesis.

4. Enhanced ionic transport mechanism by gramicidin A confined inside nanopores tuned by Atomic Layer Deposition

The development of solid state ionic transport membrane with high ion permeability, high ion selectivity and energy less function mechanism, consists of an antagonist research field [10]. Different elaboration techniques have been used in order to obtain an ionic transport membrane(ITM) owning unique properties in term of high permeability and selectivity. Conical track etched pore with charge surface modification consists one of those ITM elaboration technique[11]. For ITM with different types, anionic or cationic, selectivity is obtained under an electric field. Direct confinement of biological ionic channels inside cylindrical nanopores has been recently demonstrated [12, 13]. This membrane shows a good mechanical properties, a high suitability with the biological molecules and the ion solution. Moreover this membrane present biological selectivity properties offered by the confined biological molecule [14, 15]. Among those biological molecules used on this topic gramicidin A (gA) is one of the most widely studied due to its simple structure and to its selectivity to monovalent cations[16-18].gA is formed by a linear polypeptide of 15 hydrophobic amino acids which adopt β -helix structure. Inside the lipid membrane, the selective pore is formed by a head-head dimer of gA linked by H-bond between C-terminal functions. With this conformation, a gA channel is only permeable to monovalent cations[19, 20] and blocks anions[21]. Even though gA is one of the simplest ionic channels, its properties are not easily transferred to solid state membranes. Presently, all attempts to confine biological ionic channels inside a nanopore have shown a loss or a modification of their ionic selectivity[22]. Indeed, in biological membranes, gA selectivity in the presence of monovalent ions is induced by head to head dimer structure as the junction between the monomers blocks the anions and allows the transport of cations. It has been shown that this dimer structure is lost in aqueous solution[5]. Thus according to experimental conditions, it can be assumed that head to head structure is lost before the gA confinement.

Balme et al.[23] reports the first studies about the synthesis of hybrid membranes by confining gA in the porous polycarbonate track-etched membranes. This polycarbonate membrane present several advantages related to its uniformity and density of nanopores, wide diameter pore range, flexibility and low cost of fabrication. However these membranes present several major drawbacks (i) the diameter cannot be controlled under 15 nm and (ii) they are hydrophilic. These

drawbacks constitute the prior limitation of these membranes. Indeed to recover the biological properties, an ionic channel must be incorporated inside a nanopore of diameter close to the size of the gA hydrophobic part (~ 1 nm). In addition, the pore must be hydrophobic. In this section, we propose to investigate the ionic transport mechanisms of confined gA inside sub 10 nm hydrophobic nanopore.

Due to their high aspect ratio deposition ability discussed in chapter 1, atomic layer deposition technique was used to tune the pore diameter of a PET track etched membrane with 100 pores with an initial pores diameters of 36 nm to a final pores diameter of 10.6, 5.7 and ~ 2 nm. Nanolaminates of aluminum oxide/zinc oxide have been investigated for the PET pore reduction in order to assure a low roughness inside the nanopores preserving the main advantages of the polymeric membranes: uniformity of the nanopores and flexibility of the membrane. Then a Hexamethyldisilazane chemical treatment [24] allows coating the nanopore wall with $-\text{CH}_3$ to mimic $-\text{CH}_2-$ / gA interaction such as in a lipid membrane. In addition, HMDS plays the role of a passivation layer preventing the corrosion of ZnO [25] in NaCl medium. Figure 2 shows the complete synthesis methods. The membrane ionic transport and selectivity of NaCl, before and after gA confinement, has been studied and is discussed based on the Michaelis-Menten model of ionic co-transport.

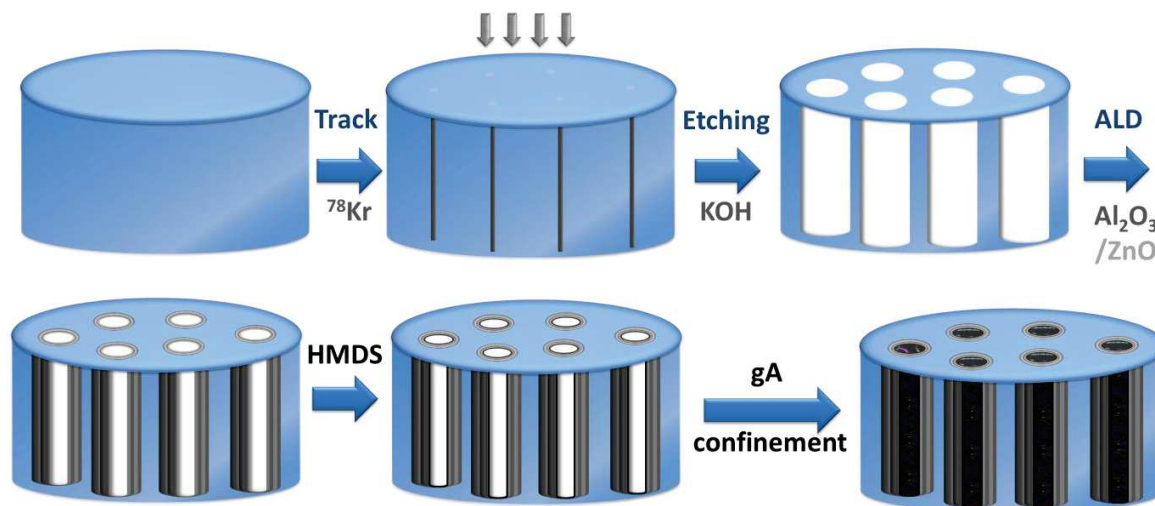


Figure2. Schematic process for hybrid membrane synthesis

4.1. Track etching technique

Nuclepore Corp which is now a division of Whatman, Inc was the first to develop the track etching technique[26]. A dense polymer film will pass through two preparation steps to give the final porous membrane.

- Step 1: irradiation of polymer film with charged particles from nuclear reactor or other radiation sources. The irradiation step leaves behind it a sensitized/damaged track on the polymer film.
- Step 2: irradiated film will be dropped into an etching bath which etches the polymer preferentially along the sensitized nucleation tracks to form pores.

Pore density is directly related to the irradiation time (more time leads to more incident charged particles). Pore diameter is directly related to the etching time.

Our Poly(ethyleneterephthalate) PET nanopore membrane has been synthesized by krypton irradiation of the PET film positioned on the trajectory of a diffracted $^{78}\text{krypton}$ ion(9.5MeV) beam in GANIL (Caen,France).A detector is set behind the film to count the number of ions crossing the film. When the number of counts (number of pores) is reached, we stop the beam so we can control the pore number down to 1 pore. In this work the pores number was fixed at 100 pores over an area of 1 mm^2 . After the Krypton irradiation, the tracked film is exposed to UV light (Fisher bioblock; VL215. MC, 312nm)for 24h in each side then the film will be immersed into a NaOH solution (3M) at 50°C . Pore size will be controlled by the NaOH immersion time. Finally the film was rinsed with demineralized water. PET membranes with a thickness of $5\text{ }\mu\text{m}$ have been used in this study.

4.2. Pores diameter estimation of PET track etched membrane

Due to the small pores diameter, we suggest to measure the pore diameter by conductive measurement. The average diameter pore size has been estimated by conductivity measurements at different NaCl concentrations (from 0.9 mM to 300 mM). The recordings of intensity/voltage (I/V) curve have been performed on potentiostat EG&G Princeton Applied Research (model 236A). These measurements used two Ag/AgCl electrodes (Tacussel), which have been prepared to have an asymmetrical potential less than 1 mV. The two compartments of the measurement cell have been separated by PET film containing ~ 100 nanopores (Table 1). Nanopores conductance (G) is directly given by the slope of the I/V curve. The both compartments have

been filled with 12 mL of saline solution at the same concentration from 0.9 to 300 mM. The current has been recorded for a voltage ramp between -250 mV and 250 mV with a step of 5 mV.s⁻¹. The conductance G corresponds to one pore for sake of comparison between the different membranes (nS.pore⁻¹). All experiments have been performed 3 times at 24±1°C. Figure 3 reports the conductivity evolution against the NaCl concentration.

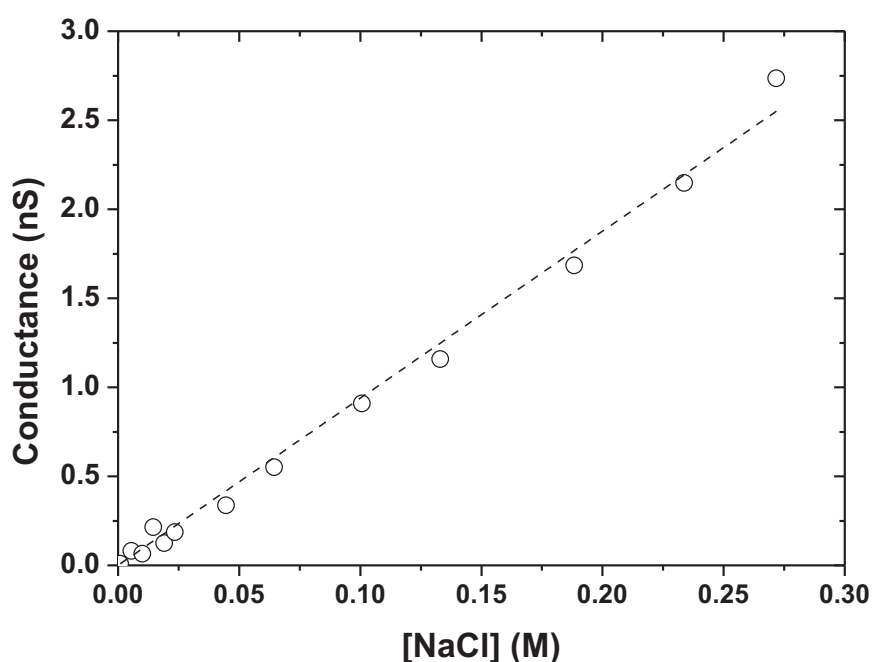


Figure 3. Conductance of nanopores as a function of NaCl concentrations

As shown in Figure 3, the conductance increases linearly with the NaCl concentration. Using equation 1, the pore size has been estimated to be around 36 nm.

$$G = \sigma K \quad (\text{Equation 1})$$

G is the conductance, σ is the solution conductivity and $\kappa = S/L$ (S =pore section area; L = pore length).

4.3. Tuning the Nanopore diameter using ALD

Pores size of track etched PET membrane has been tuned by Atomic Layer Deposition of Al_2O_3 , ZnO and nanolaminates of $\text{Al}_2\text{O}_3/\text{ZnO}$ using alternating exposure of TMA(as precursor 1;P1) and Water (as precursor 2;P2) for Al_2O_3 deposition and DEZ(P1) and Water (P2) for ZnO deposition. Due to high aspect ratio of the PET porous membrane and in order to assure a conformal coating along the pore, the ALD setup has been modified. Purge time has been raised to assure a complete evacuation inside the nanopore. All the ALD deposition on the PET track etched membrane has been carried at 60 °C. Table 1 shows the ALD deposition setup used for the tuning process of the PET porous membrane.

Table1. Setup used for the ALD deposition of PET track etched membranes

	P1 Pulse	Exposure	Purge	P2 Pulse	Exposure	Purge
Al_2O_3	0.1	20	40	2	30	60
ZnO	0.2	20	40	2	30	60

Precursor's pulses have been carried with 25 sccm dry argon flux as gas vector. The purge steps have been carried with 100 sccm dry argon flux as well. We should note before starting the ALD process that the chemical etching of PET induces the formation of carboxyl groups on the surface of the film and on the surface of nanopores walls[27, 28]which provides actives sites for the conformal coating by atomic layer deposition (ALD)[29].

Our perspective is to control PET pore size using the ALD technique with conserving the flexible properties of PET membrane. We started our study by reducing the PET pore size using Al_2O_3 ALD deposition. After the ALD deposition, the PET membrane was brittle and difficult to handle. Switching to the ZnO ALD deposition, a non-flexible membrane, hard to handle is as well obtained. A study performed by Raghavanet *al.* [30]on $\text{Al}_2\text{O}_3/\text{ZnO}$ nanolaminates synthesized by ALD reports asofter and more compliant response of the multilayers as compared to the single layers of Al_2O_3 and ZnO. These results have been attributed to the structural change from nanocrystalline to amorphous at smaller bilayer thicknesses. This study reports also a decrease of the elastic modulus when the bilayer thicknesses decrease due to a transition from a crystalline to an amorphous phase. The $\text{Al}_2\text{O}_3/\text{ZnO}$ nanolaminates have been used to control the

diameter of the PET membrane. After the ALD deposition, hydrophilic surface due to the OH terminal on ZnO[30, 31] was converted to a hydrophobic ((CH₃)₃Si-) surface terminal by ahexamethyldisilazane (HMDS) vapor exposure for 24 hours.

4.4. Structural and chemical characterization

During the ALD deposition on porous PET samples, silicon substrates, non porous PET and track etched PC membranes have been added for characterization issues. The bilayer chemical composition was analyzed by EDX (Hitachi 4500 coupled with a TermofisherEDX detector). Bilayer thickness inside the nanopore was measured by SAXS (XenocsGenX equipped with a molybdenum anode and a MAR2300 2D imaging plate detector). In order to assure a conformal coating inside the nanopore, TEM measurement has been also performed. AFM measurements (AFM NANOMAN 5 from Veeco instrument controlled with a Nanoscope V software) were performed to obtain the roughness of the surface. XPS measurement has been realized using (ESCALAB250 Thermo Electron) and the Contact angle measurement (GBX - Digidrop, Romans, France) has been performed by applying a water droplet of 2.3 μ L to the surface. The contact angle was calculated using computerized image analysis.

4.4.1. Energy dispersive X ray

Chemical composition was investigated using EDX on 35 repetitions of 5 cycles Al₂O₃/ 5cycles ZnO deposited on PET membrane. EDX measurement (Figure 4) shows as expected the presence of Zn, Al and O.

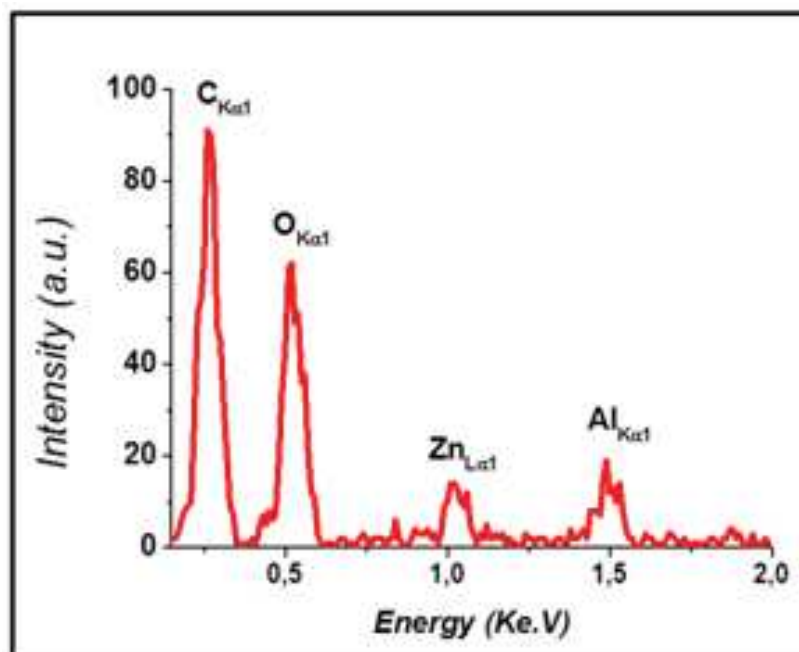


Figure 4. EDX measurement of 35 repetitions of 5 cycles ZnO/5 cycles Al₂O₃ nanolaminates deposited on PET membrane

4.4.2. SAXS measurements

SAXS profiles have been performed on 35 sequences of 5 cycles Al₂O₃/5 cycles ZnO deposited on PC track etched membrane (Whatman-Nuclepore, with pores diameter of 200 nm and a density of 7.10^8 pore cm⁻²) before and after HMDS coating (Figure 5; curves were arbitrarily shifted for clarity). SAXS measurements were performed on PC membrane due to the high material quantity needed for this type of measurements.

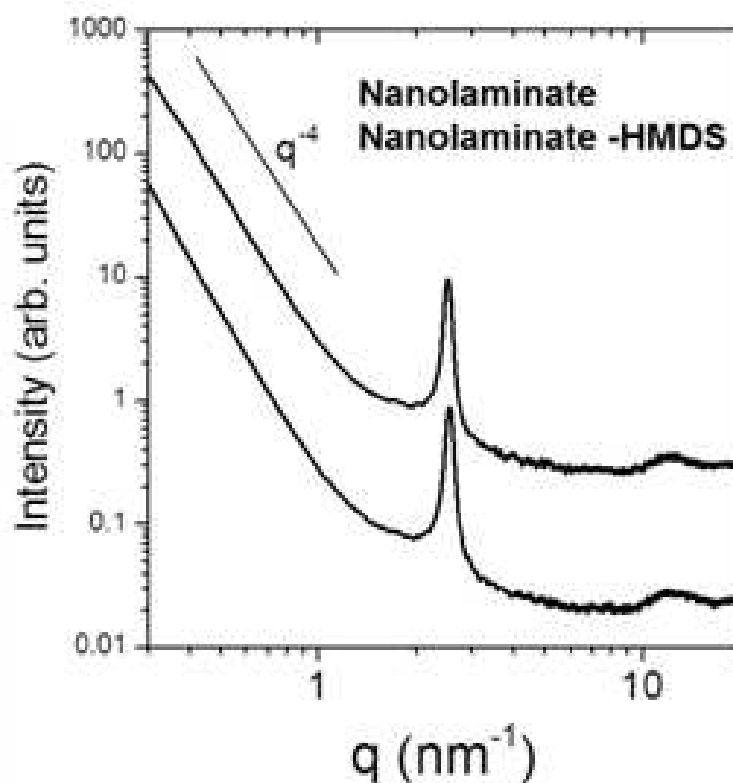


Figure 5. Profiles obtained on PC track etched membrane after 35 sequences of 5 cycles Al_2O_3 /5 cycles ZnO, before and after HMDS coating (curves were arbitrarily shifted for clarity)

SAXS profile presents 2 main features:

- A structure peak at $q = 2.53 \text{ nm}^{-1}$ corresponding to a characteristic distance of 2.48 nm in the real space. This distance corresponds to the width of a double-layer deposited by ALD.
- A q^{-4} slope is observed in the low q region, characteristic of a sharp interface between the air in pores and the layers deposited by ALD [32, 33]. This proves the quality of the deposition in terms of width control and homogeneity.

After HMDS grafting of the sample, the SAXS profile (Figure 5) appears unchanged in the q vector range accessible by our experimental setup. This is the proof that this grafting did not affect the quality of the ALD coating.

4.4.3. Transmission electron microscopy measurement

TEM microscopy has been performed on multipores PET membrane (average pores diameter 70 nm) with 12 sequences of 5 cycles Al_2O_3 /5 cycles ZnO deposited by ALD and followed by the elimination of the PET membrane by dissolving using chloroform. Figure 6 shows the TEM image of single nanopore of ~ 10 nm inner diameter.

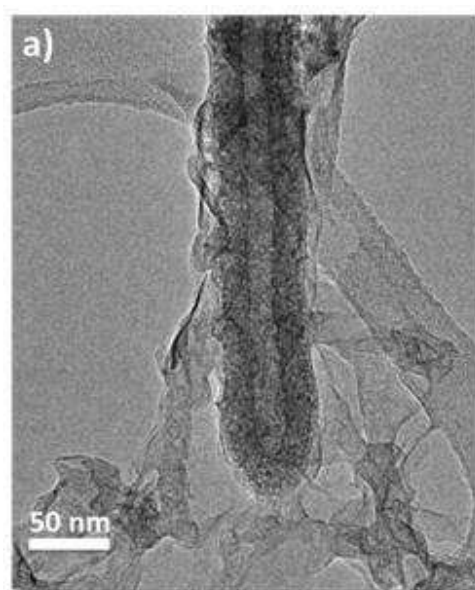


Figure 6. TEM image of single nanopore of ~ 10 nm inner diameter

Figure 6 shows the homogeneous coating induced by ALD technique inside the $13\ \mu\text{m}$ length nanopore with an outer diameter of 70 nm corresponding to the membrane average pore diameter and an inner diameter of 10 nm after the ALD coating.

4.4.4. AFM measurement

AFM measurement was performed on 3 samples; the first one is 20 cycles Al_2O_3 , the second one is 20 cycles ZnO and the third one is 2 repetitions of 5 cycles Al_2O_3 /5 cycles ZnO. All films were performed on Si substrate in order to evaluate the roughness of the surface. Table 2 reports the AFM roughness measurements.

Table 2. AFM roughness measurement

ALD	AFM roughness (Ra) (nm)
20 cycles Al_2O_3	0.34
20 cycles ZnO	0.32
2 repetitions of 5 cycles Al_2O_3 / 5cycles ZnO/Si substrate	0.25

AFM measurement performed on thin film deposited on Si substrate shows that the roughness of the nanolaminates ($R_q = 0.25$) decreases significantly comparing to single layer of ZnO ($R_q = 0.34$) and Al_2O_3 ($R_q = 0.32$). This could be related to the amorphous nature of the ZnO/ Al_2O_3 nanolaminates as showed in chapter 2 and chapter 4.

4.4.5. XPS measurements

In order to assure the CH_3 grafting after the HMDS exposure, XPS measurements was performed on PET membrane with 3 bilayers of 5 cycles Al_2O_3 / 5cycles ZnO before and after the HMDS vapor exposure step. Table 3 and table 4 report respectively the XPS Measurements before and after the HMDS exposure step.

Table 3. XPS measurement on PET membrane covered with 3 bilayers of 5 cycles Al_2O_3 / 5cycles ZnO

Name	Peak BE	Height Counts	FWHM eV	Area (P) CPS.eV	Area (N)	At. %	Q
Al2p	73.83	2921.12	1.43	4446.39	0.19	11.96	1
C1s	284.82	9118.87	1.13	14606.54	0.34	21.40	1
O1s	531.32	37845.89	2.33	90833.00	0.74	46.76	1
Zn2p3	1021.56	117034.65	1.61	213266.32	0.31	19.88	1

Table 4. XPS measurement on PET membrane covered with 3 bilayers of 5 cycles Al_2O_3 and 5 cycles ZnO treated with HMDS.

<i>Name</i>	<i>Peak BE</i>	<i>Height Counts</i>	<i>FWHM eV</i>	<i>Area (P) CPS.eV</i>	<i>Area (N)</i>	<i>At. %</i>	<i>Q</i>
Al2p	74.01	2460.77	1.45	3867.09	0.16	11.42	1
Si2p	100.38	404.69	1.50	666.70	0.02	1.30	1
C1s E	283.20	801.51	1.22	1059.86	0.02	1.70	1
C1s A	284.77	9619.08	1.17	12224.05	0.28	19.67	1
C1s B	286.37	573.88	1.28	796.35	0.02	1.28	1
C1s C	288.72	816.57	1.21	1069.60	0.02	1.72	1
C1s D	289.75	755.76	1.23	1009.32	0.02	1.62	1
O1s A	530.36	13152.76	1.56	22212.29	0.18	12.56	1
O1s B	531.67	30823.88	1.61	53758.91	0.44	30.39	1
O1s C	533.38	610.50	1.36	896.28	0.01	0.51	1
Zn2p3	1021.66	91559.88	1.65	174181.21	0.26	17.83	1

The success of the grafting has been attested by XPS measurement (Table 3 and Table 4). Silicon in low content was detected (Si 2p binding energies 100.38 eV) that corresponds to Si-CH₃ bond[34]. The last attribution is confirmed by the binding energies (283.20 eV) measured for the carbon element (C 1s)[34].

4.4.6. Contact angle measurements

In order to confirm the hydrophobicity achieved by the HMDS treatment, contact angle measurement was performed on 3 bilayers of 5 cycles Al_2O_3 / 5cycles ZnO deposited on PET film (Figure7). A contact angle of 92° on the treated HMDS surface confirms the surface hydrophobicity.

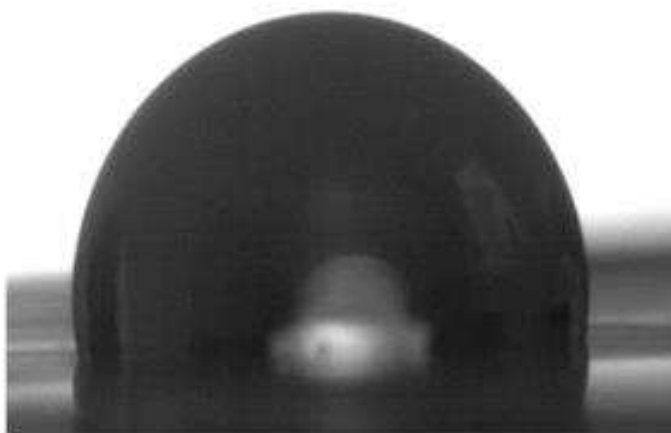


Figure 7. Contact angle of a water droplet on 3 bilayers of 5 cycles Al_2O_3 / 5cycles ZnO deposited on PET film after HMDS treatment

After this chemical and structural characterization of the $\text{Al}_2\text{O}_3/\text{ZnO}$ nanolaminates in term of roughness, bilayer thickness, pore diameter estimation by conductivity measurements and the confirmation of the CH_3 group grafting that assure a hydrophobic surface, three different ALD sequences have been performed on porous PET films and then functionalized by HMDS and finally confined with gramicidin A. Table 5 reports the PET membrane parameters before and after the ALD deposition and the HMDS grafting.

Table 5. Three different ALD sequences performed on PET track etched membranes

Nanopore	Initial pore diameter	Bilayers numbers	ALD Layer	Calculated mean pore diameter after HMDS grafting (nm)	Pore length (μm)	Pore number
NP_1	36	5	12.4	10.6	5	104
NP_2	36	6	14.9	5.7	5	114
NP_3	36	7	17.3	~ 1	5	106

4.4.7. Conductance measurements on ALD modified PET Membranes.

Conductance measurements have been performed on the 3 samples mentioned before in Table 4. The same measurements setup mentioned in section 3.2 has been used. Figure 8 reports the evolution of the conductance against the NaCl concentration for those 3 samples reported on Table 5.

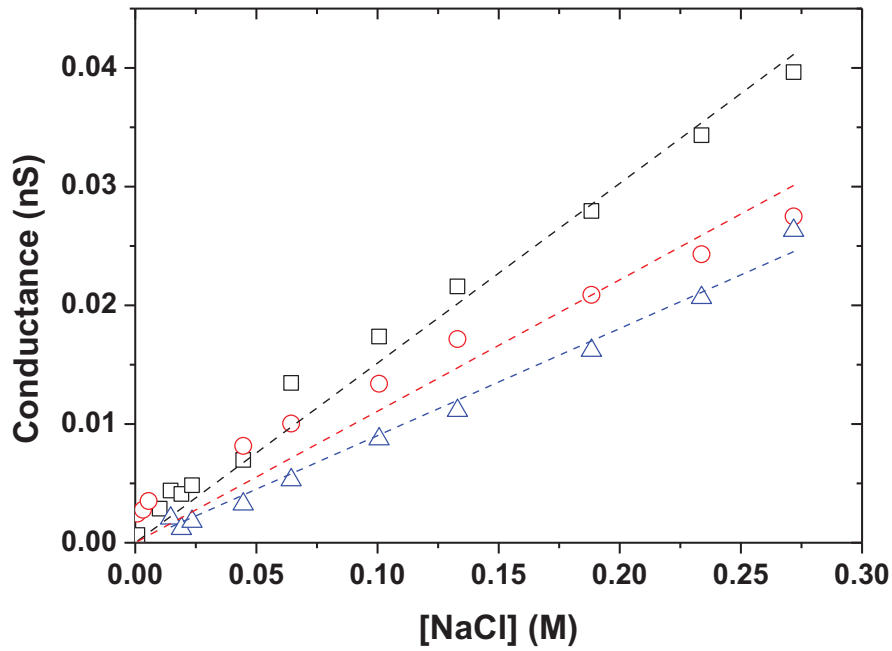


Figure 8. Evolution of conductance as the function of NaCl concentration for nanopore diameter 10.6 nm (black square), 5.7nm (red circle) and ~1 nm (blue triangle)

Based on Equation1 and the conductance measurement, the experimental length κ_{exp} has been calculated and reported on Table 6. Theoretical length κ_{th} has been also calculated based on Table 4 and Equation 2 and reported on Table 6.

$$k_{th} = \frac{S_{\text{calculated}}}{L} \quad (\text{Equation2})$$

Where $S_{\text{calculated}}$ is the pore section area based on the calculated mean pore diameter after HMDS grafting from the SAXS measurements (Table4) and L is the pore length.

Table 6. Theoretical and experimental length of NP₁, NP₂ and NP₃

Nanopore	κ_{exp} (pm)	κ_{th} (pm)
NP ₁	11.95	19.8
NP ₂	8.781	6.2
NP ₃	7.120	0.26

As shown in Table 6, the larger pores (NP₁ and NP₂) are in the expected order of magnitude of the pore dimensions. However it deviates significantly for the pore NP₃ where the measured conductance was much higher than expected one. In this range of pore radius, confinement of electrolytes could induce large departure of conductivity from the bulk value. Moreover, roughness of the walls could also be an important parameter. The roughness of surface due to ALD deposition is 0.25 nm which is not negligible in regard to the mean radius ~ 0.5 nm.

4.5. Gramicidin A confinement

gA confinement throughout PET nanopore reduced by ALD and coated by HMDS has been performed as follows: the gA solution was prepared by mixing 10 mL of pure water and 10 μ L of methanolic gA solution (10^{-4} M). The membrane was impregnated with the solution during 72 h at 6 °C. gA characterization inside ~ 100 pores membranes cannot be performed by usual techniques such as circular dichroism and FTIR due to the too small amounts of confined gA. The proof of gA confinement was obtained by electrical measurement. Two types of experiments were carried out with gA-loaded PET membranes separating the two compartments:

- First type: the analysis of transfer of sodium chloride through the membrane by diffusion under a concentration gradient was performed to determine the selectivity of confined gA via the inversion potential.
- Second type: the analysis of current intensity as a function of voltage (I/V) with the same salt concentration in the two compartments was carried out as a function of NaCl concentration.

4.5.1 Sodium chloride transfer through the membrane by diffusion under a concentration gradient

Gramicidin A loaded PET Membrane has been fixed between 2 compartments filled with asymmetric NaCl solutions:

- The first compartment (in) was filled with a 250 mM Sodium chloride solution.
- The second one (out) was filled with a 0.9 mM sodium chloride solution.

Due to this sodium chloride concentration gradient with the non-presence of a current field, the average transport of electrolyte through the membrane will be unidirectional. The different interactions of sodium cation and chloride anion with the inner pores lead to different mobilities of the ions. In order to obtain the gA loaded PET membrane ion selectivity, the voltage E_0 has been measured at $I = 0$ A. Measurements have been recorded with EPC800 patch clamp amplifier (HEKA). The reversed potential E_{rev} which is the potential caused by the ions transfer mechanism was calculated according to the Equation 3.

$$E_0 = E_{rev} + \Delta E_p \quad \text{(Equation 3)}$$

Where E_0 is the measured voltage and ΔE_p is the junction potential induced by the difference of salt concentration between both compartments of the measurement cell, calculated according to equation 4. In the present case the junction potential can be obtained by calculation because the zero of patch-clamp experiment is adjusted using a PET film without nanopore [35].

$$\Delta E_p = \frac{RT}{F} \frac{(\mu_+ - \mu_-)}{(\mu_+ + \mu_-)} \ln \frac{[NaCl]_i}{[NaCl]_o} \quad \text{(Equation 4)}$$

Where μ_- and μ_+ are the relative mobility of the anion and cation, respectively. R represents the gas constant; T is the temperature; and F is the Faraday constant.

The relative contribution of ions to the conductance is given by the ratio of their permeability coefficient P_{ion} . To obtain these relative permeations, data analyses have been performed using the Goldman-Hodgkin-Katz [36] (Equation 5).

$$E_{rev} = \frac{RT}{F} \ln \frac{\frac{P_{Na}}{P_{Cl}} [Na^+]_i + [Cl^-]_o}{\frac{P_{Na}}{P_{Cl}} [Na^+]_o + [Cl^-]_i} \quad \text{(Equation 5)}$$

Where P_X is the permeation of ion X, and $[X]_{i/o}$ represents X ion concentration inside the “in” and the “out” compartments, respectively ($X = Na^+$ or Cl^-). The permeability ratio P_{Na^+}/P_{Cl^-} has been calculated using equation 3, 4 and 5 on the NP1, NP2 and NP3 membranes loaded with gramicidin A. Values are reported in table 7 then plotted against pore size in Figure 9.

Table 7. Permeability ratio of P_{Na^+} / P_{Cl^-} of the NP1 NP2 and NP3 membranes loaded with gramicidin A

Membrane	P_{Na^+} / P_{Cl^-}
NP1	0.027
NP2	0.382
NP3	0.785

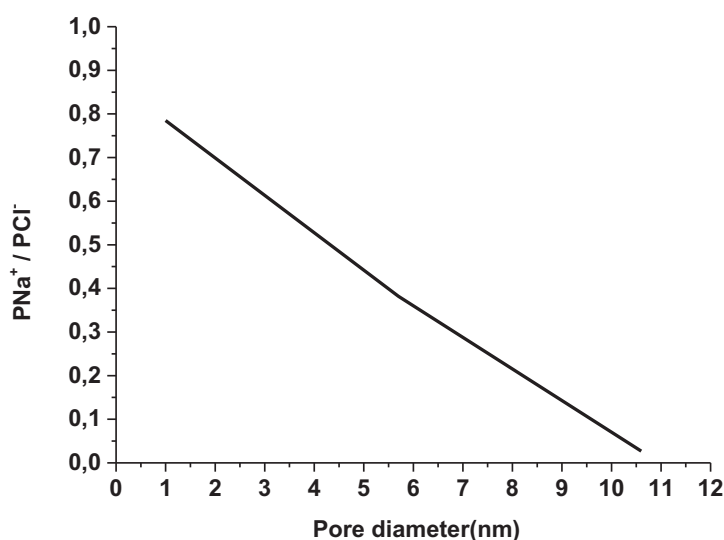


Figure 9. Permeability ratio evolution against pores size

As shown in Table 7, all membranes permeability ratio P_{Na^+} / P_{Cl^-} are < 1 . It means that confined gA exhibits a better permeability to chlorine anion than to sodium cation. As shown in Figure 9, the smaller is the pore diameter, the higher is the permeability ratio, which suggests that increasing confinement favors the cation mobility. However, the higher value corresponds to a higher permeability of the anion, contrary to the selectivity of the channel in biological membranes. In such membranes, the ionic transport properties through gA are strongly dependent on its structure. Firstly, the cationic permeation is affected by different helical

structures which gA can adopt depending on the phospholipid composition of the membranes[37]. Secondly the impermeability to Cl⁻ is due to the change in the hydration state near head-head connection of two gAs and in the β -helix structure.[38, 39] It is very likely that, when gA is confined inside thenanopore, the dimer assembly broken in solution is not recovered therefore inducing the permeability of Cl⁻. This result is in accordance with the work performed by balmeet *al.*[23] where gA has been confined inside commercial polycarbonate track-etched membrane (diameter 15 nm).

4.5.2. Sodium chloride transfer through the membrane by diffusion under an applied voltage

Gramicidin A loaded PET membrane has been fixed between 2 compartments filled with symmetric NaCl solutions under an applied voltage between -250 mV and 250 mV in this case, the ionic transport through the membrane is bidirectional due to the applied voltage. The recordings of intensity/voltage (I/V) curve have been performed as well on potentiostat EG&G princeton applied research model 236A. These measurements used two Ag/AgCl electrodes (Tacussel), which have been prepared to have an asymmetry potential less than 1 mV. The current has been recorded for a voltage ramp between -250 mV and 250 mV with a step of 5 mV.s⁻¹. This experiment aimed to obtain information on transport kinetics of both Na⁺ and Cl⁻ ions. This experiment was also carried out as a function of the concentration in order to check any possible saturation as observed in biological channels. This type of measurements was carried out on the NP1, NP2 and NP3 membranes with and without gramicidin A confinement in a NaCl concentration range between 0.9 and 300 mM. Figure 10 reports an example of this measurements series on the NP1 and NP2 membrane with and without gramicidin A confinement with a NaCl concentration of (a) 10 mMol and (b) 100 mMol.

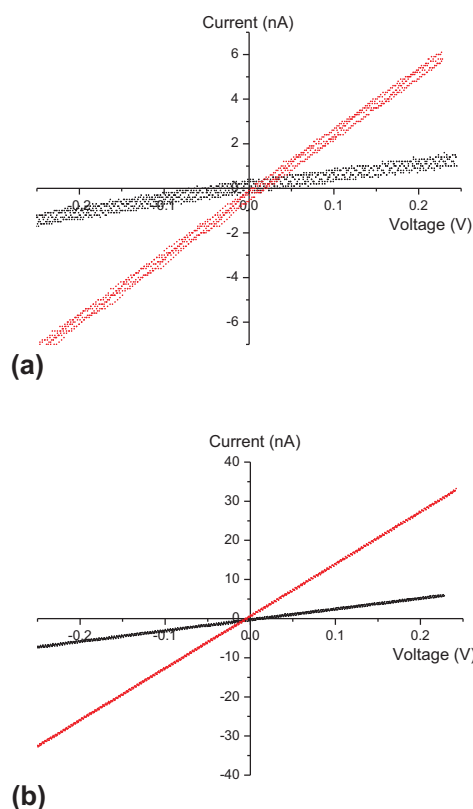
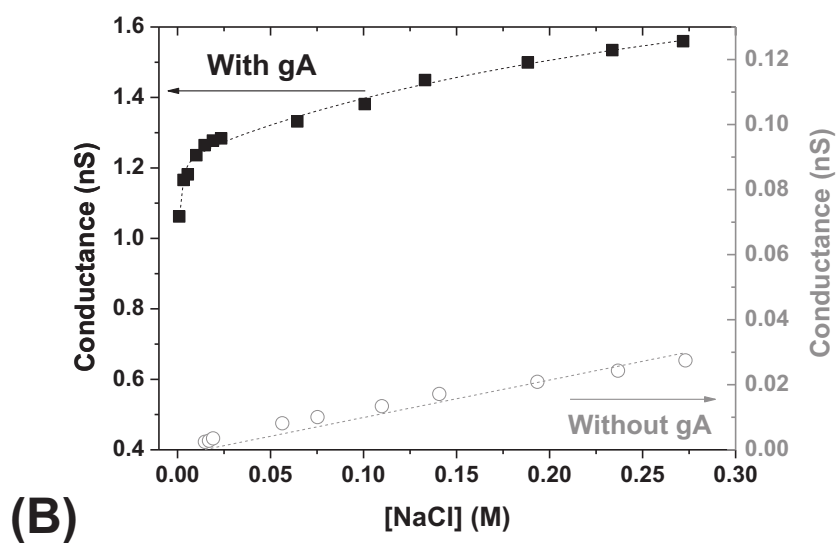
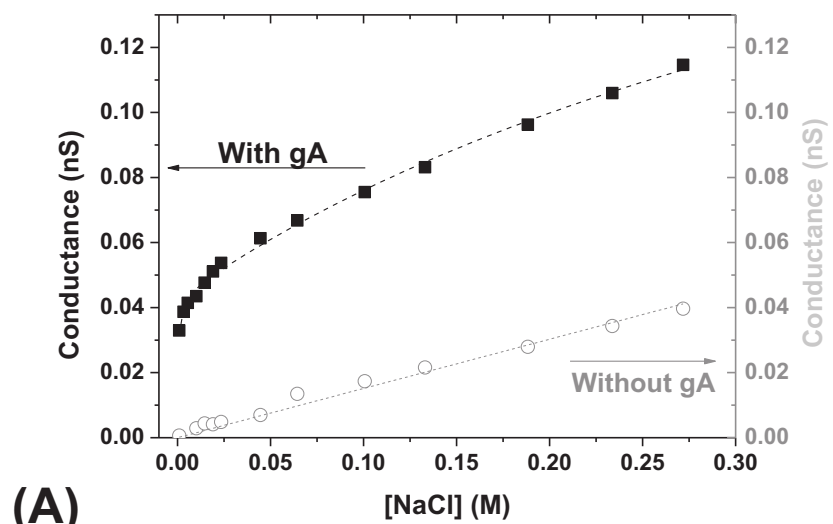


Figure 10. Examples of I/V curve obtained with (black) and without (red) gA confined in (a) NP₁ and (b) NP₂

As demonstrated in Figure 10, the measured I/V curves show a linear dependence between the applied voltage and the measured current. This linearity fits the ohmic law. This same type of measurements reported on Figure 9 was carried out with different NaCl concentration between 0.9 and 300 mM. Figure 11 reports the membrane conductance with and without gA confinement as a function of NaCl concentration.



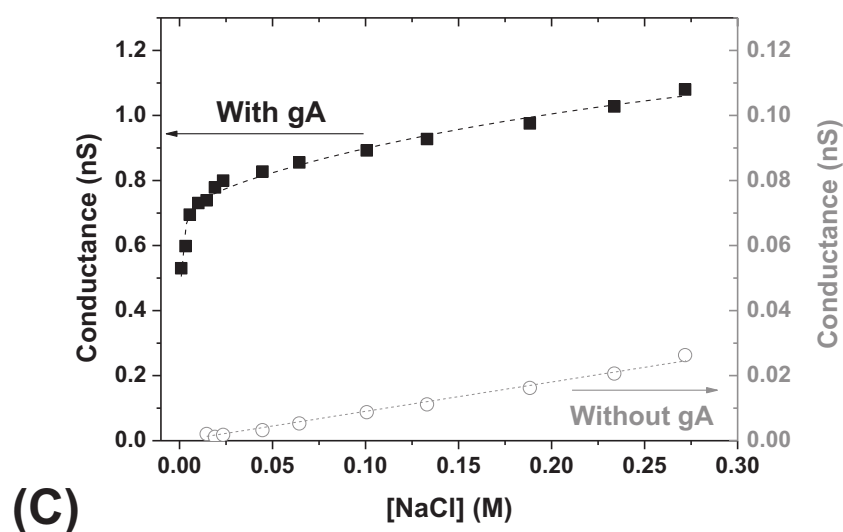


Figure 11. Evolution of nanopores conductance with and without confined gA under NaCl symmetrical concentration. (a) NP₁-gA (black square) and NP₁ (gray round), (b) NP₂-gA (black square) and NP₂ (gray round), and (c) NP₃-gA (black square) and NP₃ (gray round)

As shown in Figure 11, the membrane conductance without gA confinement as a function of NaCl concentration increases linearly with a small slope. Contrary the membrane conductance with gA as a function of NaCl concentration exhibits two regimes (Figure 11):

- A large steep increase at low concentration
- A smaller steep increase at high concentration

Even in the range of high concentrations, the variation is still one order of magnitude larger than without gA (Figure 11). It is clearly shown on Figure 11 that the conductance in the low concentration domain is several orders of magnitude larger than the conductance in high concentration domains. This suggests that the gA has specific functions for enhancing the transport of ions with respect to bulk concentration.

The nonlinear increase of the conductance with the concentration for the gA loaded PET membrane shown in Figure 11 is similar to the behavior observed for biological ionic channels including gramicidin A [16, 40]. This nonlinear increase of the conductance with the

concentration is described for single ion by a kinetic model involving the Michaelis-Menten equation (Equation 6).

$$G(c) = g_{Max} \frac{c}{K_M + c} \quad \text{(Equation 6)}$$

Where $G(C)$ is the nanoporeconductance, C is the ion concentration of the bulk solution, G_{Max} is the saturation conductivity (the maximum reached conductivity) and K_M is the Michaelis constant which is referred to the dissociation constant in the equilibrium theory. This model assumes that ionic channel is selective to only one electrolyte and the conductance reaches an asymptotic value G_{Max} where all ionic channel sites are occupied.

The present system is not as simple as such, because the transport of the two ions exists and two types of populations for each ion are likely as ion pathways outside the gramicidin channels cannot be excluded. Considering this, we extended the model to Na^+ and Cl^- co-transport, where ionic pore conductance can be described as the sum of both cation and anion conductance through confined $gA(G_{gA})$ and a conductance outside $gA (G_{out})$ (Equation 7).

$$G_T = (G_{Na^+} + G_{Cl^-}) g_A + G_{out} \quad \text{(Equation 7)}$$

Assuming that, at the entrance, each electrolyte should be assimilated to single-ion occupancy inside gA , it is possible to combine equations 6 and 7 that give the conductance in our case (Equation 8).

$$G_T = \frac{g_{Max(Na^+)}[Na^+]}{K_M(Na^+) + [Na^+]} + \frac{g_{Max(Cl^-)}[Cl^-]}{K_M(Cl^-) + [Cl^-]} + \lambda_{out}[NaCl] \quad \text{(Equation 8)}$$

Experimental data has been fitted by this model and parameters are reported in Table 8. Regarding the anionic behavior demonstrated without electric field $P_{Na^+} / P_{Cl^-} < 1$, and the same dependency between G_{ion} and P_{ion} [41], the values of fitted parameters (g_{Max} and K_M) can be assigned in such a way that $G_{Cl^-} > G_{Na^+}$.

Table 8. Permeation ratio and conductivity experiments of nanopores confined gA

Pore Size	$g_{Max}(Na^+)$ (nS)	$K_M(Na^+)$ (M)	$g_{Max}(Cl^-)$ (nS)	$K_M(Cl^-)$ (M)	λ_{out} (nS.M ⁻¹)	r^2	P_{Na}/P_{Cl}
NP ₁ -gA	0.02	0.018	0.03	$0.978 \cdot 10^{-4}$	0.21	0.99	0.027
NP ₂ -gA	0.77	0.360	1.23	$1.58 \cdot 10^{-4}$	0.00	0.99	0.382
NP ₃ -gA	0.75	0.370	0.74	$4.40 \cdot 10^{-4}$	0.00	0.98	0.785

Table 8 shows that parameter λ_{out} which presents the conductance outside gA is equal to zero excepted for NP₁-gA which is the PET membrane with a calculated average pores diameter of 10.6 (Table 5). In addition, the NP₁-gA conductance is lower than the NP₂-gA and NP₃-gA ones. This result suggests the increasing of the relative contribution of the ion transport through gramicidin when the pore size becomes very small. The value λ_{out} (0.21 nS.M⁻¹) obtained for NP₁ is on the same order of magnitude than in the absence of gramicidin (0.15 nS.M⁻¹), suggesting a bulk-like ionic environment, gramicidin excluded. The lack of G_{out} for both nP₂-gA and nP₃-gA shows that electrolyte transport occurs mainly through gramicidin and that conductance outside gA can be considered as negligible. It means that ions are docked inside gA sites, and thus it suggests an organization in β -helix gA structure, at least partially, such as in biological conditions. [42]

4.6. Molecular Dynamic simulation

From the theoretical point of view, to have an insight on the structural arrangement of the confined proteins, we have performed, using the same protocol and parameters than previously described by Wallace *et al.* [18], dynamic molecular simulations of gA inside hydrophobic nanopores (diameters 2 nm to 7.5 nm) modeled here by an assembly of carbon atoms that mimics the experimental pore (Figure 12). Molecular simulation has been performed by Sebastian Kraszewski and Fabien Picaud in the Centre Hospitalier Universitaire de Besançon.

The full atomistic molecular dynamics (MD) simulations were performed using NAMD 2.7b2 software [43]. To encapsulate the proteins in the pore of different diameters, constant temperature of 300 K (Langevin dynamics) and constant pressure of 1 atm (using the Langevin piston Nosé–Hoover method [44]) were used to recover experimental conditions. We calculated

the short- and the long-range forces every 1 and 2 time steps, respectively, with a time step of 2.0 fs. To evaluate the long-range electrostatic forces, the classical particle mesh Ewald (PME) method [45] was used, while chemical bonds between hydrogen and heavy atoms were constrained to their equilibrium value. All systems (ions, water, membrane, gA) were modeled using the CHARMM27 [46] force field. For water molecules, we applied the commonly used TIP3P model. No charge was attributed to the nanopore carbon atoms. For nanopore carbons (C-C) or nanopore carbon vs water oxygen (C-O) interactions, we used the Bedrov *et al.* [47, 48] Lennard-Jones potential parameters (CHARMM27 functional: $\sigma_{CC} = 3.895 \text{ \AA}$, $\epsilon_{CC} = 0.066 \text{ kcal mol}^{-1}$ and $\sigma_{CO} = 3.58 \text{ \AA}$, $\epsilon_{CO} = 0.0936 \text{ kcal mol}^{-1}$). For the proteins, only the monomeric gA conformation (PDB code: 1JNO) was used, corresponding to the equilibrium geometry adopted in the water solvent [49]. The gA monomers were first pre-equilibrated for at least 5 ns and then were extracted and inserted into the suitable simulation box containing the nanopore and the solvent, as described below. To accelerate the calculations and prove the influence of the pore diameter on the protein structural arrangement, we choose arbitrarily to mimic the experimental nanopore by either (i) a (16, 16) (pore diameter 2.1 nm) nor (ii) a (55, 55) (pore diameter 7.5 nm), carbon nanotubes that present a very well-known geometry, contrarily to an experimental polycarbonate nanopore membrane and a hydrophobic character close to experimental conditions. All the simulated nanotubes presented a length of 5 nm, and the solvent was precisely composed of (i) 8017 water molecules, 15 Na^+ , and 15 Cl^- ions. The complete system (a total of 28 361 atoms, periodic box of $38 \times 38 \times 194 \text{ \AA}^3$) was progressively filled by 6 gAs monomers placed randomly in front of the nanopore (only one is shown for clarity in Figure 12a). The total simulation time is 294 ns. (ii) 30 564 water molecules, 18 Na^+ , and 18 Cl^- ions. The complete system (a total of 106 948 atoms, periodic box of $85 \times 85 \times 142 \text{ \AA}^3$) was progressively filled by 36 gA monomers placed randomly in front of the nanopore (Figure 12b). The total simulation time is 368 ns.

For 7.5 nm diameter pore size, the simulations show a gA confinement in two steps : (1) The first gAs are adsorbed on the nanopore surface and lose their helix structure, (2) the following gAs are located in the pore center and keep the helix structure but lose the head to head dimer structures. Here, the small gA concentration used experimentally leads to only partial filling of the pore centre for high nanopore diameter (Figure 12b), in accordance with the significant contribution of bulk-like domains in the total conductance (Table 8). For 2 nm

diameter pore size, the simulation shows that only one gA can occupy the pore with its saved helix structure in these high confining conditions (Figure 12a), in accordance with the negligible contribution of bulk-like domains in the total conductance deduced for the smaller pores (Table 8).

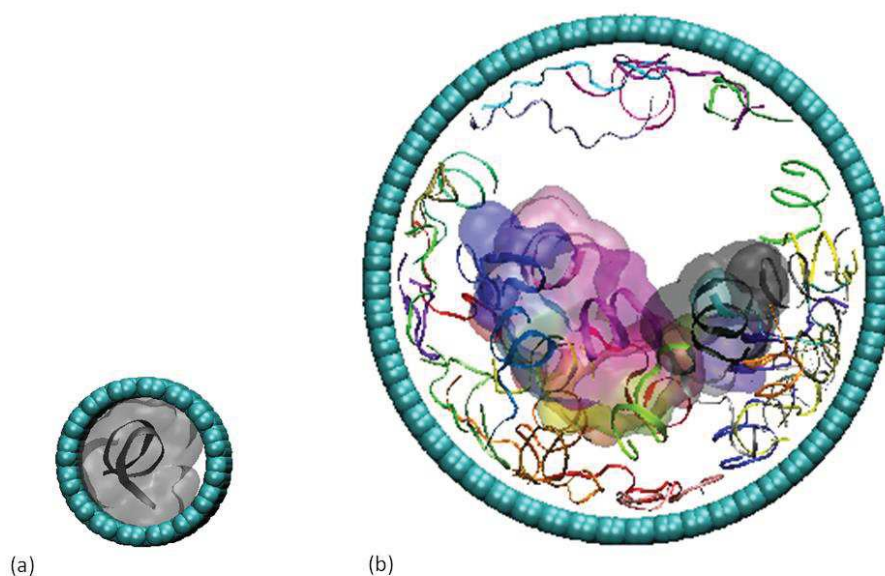


Figure 12. Snapshots of gA confinement inside a hydrophobic nanopore (blue circles) of diameter 2 nm(a) and 7.5 nm (b) obtained by dynamic molecular simulation (gA are shown in ribbon representation with its surface modeling when they are folded): a) 2 gAs have been incorporated inside the nanopore and stabilized during 20 ns (the second protein is not shown for clarity), and b) 36 gAs have been inserted progressively inside the pore during 270 ns. Some are unfolded principally on the pore wall while others keep their helix structure partially.

According to Equation 5, for a given NaCl concentration, the ratio G_{Na^+} / G_{Cl^-} is higher for NP₃-gA than for NP₂-gA, typically for NaCl bulk concentration of 250 mM (0.257 for nP₂-gA and 0.409 for nP₁-gA, respectively). These values differ slightly to those obtained with the ratio P_{Na^+} / P_{Cl^-} under dissymmetrical concentration, probably because of the difference in the experimental conditions. However, the increases of both ratios induced by the pore size reduction are similar (factor 1.6 under symmetrical conditions and factor 2.0 under

dissymmetrical conditions). If we focus on electrolyte transport inside gA, it can be noted that $K_M(\text{Cl}^-) < K_M(\text{Na}^+)$. This Michaelis constant can be associated to dissociation constants. We attributed the lowest value to the chloride ion based on the preceding experiment on diffusion under a concentration gradient, which revealed the affinity of gramicidin A for the chloride anion. However gA affinity with Cl^- decreases with nanopore diameter and thus it can be imagined to recover partially its selectivity properties for a hydrophobic pore diameter of 0.8 nm.

4.7. Conclusion on gA confinement inside tuned ALD nanopores

In conclusion, PET multipores synthesized by Track etching technique with an initial pore diameter of 36 nm has been tuned by atomic layer deposition of $\text{Al}_2\text{O}_3/\text{ZnO}$ nanolaminates to a sub 10 nm diameter. HMDS was then grafted on the surface in order to make it hydrophobic and to protect the ZnO layer from the Cl^- ions. Finally Gramicidin A was confined into the pores. The obtained biomimetic membranes keep their flexibility and have homogeneous nanopores with low roughness inside the pores. 3 different pores diameters were investigated (10.6, 5.7, ~2 nm). The resulting nanopores show a dominant anionic transport behavior explained by the loss of gA head-head dimer structure in the liquid solution. The conductance measurements reveal for the first time an enhanced of ionic transport mechanism through gA inside a polymeric solid-state nanopore as in biological membranes. However, the trend observed when decreasing the pore size might leave hopefully possibilities to transpose biological mechanisms of ionic transport when an ionic channel is directly confined inside a synthetic nanopore. Membrane with pores diameters less than 10 nm (5.7 and 2 nm) with gA confined into the nanopores show a NaCl ionic transport mechanism through a hybrid nanopore similar to the biological ones.

5. Experimental and simulation studies of unusual current blockade induced by translocation of small oxidized PEG through a single nanopore

Single nanopore technologies have different applications fields such as DNA detection[50, 51] and sequencing[52, 53], Polyethylene glycol (PEG) mass spectroscopy,[54, 55] nanoparticle detection[56, 57] and ionic separation[58, 59]. Among these technologies, molecular sensors based on single nanopores can be achieved using two strategies:

- The first strategy is inserting a biological channel inside the artificial phospholipid membrane [60]. This method has already been used successfully in PEG mass spectroscopy [54] and is presently developed for low cost DNA sequencing [51, 61]. However, the life time of such nanopores is limited due to the fragility of the lipid bilayers.
- The second strategy is based on the production of solid state nanopores with either low or high length/diameter ratio (*i.e.* low or high aspect ratio). The nanopores with low aspect ratio are produced by the Transmission Electron Microscopy (TEM) irradiation of silicon based thin films (typically Si_3N_4). The dimensions of such pores could be varied easily with diameters ranging from 5 nm to 300 nm and lengths ranging from 10 nm to 500 nm, which stimulated their extensive studies.[56]

The macromolecule discrimination is one of the applications of the nanopore technology. [54, 62] Typically, when a single macromolecule permeates through the nanopore, it induces a blockade of the background ionic current. The blockade event is characterized by the relative change of current intensity and the dwell time. Both observables are dependent on the macromolecule molar mass and the nanopore diameter. In this part of this chapter, we show that, in the case of single cylindrical nanopore with high aspect ratio (diameter 5 nm, length 13 μm) produced by track-etching and atomic layer deposition (ALD) techniques, small PEGs ($M_w = 200$ and 600 g.mol^{-1}) do not induce any blockade of ionic current. On the contrary, for oxidized PEG (noted PEG-carboxylate), an unexpected and unusual blockade of the current appears. It was shown that the characteristics of the blockade current depend on the PEG-carboxylate molar mass. Experimental results are also complemented by means of molecular dynamic simulations

of the model nanopore. An explanation of the unusual blockade of ionic current is proposed. Figure 13 shows the schematic representation of nanopore designed by atomic layer deposition and experimental setup of both carboxylate and neutral PEGs detection.

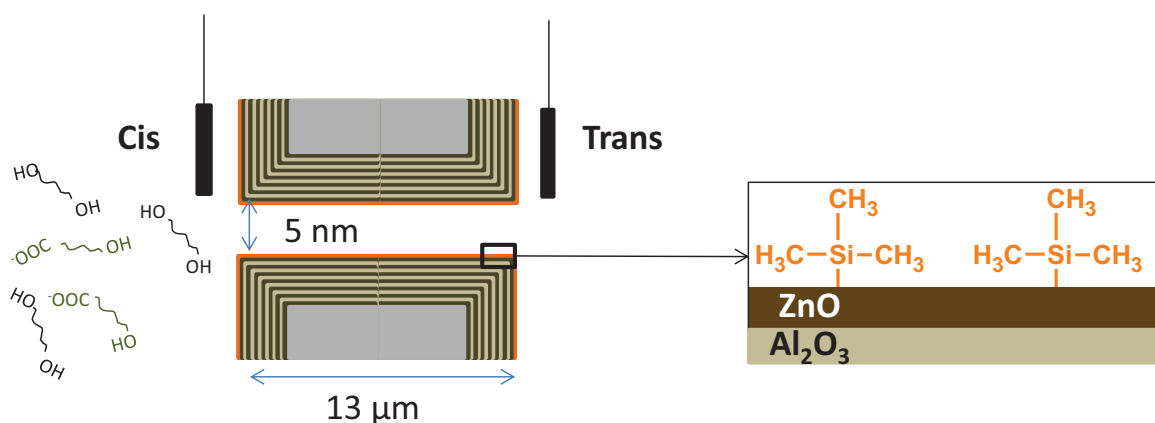


Figure 13. Schematic representation of nanopore designed by atomic layer deposition and experimental setup of both carboxylate and neutral PEGs detection

5.1. Nanopores synthesis and tuning

Single nanopore on poly(ethylene terephthalate) (PET) film with a thickness of 13 μm, a length of 24 cm and width of 4 cm has been synthesized by the track etching technique described in paragraph 3.1. The single nanopore diameter was around 20 nm. Different sequence numbers (1 to 14) of 5 cycles of Al₂O₃ followed by 5 cycles of ZnO were used to reduce the pore diameter to the sub-10 nm range using the ALD deposition setup mentioned before in paragraph 3.3. The average pores diameter after the ALD deposition was between 1 and 5 nm. After ALD deposition, all samples were functionalized by a 24 hours Hexamethyldisilazane (HMDS) vapor exposure at room temperature in order to obtain hydrophobic surfaces.

5.2. Ionic current recordings

Single nanopore was mounted between two chambers of conductivity Teflon tubes containing a NaCl solution ($\sigma \approx 80 \text{ mS.cm}^{-1}$) with a Concentration of NaCl $\approx 0.63 \text{ M}$. The current was measured between one Ag/AgCl electrode (XM410, Tacussel, France) in cis chamber and a

ground electrode (platinum, XM140, Tacussel, France) in trans chamber. The ion current was recorded by patch-clamp post amplifier (EPC800, HEKA electronics, Germany) using voltage clamp mode and a sampling frequency 25 KHz. Acquisition data were performed by Instrutech LIH 8+8 acquisition card (HEKA electronics, Germany) using a labmade routine on Igor Pro 6 (Wavemetrics, USA). A Lab-made analysis software (Matlab, Matworks, USA) was used to analyze the current data in terms of duration (Δt), depth (ΔI), relative depth ($\Delta I/I_0$) and the difference between the maximum and minimum of current (ΔI_{spike}) occurring over one translocation process. Recorded data was analyzed by balme group as described on annex A. Molecular Dynamics simulations was also performed and described on this work.

5.3. Conductance measurements

20 single nanopores membranes with a diameter close to 20 nm were synthesized and characterized. ALD deposition of $\text{Al}_2\text{O}_3/\text{ZnO}$ was performed in order to tune the pore size between 5 and 1 nm. Conductance measurements were performed on a 5 nm nanopore membrane with different NaCl concentration between 0.2 and 5M. Figure 14 shows the evolution of the conductance of a 5 nm diameter nanopore as a function of NaCl concentration.

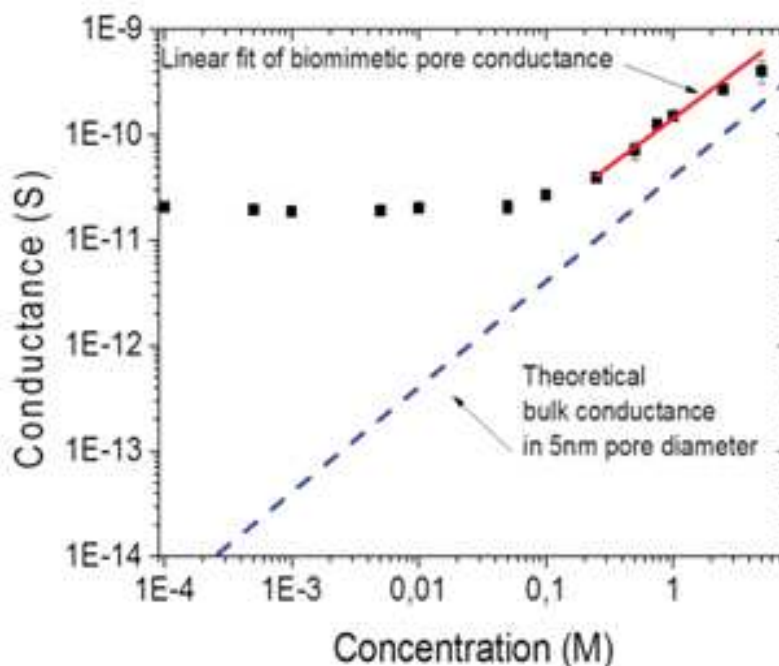


Figure 14. Evolution of the conductance of a 5 nm diameter nanopore as a function of NaCl concentration; black squares the experimental data, in dashed line the theoretical conductance assuming a bulk transport.

As shown in Figure 14, the NaCl conductance concentration dependence is not linear at low concentrations. This behavior is usually observed for charged membrane or nanoslit [63]. In this case, the ionic transport inside the nanopore is induced by two phenomena: (i) the surface transport charge and (ii) the bulk transport charge as described previously[63, 64]. Here the nanopore surface exhibits a zeta potential of -50 mV at pH 7 even if the trimethylsilane function is not charged and the surface is hydrophobic. This result is not surprising since ions can be adsorbed on hydrophobic surface depending on their polarisability, the ionic solution strength and/or the pH[65].

5.4. PEG detection

The translocation of both PEG_{Mw} and PEG_{Mw}-carboxylate ($M_w = 200$ and 600 g.mol^{-1}) from the cis compartment (Figure 13) at concentration 10^{15} and $10^{13} \text{ molecules.mL}^{-1}$ respectively, has been analyzed under 0.63 M NaCl solution, where the Debye length (0.75 nm) is smaller but of the same order of magnitude than the nanopore radius.

5.4.1. Neutral PEG detection

In order to detect the neutral PEG, a positive potential was applied to the cis chamber (compartment with $10^{15} \text{ molecules.mL}^{-1}$ PEG; Figure 13). Due to the prohibitive polarity of the applied voltage, PEG-carboxylates cannot translocate through the nanopore to be detected (Figure 15).



Figure 15. Typical current traces recorded for neutral PEG

As shown in Figure 15, no blockage current was detected. On the contrary, it has been already proven that PEG molecules could translocate through the nanopores[54, 66] as previously described by Robertson *et al.* in the case of single nanopore such as α -hemolysin,[54] or by Siwy *et al.* in the case of polymer conical nanopore[67]. In the latter case, PEG with M_w larger than 1000 g.mol^{-1} have been detected if its hydrodynamic radius was similar to the nanopore one. This contradiction was not surprising because the hydrodynamic radius of PEG is lower than the nanopore diameter and PEG molecules do not provide sufficient sterical blockage. The latter can be verified by estimating the current blockade using the model proposed by Stojilkovic *et al.*[68]. The ratio of conductance in the presence (σ) and in the absence (σ_0) of neutral PEG is equal to the ratio between the current (I) and the baseline current (I_0) at constant voltage[69]. It varies according to Equation 9:

$$\frac{\sigma}{\sigma_0} = \frac{I}{I_0} \cong (1 - \phi) e^{\left(-K \frac{\phi}{(1-\phi)}\right)} \quad \text{(Equation 9)}$$

Here, ϕ represents the polymer volume fraction which, for one molecule in the pore, can be estimated as $\phi \approx r_{\text{PEG}}^3 / (L r_{\text{pore}}^2) \approx 10^{-5}$ (L is the pore length, r_{PEG} (0.37 for PEG with $M_w=200 \text{ g.mol}^{-1}$ and 0.63 for PEG with $M_w=600 \text{ g.mol}^{-1}$) [70] and r_{pore} is the radii of the nanopore). K (≈ 2.7) is an experimental factor which depends on the PEG mass [68]. In our case, Equation 9 leads to $I/I_0 \approx 1 - \phi = 1 - 10^{-5}$. Thus the current blockade induced by the neutral PEG translocation is too small to be detected.

5.4.2. PEG-Carboxylate detection

In order to detect the charged PEG-carboxylate molecules, a negative potential was applied to the cis chamber. In the present case, the charged PEG-carboxylate molecules could enter the pore and we observed a blockade of ionic current between two characteristic spikes for all samples (Figure 16b and 16c).

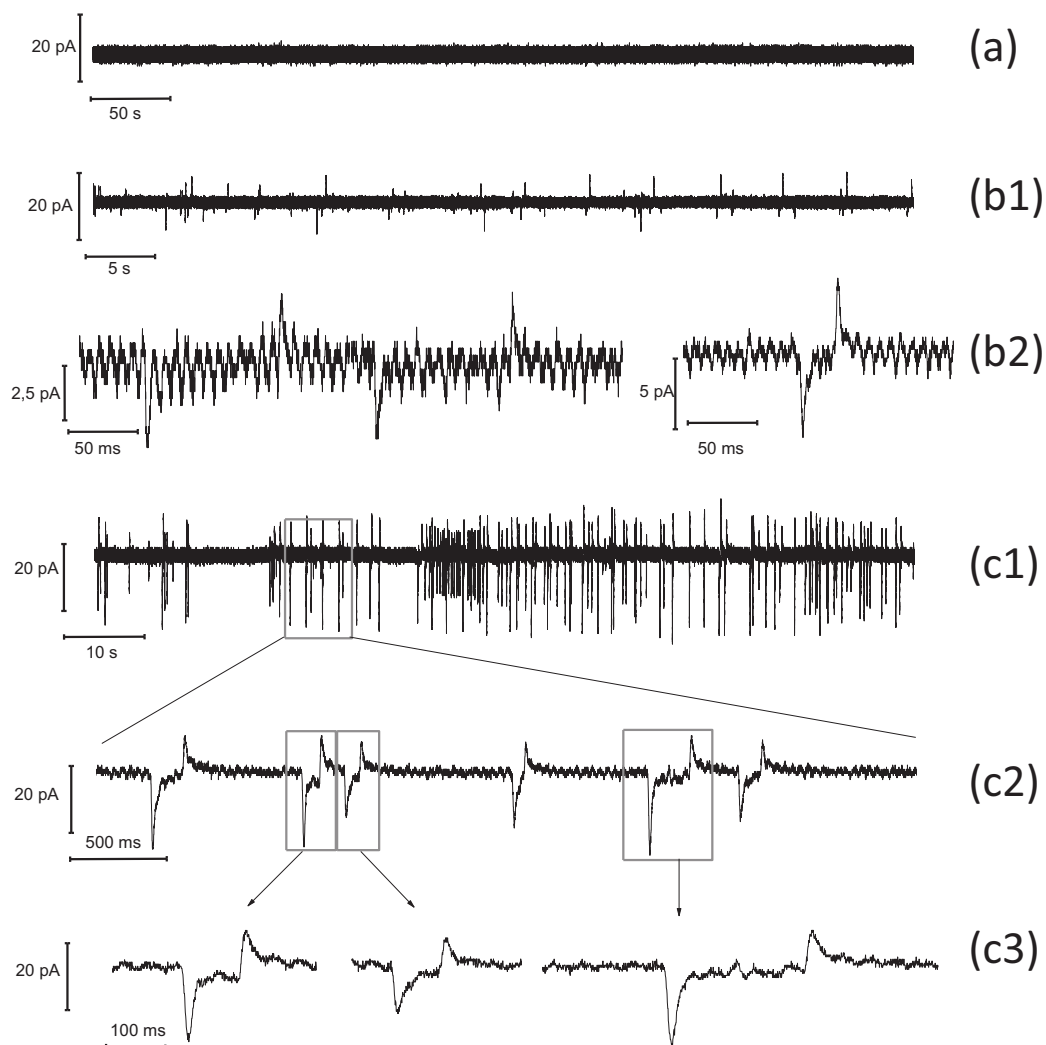


Figure 16. Typical current traces recorded for: (a) neutral PEG; (b1-2) PEG₂₀₀-carboxylate; (c1-3) PEG₆₀₀-carboxylate

Based on Equation 9 and the $I/I_0 \approx 1 - 10^{-5}$ value, this result is unexpected. Moreover this kind of blockade signal has not been reported before in the literature for macromolecule detection using single nanopores. According to the experimental protocol described in the literature[54, 62] and the absence of signal for neutral PEG detection when positive potential was applied, these current blockades could only be assumed as coming from negative PEG-carboxylate translocation through the nanopore. Three parameters could be used to characterize the blockade current (Figure 16 and Table 9): (i) the relative magnitude of the current blockade

$\Delta I/I_0$), (ii) the dwell time Δt and (iii) the spike magnitude ΔI_{spike} . The histogram values of each parameter are shown on Figure 17.

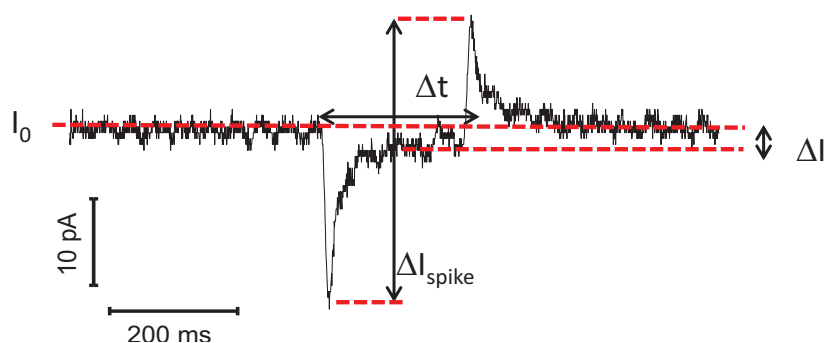


Figure 17. Detail of blockade current parameters are $\Delta I = I_0 - I$, Δt and $\Delta I_{\text{spike}} = I_{\text{max}} - I_{\text{min}}$

Table 9. Average and square deviation of the 3 parameters issued from the experimental measurements for the different PEG-carboxylate molar mass

PEG-carboxylate Mw (g.mol ⁻¹)	$\Delta I/I_0$	ΔI_{spike} (pA)	Δt (s)	$r_{\text{PEG}}^{2/3}$ (nm)
200	0.02 ± 0.01	6.7 ± 0.7	0.10 ± 0.05	0.37
600	0.08 ± 0.04	31 ± 10	0.18 ± 0.08	0.63

As shown in Table 9, those three parameters strongly depend from the molecular weight of the PEG carboxylate which is promising for mass spectrometry applications. Those experimental data were investigated and studied from the fundamental point of view by Balme team at the IEM laboratory (Annex-A-). This study contains also a simulation model in order to understand the blockage signal performed by Sebastian Kraszewski in the “Laboratoire de Nanomédecine, Imagerie et Thérapeutique, Universités Franche-Comté, (Centre Hospitalier Universitaire de Besançon) (annex-A-)”. In summary, organized shell of cations around the PEG carboxylate molecules may play a major role on blocking the signal since it does not exist for neutral PEG. It can be noted that PEG carboxylate and cation move in the opposite way under an electric field. When the PEG carboxylate diffuses inside the nanopore, the mean ionic current is clearly

lowered compared to the situation where the nanopore is empty of charged PEG. The entrance and exit events lead also to sudden decrease and increase of the average current, similar to the experimental spikes. The higher PEG experimental residence time into the nanopore compared to the simulation can be explained by an interaction between the pore and the PEG molecule.

5.5. Conclusion on PEG translocation

We have studied the translocation of different PEG molecules with $M_w = 200\text{g.mol}^{-1}$ and 600g.mol^{-1} through nanopores with high aspect ratio tailored by atomic layer deposition (ALD). Neutral PEG was not detected in a classical experimental setup. In contrast it is possible to detect the translocation of PEG-carboxylate molecules through the nanopores, which causes an unusual blockade of the ionic current, this blockade strongly depends of the macromolecule molar mass. Such a blockade is interpreted as a structuring of a cation shell around the PEG-carboxylate which perturbs the ionic transport near the surface of the nanopore. This work shows that the transport phenomena in the nanopore with high aspect ratio induced by the macromolecule translocation are not easy to understand. They require additional experimental and computational studies. It is also shown that it is possible to detect small charged macromolecules with hydrodynamic radius lower than the radius of the nanopore. However, more experiments should be performed using macromolecules, nanopores with different chemical functions/charges and other saline solution in order to better illustrate these phenomena.

6. Polycarbonate porous membrane for gas purification

Today Global warming, depletion of fossil fuels and pollution pushed the development of several research field based on the renewable nonpolluting energy. Among those renewable energy sources, Hydrogen is one of the most promoting energy vectors to the future. From the most known production methods reforming of natural gas or liquid hydrocarbons and biomass gasification are two large-scale production methods. Despite the large production advantage, the produced hydrogen are impure and must be purified [71]. Moreover environment pollution problem pushes the researcher to develop different purifications process to reduce the amount of toxins that they are the by-products of fossil fuels. Different technologies have been used for natural gas purification such as absorption, adsorption, and cryogenic distillation. But these

methods require high treatment cost due to regeneration process, large equipment's, and broad area for the big equipment's[72]. Among those purification processes, membrane technologies are promising on this domain due their lower capital cost, easy operation process, and high CO₂ removal percentage. Gas separation using polymeric membranes has taken its first commercial scale in late 1970's after the demonstration of rubbery membranes back in 1830's [73]. Polymeric membranes for gas purification process are an interesting topic due to the low cost and the large production scale. Despite this advantage, porous polymeric membrane synthesized by different techniques present a porous diameter on the nanometer range which is not suitable for H₂/CO₂ separation mechanism which takes place in the Angstrom range due to the kinetic diameter of H₂ and CO₂, 2.89 and 3.3 Å respectively. In this section, we will present our first results and our perspectives on polycarbonate track etched porous membrane tuned by ALD for gas purification applications.

6.1. Membrane preparation

Commercial polycarbonate track etched membrane with an initial pore diameter of 15 nm has been used to perform this part of this study. Nanolaminates of Al₂O₃/ZnO were deposited on those membranes in order to reduce the pores diameter with conserving the flexibility and the pore smoothness properties of the membranes. The same ALD setup and sequences mentioned in paragraph 3.3 has been used.

6.2. Gas separation setup

A simple home made cell (Figure 18) was used to measure the permeability of the membrane. The cell was fixed into an oven with a fixed temperature of 25 °C. Three pressure detectors were used to measure the pressure in the input and the output of the system. The system was evacuated using a Turbo molecular pump. Input and output pressure were collected using Labview software.

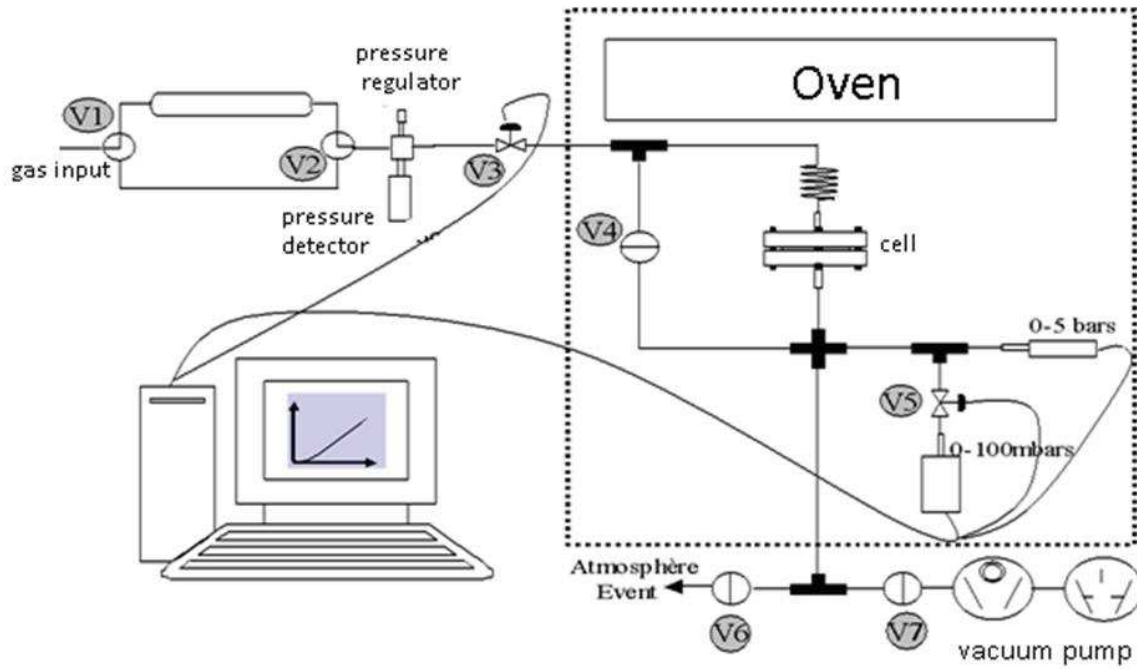


Figure18. Gas separation setup

Using Fick's second law (Equation 10) and Henry law (Equation 11), we can extract the permeability of the membrane (P_e) according to the volume downstream of the unit (V), the thickness of the tested membranes, the surface area of the membrane (A), the temperature (T) and the upstream pressure (P_1) (Equation 12).

$$D\left(\frac{\delta^2 C}{\delta x^2}\right) = \frac{\delta C}{\delta t} \quad (\text{Equation10})$$

$$C = S \cdot P \quad (\text{Equation11})$$

$$P_e = S \cdot D = \frac{V_e}{A R T P_1} \left(\frac{dP_2}{dt} \right) \quad (\text{Equation12})$$

P_e : Permeability ($\text{mol} \cdot \text{m}^{-1} \cdot \text{s}^{-1} \cdot \text{Pa}^{-1}$)

V: volume downstream of the unit ($V = 3.74 \cdot 10^{-5} \text{ m}^3$)

e: thickness of the tested membrane ($15 \mu\text{m}$)

A: Surface area of the membrane ($A = 1.73 \cdot 10^{-3} \text{ m}^2$)

R: gas constant ($R = 8.314 \text{ J} \cdot \text{mol}^{-1} \cdot \text{K}^{-1}$)

T: temperature ($T = 298 \text{ K}$)

P1: upstream pressure ($P1 = 3.105 \text{ Pa}$)

Where $\frac{dP_2}{dt}$ is the slope of the measured output pressure in function of time which is the collected data (Figure 19).

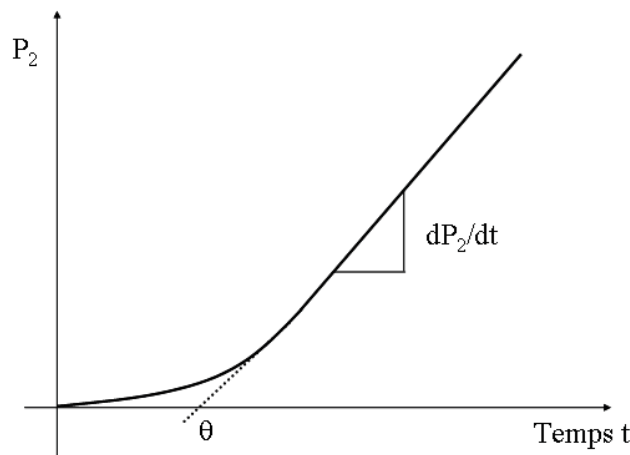


Figure 19. The output measured pressure as a function of time

6.3. First results and discussion

3 bilayers of 5 cycles Al_2O_3 /5 cycles ZnO have been deposited on polycarbonate track etched membrane with an initial pores diameter of 15 to 20 nm. The estimated pores diameter after the Atomic Layer Deposition based on the SAXS measurement is between 0.12 and 5.12 nm. After the ALD deposition, membrane permeability and selectivity was tested under He and CO_2 . Helium was used instead of hydrogen for security reason. We should note that the kinetic diameter of He and H_2 are in the same order of magnitude 2.6 and 2.89 Å respectively. Figure 20 shows the output measured pressure before and after ALD for both Helium and CO_2 .

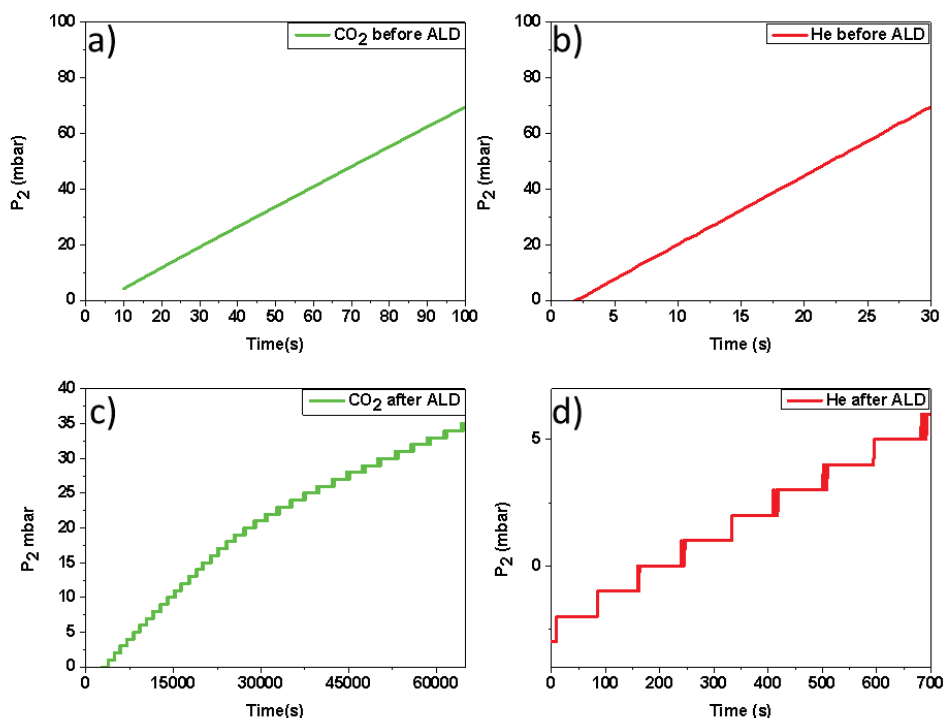


Figure 20. Gas permeability measurements a) CO₂ on PC membrane without ALD deposition b) He on PC membrane without ALD deposition c) CO₂ on PC membrane after ALD pores reduction d) He on PC membrane after ALD pores reduction

Using equation 12, membrane permeability for He and CO₂ has been extracted from Figure 20 and reported on Table 10. Moreover CO₂/He selectivity which is the permeability ratio was calculated and reported on the same table.

Table 10. Membrane permeability and selectivity on He and CO₂ before and After Pores reduction by ALD.

	PC before ALD	PC after ALD
Pe (He) Barrer	8305,41	38,94
Pe(CO ₂) Barrer	2375,61	2,753
S(He/CO ₂)	3,5	14,14

As shown in Table 10, membrane selectivity between He and CO₂ was enhanced from 3.5 to 14.14 nm. This selectivity value was not reported yet on track etched membranes. Vijay *et*

al. reports on his study a H_2/CO_2 selectivity between 1.5 and 4 on polycarbonate track etched membrane with an etching time between 1 and 35 minutes [74]. Despite this advantage a decrease on the gas permeability was observed.

6.4. Conclusion and perspectives

ALD modified polycarbonate membranes have been elaborated for gas purification combining the track etching technique and the ALD technique. This elaboration method offers several advantages such as a flexible membrane with a smooth surface inside the pores and a sub 5 nm pores. Permeability measurements before and after the ALD modification show improvement of the (He/CO_2) membrane selectivity from 3.5 to 14.14 with a decrease on the gas permeability through the membrane. This first results opened different perspectives to be investigated. First, in order to solve the polydispersivity of the pores diameters on the commercial PC membrane, PET track etched membrane will be elaborated and then tested. Membrane permeability after the ALD deposition can be enhanced during the etching setup in order to obtain a high pores density membranes. A chemical functionalization of the inner pore surface can be also an interesting perspective.

7. General conclusion

Track etched technique on PET membrane combined with the Atomic Layer Deposition of $\text{Al}_2\text{O}_3/\text{ZnO}$ nanolaminates and the HMDS vapor grafting process lead to the elaboration of a flexible, homogenous, hydrophobic and smooth porous membrane.

- Multipores membranes with sub 10 nm pores diameter can be grafted by biological function such as gramicidin A to synthesize a cationic transport membrane that demonstrate to the first time a NaCl ionic transport mechanism through a hybrid nanopore similar to the biological ones.
- Single pore membrane with sub 5 nm pore diameter synthesized show an unusual signal blockage due to the translocation of PEG-carboxylate molecules through the pores. This blockade strongly depending on the macromolecule molar mass.
- Polycarbonate track etched membrane tuned by $\text{Al}_2\text{O}_3/\text{ZnO}$ nanolaminates shows an increase on the selectivity between He and CO_2 from 3.5 to 14.1 when the pore diameter go from 15 to 0.3 nm. More studies should be performed on this field in order to increase the membrane permeability. As a perspective, high density track etched membrane can be an ideal solution to increase the membrane permeability. Conical pores can be another suggestion to increase the permeability and finally chemical modification of the inner pores surface in order to increase the selectivity.

REFERENCES

1. Encyclopedia of Polymer Science and Technology. Copyright John Wiley & Sons, Inc. p. 188-249.
2. S. Loeb and S. Sourirajan, Saline Water Conversion-II,, 1963, American Chemical Society: Washington, D.C.
3. Gilani, N., et al., Separation of methane-nitrogen mixtures using synthesis vertically aligned carbon nanotube membranes. *Applied Surface Science*, 2012. 258(10): p. 4819-4825.
4. Lakshmi, B.B., C.J. Patrissi, and C.R. Martin, Sol-gel template synthesis of semiconductor oxide micro- and nanostructures. *Chemistry of Materials*, 1997. 9(11): p. 2544-2550.
5. Velleman, L., et al., Structural and chemical modification of porous alumina membranes. *Microporous and Mesoporous Materials*, 2009. 126(1-2): p. 87-94.
6. Abou Chaaya, A., et al., Enhanced Ionic Transport Mechanism by Gramicidin A Confined Inside Nanopores Tuned by Atomic Layer Deposition. *Journal of Physical Chemistry C*, 2013. 117(29): p. 15306-15315.
7. Ott, A.W., et al., Modification of porous alumina membranes using Al₂O₃ atomic layer controlled deposition. *Chemistry of Materials*, 1997. 9(3): p. 707-714.
8. Cameron, M.A., et al., Atomic layer deposition of SiO₂ and TiO₂ in alumina tubular membranes: Pore reduction and effect of surface species on gas transport. *Langmuir*, 2000. 16(19): p. 7435-7444.
9. Chen, P., et al., Atomic layer deposition to fine-tune the surface properties and diameters of fabricated nanopores. *Nano Letters*, 2004. 4(7): p. 1333-1337.
10. Guo, W., et al., Energy Harvesting with Single-Ion-Selective Nanopores: A Concentration-Gradient-Driven Nanofluidic Power Source. *Advanced Functional Materials*, 2010. 20(8): p. 1339-1344.
11. Siwy, Z.S. and S. Howorka, Engineered voltage-responsive nanopores (vol 39, pg 1115, 2010). *Chemical Society Reviews*, 2010. 39(12): p. 5067-5067.
12. Balme, S., et al., New Bioinspired Membrane Made of a Biological Ion Channel Confined into the Cylindrical Nanopore of a Solid-State Polymer. *Nano Letters*, 2011. 11: p. 712-716.
13. Thiele, D., et al., Structure and ionic selectivity of a hybrid polyene/artificial polymer solid state membrane. *Soft Matter*, 2013. advance article.
14. Kocer, A., L. Tauk, and P. Dejardin, Nanopore sensors: From hybrid to abiotic systems. *Biosensors & Bioelectronics*, 2012. 38(1): p. 1-10.
15. Hall, A.R., et al., Hybrid pore formation by directed insertion of alpha-haemolysin into solid-state nanopores. *Nature Nanotechnology*, 2010. 5(12): p. 874-877.
16. Sawyer, D.B., et al., Gramicidin-a, Gramicidin-B, and Gramicidin-C Form Structurally Equivalent Ion Channels. *Biophysical Journal*, 1990. 58(5): p. 1207-1212.
17. Shvinka, N.E. and G. Caffier, Selectivity for cations in potassium and gramicidin channels of the muscle fibre membrane. *Biomed. Biochim. Acta.*, 1988. 47(6): p. 481-487.
18. Wallace, B.A., Common structural features in gramicidin and other ion channels. *Bioessays*, 2000. 22(3): p. 227-234.
19. Allen, T.W., O.S. Andersen, and B. Roux, Ion permeation through a narrow channel: Using gramicidin to ascertain all-atom molecular dynamics potential of mean force methodology and biomolecular force fields. *Biophysical Journal*, 2006. 90(10): p. 3447-3468.
20. Hinton, J.F., et al., Thermodynamic Parameters for the Binding of Divalent-Cations to Gramicidin-a Incorporated into a Lipid Environment by Ti-205 Nuclear Magnetic-Resonance. *Biophysical Journal*, 1989. 55(2): p. 327-330.
21. Roux, B., Valence selectivity of the gramicidin channel: A molecular dynamics free energy perturbation study. *Biophysical Journal*, 1996. 71(6): p. 3177-3185.

22. Strathmann, H., Membrane separation processes: Current relevance and future opportunities. *Aiche Journal*, 2001. 47(5): p. 1077-1087.
23. Balme, S., et al., New Bioinspired Membrane Made of a Biological Ion Channel Confined into the Cylindrical Nanopore of a Solid-State Polymer. *Nano Letters*, 2011. 11(2): p. 712-716.
24. Sakamoto, S., et al., Ordered hexagonal array of Au nanodots on Si substrate based on colloidal crystal templating. *Nanotechnology*, 2008. 19(40).
25. Cimatu, K.A., et al., Nanoscale Chemical Imaging of Zinc Oxide Nanowire Corrosion. *Journal of Physical Chemistry C*, 2012. 116(18): p. 10405-10414.
26. Fleische, R.I., P.B. Price, and R.M. Walker, NUCLEAR TRACKS IN SOLIDS. *Scientific American*, 1969. 220(6): p. 30-&.
27. Dejardin, P., et al., Streaming potential in cylindrical pores of poly(ethylene terephthalate) track-etched membranes: Variation of apparent zeta potential with pore radius. *Langmuir*, 2005. 21(10): p. 4680-4685.
28. Powell, M.R., et al., Electric-field-induced wetting and dewetting in single hydrophobic nanopores. *Nature Nanotechnology*, 2011. 6(12): p. 798-802.
29. Jur, J.S., et al., Temperature-Dependent Subsurface Growth during Atomic Layer Deposition on Polypropylene and Cellulose Fibers. *Langmuir*, 2010. 26(11): p. 8239-8244.
30. Raghavan, R., et al., Nanocrystalline-to-amorphous transition in nanolaminates grown by low temperature atomic layer deposition and related mechanical properties. *Applied Physics Letters*, 2012. 100(19).
31. Elam, J.W., Z.A. Sechrist, and S.M. George, ZnO/Al₂O₃ nanolaminates fabricated by atomic layer deposition: growth and surface roughness measurements. *Thin Solid Films*, 2002. 414(1): p. 43-55.
32. G, P., X-ray low angle scattering of dense colloid systems. Part I. (Die Röntgenkleinwinkelstreuung von dichtgepackten kolloiden systemen. I. Teil.). *Koll. Zeit.*, 1951. 124: p. 83-114.
33. Porod, G., Die Röntgenkleinwinkelstreuung von dichtgepackten kolloiden Systemen. *Koll. Zeit.*, 1952. 125: p. 51-57.
34. Puniredd, S.R., O. Assad, and H. Haick, Highly stable organic modification of Si(111) surfaces: towards reacting Si with further functionalities while preserving the desirable chemical properties of full Si-C atop site terminations. *Journal of the American Chemical Society*, 2008. 130(29): p. 9184-5.
35. Barry, P.H. and J.W. Lynch, LIQUID JUNCTION POTENTIALS AND SMALL-CELL EFFECTS IN PATCH-CLAMP ANALYSIS. *Journal of Membrane Biology*, 1991. 121(2): p. 101-117.
36. Pickard, W., Generalizations of the Goldman-Hodgkin-Katz equation. *Mathematical biosciences*, 1976. 30: p. 99-111.
37. Smart, O.S., J.M. Goodfellow, and B.A. Wallace, The pore dimensions of gramicidin A. *Biophysical Journal*, 1993. 65(6): p. 2455-2460.
38. Hinton, J.F., et al., Thermodynamic parameters for the binding of divalent cations to gramicidin A incorporated into a lipid environment by Tl₂O₅ nuclear magnetic resonance. *Biophysical Journal*, 1989. 55(2): p. 327-330.
39. Allen, T.W., O.S. Andersen, and B. Roux, Molecular dynamics potential of mean force calculations as a tool for understanding ion permeation and selectivity in narrow channels. *Biophysical Chemistry*, 2006. 124(3): p. 251-267.
40. Neher, E., J. Sandblom, and G. Eisenman, Ionic Selectivity, Saturation, and Block in Gramicidin-a Channels .2. Saturation Behavior of Single Channel Conductances and Evidence for Existence of Multiple Binding-Sites in Channel. *Journal of Membrane Biology*, 1978. 40(2): p. 97-116.
41. Strickholm, A., Ionic Permeability of K, Na, and Cl in Potassium-Depolarized Nerve - Dependency on Ph, Cooperative Effects, and Action of Tetrodotoxin. *Biophysical Journal*, 1981. 35(3): p. 677-697.

42. Roux, B. and M. Karplus, Ion-Transport in a Model Gramicidin Channel - Structure and Thermodynamics. *Biophysical Journal*, 1991. 59(5): p. 961-981.
43. Phillips, J.C., et al., Scalable molecular dynamics with NAMD. *Journal of Computational Chemistry*, 2005. 26(16): p. 1781-1802.
44. Feller, S.E., et al., CONSTANT-PRESSURE MOLECULAR-DYNAMICS SIMULATION - THE LANGEVIN PISTON METHOD. *Journal of Chemical Physics*, 1995. 103(11): p. 4613-4621.
45. Darden, T., D. York, and L. Pedersen, PARTICLE MESH EWALD - AN N.LOG(N) METHOD FOR EWALD SUMS IN LARGE SYSTEMS. *Journal of Chemical Physics*, 1993. 98(12): p. 10089-10092.
46. MacKerell, A.D., et al., All-atom empirical potential for molecular modeling and dynamics studies of proteins. *Journal of Physical Chemistry B*, 1998. 102(18): p. 3586-3616.
47. Bedrov, D., et al., Passive transport of C-60 fullerenes through a lipid membrane: A molecular dynamics simulation study. *Journal of Physical Chemistry B*, 2008. 112(7): p. 2078-2084.
48. Jorgensen, W.L., et al., COMPARISON OF SIMPLE POTENTIAL FUNCTIONS FOR SIMULATING LIQUID WATER. *Journal of Chemical Physics*, 1983. 79(2): p. 926-935.
49. Bonhenry, D., et al., Stability of the gramicidin-A channel structure in view of nanofiltration: a computational and experimental study. *Soft Matter*, 2011. 7(22): p. 10651-10659.
50. Fologea, D., et al., Detecting single stranded DNA with a solid state nanopore. *Nano Letters*, 2005. 5(10): p. 1905-1909.
51. Storm, A.J., et al., Fast DNA translocation through a solid-state nanopore. *Nano Letters*, 2005. 5(7): p. 1193-1197.
52. Hall, A., et al., Hybrid Biological/Solid-State Nanopores. *Biophysical Journal*, 2011. 100(3): p. 168-168.
53. Manrao, E.A., et al., Reading DNA at single-nucleotide resolution with a mutant MspA nanopore and phi29 DNA polymerase. *Nature Biotechnology*, 2012. 30(4): p. 349-U174.
54. Robertson, J.W.F., et al., Single-molecule mass spectrometry in solution using a solitary nanopore. *Proceedings of the National Academy of Sciences of the United States of America*, 2007. 104(20): p. 8207-8211.
55. Kasianowicz, J.J., et al., Nanoscopic Porous Sensors. *Annual Review of Analytical Chemistry*, 2008. 1: p. 737-766.
56. Tsutsui, M., et al., Single-Nanoparticle Detection Using a Low-Aspect-Ratio Pore. *Acs Nano*, 2012. 6(4): p. 3499-3505.
57. Bacri, L., et al., Dynamics of Colloids in Single Solid-State Nanopores. *Journal of Physical Chemistry B*, 2011. 115(12): p. 2890-2898.
58. Siwy, Z.S. and S. Howorka, Engineered voltage-responsive nanopores. *Chemical Society Reviews*, 2010. 39(3): p. 1115-1132.
59. Vlassiuk, I., S. Smirnov, and Z. Siwy, Ionic selectivity of single nanochannels. *Nano Letters*, 2008. 8(7): p. 1978-1985.
60. Kowalczyk, S.W., T.R. Blosser, and C. Dekker, Biomimetic nanopores: learning from and about nature. *Trends in Biotechnology*, 2011. 29(12): p. 607-614.
61. Schneider, G.F. and C. Dekker, DNA sequencing with nanopores. *Nature Biotechnology*, 2012. 30(4): p. 326-328.
62. Baaken, G., et al., Nanopore-Based Single-Molecule Mass Spectrometry on a Lipid Membrane Microarray. *Acs Nano*, 2011. 5(10): p. 8080-8088.
63. Schoch, R.B., J.Y. Han, and P. Renaud, Transport phenomena in nanofluidics. *Reviews of Modern Physics*, 2008. 80(3): p. 839-883.
64. Shimizu, S., et al., Stochastic Pore Blocking and Gating in PDMS-Glass Nanopores from Vapor-Liquid Phase Transitions. *Journal of Physical Chemistry C*, 2013. 117(19): p. 9641-9651.
65. Zimmermann, R., et al., Hydroxide and hydronium ion adsorption - A survey. *Current Opinion in Colloid & Interface Science*, 2010. 15(3): p. 196-202.

66. Lan, W.J., et al., Nanoparticle Transport in Conical-Shaped Nanopores. *Analytical Chemistry*, 2011. 83(10): p. 3840-3847.
67. Siwy, Z., et al., Rectification and voltage gating of ion currents in a nanofabricated pore. *Europhysics Letters*, 2002. 60(3): p. 349-355.
68. Stojilkovic, K.S., et al., Conductivity and microviscosity of electrolyte solutions containing polyethylene glycols. *Journal of Chemical Physics*, 2003. 119(13): p. 6973-6978.
69. Krasilnikov, O.V., C.G. Rodrigues, and S.M. Bezrukov, Single polymer molecules in a protein nanopore in the limit of a strong polymer-pore attraction. *Physical Review Letters*, 2006. 97(1).
70. Gassara, S., et al., Pore size tailoring of poly(ether imide) membrane from UF to NF range by chemical post-treatment using aminated oligomers. *Journal of Membrane Science*, 2013. 436: p. 36-46.
71. Rusmidah, A.W.a.A., *Natural Gas*, 2010: Universiti Teknologi Malaysia.
72. Akkil, M.I.F.a.A., Meeting Technical Challenge in Developing High CO₂ Gas Field Offshore, in *Petronas Carigali Sdn. Bhd* 2008.
73. R. W. Baker, E.L.C., W. Eykamp, W. J. Koros, R. L. Riley, and H. Strathmann., *Membrane Separation Systems—Recent Developments and Future Directions*, N.D. Corporation, Editor 1991.
74. Vijay, Y.K., et al., Nanofilter for hydrogen purification. *International Journal of Hydrogen Energy*, 2003. 28(9): p. 1015-1018.

General Conclusion

General Conclusion

In this work we reported the design of novel nanomaterials using the atomic layer deposition technique combined with other techniques such as electrospinning and track etching technique in order to investigate their properties and the influence of their chemical and structural compositions on the optical, electrical and mechanical properties. Different applications have been investigated and reported on 4 chapters.

One of the most fascinating aspects of nanomaterials is their unique optical properties. In this thesis we report on the structural, chemical and optical properties evolution of Zinc oxide thin film deposited by ALD when the film thickness increases from 25 to 250 nm. The structural characterizations of this ZnO ultrathin films shows a transition from amorphous to polycrystalline state when the ZnO thickness increases coupled with an augmentation of the grain size and the Zn/O ratio. Due to a decrease of the defects point concentration and an improvement of the film crystallinity, an uncharacteristic change of the band gap and the Urbach energy have been reported by transmittance measurements. The same behavior was observed by photoluminescence and absorption measurement. Moreover the crystalline structure improvement when the ZnO thickness increase was reflected in the photoluminescence spectra by an increasing on the UV emissions intensity. The oxygen excess is attributed to the formation of Zn vacancies, oxygen interstitials and adsorbed molecular oxygen on the surface of grains. Optical and structural properties of $\text{Al}_2\text{O}_3/\text{ZnO}$ nanolaminates elaborated by ALD have been as well investigated. Nanolaminates structures allow the tailoring of structural and optical parameters. Single layer thickness, grain size, mean square roughness, band gap and PL have been calculated. From the analysis of optical and structural properties, it was determined that Al diffused into the interface of $\text{ZnO}/\text{Al}_2\text{O}_3$ bilayers, forming defect states which increased the visible peak of the photoluminescence spectra. The improvement on the ZnO crystalline quality leads to a blue shift of the band gap and the excitonic peak position of ZnO single layers and was explained by the quantum confinement.

One of the advantages of the nanostructured materials is the increment of the active surface area. Combining the high surface area offered by the electrospinning technique and the conformal coating on high aspect ratio advantage of the ALD technique, ZnO 1D nanostructures

have been synthesized then tested as UV photodetectors. An improvement on the UV photoresponse current with a factor of 250 was observed on the ZnO 1D nanostructures based photodetectors in comparison with the thin film of ZnO. Moreover, an improvement on the UV photoresponse current has been registered when the spinning time increases as well as a decrease on the recovery time. The influence of the ZnO layer thickness deposited on the polymer nanofibers has been also investigated. Electrical measurement shows a decrease of the dark current when the ZnO thickness decreases which lead to an increase of the UV photoresponse current. The temperature influence was also investigated. 250 cycles ZnO deposited at 100°C on PAN nanofibers shows the higher UV photoresponse current and the lower recovery time. Electrode distance investigations show a decrease on the recovery time. Device stability test reports a small decrement on the UV photoresponse current with a stable recovery time. The investigation of Al doped ZnO and $\text{Al}_2\text{O}_3/\text{ZnO}$ nanolaminates for UV detection application can be interesting perspectives for this PhD and is under investigation in our group.

The second part of this work was dedicated to the study of the mechanical properties evolution of $\text{Al}_2\text{O}_3/\text{ZnO}$ nanolaminates with different bilayers thickness. For this aim, tensile test was performed at the EMPA laboratory (Switzerland) on $\text{Al}_2\text{O}_3/\text{ZnO}$ nanolaminates deposited by the atomic layer deposition technique. Structural properties studies of nanolaminates show a transition from an amorphous state to a crystalline state when the bilayer thickness increases with a change in the preferential growth orientation from (002) to (100) when increasing the bilayer thickness from 9.25 nm to 185 nm. Tensile tests measurement shows a decrease on the saturation crack density when the bilayer thickness decrease from 185 to 0.92 nm. This behavior was linked to the bilayers delamination during the tensile test that leads to less cracks formation. This behavior can also be due to the nanolaminates transition from a crystalline state to an amorphous state. We can also point out that the delamination starting strain for the $\text{Al}_2\text{O}_3/\text{ZnO}$ nanolaminates are lower than the corresponding value for the Al_2O_3 which consist of the first layer (interface polymer/nanolaminates). The critical strain of $\text{Al}_2\text{O}_3/\text{ZnO}$ nanolaminates decreases when the bilayer thickness decreases, which can be due to the nanolaminates transition from a crystalline state to an amorphous state. In order to go deeper on this study we suggest as perspective to perform tensile test on:

1. PET surface treated using Oxygen plasma in order to increase the active site on the PET film.
2. NaOH surface treatment under UV in order to increase the active site on the PET film.
3. Another solution will be to deposit nanolaminates with ZnO as first layer. This approach is supported by the fact that the ZnO films deposited on the PET substrate shows less delamination than the alumina films.

Based on these mechanical properties investigations and the nanoindentation tests performed by Raghavan *et al.*, the $\text{Al}_2\text{O}_3/\text{ZnO}$ nanolaminates have been used to tune the pores size of track etched PC and PET membranes with conserving the main advantages of the track etched membrane (flexibility and smooth pore surface). Multipores PET membranes with sub 10 nm pores diameter after ALD deposition was functionalized by CH_3 groups then grafted by gramicidin A to design a cationic transport membrane. The ALD tuned multipores membrane shows for the first time a NaCl ionic transport mechanism through a hybrid nanopore similar to the biological ones. Single nanopore membrane with sub 5 nm pore diameter synthesized with the same technique (track etching followed by ALD nanolaminates deposition and CH_3 functionalization) shows an unusual signal blockage due to the translocation of PEG-carboxylate molecules through the pores. This blockade strongly depends on the macromolecule molar mass. This single nanopore membrane can be promising for mass spectrometry and DNA sequencing. Polycarbonate track etched multipores membrane was also tuned by $\text{Al}_2\text{O}_3/\text{ZnO}$ ALD and tested as gas purification membrane. Permeability tests before and after the ALD deposition show an increase on the selectivity between He and CO_2 from 3.5 to 14.1 when the pore diameter go from 15 to 0.3nm. As perspective to this work, high density track etched membrane can be an ideal solution to increase the membrane permeability. Conical pores can be another solution to increase the permeability. Finally chemical modification can be an interesting perspective in order to increase the selectivity.

During this PHD work different types of ALD reactors have been designed and installed. A radio frequency RF generator was coupled to the ALD reactor for nitride and carbide deposition for different applications such as gas sensor ,UV sensor, gas separation and others.

This reactor can be as well used for oxide deposition under plasma in order to investigate the plasma effect on the structural optical electrical and mechanical properties of ALD thin film. A fluidize bed reactor have been as well established coupled with a plasma system for ALD deposition on powders for battery applications. High temperature ALD reactors up to 1000 °C have been installed for nitride deposition for osmotic energy harvesting.

Annex-a-

Experimental and simulation studies of unusual current blockade induced by translocation of small oxidized PEG through a single nanopore

*Simon CABELLO-AGUILAR^a, Adib ABOU CHAAYA^a, Fabien PICAUD^b, Mikhael BECHELANY^a, Céline POCHAT-BOHATIER^a, Semen YESYLEVSKYY^c, Sebastian KRASZEWSKI^b, Mirna Chaker BECHELANY^d, Fabrice ROSSIGNOL^d, Emmanuel BALANZAT^e, Jean-Marc JANOT^a, Philippe MIELE^a, Philippe DEJARDIN^a and Sébastien BALME^{*a,f}*

^a *Institut Européen des Membranes, UMR5635 CNRS-UM2-ENSCM, Place Eugène Bataillon, 34095 Montpellier cedex 5, France. Email. sebastien.balme@univ-montp2.fr*

^b *Laboratoire de Nanomédecine, Imagerie et Thérapeutique, Université Franche-Comté, Centre Hospitalier Universitaire de Besançon, 16 route de Gray, 25030 Besançon cedex, France*

^c *Department of Physics of Biological Systems, Institute of Physics of the National Academy of Sciences of Ukraine, Prospect Nauky 46, Kiev-28, 03680, Ukraine*

^d *SPCTS (UMR CNRS 7315), Centre Européen de la Céramique, 12 rue Atlantis, 87068 Limoges, France*

^e *Centre de recherche sur les Ions, les Matériaux et la Photonique, UMR6252 CEA-CNRS-ENSICAEN, 6 Boulevard du Maréchal Juin, 14050 Caen Cedex 4, France*

^f *Institut Charles Gerhardt UMR 5253 CNRS-UM2-ENSCM-UM1, Place Eugène Bataillon, 34095 Montpellier cedex 5, France*

KEYWORDS : Nanopore, Atomic layer deposition, sensor, PEG mass spectroscopy

ABSTRACT

Detection of the single macromolecule based on the use of artificial nanopores is an attractive and promising field of research. In this work, we report a device based on a 5 nm single nanopore with high length/diameter ratio, tailored by the track etching and atomic layer deposition techniques. The translocation of neutral Polyethylene glycol (PEG) and charged Polyethylene glycol-carboxylate (PEG-carboxylate) molecules of low molar mass (200 and 600 g.mol⁻¹) through this nanodevice was studied. It was shown that charged PEG-carboxylate molecules, which permeate through the pore, promote an unusual blockade of ionic current whereas the neutral PEG molecules do not show such behaviour. The molecular dynamic simulation shows that both neutral and charged PEGs permeate through the nanopore close to its inner surface. The main difference among the two macromolecules is the existence of structured shell of cations around the charged PEG, which is likely to cause the observed unusual current blockade.

INTRODUCTION

Single nanopore technologies have opened the route to multiple applications such as DNA detection^{1, 2} and sequencing,³ Polyethylene glycol (PEG) mass spectroscopy,^{4, 5} nanoparticle detection^{6, 7} and ionic separation.^{8, 9} There are two major strategies in using the single nanopores as molecular sensors. The first one is inserting a biological channel inside the artificial phospholipid membrane.¹⁰ This method has already been used successfully in PEG mass spectroscopy⁴ and is presently developed for low cost DNA sequencing.^{2, 11} However, the life time of such nanopores is limited due to the fragility of the lipid bilayers. The second approach is based on the production of solid state nanopores with either low or high length/diameter ratio (*i.e.* low or high aspect ratio). The nanopores with low aspect ratio are produced by the Transmission Electron Microscopy (TEM) irradiation of silicon based thin films (typically Si₃N₄). The dimensions of such pores could be varied easily with diameters ranging from 5 nm to 300 nm and lengths ranging from 10 nm to 500 nm,

which stimulated their extensive studies.⁶ Single nanopores with high aspect ratio (length to diameter ratio larger than 1000) are produced by the single track-etching technique.^{8,12} These pores could be either conical or cylindrical and their surface properties could be modified easily due to carboxylate functionalization induced by chemical etching which is possible for minimal diameter around 20 nm.¹³ However recent works have shown the possibility of designing the nanopores with high aspect ratio with diameter ranging from 2 nm to 10 nm using atomic layer deposition on PET track-etched membrane.^{14,15}

The macromolecule discrimination is one of the applications of the nanopore technology.^{4,16} Typically, when a single macromolecule permeates through the nanopore, it induces a blockade of the background ionic current. The blockade event is characterized by the relative change of current intensity and the dwell time. Both observables are dependent on the macromolecule molar mass and the nanopore diameter. This allowed detecting large PEG (Molar mass $M_w > 1000 \text{ g.mol}^{-1}$) for mass spectroscopy⁴ or estimating small diameter of conical polymer nanopores from the size of the smallest blocked macromolecule (or largest penetrating macromolecule).^{17,18} Experimentally, these characterizations are based on the ionic current detection through nanopore which is different from the bulk one. In other words, the influences of the Donnan effect and the diffuse double layer cannot be disregarded.^{19,20}

In this paper, we show that, in the case of single cylindrical nanopore with high aspect ratio (diameter 5 nm, length 13 μm) produced by track-etching and atomic layer deposition (ALD) techniques, small PEGs ($M_w = 200$ and 600 g.mol^{-1}) do not induce any blockade of ionic current. On the contrary, for oxidized PEG (noted PEG-carboxylate), an unexpected and unusual blockade of the current appears. It was shown that the characteristics of the blockade current depend on the PEG-carboxylate molar mass. Experimental results are also complemented by means of molecular dynamics simulations of the model nanopore. An explanation of the unusual blockade of ionic current is proposed.

Materials and Methods

Materials

Diethyl Zinc (DEZ) ($\text{Zn}(\text{CH}_2\text{CH}_3)_2$, 95% purity, CAS: 557-20-0), Trimethylaluminum (TMA) ($\text{Al}(\text{CH}_3)_3$, 97% purity, CAS: 75-24-1) were purchased from Sterm chemical. Sodium chloride (S9888), and Hexamethyldisilazane (HMDS) (reagent grade, $\geq 99\%$) were obtained from Sigma Aldrich. Demineralized water was obtained by milliQ system (Millipore). Poly(EthyleneTerephthalate) (PET) film (thickness 13 μm , biaxial orientation) was purchased from Goodfellow. Polyethyleneglycol (PEG) was bought from MERCK-Schuchardt, Germany ($M_w = 200$ Da Art.807483 and $M_w = 600$ Da Art.807486). The infrared spectra of both PEG samples in a dry state have been recorded in order to detect precisely their structure and purity (Fig. SI1). The presence of a peak at 1720 cm^{-1} clearly indicates the existence of C=O groups, due to the oxidation of the alcohol terminal groups $\text{HO}-(\text{CH}_2\text{CH}_2\text{O})_n-\text{CH}_2\text{CH}_2\text{OH}$ to the carboxylates $\text{HOCH}_2-\text{CH}_2\text{O}(\text{CH}_2\text{CH}_2\text{O})_n-\text{CH}_2\text{COOH}$.²¹ Thus the sample contained both the PEG-Carboxylate (less than 1%) carrying a negative charge ($\text{pK}_a \sim 4-5$) and the neutral PEG at pH 7.

PET Nanopores production

Single nanopore on poly(EthyleneTerephthalate) (PET) film has been built using a single track technique. PET film (thickness 13 μm , length 24 cm, width 4 cm) was placed on the trajectory of a diffracted $^{78}\text{Krypton}$ ion (9.5 MeV) beam in GANIL (Caen France). A detector was positioned behind the film in order to count the number of ions crossing the film. When the detector counted one, the beam was stopped. The PET film was kept in an inert Helium atmosphere to preserve the tracks. The chemical etching has been carried out by exposing the tracked film 24 h per side to an ultraviolet

light (Fisher Bioblock; VL215.MC, 312 nm), then immersing it during 5 minutes in NaOH solution (3M) at 50°C. Finally the film was rinsed with demineralized water.

Design of 5 nm single nanopore and characterization

Al₂O₃/ZnO ultrathin films have been designed using a custom-made ALD setup.²² Alternating exposures of TMA and H₂O at 60 °C with the following cycle times: 0.1 s pulse (TMA), 20 s exposure, and 40 s purge with dry Argon and a 2 s pulse (H₂O), 30 s exposure and 60 s purge were used to deposit the Al₂O₃ ALD ultrathin films. Alternating exposures of DEZ and H₂O with the following cycle times: 0.2 s pulse (DEZ), 20 s exposure, and 40 s purge with dry Argon and a 2 s pulse (H₂O), 30 s exposure and 60 s purge were used to deposit the ZnO ALD films. The experimental conditions were fixed conservatively to ensure completion of the ALD surface reactions and to prevent mixing of the reactive gases. The growth per cycle was about 2 Å/cycle and 2.1 Å/cycle for Al₂O₃ and ZnO respectively.^{23, 24}

Different sequence numbers (1 to 14) of 5 cycles of Al₂O₃ followed by 5 cycles of ZnO, were used to reduce the pore diameter to the sub-10 nm range. After ALD deposition, all samples were functionalized by a 24 hours Hexamethyldisilazane (HMDS) vapor exposure at room temperature in order to obtain hydrophobic surfaces. The expected result from the HMDS treatment was the replacement of the -OH bond on the surface of the ALD layer by a hydrophobic ((CH₃)₃Si-) bond.^{14, 15}

The nanolaminates structural and chemical compositions were analyzed by scanning electron microscopy (SEM, S-4800, Hitachi), Energy-dispersive X-ray spectroscopy (SEM, S-4500, coupled with a Thermofisher EDX detector), AFM (AFM NANOMAN 5 from Veeco instrument controlled with a Nanoscope V software) and SAXS (Xenocs GenX equipped with a molybdenum anode and a MAR2300 2D imaging plate detector) as described elsewhere.¹⁴ The HMDS nanopores modification was validated by XPS measurements (ESCALAB 250 Thermo Electron) and the determination of the

contact angle (GBX - Digidrop, Romans, France).¹⁴ TEM nanopore imaging was obtained using a Transmission Electron Microscope (JEOL 2010). TEM was performed on 13 μm thick multipore PET membrane (average pores diameter 70 nm) after 12 sequences of 5 cycles Al_2O_3 /5 cycles ZnO deposited by ALD. In order to eliminate the PET membrane, the sample has been annealed at 450°C under air.

Ionic current recordings

Single nanopore was mounted between two chambers of conductivity Teflon tubes containing a NaCl solution ($\sigma \approx 80 \text{ mS.cm}^{-1}$) Concentration NaCl $\approx 0.63 \text{ M}$. The current was measured between one Ag/AgCl electrode (XM410, Tacussel, France) in cis chamber and a ground electrode (platinum, XM140, Tacussel, France) in trans chamber. The ion current was recorded by patch-clamp post amplifier (EPC800, HEKA electronics, Germany) using voltage clamp mode and a sampling frequency 25 KHz. Acquisition data were performed by Instrutech LIH 8+8 acquisition card (HEKA electronics, Germany) using a lab made routine on IgorPro 6 (Wavemetrics, USA). A lab-made analysis software (Matlab, Matworks, USA) was used to analyze the current data in terms of duration (Δt), depth (ΔI), relative depth ($\Delta I/I_0$) and the difference between the maximum and minimum of current (ΔI_{spike}) occurring over one translocation process.

Multivariate data analyses.

All data analysis was performed using “The Unscrambler®X” v10.2 software (CAMO Software). The experimental data are gathered in a X matrix organized as follows: the rows represent different experimental events and three columns correspond to ΔI , Δt and ΔI_{spike} values respectively. Then, each column was mean-centered and scaled to unit variance prior to further analysis to give each descriptor an equal influence on the analysis. The Principal component analysis (PCA) was obtained

as follow: The X variables are summarized by the matrix of scores, T. The loading matrix P^T shows the influence of each variable on the projection. The data matrix X is then expressed as the product of these two matrices ($T.P^T$, named as the principal components), plus an additional matrix of residuals (E) as $X = T.P^T + E$. The rows in the residual matrix E represent the distance of a compound to the model.

Molecular Dynamics simulations

All-atom molecular dynamics simulations were performed using NAMD 2.7b2 software²⁵. The constant temperature of 300 K (maintained by the Langevin dynamics method) and the constant pressure of 1 atm (maintained using the Langevin piston Nosé-Hoover method²⁶) were used to mimic experimental conditions. The short- and the long-range forces were calculated every 1 and 2 time steps respectively, with a time step of 2.0 fs. The classical particle mesh Ewald (PME) method²⁷ was used to evaluate the long-range electrostatic forces. The bond lengths between the hydrogens and the heavy atoms were constrained to their equilibrium values using the SHAKE/RATTLE algorithm.²⁸

CHARMM27²⁹ force field was used with TIP3P water model. The nanopore was mimicked by an assembly of neopentane molecules with fixed position for the central carbon atoms of neopentane, while the methyl groups constituting each molecule were free. The mean distance between the fixed centers of masses of neopentane molecules is chosen according to the work of Makowski *et al.*³⁰ The PEG-carboxylate molecules were pre-equilibrated separately for at least 6.5 ns and then inserted into the simulation box containing the nanopore and the solvent, as described below.

The nanopore was composed of 150 neopentane molecules arranged in a tubular geometry to obtain a pore diameter equal to 6 nm and a length of 4 nm. A constant electric field of 20 mV/nm was applied along the pore to reproduce an experimental voltage of 200 mV in the simulation box (noted

that the electric field inside nanopore is $E = 5 \times 10^7 \text{ V.m}^{-1}$). The compositions and simulation parameters of the studied systems were the following:

(i) 11263 water molecules, 109 Na^+ and 107 Cl^- ions to ensure electroneutrality (Concentration 0.54M). The complete system (36557 atoms, periodic box of $62.5 \times 62.5 \times 97.6 \text{ \AA}^3$) contains the PEG_{200} -carboxylate, charged and placed in front of the nanopore. The total simulation time was 15.6 ns.

(ii) 11219 water molecules, 109 Na^+ and 107 Cl^- ions to ensure electroneutrality. The complete system (36513 atoms, periodic box of $62.5 \times 62.5 \times 97.6 \text{ \AA}^3$) contains the PEG_{600} -carboxylate, charged and placed in front of the nanopore. The total simulation time was 208.6 ns.

The same protocol was used by replacing the PEG carboxylates by the PEG and neutralizing the system by the corresponding number of the counter ions.

Results and discussion

Single nanopore fabrication

A high aspect ratio 5 nm nanopore based on polymer nanopore designed by ALD (figure 1) has been built following a procedure described elsewhere.^{14,15} In brief, single nanopores were produced using the track-etching technique on polyethylene terephthalate (PET) film (thickness 13 μm) following usual synthesis method.¹³ 20 single nanopores with a diameter close to 20 nm were synthesized and characterized. In order to tune the size (5 nm \pm 1 nm range) and the properties of the single nanopores, an ultrathin homogeneous film of oxides (Al_2O_3 and ZnO) was deposited on the inner surface of the pores using atomic layer deposition (ALD) technique. With this technique, we control the thickness of each layer, due to two separated self-limiting surface reactions, that provide a high degree of precision, as demonstrated in the literature for high aspect ratio structures.^{23, 31} The nanolaminate layer of $\text{Al}_2\text{O}_3/\text{ZnO}$ provides a soft coating with good adhesion on the polymer

surface²³, reduction of the roughness of the pore surface³² and permits a homogeneous coating along the nanopore (Figure 2a). An oxide bilayer thickness of 2.48 nm was determined by SAXS measurement inside the nanopore for Al₂O₃/ZnO nanolaminate.¹⁴ After the ALD deposition, the hydrophilic ZnO surface, covered with -OH groups, was converted to hydrophobic (CH₃)₃Si- surface by a Hexamethyldisilazane (HMDS) treatment (Figure 1).^{14, 15, 33} In addition, the HMDS plays an important role by preventing the corrosion of the ZnO coating in the NaCl solution.³⁴

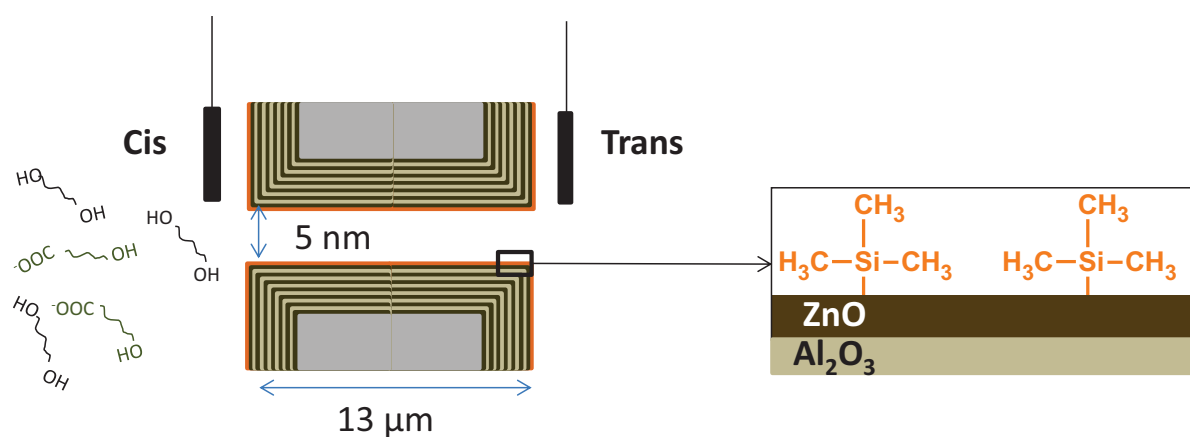


Figure 1: Schematic representation of nanopore designed by atomic layer deposition and experimental setup of both carboxylate and neutral PEGs detection.

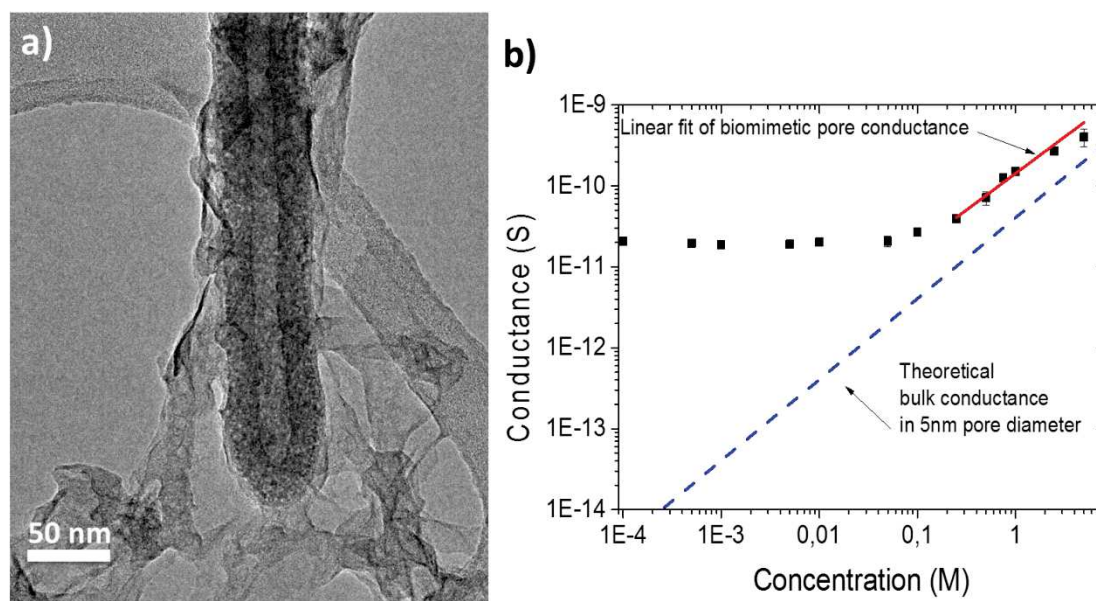


Figure 2: Single nanopore characterisations (a) TEM image of single nanopore of ~ 10 nm diameter which shows the homogeneous coating induced by ALD technique inside the $13\ \mu\text{m}$ length nanopore; The TEM image has been obtained on multipore PET membrane (average pores diameter 70 nm) after 12 sequences of 5 cycles Al_2O_3 /5 cycles ZnO deposited by ALD and followed by the elimination of the PET membrane. (b) Evolution of the conductance of a 5 nm diameter nanopore as a function of NaCl concentration; black squares the experimental data, in dashed line the theoretical conductance assuming a bulk transport.

The geometry of the 5 nm nanopore was characterized using concentration conductance dependence (Figure 2b) and a simple model of bulk transport in the range of NaCl concentration from 0.2 to 5 M. The diameter of the nanopore could be considered homogenous along its length ($13\ \mu\text{m}$) due to the conformal coating of ALD as shown on Figure 2a. The NaCl conductance concentration dependence is not linear at low concentrations. This behavior is usually observed for charged membrane or nanoslit¹⁹. In this case, the ionic transport inside the nanopore is induced by two phenomena: (i) the surface transport charge and (ii) the bulk transport charge as described previously.^{19, 20} Here the nanopore surface exhibits a zeta potential of -50 mV at pH 7 even if the trimethylsilane function is not charged and the surface is hydrophobic. This result is not surprising since ions can be adsorbed on hydrophobic surface depending on their polarisability, the ionic solution strength and/or the pH.³⁵ The translocation of both PEG_{Mw} and PEG_{Mw} -carboxylate ($M_w = 200$ and $600\ \text{g.mol}^{-1}$) from the cis compartment (Figure 1) at concentration 10^{15} and $10^{13}\ \text{molecules.mL}^{-1}$ respectively, has been analyzed under 0.63 M NaCl solution, where the Debye length (0.75 nm) is smaller but of the same order of magnitude than the nanopore radius.

PEG detection

We attempted first to detect the neutral PEG by applying positive potential to the cis chamber. Under this condition, PEG-carboxylates cannot translocate through the nanopore due to prohibitive polarity of the applied voltage. On the contrary, it has been already proven that PEG molecules could translocate through the nanopores^{4,36} as previously described in the case of single nanopore such as α -hemolysin,⁴ or polymer conical nanopore.¹⁷ In the latter case, PEG with M_w larger than 1000 g.mol⁻¹ have been detected if its hydrodynamic radius was similar to the nanopore one. In the present case the ionic current traces have exhibited no blockade events induced by PEG translocation (Figure 3a). This experimental result is not surprising because the hydrodynamic radius of PEG is lower than the nanopore diameter and PEG molecules do not provide sufficient sterical blockage. The latter can be verified by estimating the current blockade using the model proposed by Stojilkovic et al.³⁷ The ratio of conductance in the presence (σ) and in the absence (σ_0) of neutral PEG is equal to the ratio between the current (I) and the baseline current (I_0) at constant voltage³⁸. It varies according to the relation:

$$\frac{\sigma}{\sigma_0} = \frac{I}{I_0} \cong (1 - \phi) e^{\left(-K \frac{\phi}{(1-\phi)}\right)} \quad (1)$$

Here, ϕ represents the polymer volume fraction which, for one molecule in the pore, can be estimated as $\phi \approx r_{\text{PEG}}^3 / (L r_{\text{pore}}^2) \approx 10^{-5}$ (L is the pore length, r_{PEG} (table 1) and r_{pore} are the radii of PEG³⁹ and the nanopore respectively). K (≈ 2.7) is an experimental factor which depends on the PEG mass.³⁷ In our case, Equation 1 leads to $I/I_0 \approx 1 - \phi = 1 - 10^{-5}$. Thus the current blockade induced by the neutral PEG translocation is too small to be detected.

PEG-Carboxylate detection

When a negative potential was applied to the cis chamber (the chamber where the sample is placed), the charged PEG-carboxylate molecules could enter the pore and we observed a blockade of ionic current between two characteristic spikes for all samples (Figure 3b and 3c).

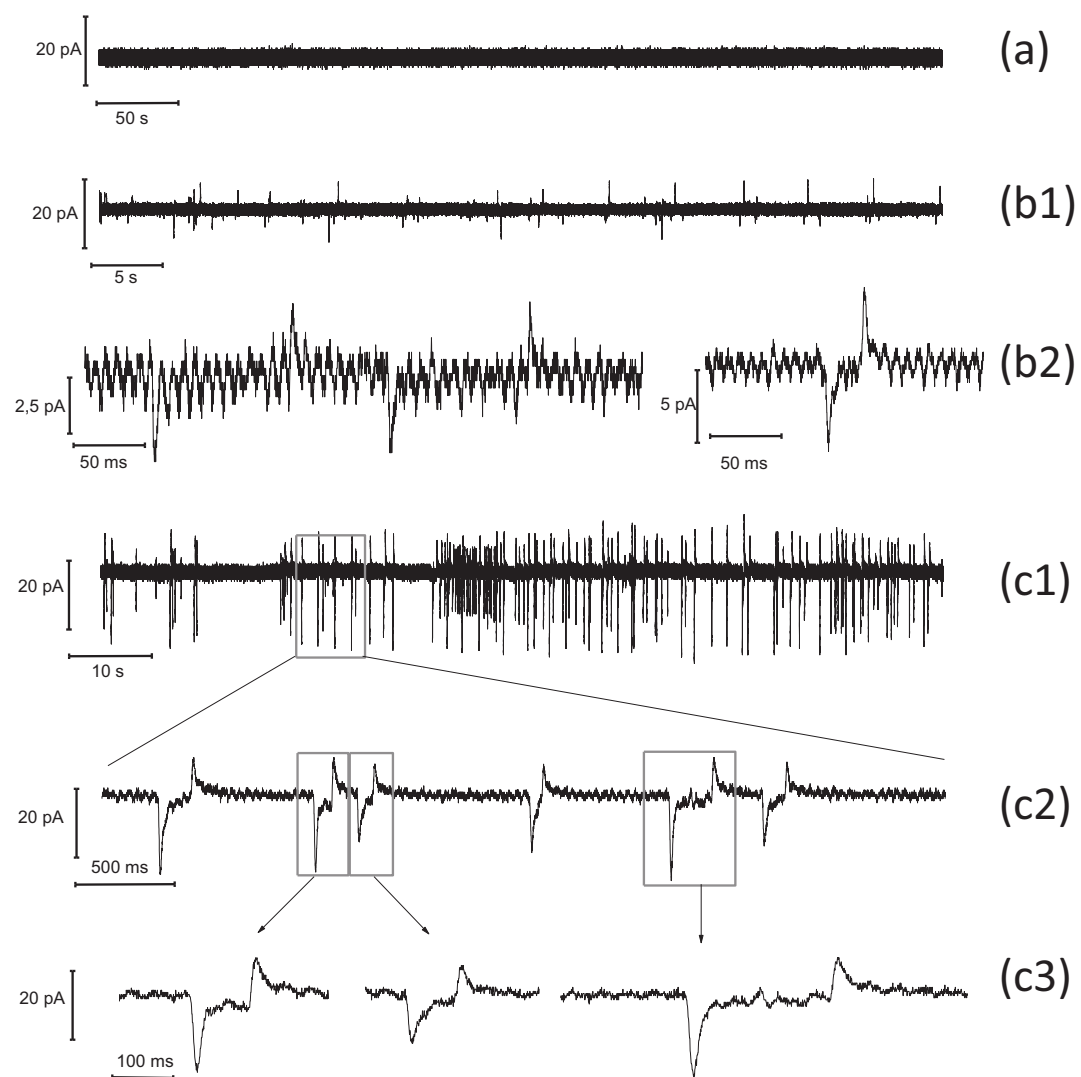


Figure 3: Typical current traces recorded for: (a) neutral PEG; (b1-2) PEG₂₀₀-carboxylate; (c1-3) PEG₆₀₀-carboxylate.

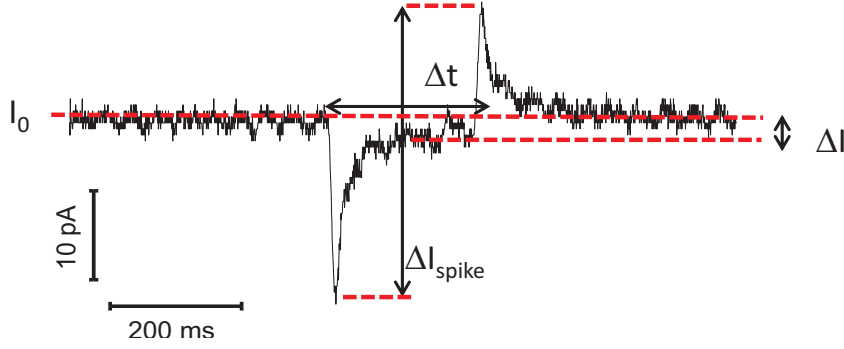


Figure 4 : detail of blockade current parameters are $\Delta I = I_0 - I$, Δt and $\Delta I_{\text{spike}} = I_{\text{max}} - I_{\text{min}}$

Taking into account the small size of the PEGs and the previous argument based on equation 1, this result is unexpected. Indeed, it is very likely that the translocation of the PEG-carboxylate could not be detected as for the neutral PEG. Moreover this kind of blockade signal has not been reported before in the literature for macromolecule detection using single nanopores. According to the experimental protocol described in the literature^{4, 16} and the absence of signal for neutral PEG detection when positive potential was applied, these current blockades could only be assumed as coming from negative PEG-carboxylate translocation through the nanopore. Three parameters could be used to characterize the blockade current (Figure 4 and Table 1): (i) the relative magnitude of the current blockade $\Delta I/I_0$, (ii) the dwell time Δt and (iii) the spike magnitude ΔI_{spike} . The histogram values of each parameter are shown on Figure 5.

There are several discrepancies between the observed experimental blockade current and the theoretical estimations:

- (i) The average values of $\Delta I/I_0$ (0.02 and 0.08 for PEG₂₀₀-carboxylate and PEG₆₀₀-carboxylate respectively) differ by 3 to 4 orders of magnitude from the values expected from Equation 1, where the conductance would be affected only by the tiny 10^{-5} volume fraction of PEG-carboxylate.
- (ii) The average dwell times measured for different molecules (0.1 s for PEG₂₀₀-carboxylate and 0.18 s for PEG₆₀₀-carboxylate) are larger by a factor 2 or 4 than the translocation times

determined from their classical electrophoretic velocity v (equation 2), assuming that the monocharged macromolecule adopts a coil structure:

$$v = \frac{|e| E}{6\pi\eta r} \quad (2)$$

where $e = -1.6 \times 10^{-19}$ C is the electron charge, r is the effective radius of PEG_{MW}-carboxylate (see table 1) under experimental electric field of 1.54×10^4 V/m, and η is the viscosity of water. According to this formula, the translocation time for (PEG₂₀₀ and PEG₆₀₀)-carboxylate should be 0.041 s and 0.046 s respectively.

- (iii) The spikes of the current observed at the beginning and the end of the blockade current have never been reported in the case of artificial nanopores. Similar spikes were observed in the literature during the fusion of vesicles with the cell membrane⁴⁰ that leads to an electrostatic capacitance modification of the cell membrane during the process (mainly due to the increase of the membrane area).

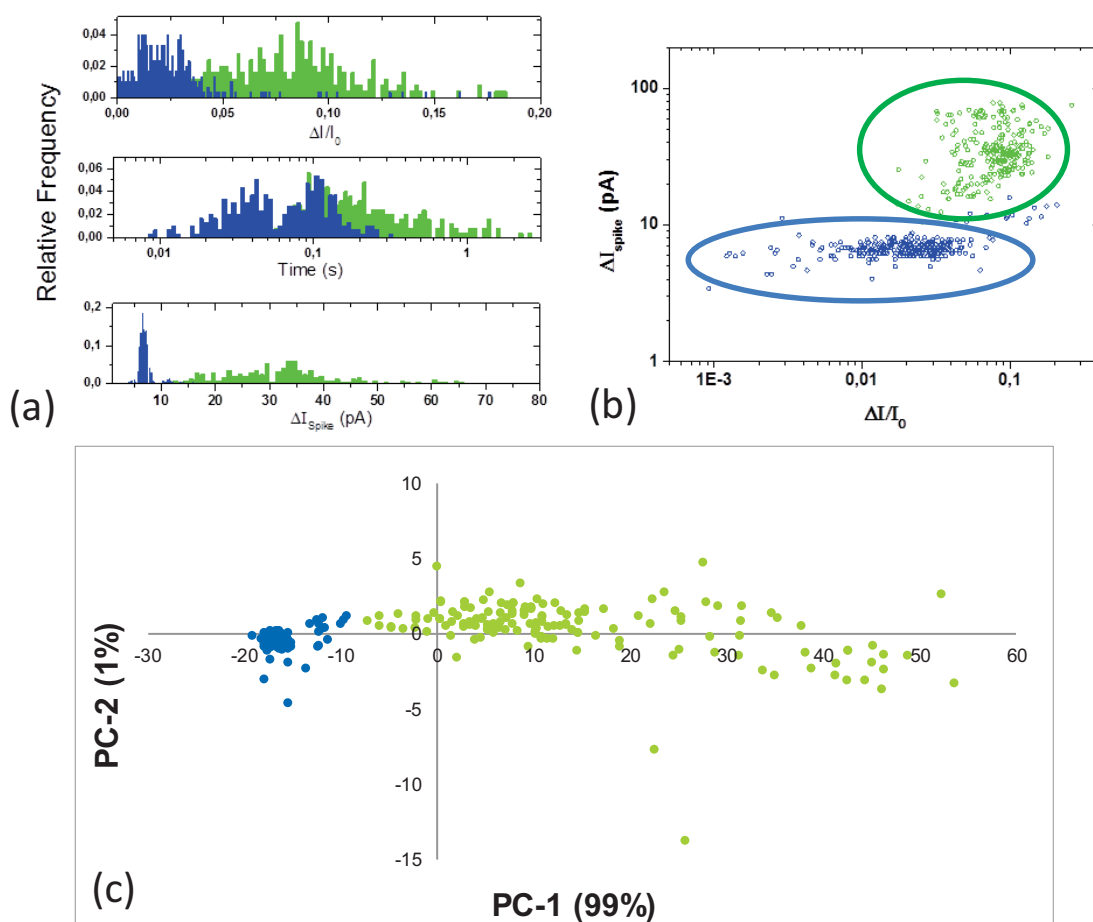


Figure 5: Distribution of the blockade current parameter: (a) dwell time Δt , (b) ΔI_{spike} and (c) $\Delta I/I_0$ for PEG_{MW}-carboxylate ($M_w = 200$ blue, and $M_w = 600$ green) (b) Map of the translocation events as ΔI_{spike} vs $\Delta I/I_0$ (c) Principal component (PC) analysis

We plotted the maps of the translocation events as a function of 2 out of 3 experimental parameters (Figure 5 and Figure S12). Regardless of the choice of parameters, all events associated with the PEG₂₀₀-carboxylate and PEG₆₀₀-carboxylate form two well distinguished groups. With the aim of getting efficient mapping of the blockade current signals in relation with the different PEG-carboxylate molar mass, a Principal Component Analysis (PCA) was performed on a set of 150 events randomly taken in the two groups of PEG-carboxylates ($M_w=200$ and 600). Each event was described by the raw experimental blockade parameters ΔI , Δt and ΔI_{spike} . Figure 5c shows the score plot corresponding to the first two principal components (PC). The two PEG classes can be distinguished:

PEG₂₀₀-carboxylate events are grouped in a well-defined cluster with a score on PC-1 equal to -20, the cluster of PEG₆₀₀-carboxylate broadens between the score -5 to 40 on PC-1 without overlapping. The first component (PC-1) captures 99.89 % of the variance and can therefore summarize alone the information carried by the original variables (ΔI , Δt and ΔI_{spike}). The projection of each event on PC-1 allows therefore getting the greatest source of information in the data set. The weight of each original variable on PC-1, called loading, reflects how much the individual variable contributes to that PC, and how well the PC takes into account the variation contained in a variable. PCA results show that the ΔI , Δt and ΔI_{spike} loadings on PC-1 are 0.069, -0.003 and 0.998 respectively meaning that ΔI_{spike} contributes highly to the separation of the events on PC-1. The PC analysis clearly shows that signal can be assigned to the PEG-carboxylate translocation through the nanopore and allows discriminating PEG₂₀₀-carboxylate from PEG₆₀₀-carboxylate. In addition, the PCA result shows that unusual ΔI_{spike} parameter is the more discriminant than the other ones. However, at this stage it is necessary to give an explanation of the unusual blocking currents.

Table 1 Average and square deviation of the 3 parameters issued from the experimental measurements for the different PEG-carboxylate molar mass. Theoretical Δt according to (eq. 2) with $E = 1.55 \cdot 10^4 \text{ V.m}^{-1}$

PEG-carboxylate Mw (g.mol ⁻¹)	$\Delta I/I_0$	ΔI_{spike} (pA)	Δt (s)	$r_{\text{PEG}}^{2/3}$ (nm)	Theoretical Δt (s)
200	0.02 ± 0.01	6.7 ± 0.7	0.10 ± 0.05	0.37	0.041
600	0.08 ± 0.04	31 ± 10	0.18 ± 0.08	0.63	0.046

Molecular dynamic simulation

In order to illustrate that both neutral PEG and PEG-carboxylate could be inserted into a single nanopore, all atom Molecular Dynamics (MD) simulations were performed. The PEGs molecules with different molar masses M_w were used in order to reproduce experimental conditions (number of monomers $n = 5, 13$ for PEG $M_w = 200$, and 600 respectively). Each PEG molecule was placed at the

distance of 2 nm from the nanopore entrance at the beginning of the simulation. A nanopore made of neopentane molecules arranged in a tubular geometry, which mimics the dielectric properties of experimental conditions well enough, was used (the pore is covered by the methyl groups both in experiment and in simulations). The diameter of the nanopore was 6 nm and the length was 4 nm, mimicking an experimental nanopore entrance. A fixed voltage of 200 mV was applied along the pore. Spontaneous insertion of the PEGs into the nanopore was observed in all simulations (Table 2). For PEG-carboxylate, the dynamics of the insertion shows dependency on the molar mass M_w while the mechanism of insertion is quite similar in all cases. The PEG diffuses randomly in the solvent, adopting sometimes a compact spherical conformation, until one of its terminals attaches to the nanopore wall (Figure 6). Then the PEG- carboxylate molecule unfolds and permeates progressively into the pore until its total insertion. The unfolding time of the PEG-carboxylate depends on its molar mass. The most striking fact is that the PEG₆₀₀ carboxylate molecule stays inside the nanopore during the whole simulation time (for 185 ns), while the PEG₂₀₀-carboxylate is moving throughout the nanopore quickly in 4.9 ns. It can be noted that velocity ratio $V_{th}/V_{exp} = 6.2 \cdot 10^3$ is in same order the electric field ratio $E_{th}/E_{exp} = 3.2 \cdot 10^3$. For neutral PEG, the insertion mechanism is similar; however the insertion time does not seem to depend on the molar mass. Note that these molecular dynamics results have been obtained over a shorter nanopore length than the experimental one. They should thus be taken into account cautiously. However they suggest that both neutral PEG and PEG-carboxylates can enter and translocate easily through the nanopores.

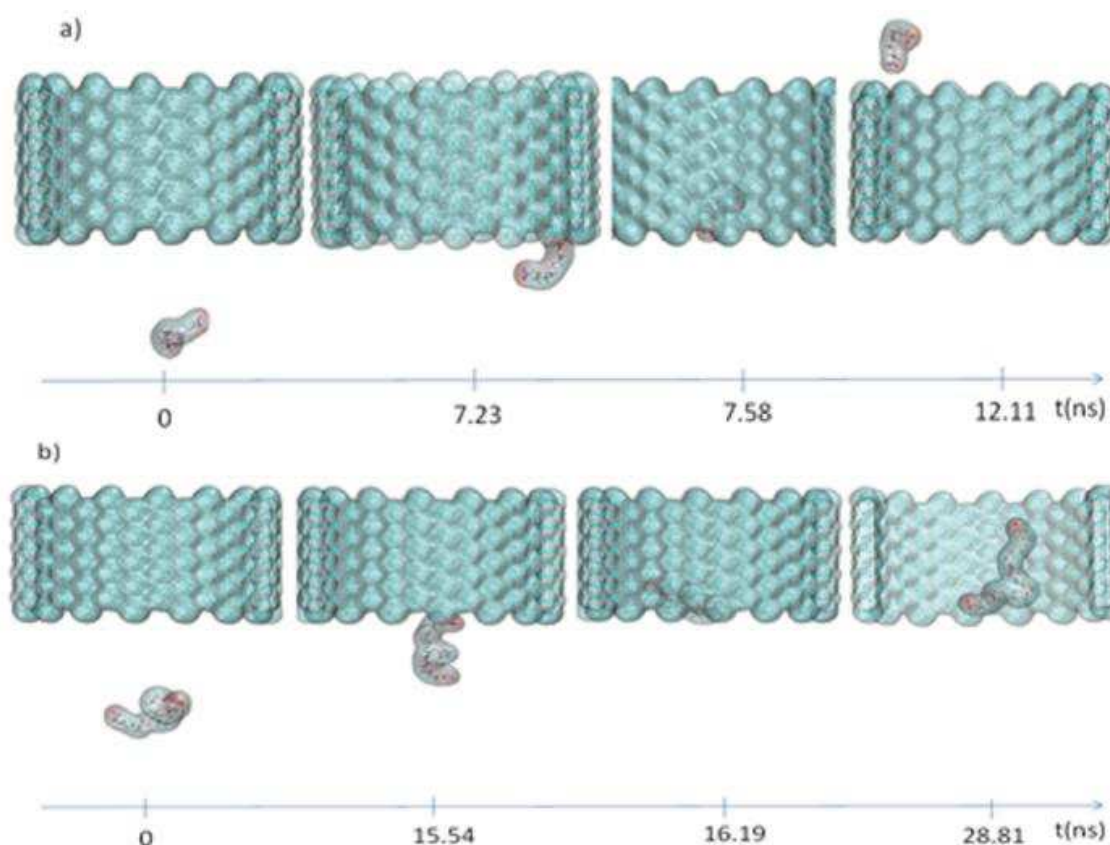


Figure 6: Snapshots of MD simulations from the insertion of PEG_{MW}-carboxylate with different M_W: (a) 200 and (b) 600 in a neopentane of 6 nm diameter and 4 nm length. Only one part of the PEG_{MW}-carboxylate participates to the insertion of the molecule. Then, it diffuses rapidly along the nanopore wall until the complete molecular incorporation.

Table 2. Theoretical times of insertion for the different neutral PEG and PEG-carboxylate molar mass in a nanopore with 6 nm diameter. The errors have been calculated through the fluctuations of the PEG position near the entrance of the pore.

	M _w (g.mol ⁻¹)	Beginning of insertion	End of insertion	Insertion duration
Neutral PEG	200	10.0 ± 0.1 ns	12.3 ± 0.2 ns	2.3 ± 0.2 ns
	600	0.2 ± 0.1 ns	2.1 ± 0.1 ns	1.9 ± 0.2 ns
PEG-carboxylate	200	7.2 ± 0.4 ns	7.6 ± 0.3 ns	0.4 ± 0.2 ns
	600	15 ± 1 ns	16 ± 1 ns	0.7 ± 0.5 ns

To go further, a detailed analysis of the simulations results was performed to extract the different behaviors between both neutral PEG and PEG-carboxylates during their insertion into a nanopore. Figure 7 shows the normalized radial distribution as the function of the ion and the PEGs molecules in the simulation box. A value of 1 indicates the more favorable position between the two species during the simulations.

It is clearly seen that the PEG carboxylates are located a little bit further from the pore wall than the neutral PEG. The maximum differences distance between the both neutral PEG and PEG carboxylate can reach 0.7 Å for the PEG₂₀₀ and 0.9 Å for the PEG₆₀₀ during the simulation. The ion distribution inside the nanopore is not homogenous as should be expected in a bulk system. They mainly organize in ring at around 10 Å of the surface wall. This kind of ionic organization has been previously reported by Cazade et al.⁴¹ in the case of carbon nanotube (diameter 3 nm). The radial distribution of the ions positions are affected by the PEG during the simulation (Figure 7). Due to the small shift of the mean center of mass and the different charges of both neutral PEG and PEG-carboxylates, the ions are located nearer the pore (around 10 ± 0.5 Å) with a charged PEG compared to a neutral one (around 11 ± 0.5 Å). It can be noted that the ions centers of mass are already moved away from the pore wall of a distance equal to around 1 Å when the macromolecule is inserted. Such small differences could not be at the origin of the blockade appearance.

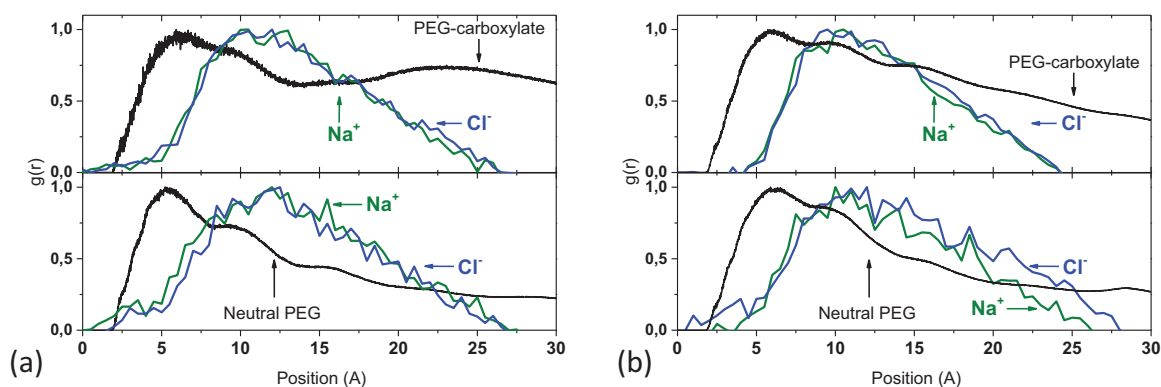


Figure 7: Normalized radial distribution function ($g(r)$), normalized to the maximum, of both PEG-carboxylate (black line) and neutral PEG (black line), ion Na^+ (green line) and ion Cl^- (blue line) as a function of wall pore distance for the PEGs molar mass 200 (a) and 600 (b). Here the position 0 Å and position 30 Å correspond to the wall of nanopore and center of nanopore respectively.

The analyses of the ionic mean positions around both neutral PEG and PEG-carboxylate have also been performed (Figure 8). It is clear that the anions are not organized around the neutral PEG or PEG-carboxylate on a long distance. On the contrary, the cation distributions present clearly an important peak only around the PEG-carboxylates at a distance of 3 ± 0.5 Å. These peaks come from the global annealing of the charges around the PEG carboxylates and the attractive interactions regarding the negatively charged PEG and the cations that allow compensating the charges depletion around the PEG.

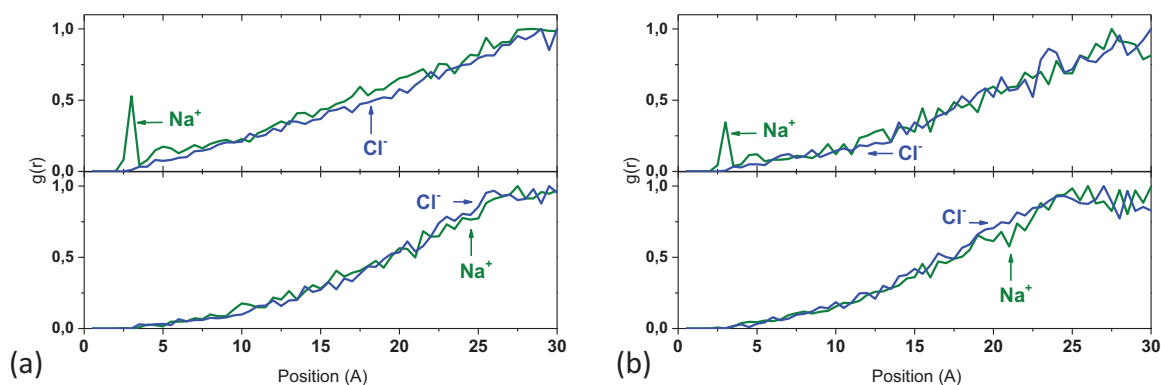


Figure 8: Normalized radial distribution function ($g(r)$), normalized to the maximum, of ion Na^+ (green line) and ion Cl^- (blue line) as a function of the distance of the PEG-ion for the PEGs molar mass 200 (a) and 600 (b). Here the position 0 Å corresponds to the position of neutral PEG or PEG-Carboxylate.

Unusual blockade current interpretation

To sum up, our experiments have shown that neutral PEG translocation through 5 nm nanopore does not lead to the blockade signal of ionic current in accordance with the equation 1. In contrast, PEG carboxylate translocation induces blockades of ionic current between two unusual current spikes, which could not be predicted by any model until now. In addition, the dwell times of PEG carboxylates are longer than expected from equation 2. Finally the parameters of the blockade events are directly depending on the molar mass of the PEG-carboxylate. The possible explanation of this observation, based on the molecular dynamics results could be the following.

The molecular dynamics simulations clearly show that both PEG and PEG-carboxylate (i) adopt unfolded structure on the pore entrance and inside the nanopore and (ii) have interactions with the nanopore surface which cannot be neglected during the permeation. This can explain long dwell times, which are not consistent with the model of transport of spherical coils in bulk solvent as assumed in equation 2. However regarding molecular dynamics simulation results, it is very difficult to point out particular evidence of the origin of the unusual blockade current. The only differences in overall ionic distributions between the PEG and PEG-carboxylates in our simulations are small shifts of the radial distribution maxima. This shift is so small that it is unlikely to cause such dramatic effects as blocking of the current. However, organized shell of cations around the PEG carboxylate molecules may play a major role since it does not exist for neutral PEG. It can be noted that PEG carboxylate and cation move in the opposite way under electric field. The ionic current through the nanopore has been estimated in Figure 9, together with the PEG₂₀₀ mass incorporation where entrance and exit events have been obtained during the simulations. A value of 34 nA for the PEG corresponds to a total encapsulation of the molecules in the nanopore. As expected, the ionic current is very fluctuating, due to the random flow of charges in the nanopore. However, performing averages of the current depending on the PEG incorporation leads to specific values close to the experimental behavior. Indeed, when the PEG carboxylate diffuses inside the nanopore the mean ionic current is clearly lowered compared to the situation where the nanopore is empty of charged PEG. The entrance and exit events lead also to sudden decrease and increase of the average current,

similar to the experimental spikes. For the PEG, the same calculations lead to comparable observations. However, the blockade current (ΔI) is clearly lower (close to 0, as theoretically estimated) and the spikes values are so small that it could be not observed experimentally. The electrostatic interaction in the nanopore between the charged macromolecules and their neighborhood are thus responsible for a high current modification observed in our experiments.

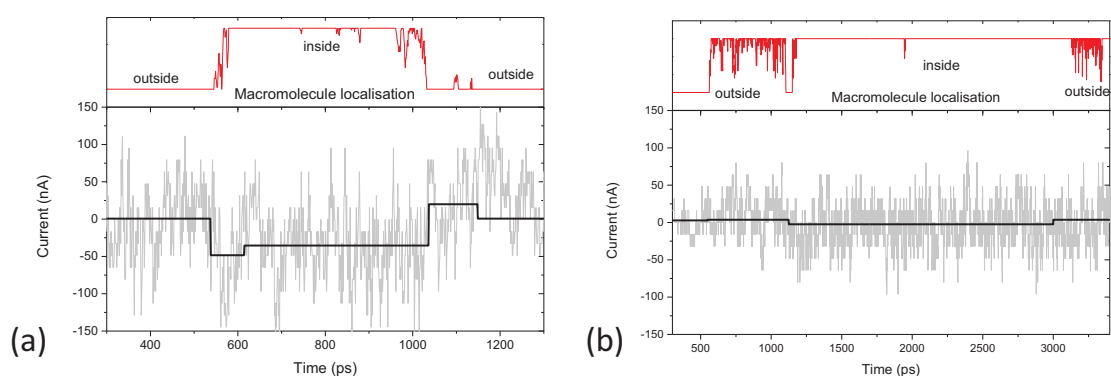


Figure 9: Ionic current calculated by MD simulation (bottom) and macromolecule localization (top) for: (a) PEG₂₀₀-carboxylate; ($M_w=200\text{g.mol}^{-1}$) and (b) neutral PEG₂₀₀.

Experimental measurement of ionic (Figure 2b) current shows clearly that the nanopore exhibits similar conductance concentration dependence than surface charge nanopore while the trimethylsilane functional groups are not charged. The charge appears due to the ions located close to the pore wall, which form a pseudo electrical layer close to the nanopore surface. Thus the recorded current is composed by the ionic fluxes from both bulk solution (in the middle of the pore) and from bulk solution (in interaction near the wall). The latter acts as a capacitance and cannot be disregarded as suggested in the work performed by Schoch *et al.* and Shimizu *et al.* on nanoslits.^{19, 20} Based on this and taking into account the position of the PEG carboxylates near the nanopore wall (shown by MD simulation), the charged macromolecule penetrates inside the nanopore with its close cation shell. Then it blocks the flowing positive charges (partially or over the full length of pore) and releases it only when it leaves the nanopore. This could contribute to perturb the ionic flow close to

the nanopore surface since these charges mobility should decrease compared to the ones which participate to the permanent current. It is possible to speculate that the PEG-carboxylate molecule in interaction with the cations impose a barrier to the opposite cation flow in the nanopore, which comes from the high difference of drift velocity between the macromolecule and the permeating ion. This should affect the nanopore conductance by lowering the current as observed in the experiments data.

The spikes of the current observed at the entrance and the exit of the PEG-carboxylate molecules could also be explained by the same mechanism. When the PEG-carboxylate enters the nanopore, the organization of the cation shell partially blocks their pore entrance which induces charge depletion inside the nanopore. Thus, the ionic current should strongly decrease until the depletion is balanced by the influx of ions from solutions. In contrast, when the PEG-carboxylate molecule exits the pore, it does not partially block cation flux, which induces the entrance of cation inside the pore and causes a strong increase of the current before the ionic distribution recovers its equilibrium state. This phenomena could be linked to an increase of the pore capacitance upon the insertion of the PEG-carboxylates which is dependent on their cation shell directly connected with the PEG-carboxylate molecular mass (Figure 5b).

Conclusion

We have studied the translocation of different PEG molecules with $M_w = 200 \text{ g.mol}^{-1}$ and 600 g.mol^{-1} through nanopores with high aspect ratio tailored by atomic layer deposition. Neutral PEG was not detected in a classical experimental setup. In contrast it is possible to detect the translocation of PEG-carboxylate molecules through the pores, which causes an unusual blockade of the ionic current, this blockade strongly depending on the macromolecule molar mass.

Such a blockade is interpreted as a structuring of a cation shell around the PEG-carboxylate which perturbs the ionic transport near the surface of the pore. The volume polarization and capacitance effects caused by the difference of drift velocities between the PEG-carboxylate and small permeating cations may thus also induce such experimental behavior.

This work shows that the transport phenomena in the nanopores with high aspect ratio induced by the macromolecule translocation are not easy to understand. They require additional experimental and computational studies. It is also shown that it is possible to detect small charged macromolecules with hydrodynamic radius lower than the radius of the nanopore. However, more experiments should be performed using macromolecules, nanopores with different chemical functions/charges and other saline solution in order to better illustrate these phenomena.

Acknowledgment

The authors are indebted to Dr. Jean-Baptiste Thibaud (Laboratoire de Biochimie et Physiologie Moléculaire des Plantes, Montpellier) for the fruitful discussion. This study has received financial support from "Health" theme (axe santé) of the European Membrane Institute and the Carnot Institute CED2. Single tracks have been produced in GANIL (Caen, France) in the framework of an EMIR project. Computations have been performed on the supercomputer facilities of the Mésocentre de calcul de Franche-Comté.

References

- (1) Fologea, D.; Gershow, M.; Ledden, B.; McNabb, D. S.; Golovchenko, J. A.; Li, J. L., Detecting single stranded DNA with a solid state nanopore. *Nano Lett* **2005**, 5 (10), 1905-1909.

- (2) Storm, A. J.; Storm, C.; Chen, J. H.; Zandbergen, H.; Joanny, J. F.; Dekker, C., Fast DNA translocation through a solid-state nanopore. *Nano Lett* **2005**, 5 (7), 1193-1197.
- (3) Hall, A.; Scott, A.; Rotem, D.; Mehta, K.; Bayley, H.; Dekker, C., Hybrid Biological/Solid-State Nanopores. *Biophys J* **2011**, 100 (3), 168-168, Manrao, E. A.; Derrington, I. M.; Laszlo, A. H.; Langford, K. W.; Hopper, M. K.; Gillgren, N.; Pavlenok, M.; Niederweis, M.; Gundlach, J. H., Reading DNA at single-nucleotide resolution with a mutant MspA nanopore and phi29 DNA polymerase. *Nat Biotechnol* **2012**, 30 (4), 349-U174.
- (4) Robertson, J. W. F.; Rodrigues, C. G.; Stanford, V. M.; Robinson, K. A.; Krasilnikov, O. V.; Kasianowicz, J. J., Single-molecule mass spectrometry in solution using a solitary nanopore. *P Natl Acad Sci USA* **2007**, 104 (20), 8207-8211.
- (5) Kasianowicz, J. J.; Robertson, J. W. F.; Chan, E. R.; Reiner, J. E.; Stanford, V. M., Nanoscopic Porous Sensors. *Annu Rev Anal Chem* **2008**, 1, 737-766.
- (6) Tsutsui, M.; Hongo, S.; He, Y. H.; Taniguchi, M.; Gemma, N.; Kawai, T., Single-Nanoparticle Detection Using a Low-Aspect-Ratio Pore. *Acs Nano* **2012**, 6 (4), 3499-3505.
- (7) Bacri, L.; Oukhaled, A. G.; Schiedt, B.; Patriarche, G.; Bourhis, E.; Gierak, J.; Pelta, J.; Auvray, L., Dynamics of Colloids in Single Solid-State Nanopores. *J Phys Chem B* **2011**, 115 (12), 2890-2898.
- (8) Siwy, Z. S.; Howorka, S., Engineered voltage-responsive nanopores. *Chem Soc Rev* **2010**, 39 (3), 1115-1132.
- (9) Vlassiuk, I.; Smirnov, S.; Siwy, Z., Ionic selectivity of single nanochannels. *Nano Lett* **2008**, 8 (7), 1978-1985.
- (10) Kowalczyk, S. W.; Blosser, T. R.; Dekker, C., Biomimetic nanopores: learning from and about nature. *Trends Biotechnol* **2011**, 29 (12), 607-614.
- (11) Schneider, G. F.; Dekker, C., DNA sequencing with nanopores. *Nat Biotechnol* **2012**, 30 (4), 326-328.
- (12) Sirijarukul, S.; Balanzat, E.; Vasina, E. N.; Dejardin, P., Flat sheet membrane with controlled variation of pore density and pore size in a direction parallel to the surface. *J Membrane Sci* **2007**, 296 (1-2), 185-194.
- (13) Apel, P. Y., Track etching technique in membrane technology. *Radiation Measurements* **2001**, 34, 559-566.
- (14) Abou Chaaya, A.; Le Poitevin, M.; Cabello-Aguilar, S.; Balme, S.; Bechelany, M.; Kraszewski, S.; Picaud, F.; Cambedouzou, J.; Balanzat, E.; Janot, J. M.; Thami, T.; Miele, P.; Dejardin, P., Enhanced Ionic Transport Mechanism by Gramicidin A Confined Inside Nanopores Tuned by Atomic Layer Deposition. *J Phys Chem C* **2013**, 117 (29), 15306-15315.
- (15) Cabello-Aguilar, S.; Balme, S.; Abou Chaaya, A.; Bechelany, M.; Balanzat, E.; Janot, J. M.; Pochat-Bohatier, C.; Miele, P.; Dejardin, P., Slow translocation of polynucleotides and their discrimination by α -hemolysin inside a single track-etched nanopore designed by atomic layer deposition. *Nanoscale* **2013**, 5, 9582-9586.
- (16) Baaken, G.; Ankri, N.; Schuler, A. K.; Ruhe, J.; Behrends, J. C., Nanopore-Based Single-Molecule Mass Spectrometry on a Lipid Membrane Microarray. *Acs Nano* **2011**, 5 (10), 8080-8088.
- (17) Siwy, Z.; Gu, Y.; Spohr, H. A.; Baur, D.; Wolf-Reber, A.; Spohr, R.; Apel, P.; Korchev, Y. E., Rectification and voltage gating of ion currents in a nanofabricated pore. *Europhys Lett* **2002**, 60 (3), 349-355.
- (18) Lev, A. A.; Korchev, Y. E.; Rostovtseva, T. K.; Bashford, C. L.; Edmonds, D. T.; Pasternak, C. A., Rapid Switching of Ion Current in Narrow Pores - Implications for Biological Ion Channels. *P Roy Soc B-Biol Sci* **1993**, 252 (1335), 187-192.
- (19) Schoch, R. B.; Han, J. Y.; Renaud, P., Transport phenomena in nanofluidics. *Rev Mod Phys* **2008**, 80 (3), 839-883.

- (20) Shimizu, S.; Ellison, M.; Aziz, K.; Wang, Q. H.; Ulissi, Z.; Gunther, Z.; Bellisario, D.; Strano, M., Stochastic Pore Blocking and Gating in PDMS-Glass Nanopores from Vapor-Liquid Phase Transitions. *J Phys Chem C* **2013**, *117* (19), 9641-9651.
- (21) Hojo, K.; Susuki, Y.; Sasaki, M.; Maeda, M.; Smith, T. J.; Kawasaki, K., Improved preparation of an amino acid type poly(ethylene glycol) derivative. *Chem Pharm Bull* **2002**, *50* (7), 1001-1003, Wang, J. Q.; He, L. N.; Miao, C. X.; Gao, J., The Free-Radical Chemistry of Polyethylene Glycol: Organic Reactions in Compressed Carbon Dioxide. *Chemsuschem* **2009**, *2* (8), 755-760.
- (22) Bachmann, J.; Zierold, R.; Chong, Y. T.; Hauert, R.; Sturm, C.; Schmidt-Grund, R.; Rheinlander, B.; Grundmann, M.; Gosele, U.; Nielsch, K., A practical, self-catalytic, atomic layer deposition of silicon dioxide. *Angew Chem Int Edit* **2008**, *47* (33), 6177-6179.
- (23) Raghavan, R.; Bechelany, M.; Parlinska, M.; Frey, D.; Mook, W. M.; Beyer, A.; Michler, J.; Utke, I., Nanocrystalline-to-amorphous transition in nanolaminates grown by low temperature atomic layer deposition and related mechanical properties. *Appl Phys Lett* **2012**, *100* (19).
- (24) Elias, J. E.; Bechelany, M.; Utke, I.; Erni, R.; Hosseini, D.; Michler, J.; Philippe, L., Urchin-inspired zinc oxide as building blocks for nanostructured solar cells. *Nano Energy* **2012**, *1* (696-705).
- (25) Phillips, J. C.; Braun, R.; Wang, W.; Gumbart, J.; Tajkhorshid, E.; Villa, E.; Chipot, C.; Skeel, R. D.; Kalé, L.; Schulten, K., Scalable molecular dynamics with NAMD. *Journal of Computational Chemistry* **2005**, *26* (16), 1781-1802.
- (26) Feller, S., Constant pressure molecular dynamics simulation: The Langevin piston method. *J. Chem. Phys.* **1995**, *103* (11), 4613.
- (27) Darden, T.; York, D.; Pedersen, L., Particle mesh Ewald: An N.log(N) method for Ewald sums in large systems. *J. Chem. Phys.* **1993**, *98* (12), 10089-10092.
- (28) Ryckaert, J.-P.; Ciccotti, G.; Berendsen, H. J. C., Numerical integration of the cartesian equations of motion of a system with constraints: molecular dynamics of n-alkanes. *J. Comput. Phys.* **1977**, *23*, 327-341, Andersen, H. C., Rattle: a velocity version of the SHAKE algorithm for molecular dynamics calculations. *J. Comput Phys.* **1983**, *52*, 24-34.
- (29) MacKerell, A. D.; Bashford, D.; Bellott, Dunbrack, R. L.; Evanseck, J. D.; Field, M. J.; Fischer, S.; Gao, J.; Guo, H.; Ha, S.; Joseph-McCarthy, D.; Kuchnir, L.; Kuczera, K.; Lau, F. T. K.; Mattos, C.; Michnick, S.; Ngo, T.; Nguyen, D. T.; Prodhom, B.; Reiher, W. E.; Roux, B.; Schlenkrich, M.; Smith, J. C.; Stote, R.; Straub, J.; Watanabe, M.; Wirkiewicz-Kuczera, J.; Yin, D.; Karplus, M., All-Atom Empirical Potential for Molecular Modeling and Dynamics Studies of Proteins *The Journal of Physical Chemistry B* **1998**, *102* (18), 3586-3616.
- (30) Makowski, M.; Czaplewski, C.; Liwo, A.; Scheraga, H. A., Potential of Mean Force of Association of Large Hydrophobic Particles: Toward the Nanoscale Limit. *J Phys Chem B* **2010**, *114* (2), 993-1003.
- (31) Marichy, C.; Bechelany, M. B.; Pinna, N., Atomic Layer Deposition of Nanostructured Materials for Energy and Environmental Applications. *Advanced Materials* **2012**, *24*, 1017-1032.
- (32) Jensen, J. M.; Oelkers, A. B.; Toivola, R.; Johnson, D. C.; Elam, J. W.; George, S. M., X-ray reflectivity characterization of ZnO/Al₂O₃ multilayers prepared by atomic layer deposition. *Chem Mater* **2002**, *14* (5), 2276-2282.
- (33) Bechelany, M.; Brodard, P.; Philippe, L.; Michler, J., Extended domains of organized nanorings of silver grains as surface-enhanced Raman scattering sensors for molecular detection. *Nanotechnology* **2009**, *20* (45).
- (34) Cimat, K. A.; Mahurin, S. M.; Meyer, K. A.; Shaw, R. W., Nanoscale Chemical Imaging of Zinc Oxide Nanowire Corrosion. *J Phys Chem C* **2012**, *116* (18), 10405-10414.

- (35) Zimmermann, R.; Freudenberg, U.; Schweiss, R.; Kuttner, D.; Werner, C., Hydroxide and hydronium ion adsorption - A survey. *Curr Opin Colloid In* **2010**, *15* (3), 196-202.
- (36) Lan, W. J.; Holden, D. A.; Zhang, B.; White, H. S., Nanoparticle Transport in Conical-Shaped Nanopores. *Anal Chem* **2011**, *83* (10), 3840-3847.
- (37) Stojilkovic, K. S.; Berezhkovskii, A. M.; Zitserman, V. Y.; Bezrukov, S. M., Conductivity and microviscosity of electrolyte solutions containing polyethylene glycols. *J Chem Phys* **2003**, *119* (13), 6973-6978.
- (38) Krasilnikov, O. V.; Rodrigues, C. G.; Bezrukov, S. M., Single polymer molecules in a protein nanopore in the limit of a strong polymer-pore attraction. *Phys Rev Lett* **2006**, *97* (1).
- (39) Gassara, S.; Chinpa, W.; Quemener, D.; Ben Amar, R.; Deratani, A., Pore size tailoring of poly(ether imide) membrane from UF to NF range by chemical post-treatment using aminated oligomers. *J Membrane Sci* **2013**, *436*, 36-46.
- (40) Sombers, L. A.; Hanchar, H. J.; Colliver, T. L.; Wittenberg, N.; Cans, A.; Arbault, S.; Amatore, C.; Ewing, A. G., The effects of vesicular volume on secretion through the fusion pore in exocytotic release from PC12 cells. *J Neurosci* **2004**, *24* (2), 303-309, Simonsson, L.; Kurczy, M. E.; Trouillon, R.; Hook, F.; Cans, A. S., A functioning artificial secretory cell. *Sci Rep-Uk* **2012**, *2*.
- (41) Cazade, P. A.; Dweik, J.; Coasne, B.; Henn, F.; Palmeri, J., Molecular Simulation of Ion-Specific Effects in Confined Electrolyte Solutions Using Polarizable Forcefields. *J Phys Chem C* **2010**, *114* (28), 12245-12257.

Supporting information

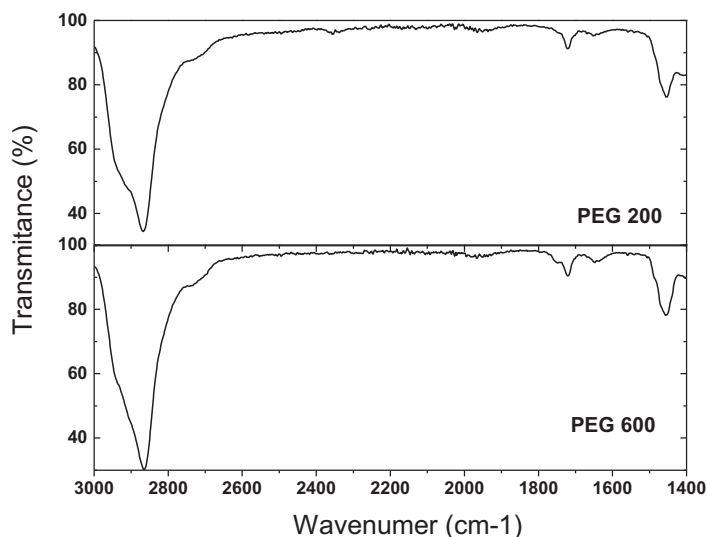
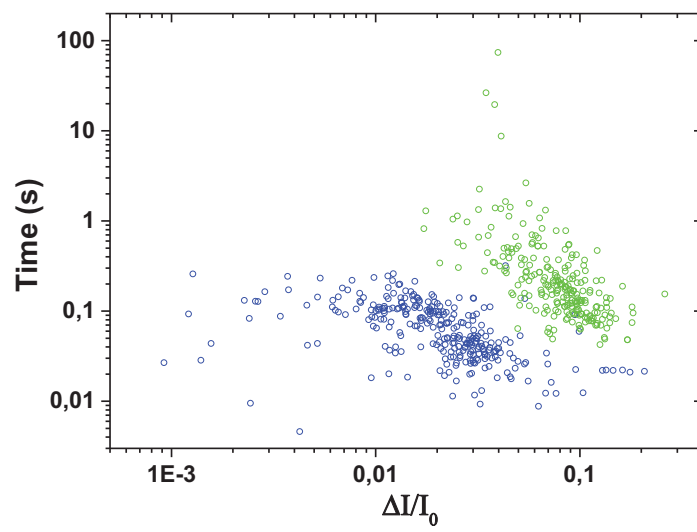
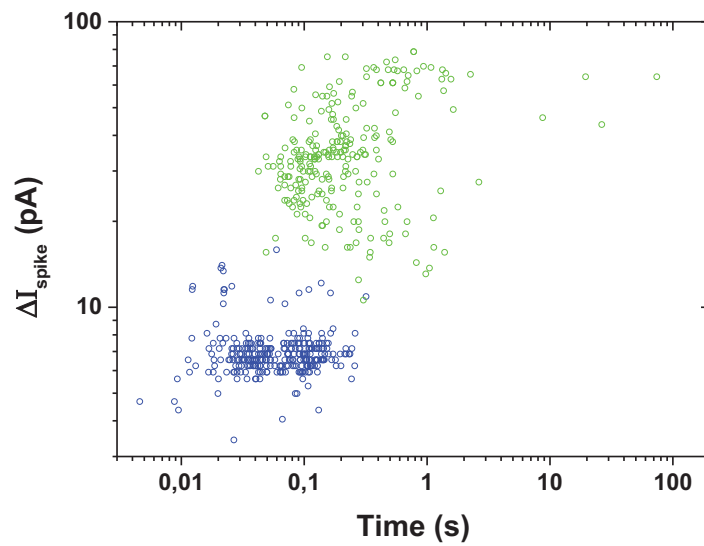


Figure SI1 : FTIR spectra of PEGs samples.



dwel time



dwel time

Figure SI2 : Map of the translocation events as a function of 2 among the 3 experimental parameters

Annex-b-

Nanowires with controlled porosity for hydrogen production†

Cite this: *J. Mater. Chem. A*, 2013, **1**, 2133

Mikhael Bechelany,* Adib Abou Chaaya, Fabien Frances, Ouadia Akdim, Didier Cot, Umit B. Demirci* and Philippe Miele

Porous nanowires are of great interest for applications in solar cells, thermoelectrics, gas sensors, fuel cells and catalysis. Here we report on a general methodology for NWs with highly ordered connected macroporosity using a low-cost and scalable synthesis method based on the combination of hard templating with electrodeposition. The greatly improved catalytic performance of these porous NWs (ca. 600% increasing compared to dense NWs) in the hydrolysis of ammonia borane makes them exciting materials for the implementation of hydrolytic boron hydrides as hydrogen carriers for fuel cell applications.

Received 22nd October 2012
Accepted 28th November 2012

DOI: 10.1039/c2ta00794k

www.rsc.org/MaterialsA

A Introduction

Global warming, depletion of the resources and increasing costs have made fossil fuels undesirable for our future. Alternative solutions have been searched for and intense research has been dedicated to hydrogen.¹ Of the solutions envisaged, liquid-phase hydrogen storage materials (e.g. aqueous solutions of hydrolytic boron hydrides, hydrazine or formic acid) are attractive by the fact that, in the presence of a metal-based catalyst and under mild conditions, they are able to liberate hydrogen.² Catalytic hydrolysis of ammonia borane has particularly attracted a great deal of attention³ and most of the works focused on developing cheap and reactive metal-based catalysts.² Cobalt is representative of that; it is known as one of the less expensive metals and its reactivity can be improved *via* various strategies. An efficient approach to tune the reactivity of a catalytic material like cobalt is nanostructuring:⁴ e.g. monodisperse nanoparticles,⁵ nanoparticles dispersed onto a support,⁶ core-shell particles,⁷ and alloys.^{8,9}

From the abundant literature dedicated to catalysis in hydrolysis of ammonia borane, it stands out that the catalytic activity can be enhanced by (i) increasing the specific surface area of the catalysts and (ii) preventing the nanostructures agglomeration.⁴ Both are key factors, and our nanostructured catalysts (discussed herein) were developed accordingly.

Moreover, in order to improve the performance of nanomaterials in environmental, health and renewable energy

applications, a lot of research is devoted to understand the effect of size, morphology, organization, crystallinity and porosity on the performance of the target devices.¹⁰ Nanodesign of materials, with hierarchical nanometric channels,¹¹ containing both interconnected macroporous and mesoporous structures, is under investigation for a wide range of applications in different fields such as solar cells,¹² hydrogen generation¹³ and sensors.¹⁴ Among these nanomaterials, porous nanowires (p-NWs) have attracted a lot of attention because they present the advantages of both 1D nanostructures and high surface area materials. Different methods have been investigated for the synthesis of p-NWs including hard templating,¹⁵ block-copolymer self-assembly,¹⁶ dealloying,¹⁷ and hydrothermal growth.¹⁸

The present work describes the synthesis of Co NWs with highly ordered connected macroporosity using an easy process based on hard templating (track etched polycarbonate membrane and polystyrene spheres) together with electrodeposition. Track etched polycarbonate membranes¹⁹ as well as colloidal crystals²⁰ are widely investigated as hard templates due to their easy synthesis process and commercial availability. Our study reveals a high performance of these hierarchical nanostructures in the hydrolysis of ammonia borane. With proper control of the size of the NWs, the macroporosity dimension as well as the connection between the macropores, the mass transport and the surface area along the materials mass can be tuned and/or improved. In other words, nano-designing the porosity inside the NWs may provide a solution for the synthesis of practical catalysts for ammonia borane hydrolysis and H₂ generation as well as for applications in different fields such as solar cells,²¹ thermoelectrics,²² gas sensors,²³ and fuel cells.²⁴

European institute of membranes (IEM, UMR 5635, ENSCM-UM2-CNRS), University of Montpellier 2, Place E. Bataillon, F-34095, Montpellier, France. E-mail: Mikhael.Bechelany@univ-montp2.fr; umit.demirci@um2.fr; Fax: +33 04 6714 9119; Tel: +33 04 6714 9167

† Electronic supplementary information (ESI) available. See DOI: 10.1039/c2ta00794k

B Materials and methods

1 Materials

Ammonia borane (AB, NH_3BH_3) from Sigma Aldrich, 97%, was stored and handled in an argon-filled glove box (MBraun M200B, $\text{H}_2\text{O} < 0.1$ ppm, $\text{O}_2 < 0.1$ ppm) to prevent the sample from moisture and air. Cobalt(II) chloride hexahydrate ($\text{CoCl}_2 \cdot 6\text{H}_2\text{O}$), sodium chloride (NaCl), boric acid (H_3BO_3), potassium iodide (KI), iodine (I_2), ethanol, chloroform and toluene were purchased from Sigma Aldrich and used as received. Ultra-pure deionized water (Milli-Q grade; resistivity $> 18 \text{ M}\Omega \text{ cm}$) was used to dissolve AB. Commercially available PS microsphere suspension (radii $\sim 500 \text{ nm}$, 100 nm , 50 nm , and 35 nm , 4 wt% aqueous dispersion) was bought from Duke Scientific. WhatmanCyclopore polycarbonate membranes (25 mm membrane diameter and $13 \mu\text{m}$ membrane thickness) with different pore diameters from Aldrich were used.

2 Synthesis of porous NWs

A commercially available polycarbonate membrane is used as the nanoelectrode. In a typical experiment, a 200 nm thick gold layer serving as the back electrode is evaporated using a physical vapor deposition (PVD) process onto one side of the membrane. Additionally, the specimens are immersed in water at 80°C for 30 min in order to activate the alcoholic functions ($-\text{OH}$) and carboxylic acid groups ($-\text{COOH}$) on the surface of the membrane and inside the pores. 20 μL of PS nanosphere suspension (4 wt% aqueous dispersion) are diluted with an equal volume of ethanol and deposited (drop-by-drop using a micro-pipette) onto the surface of the membrane. The suspension is then dried in air at room temperature for 30 min, and the spheres self-assembled into a close-packed colloidal crystal structure with three-dimensional ordered lattices *via* attractive capillary forces inside the pores membrane. After drying, the PC membrane with PS is heated in an oven (at 110°C for 10 min) to sinter the PS and adhere it to the membrane pores. Electroplating is done in a glass cell, with a reference electrode and a counter-electrode consisting of a Pt grid. The porous nanowires (p-NWs) formation, which takes place inside the pores of the membrane, is carried out at -2 V from a 1 M CoCl_2 , $6\text{H}_2\text{O}$ + 0.7 M H_3BO_3 + 0.11 M NaCl aqueous solution, without agitation and at room temperature. By subsequently dissolving the PC membrane and the PS spheres in chloroform and toluene, freestanding p-NWs are obtained. $\sim 15 \text{ mg}$ of NWs has been obtained in a typical experiment.

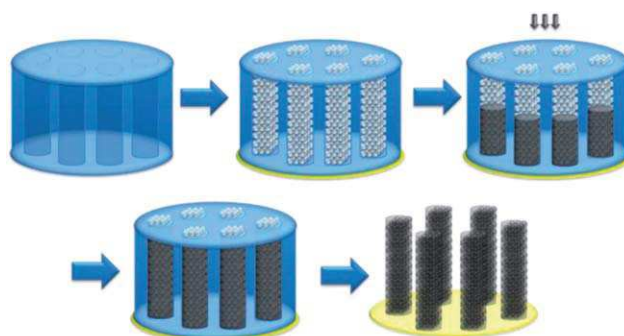
The NWs are then observed by scanning electron microscopy (SEM, S-4800, Hitachi), Energy-dispersive X-ray spectroscopy (SEM, S-4500, EDX-ThermoFisher), X-ray diffraction (PAN-AlyticalXpert-PRO diffractometer equipped with a X'celerator detector using Ni-filtered Cu-radiation), BET (Micromeritics ASAP-2020), and XPS (performed at "Science et Surface", in Ecully, France, using a PHI Quantera SXM spectrometer equipped with an Al $K\alpha$, $h\nu = 280 \text{ eV}$, 47.7 W; the spectrometer binding energy (BE) scale was calibrated using the position of C 1s core level, 284.8 eV).

3 Hydrolysis of ammonia borane

The hydrogen generation measurement by hydrolysis of AB is performed as follows. The catalyst (15 mg) is introduced into the reactor consisting of a glass tube (27.5 mL) sealed with a silicon septum. The reactor is then placed in a water bath thermostated at 50°C and connected to a water-filled inverted burette. An acidic and a cold trap are put between the reactor and the burette to condensate ammonia and steam. An aqueous solution of NH_3BH_3 (1 M) is prepared. To start the hydrolysis, 4 mL of the NH_3BH_3 solution (*ca.* 120 mg of the hydride) is injected into the reactor. The H_2 evolution is then measured. Actually, the experiment is video-recorded so that the H_2 generation is analyzed afterwards. The hydrogen generation rates (HGRs) in mL min^{-1} are calculated by dividing the H_2 volume (ideally, at 50% of conversion of NH_3BH_3) by the time necessary to reach this volume; a HGR in $\text{mL min}^{-1} \text{g}_{\text{Co}}^{-1}$ is also calculated by dividing by the weight of the cobalt catalyst.

C Results and discussion

The schematic view in Scheme 1 illustrates the processes involved in the formation of the p-NWs with highly ordered connected macroporosity. The p-NWs have been obtained by combining self-assembly of polystyrene spheres together with electrodeposition. After evaporating a thin gold layer serving as the back electrode on the PC membrane, the specimens are immersed in water at 80°C for 30 min in order to activate the alcoholic functions ($-\text{OH}$) and carboxylic acid groups ($-\text{COOH}$) on the surface and inside the pores of the membrane. The PS nanosphere suspension is deposited onto the surface of the membrane. The suspension is then dried. The PS spheres self-assemble into a close-packed colloidal crystal structure with three-dimensional ordered lattices *via* attractive capillary forces inside the membrane pores. The PC membrane with the PS spheres is heated in an oven (at 110°C for 10 min) to sinter the PS and adhere it to the membrane pores. The membrane is then fixed with the electrode facing down onto a conducting substrate (Al plate) and the opposite area is exposed to the electrolyte. Electroplating is done in a glass cell, with a reference electrode and a counter-electrode consisting of a Pt grid. The p-NW formation, which takes place inside the pores of the



Scheme 1 Schematic view of the synthesis route for p-NWs with controlled connected macroporosity.

membrane, is carried out at -2 V from a 1 M $\text{CoCl}_2 \cdot 6\text{H}_2\text{O}$ + 0.7 M H_3BO_3 + 0.11 M NaCl aqueous solution, without stirring and at room temperature. By subsequently dissolving the PC membrane and the PS spheres in chloroform and toluene, freestanding p-NWs are obtained.

The NWs were then observed by scanning electron microscopy (Fig. 1). Fig. 1a shows that the electrodeposition of Co inside the membrane channels followed by the membrane and spheres elimination creates a close-packed array of aligned and monodispersed p-NWs (see the movie in the ESI†). No residual carbon was observed after membrane and sphere dissolution as attested by EDX characterization (Fig. 1d). The XRD diffraction of the porous Co NWs is shown in ESI S11.† The diffraction peaks correspond to (100), (002) and (101) of the hexagonal phase of cobalt that is generally observed for materials elaborated by electrodeposition.²⁵ The SEM image (Fig. 1c) of the backside of a part of the membrane shown in Fig. 1 clearly shows that these parallel and straight NWs are porous (see the movie in the ESI†). The as-produced NWs show a uniform radius ($r = 500$ nm), which matches that of the PC membrane channels.

Fig. 1c shows that 3D ordered macropores are formed inside the submicron wire structures. These macropores are the replication of the 100 nm radius ordered PS spheres. Fig. 1b shows that smaller holes appeared to connect the macropores between them; these holes result from the contact between the original PS spheres. Our 1D nanostructures consist then in hierarchical submicron wires. The macropores are all connected together with holes.

The advantage of this PC membrane/PS sphere patterning method compared to other lithographic methods is that it is simple and fast. In addition, both the diameter of the NWs and the size of the connected macroporosity can be controlled to a certain extent so that pattern variations can be easily achieved. By modifying the size of the PC membrane pores, p-NWs of different diameters can be obtained and, effectively, were elaborated in the present work. Fig. 2a and Fig. 2b and c show

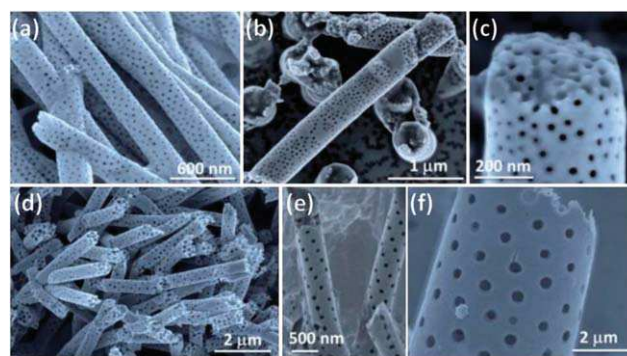


Fig. 2 SEM images of Co p-NWs obtained by using (a) PC membrane with $r = 100$ nm and PS spheres with $R_1 = 35$ nm, (b and c) PC membrane with $r = 200$ nm and PS spheres with $R_1 = 35$ nm, (d) PC membrane with $r = 200$ nm and PS spheres with $R_1 = 50$ nm, (e) PC membrane with $r = 200$ nm and PS spheres with $R_1 = 100$ nm and (f) PC membrane with $r = 2500$ nm and PS spheres with $R_1 = 500$ nm.

p-Co NWs obtained by using PC membranes with $r = 100$ nm and $r = 200$ nm, respectively. The radius (R_1) of the PS spheres was fixed to 35 nm. By changing the size of the PS spheres, we obtained Co p-NWs with different macroporosity. Fig. 2d and e show the Co p-NWs obtained by using PS spheres of $R_1 = 50$ nm and $R_1 = 100$ nm, respectively, inside PC membrane pores with $r = 200$ nm. Fig. 2f shows Co p-NWs resulting from using a PC membrane with $r = 2500$ nm and PS spheres of $R_1 = 500$ nm.

We note here that it is also possible to tune the porosity inside the single p-NWs. Fig. 3a and b show SEM images of porous Co NWs obtained by infiltrating a PC membrane of $r = 500$ nm with a suspension of PS spheres ($R_1 = 35$ nm) followed by a PS suspension of $R_2 = 100$ nm. Fig. 3b and c show p-Co NWs obtained by infiltrating a PC membrane of $r = 500$ nm with a suspension of 50% PS spheres ($R_1 = 100$ nm) and 50% PS spheres ($R_2 = 35$ nm). Fig. 3d shows p-NWs resulting from the infiltration of a PC membrane of $r = 2500$ nm with a suspension of 50% PS spheres ($R_1 = 500$ nm) and 50% PS spheres ($R_2 = 35$ nm). It is also possible to tune the connected holes (mesoporosity) inside the NWs by heating the PS spheres at different times and different temperatures.²⁶

The specific surface S_1 ($\text{m}^2 \text{g}^{-1}$) of non-porous NWs is reported below (see ESI S12†):

$$S_1 (\text{m}^2 \text{g}^{-1}) = \frac{2}{D} \left(\frac{1}{r} + \frac{1}{L} \right) \quad (1)$$

where r is the NW radius, L is the NW length and D is the cobalt density.

For p-NWs infiltrated with one size of PS spheres, the specific surface S_2 ($\text{m}^2 \text{g}^{-1}$) is (see ESI S13†):

$$S_2 (\text{m}^2 \text{g}^{-1}) = \frac{\frac{\pi\sqrt{2}}{2R_1}}{\left(1 - \frac{\pi\sqrt{2}}{6}\right) \times D} + \frac{2}{D} \left(\frac{1}{r} + \frac{1}{L} \right) \quad (2)$$

where R_1 is the PS sphere radius and D is the cobalt density.

Assuming that we use two kinds of different size PS spheres R_1 and R_2 ($R_1 > R_2$), the specific surface area S_3 ($\text{m}^2 \text{g}^{-1}$) is:

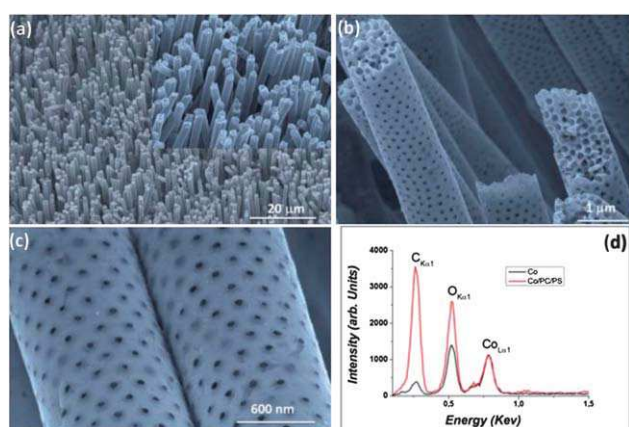


Fig. 1 (a–c) SEM images at different magnifications of Co p-NWs obtained by using a PC membrane with $r = 500$ nm and PS spheres with $R_1 = 100$ nm and (d) EDX spectra of the resulting Co NWs before (red spectrum) and after (black spectrum) elimination of PC/PS.

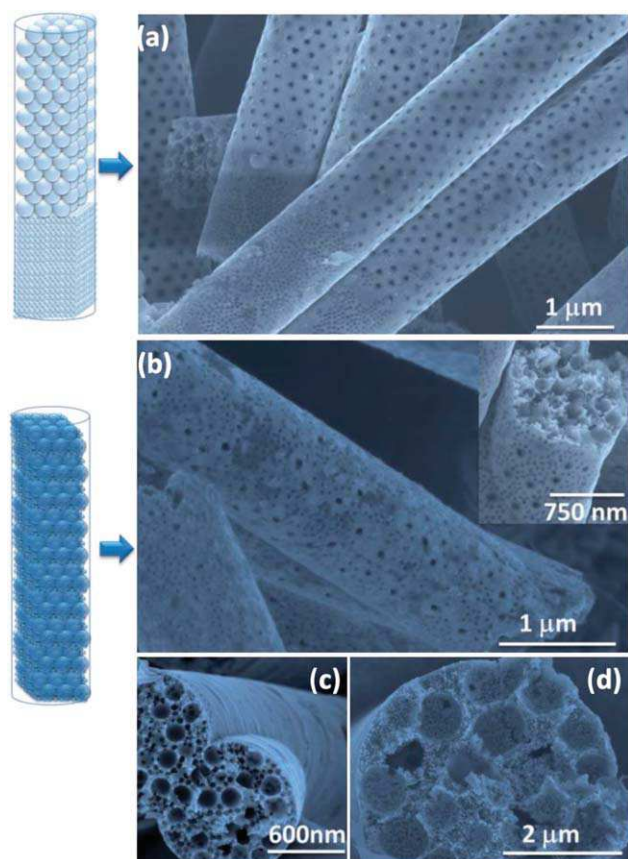


Fig. 3 SEM images of Co p-NWs obtained (a) by infiltrating a PC membrane of $r = 500$ nm pore with a suspension of PS spheres ($R_1 = 35$ nm) followed by a PS suspension ($R_2 = 100$ nm), (b and c) by infiltrating a PC membrane of $r = 500$ nm with a suspension of 50% PS spheres ($R_1 = 100$ nm) and 50% PS spheres ($R_2 = 35$ nm) and (d) by infiltrating a PC membrane of $r = 2500$ nm with a suspension of 50% PS spheres ($R_1 = 500$ nm) and 50% PS spheres ($R_2 = 35$ nm).

$$S_3 (\text{m}^2 \text{g}^{-1}) = \frac{\frac{\pi\sqrt{2}}{2} \left[\frac{1}{R_1} + \frac{1}{R_2} \times \left(1 - \frac{\pi\sqrt{2}}{6} \right) \right]}{\left(1 - \frac{\pi\sqrt{2}}{6} \right)^2 \times D} + \frac{2}{D} \left(\frac{1}{r} + \frac{1}{L} \right) \quad (3)$$

The theoretical calculation of the specific surface area is detailed in the ESI (SI2, SI3 and SI4†) and is in agreement with another more elaborated model developed elsewhere by Cooke and Rowe.²⁷ The calculated specific surface area for typical nanostructures is summarized in Table 1. This table shows that the NW diameter, the macropore sizes and the surface areas can be tuned in a wide range using PC membranes and PS spheres with different radii. The specific surface areas have been confirmed for some selected samples using the BET method (ESI SI6†) and they are reported in Table 2. The experimental measurements by BET of the surface area of the p-NWs are slightly superior to the calculated values. This phenomenon could be attributed to the Co NWs roughness induced by the small Co nanocrystallites produced by electrodeposition (XRD measurement; ESI, SI1†). The comparison of calculated surface

Table 1 Calculated surface area for non-porous NWs, Co p-NWs with one size of PS spheres and Co p-NWs with two sizes of PS spheres

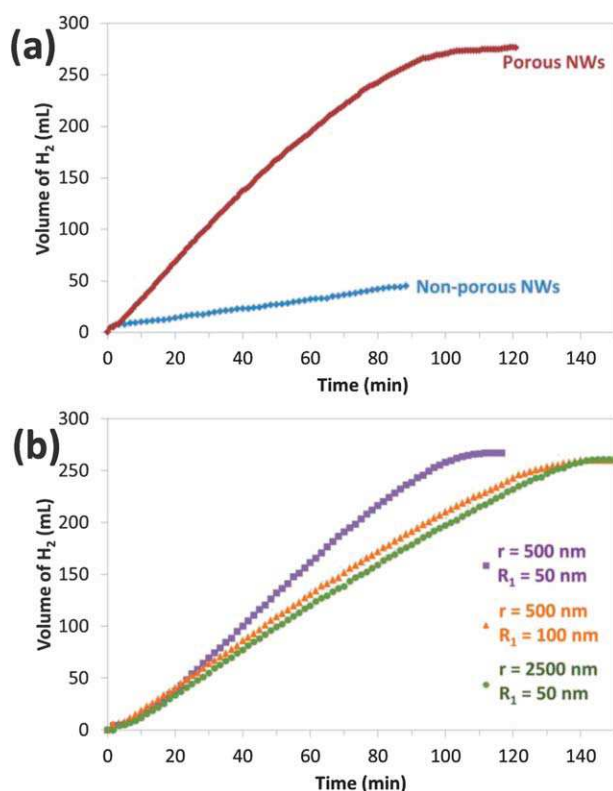
NWs radius (r) [nm]	First PS spheres radius (R_1) [nm]	Second PS spheres radius (R_2) [nm]	S [$\text{m}^2 \text{g}^{-1}$]
100			2.26
100	35		29.76
200			1.14
200	35		28.64
200	50		20.34
200	50	35	102.63
500			0.466
500	35		27.966
500	50		19.66
500	100		10.086
500	50	35	101.956
500	100	35	64.956
2500			0.107
2500	50		19.307
2500	100		9.727
2500	500		2.027
2500	100	35	64.597

areas, BET results and the experimental measurements of the hydrogen generation rate for different non-porous and porous Co NWs are summarized in Table 2. The hydrogen evolutions for non-porous and porous Co NWs are presented in Fig. 4a. As expected, bringing a porosity to the Co NWs ($r = 100$ nm; blue curve vs. $r = 100$ nm and $R_1 = 35$ nm; red curve) significantly improves the reactivity of the catalyst. The p-NWs hydrolyze totally ammonia borane within 90 min whereas with the non-porous NWs the conversion reaches solely 33%. Hydrogen generation rates of ca. 0.5 and 3.4 mL min^{-1} were calculated, respectively. The improvement is concomitant with the increase of the specific surface area (Table 2), and is in agreement with Özkaz's observations.⁴ Because of the magnetic properties of cobalt, the non-porous and p-NWs were analyzed by XPS (ESI; SI5†) in the presence of the polycarbonate membrane and/or PS spheres (*i.e.* before its destruction). Carbon in high contents was thus detected. The presence of oxygen may be attributed to mainly O=C bonds (O 1s binding energies 531.5–532.2 eV), and in a lesser extent to O-Co bonds (O 1s binding energies 530.1–530.3 eV) and to O-B bonds (O 1s binding energies 533.0–533.7 eV). The last attribution is confirmed by the binding energies (192.3–192.4 eV) measured for the boron element (B 1s).²⁸ With respect to Co 2p3/2, the binding energies (781.3–781.6 eV) are ascribed to an oxidized state, which likely occurred post-synthesis.²⁸ The same samples were then analyzed after being used in a hydrolysis experiment. The characterization was performed after a thorough washing with deionized water. No difference was observed in comparison to the fresh samples, except for the fact that, as generally observed with the cobalt catalysts,²⁸ more boron in the borate form are found after hydrolysis. For example, its content on the surface of the p-NWs was found to be higher than 25 at.%, whereas it was less than 1 at.% before hydrolysis.

The reactivity of the p-NWs was compared. The hydrogen evolutions are shown in Fig. 4b. First, we varied the radius of the

Table 2 Calculated specific surface area, BET measurement and hydrogen generation rate, HGR (mL min^{-1} and $\text{mL min}^{-1} \text{g}_{\text{Co}}^{-1}$), of non-porous and Co p-NWs

Co NWs catalyst	Calculated S [$\text{m}^2 \text{g}^{-1}$]	BET measurement [$\text{m}^2 \text{g}^{-1}$]	HGR [mL min^{-1}]	HGR [$\text{mL min}^{-1} \text{g}_{\text{cata}}^{-1}$]
Non-porous, $r = 100 \text{ nm}$	2.26	1.2	0.5	33
$r = 100 \text{ nm}$, $R_1 = 35 \text{ nm}$	29.76		3.4	227
$r = 500 \text{ nm}$, $R_1 = 50 \text{ nm}$	19.66	23.5	2.7	180
$r = 500 \text{ nm}$, $R_1 = 100 \text{ nm}$	10.086	14.7	2.2	147
$r = 2500 \text{ nm}$, $R_1 = 50 \text{ nm}$	19.307		2	133

**Fig. 4** Hydrogen evolution (mL), obtained with (a) non-porous Co NWs $r = 100 \text{ nm}$ (blue curve), and Co p-NWs $r = 100 \text{ nm}$ and $R_1 = 35 \text{ nm}$ (red curve) and (b) Co p-NWs $r = 500 \text{ nm}$, and $R_1 = 50 \text{ nm}$ (violet curve); $r = 500 \text{ nm}$, and $R_1 = 100 \text{ nm}$ (orange curve); $r = 2500 \text{ nm}$, and $R_1 = 50 \text{ nm}$ (green curve).

PS spheres (R_1) while keeping constant the radius of the NWs (*i.e.* $r = 500 \text{ nm}$). With the decrease of R_1 from 100 to 50 nm, thus of the pores size, the reactivity of the catalysts is improved: 2.2 (yellow curve) and 2.7 mL min^{-1} (violet curve), respectively. This is consistent with the increase of the specific surface area (Table 2), and confirms the results discussed above. Second, we varied the radius of the NWs ($r = 500$ and 2500 nm) while keeping constant the radius of the PS spheres (*i.e.* $R_1 = 50 \text{ nm}$). The as-obtained materials showed similar specific surface areas (Table 2). Such a change was however detrimental to the reactivity of the NWs. The hydrogen generation rate decreased, with values of 2.7 (violet curve) and 2 mL min^{-1} (green curve), respectively. This may be explained by mass transport limitations. With a radius of 2500 nm, the diffusion path is long and the ammonia borane molecules have more chances to hydrolyze on the reactive surface of the first hundred nm than to diffuse

up to the NW core. From these results, we can conclude that (i) the increase of the specific surface area of the NWs by providing an internal porosity is an efficient approach to gain catalytic reactivity, and (ii) the radius of the NWs is a critical factor due to diffusion limitations. Therefore, we believe that the reactivity of the NWs could be further tuned by mixing PS spheres with different diameters; such a work is in progress.

D Conclusions

In summary, we have investigated a novel route to produce NWs with highly ordered macroporosity by the combination of electrodeposition and hard templating (PS nanospheres and PC membrane). The process allows a good tuning of the porosity, the specific surface area and the radius of the obtained Co NWs. A significantly improved catalytic performance in the hydrolysis of ammonia borane has been observed. In this study we have elucidated a correlation between the radius, the porosity size and the specific surface area of the Co NWs, and the catalytic activity. We can conclude that the increase of the specific surface area of the NWs, which is provided by the porosity, is an efficient approach to gain catalytic reactivity, and that the radius of the NWs seems to be a critical factor likely due to diffusion limitations. This method opens the door for the synthesis of a wide range of metallic and semiconducting NWs. The technique we propose herein is versatile since we are able to synthesize metal NWs and bimetallic NWs with different compositions using electrodeposition, but also oxide and non-oxide using, for instance, atomic layer deposition. The possibility of tuning the surface area, the size of the connected macroporosity, and the chemical composition should allow the applications of these p-NWs in other fields such as sensors, photocatalytic, and photovoltaic applications.

Acknowledgements

We thank Dr Julien Cambedouzou, Mr Abdeslam El-mansouri, Mr Jordan Rey and Mr Kevin Wisniewski for scientific discussion. The present work was funded by the Agence National pour la Recherche (ANR) through the project JCJC BoraHCx.

Notes and references

- U. Eberle, M. Felderhoff and F. Schueth, *Angew. Chem., Int. Ed.*, 2009, **48**, 6608–6630.
- H.-L. Jiang, S. K. Singh, J.-M. Yan, X.-B. Zhang and Q. Xu, *ChemSusChem*, 2010, **3**, 541–549.

- 3 U. Sanyal, U. B. Demirci, B. R. Jagirdar and P. Miele, *ChemSusChem*, 2011, **4**, 1731–1739.
- 4 S. Ozkar, *Appl. Surf. Sci.*, 2009, **256**, 1272–1277.
- 5 O. Metin, V. Mazumder, S. Ozkar and S. Sun, *J. Am. Chem. Soc.*, 2010, **132**, 1468–1469.
- 6 P.-Z. Li, A. Aijaz and Q. Xu, *Angew. Chem., Int. Ed.*, 2012, **51**, 6753–6756.
- 7 H.-L. Jiang, T. Akita and Q. Xu, *Chem. Commun.*, 2011, **47**, 10999–11001.
- 8 F. Y. Qiu, Y. J. Wang, Y. P. Wang, L. Li, G. Liu, C. Yan, L. F. Jiao and H. T. Yuan, *Catal. Today*, 2011, **170**, 64–68.
- 9 D. Sun, V. Mazumder, O. Metin and S. Sun, *ACS Nano*, 2011, **5**, 6458–6464.
- 10 S. Guo and E. Wang, *Acc. Chem. Res.*, 2011, **44**, 491–500.
- 11 Z. Y. Yuan and B. L. Su, *J. Mater. Chem.*, 2006, **16**, 663–677.
- 12 (a) J. Elias, M. Bechelany, I. Utke, R. Erni, D. Hosseini, J. Michler and L. Philippe, *Nano Energy*, 2012, **1**, 696–705; (b) J. Elias, C. Levy-Clement, M. Bechelany, J. Michler, G.-Y. Wang, Z. Wang and L. Philippe, *Adv. Mater.*, 2010, **22**, 1607–1612.
- 13 (a) C. E. Bunker and M. J. Smith, *J. Mater. Chem.*, 2011, **21**, 12173–12180; (b) P. E. de Jongh and P. Adelhelm, *ChemSusChem*, 2010, **3**, 1332–1348; (c) H. Reardon, J. M. Hanlon, R. W. Hughes, A. Godula-Jopek, T. K. Mandal and D. H. Gregory, *Energy Environ. Sci.*, 2012, **5**, 5951–5979.
- 14 C. Marichy, M. Bechelany and N. Pinna, *Adv. Mater.*, 2012, **24**, 1017–1032.
- 15 (a) F. Li, J. B. He, W. L. L. Zhou and J. B. Wiley, *J. Am. Chem. Soc.*, 2003, **125**, 16166–16167; (b) Y. Y. Wu, T. Livneh, Y. X. Zhang, G. S. Cheng, J. F. Wang, J. Tang, M. Moskovits and G. D. Stucky, *Nano Lett.*, 2004, **4**, 2337–2342.
- 16 X. Chen, M. Knez, A. Berger, K. Nielsch, U. Goesele and M. Steinhart, *Angew. Chem., Int. Ed.*, 2007, **46**, 6829–6832.
- 17 L. Liu, E. Pippel, R. Scholz and U. Goesele, *Nano Lett.*, 2009, **9**, 4352–4358.
- 18 K. Koczur, Q. Yi and A. Chen, *Adv. Mater.*, 2007, **19**, 2648–2652.
- 19 J. H. Moon and S. Yang, *Chem. Rev.*, 2010, **110**, 547–574.
- 20 (a) A. Stein, F. Li and N. R. Denny, *Chem. Mater.*, 2008, **20**, 649–666; (b) X. Ye and L. Qi, *Nano Today*, 2011, **6**, 608–631.
- 21 (a) M. Bechelany, E. Berodier, X. Maeder, S. Schmitt, J. Michler and L. Philippe, *ACS Appl. Mater. Interfaces*, 2011, **3**, 3866–3873; (b) Y. Qu, L. Liao, Y. Li, H. Zhang, Y. Huang and X. Duan, *Nano Lett.*, 2009, **9**, 4539–4543.
- 22 G. Yuan, R. Mitdank, A. Mogilatenko and S. F. Fischer, *J. Phys. Chem. C*, 2012, **116**, 13767–13773.
- 23 L. Jia, W. Cai, H. Wang, F. Sun and Y. Li, *ACS Nano*, 2009, **3**, 2697–2705.
- 24 Z.-Y. Zhou, N. Tian, J.-T. Li, I. Broadwell and S.-G. Sun, *Chem. Soc. Rev.*, 2011, **40**, 4167–4185.
- 25 Z. Liu, P.-C. Chang, C.-C. Chang, E. Galaktionov, G. Bergmann and J. G. Lu, *Adv. Funct. Mater.*, 2008, **18**, 1573–1578.
- 26 L. Jia, G. P. Mane, C. Anand, D. S. Dhawale, Q. Ji, K. Ariga and A. Vinu, *Chem. Commun.*, 2012, **48**, 9029–9031.
- 27 A. J. Cooke and R. K. Rowe, *J. Environ. Eng.*, 1999, **125**, 126–136.
- 28 (a) O. Akdim, U. B. Demirci and P. Miele, *Int. J. Hydrogen Energy*, 2011, **36**, 13669–13675; (b) U. B. Demirci and P. Miele, *Phys. Chem. Chem. Phys.*, 2010, **12**, 14651–14665.

Annex-c-

A highly efficient gold/electrospun PAN fiber material for improved laccase biocathodes for biofuel cell applications†

Cite this: *J. Mater. Chem. A*, 2014, 2, 2794

D. Selloum,^{‡,ab} A. Abou Chaaya,^{‡,a} M. Bechelany,^a V. Rouessac,^a P. Miele^a and S. Tingry^{*a}

We explore for the first time the ability of a three-dimensional polyacrylonitrile/gold material prepared by a low-cost and scalable synthesis method, based on the combination of electrospinning and sputtering, as a new material with large surface area to provide high loadings of enzymes to enhance the electrochemical performances of enzyme electrodes in biofuel cells (BFCs). An ethanol/O₂ BFC has been developed based on enzymatic reactions performed at both the cathode and anode with immobilization of the respective enzymes and mediators on the three-dimensional nanostructured electrodes. The power density delivered is 1.6 mW cm⁻² at 0.75 V, which is five times the power density delivered by the BFC built on flat bioelectrodes. The greatly improved performance of these synthesized nanostructured electrodes makes them exciting materials for their implantation in biofuel cell applications.

Received 5th November 2013
Accepted 4th December 2013

DOI: 10.1039/c3ta14531j

www.rsc.org/MaterialsA

A Introduction

Biofuel cells (BFCs) have recently attracted considerable attention for the conversion of chemical energy to electricity through biological catalysts immobilized on electrodes.¹ There are two types of BFCs depending on the nature of the catalyst to perform redox reactions at the electrodes: enzymatic BFCs use enzymes^{1,2} and microbial BFCs use bacteria.^{3,4} These devices are built from the assembly of a bioanode, which oxidizes the fuel substrate, and with a biocathode which reduces the oxidizer. Enzymatic BFCs operate with fuels such as glucose, ethanol, methanol and oxidant as oxygen. An important aspect of the performance and stability of these devices is the density of electrochemically active enzymes on the electrode.⁵ In recent years, effort has been made to develop new materials for integrated enzyme electrodes that maximize enzyme loading and move from the classic two-dimensional loading to highly ordered three-dimensional structures with improved enzyme stabilization.⁶ Some new materials have been explored for electrodes in BFCs based on carbon materials such as single wall⁷ and multiwall⁸ carbon nanotubes, carbon nanofibers,⁹ and carbon fiber papers¹⁰ as well as on gold materials such as gold nanoparticles (NPs) loaded on

macroporous gold electrodes¹¹ or on carbon paper.¹² For instance, very promising results have been obtained for glucose biofuel cells with generated power densities of 1.3 mW cm⁻² at 0.6 V with compressed carbon nanotube matrices,¹³ or 1.39 mW cm⁻² at 0.77 V with electrodes based on Au nanowires electrochemically grown inside the pores of anodized aluminium oxide.¹⁴ A few ethanol biofuel cells have also been developed based on dehydrogenase enzymes immobilized on carbon fiber paper as commercial conductive materials.^{10,11,14,15,32} Alcohol fuels are oxidized to aldehydes in the presence of alcohol dehydrogenase and NAD⁺ as cofactor at the anode. At the cathode, oxygen is reduced in the presence of the enzymes laccase or bilirubin oxidase. For example, works on BFCs reported maximum power output of 1.56 mW cm⁻² at 0.55 mV¹⁵ and 0.39 mW cm⁻² at 0.51 mV¹⁰ with the cofactor NAD⁺ in solution.

In this work, contrary to reported ethanol BFCs based on commercial carbon fiber papers, we have explored the synthesis and the ability of a three-dimensional polyacrylonitrile material prepared by electrospinning combined with sputtering as a new nanostructured material. This material offers a large surface area to provide high loadings of enzymes to enhance the electrochemical performances of enzyme electrodes in BFCs. Electrospinning is a unique process that effectively produces a mat of small fibers with controllable compositions and sizes in a matter of minutes from a variety of polymer precursors.¹⁶ This fibrous structure affords an easy handling and a high specific surface area compared to fibers obtained by a conventional spinning method. Electrospun nanofiber mats are durable and easily separable and can also be processed in a highly porous form to relieve the mass-transfer limitation of the substrate through the mats.¹⁷ Because of these attractive features,

^aInstitut Européen des Membranes, UMR 5635, ENSCM-UMI-CNRS, Place Eugène Bataillon, 34095 Montpellier, France. E-mail: sophie.tingry@univ-montp2.fr; Tel: +33467149157

^bLaboratoire de Croissance et de Caractérisation de Nouveaux Semiconducteurs (LCCNS), Faculté de Technologie, Université Setif 1, Setif 19000, Algeria

† Electronic supplementary information (ESI) available. See DOI: 10.1039/c3ta14531j

‡ These authors contributed to this work equally.

electrospun nanofibers have generated much attention as supports for enzyme immobilization. To immobilize enzymes on electrospun nanofibers, many approaches have been used, including grafting enzymes on a fiber surface that possesses reactive groups, physical adsorption, and incorporation of enzymes into nanofibers *via* electrospinning followed by crosslinking reactions.^{17,18} This new approach of enzyme coatings on non-conductive nanofibers, yielding high activity and stability, presents potential applications in the fields of biocatalysts for polymer synthesis, biosensors and biocatalysis/separation.¹⁸ However, only a few studies describe the immobilization of redox enzymes, such as catalase^{19,20} and peroxidase,²¹ on poly(acrylonitrile-*co*-acrylic acid) nanofibrous membranes filled with carbon nanotubes to confer a conductivity to the membrane and to increase both the amount and the activity retention of the enzymes.

In this paper, we show that starting from a polymer solution, sub-micron fibers are synthesized using the electrospinning technique. With the aim of improving BFC electrical performances, we present a method for the preparation of a new material based on this electrospun PAN material modified by a thin film of gold obtained by sputtering in order to make these nanofibers conductive materials. Carbon nanoparticles mixed with the enzyme laccase are loaded on the macro-porous fiber mat and the resulting electrode is proposed for the first time as an effective O₂ reduction biocathode. Laccase is considered as an attractive biocatalyst to reduce molecular oxygen to water at very high redox potentials.^{22–25} The resulting Laccase/Au/PAN biocathode is then associated with an alcohol dehydrogenase/Au/PAN bioanode to construct an ethanol/O₂ biofuel cell with enhanced power output.

B Materials and methods

Materials

Polyacrylonitrile (PAN) ($M_w = 150\,000$) and dimethylformamide (ACS reagent, $\geq 99.8\%$) were purchased from Sigma Aldrich. p-Type (100) silicon wafer was obtained from MEMC Korea company. Laccase from *Trametes versicolor* (20 U mg⁻¹ solid), diaphorase (3–20 U mg⁻¹), alcohol dehydrogenase (300 U mg⁻¹), β -nicotinamide adenine dinucleotide sodium salt (NAD⁺), 2-methyl-1,4-naphthoquinone VK3, acetone, polyethyleneimine (PEI), 2,20-azobis(3-ethylbenzothiazoline-6-sulfonate) diammonium salt (ABTS), Nafion® solution (5 wt%), potassium hexacyanoferrate(III) (K₃(FeCN)₆), sodium phosphate dibasic dihydrate (Na₂HPO₄·2H₂O) and sodium phosphate monobasic monohydrate (NaH₂PO₄·H₂O) were purchased from Sigma-Aldrich and used without further purification. The phosphate buffer was prepared with Na₂HPO₄·2H₂O and NaH₂PO₄·H₂O (pH 5, pH 7 or pH 9, 0.1 M).

Carbon nanoparticle powder as Super-P (0.04 μ m grain size, specific surface area 62 m² g⁻¹) was purchased from TIMCAL.

Electrode design

Electrospinning solution was prepared by dissolving 10 wt% (weight ratio) of PAN in dimethylformamide. The solution was

maintained under agitation for 1 hour and then heated in an 80 °C oil bath for 10 min. The polymer solution was electrospun at room temperature in an ambient air atmosphere under an applied voltage of 25 kV with a flow rate of 3 mL h⁻¹ using a 0.7 mm diameter syringe connected to the positive output of the generator. An aluminum disk placed 25 cm from the tip of the syringe was related to the negative output of the generator. The electrostatic field applied between the syringe and the disk collector provides the transformation of the droplet to a Taylor cone. The droplet is then stretched under the electrostatic field to form a net submicron fiber after the evaporation of the solvent. The electrospinning machine is a home-made machine using an HPx 600 605 generator (physical instruments) and a KDS 100 syringe pump.

The schematic process for the design of the electrode is reported in the ESI (Fig. S1a†). Silicon wafer was cut into (10 × 20 mm²) pieces and was fixed on the aluminum disk using carbon glue. Electrospinning was performed for 5 min in order to cover the Si substrate with homogeneous nanofiber layers. After electrospinning, PAN nanofibers were fixed tightly on the Si substrate using carbon glue in order to ensure mechanical adhesion and electrical connection between PAN nanofibers and the support substrate (Fig. S1b, ESI†). Gold coating was performed using sputtering (Edwards Scancoat Six) in an argon plasma discharge. Operating conditions were: working pressure 10⁻¹ mbar, voltage 1.7 kV, substrate temperature close to 20 °C, and current 10 mA. The deposition time was adjusted to obtain the desired thickness of gold. After gold sputtering, an operating window was defined on the substrate using Kapton tape (Fig. S1b, ESI†).

Electrode characterization

The structural and chemical compositions of the Au/Si electrodes were analyzed by scanning electron microscopy (SEM, S-4800, Hitachi), energy-dispersive X-ray spectroscopy (SEM, S-4500, coupled with a Thermofisher EDX detector), X-Ray diffraction (PANalyticalXpert-PRO diffractometer equipped with an X'celerator detector using Ni-filtered Cu-radiation). The thicknesses of Au layers were measured on Si substrates using a Semilab GES5E spectroscopic ellipsometer (extended visible: 1.23–5 eV). The ellipsometric measurements were carried out at a fixed incident angle of 75°, close to Brewster's angle for the silicon substrate, and a variable wavelength between 300 nm and 1 μ m. Then the experimental tan (ψ) and cos (δ) data were fitted using Winelli II software using a single homogeneous layer Au adjusted model to obtain the film thicknesses with a goodness of fit over 0.999 in the full wavelength range.

The measurements of electrical conductivity were performed by the two point contacts method in which 2 contact pads were connected on the testing sample surface. A constant current was applied through the outer current probes using an EG&G Instrument (Princeton Applied Research). The voltage drop across the two inner voltage probes was measured. The electrical resistivity R was calculated from the slope of the I - V curve then the conductivity $G = 1/R$ was extracted.

Electrochemical measurements were performed on a potentiostat Autolab (Eco chemie, Netherlands) at 25 °C in

phosphate buffer, with a conventional three-electrodes system composed of a stainless steel auxiliary electrode, a calomel saturated reference electrode and the electrode material as the working electrode. Cyclic voltammograms were measured in $\text{K}_3(\text{FeCN})_6$ (10 mM) at pH 7 with a scan rate of 10 mV s^{-1} . Polarization curves were determined in dioxygen-saturated phosphate buffer at pH 5 after stabilization of the biocathode open circuit potential. For the electrochemical characterization of the biofuel cell, the biocathode was set as the working electrode while the bioanode was plugged as the counter-reference electrode. The two bioelectrodes were separated by a Nafion® 117 perfluorinated membrane. The cathode compartment of the cell contained 40 mL phosphate buffer solution 0.1 M, pH 5 saturated with O_2 . The anode compartment of the cell contained 40 mL phosphate buffer 0.1 M solution pH 9 with 160 μL ethanol. The equilibration time was maintained for 5 min before data collection to reach the maximum open circuit potential.

Bioelectrode preparation

The biocathode to be employed in the electroreduction of oxygen was prepared by adsorption of enzymes and mediators on the surface of the electrodes by drop casting. 333 μL of lactase (15 mg mL^{-1}) and Super-P (15 mg mL^{-1}) in phosphate buffer 0.1 M (pH 5) solution were mixed on a vortex mixer. Sequentially, 100 μL of the solution was mixed with 90 μL ABTS (5.4 mg mL^{-1}) and 10 μL Nafion. 10 μL of the resultant solution was coated onto the defined area of the Si/PAN/Au electrode (geometrical surface = 0.15 cm^2) and the electrode was dried at room temperature and kept in a low humidity environment. The enzyme loading was estimated to be $75 \mu\text{g cm}^{-2}$.

The bioanode to be employed in the oxidation of ethanol was prepared by adsorption of successive coatings separated by a drying step at room temperature. 167 μL of ADH (30 mg mL^{-1}) and Super-P (15 mg mL^{-1}) in phosphate buffer 0.1 M (pH 7) solution were mixed on a vortex mixer and 10 μL of the obtained solution was pipetted onto the electrode and dried at room temperature. The same procedure was conducted for the immobilization of NAD^+ (30 mg mL^{-1}) and then diaphorase (20 mg mL^{-1}). The last coating on the electrode consisted of pipetting 10 μL of VK3 (60 mg mL^{-1}), 190 μL acetone and 10 μL PEI, followed by drying.

C Results and discussion

Characterization of the PAN/gold electrospun nanofibers

Fig. 1(a) shows the SEM images of electrospun nanofibers (NFs) on Si substrates after gold deposition. These images indicate a conformal diameter ($\sim 200 \text{ nm}$) of the nanofibers obtained by this method. The PAN/Au NFs develop a rough surface with Au nanoparticle diameters less than 20 nm as attested by HRSEM images (Fig. 1a). In our case, thin layers of Au were deposited by PVD (physical vapour deposition) through the PAN nanofiber mat. We choose to use the sputtering (which provides a high mobility of Au atoms) instead of thermal or electron beam evaporation (which provides a line of sight vapor stream). In

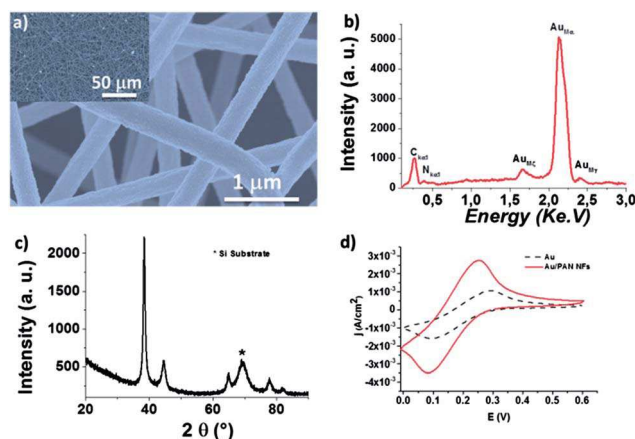


Fig. 1 (a) SEM images at different magnifications of PAN/Au NFs obtained by electrospinning for 240 s followed by sputtering for 600 s; (b and c) EDX spectra and XRD pattern of the resulting PAN/Au NFs, and (d) cyclic voltammetry of 10 mM $\text{K}_3\text{Fe}(\text{CN})_6$ at Au electrodes and PAN/Au electrodes in phosphate buffer pH 7; the scan rate is 20 mV s^{-1} .

fact, the high mobility of the Au atoms as well as the high porosity of the mat during the sputtering process will enable the Au to cover the entire nanofiber mat except where the PAN nanofibers contacted each other resulting on a mat of conductive PAN/Au materials.^{26,27} Due to the shadowing effect related to our deposition technique, the gold coating will not cover a single PAN nanofiber by a homogeneous way from both sides. However as shown in the SEM image (Fig. S2,† ESI cross-section), the gold will cover all the PAN NFs and will reach the Si electrode surface ensuring a good electrical contact between the NFs and the substrate.

EDX measurement (Fig. 1b) was performed on the sample in order to evaluate the chemical composition. The presence of Au, C and N can be observed. XRD (Fig. 1c) shows peaks at $2\theta = 38.18, 44.39, 64.6, 77.6$ and 81.7° corresponding to (111), (200), (220), (311) and (222) of the centered cubic phase of gold, as generally observed with the gold materials deposited by sputtering.²⁶ The crystallite size calculated using the Scherrer formula is $\sim 14 \text{ nm}$, which matched well with the SEM observations. The benefit of PAN was illustrated by cyclic voltammetry with the evolution of i_p as the peak current and ΔE_p as the separation between the oxidation and reduction peak potentials. As shown in Fig. 1d, the presence of PAN notably improves both the anodic peak current by 2.5 times and the reversibility of $\text{Fe}(\text{CN})_6^{3-}/\text{Fe}(\text{CN})_6^{4-}$ as ΔE decreases from 200 to 170 mV, suggesting that the effective electroactive area and the electronic conductivity are increased, which is due to the 3D nanostructure of the electrospun PAN fibers.

Influence of deposition parameters

The results of the ellipsometric measurements of Au thin film thicknesses deposited by sputtering on a flat Si substrate are reported in Table 1. Gold film thicknesses of 70, 142, 213 and 284 nm were obtained respectively for 300, 600, 900 and 1200 seconds of sputtering that corresponds to an average growth rate of 14.2 nm min^{-1} .

Table 1 Grain size, electronic conductivity ΔE and anodic current density i_p as a function of the Au film thickness

Sputtering time (s)	Thickness (nm)	Grain size LC (Å)	ΔE (mV)	i_{pox} (mA cm ⁻²)
300	70	98.1	220	2.20
600	142	140.89	170	2.75
900	213	147.5	200	2.60
1200	284	156.88	170	1.63

XRD diffraction patterns of Au/PAN/Si electrodes with different thicknesses of gold layers are shown in Fig. 2e. It was found that the thinnest samples (Au thickness of 70 nm)

showed weak X-ray diffraction peaks at $2\theta = 38.18$ and 44.39 that can result from low (<10 nm) grain size dimensions. The increase of thickness led to the appearance of stronger XRD peaks. For thicker samples (213 and 284 nm), strong peaks have been observed. The growth of Au layers is assisted by the grain size growth (Table 1) as attested by the SEM images (Fig. 2a–d).

The optimized Au film thickness was fixed from the electronic conduction and the electroactive area of the material determined from the cyclic voltammogram of the redox probe $\text{Fe}(\text{CN})_6^{3-}$ in solution. The values of ΔE_p (Table 1) show that the materials with gold thicknesses 142 and 284 nm show the best electronic conductivity. However, the intensity of the oxidation peak current is unusually low for the thicker material, suggesting a poor electroactive area for the species attributed to the presence of cracks as attested by SEM images (Fig. S3, ESI†) resulting from the stress of the gold deposited on PAN nanofibers. The Au film of 142 nm was thus selected to prepare the effective O_2 reduction biocathode based on electrospun PAN/Au NFs.

The dependence of the increase of the PAN quantity on the electrode characteristics was evaluated. Table 2 shows the conductivity of PAN/Au nanofibers as a function of the PAN quantity (different electrospinning times) for the same Au thickness. For the films between 30 and 240 s electrospinning times, the conductivity decreases slightly. A dramatic decrease is observed for the 600 s electrospinning PAN time, which could be attributed to the decrease of the thickness of gold on individual PAN nanofibers resulting from the higher surface area of the resulting PAN electrode. This induces and results in a decrease of conductivity as shown in the previous section. The influence of the PAN quantity was confirmed by cyclic voltammetry with the redox probe $\text{Fe}(\text{CN})_6^{3-}$ in solution (not shown here). The PAN quantity of 240 s electrospinning time was thus chosen for the electrodes that correspond to a good compromise between the electrical conductivity and the active surface area.

Application of PAN/Au NFs as bioelectrodes in BFCs

Bioelectrodes modified by enzymes are the key for the performance of BFCs. Since the power output can be enhanced by using electrode materials with high surface area, the electrospun PAN/Au NFs were thus used as a support for enzyme immobilization in order to prepare bioelectrodes for oxygen reduction reaction. The combination of laccase and ABTS, used to facilitate the electron transfer by diffusion from the active site of the enzymes to the electrode, has been reported showing a number of attractive features for oxygen reducing fuel cell

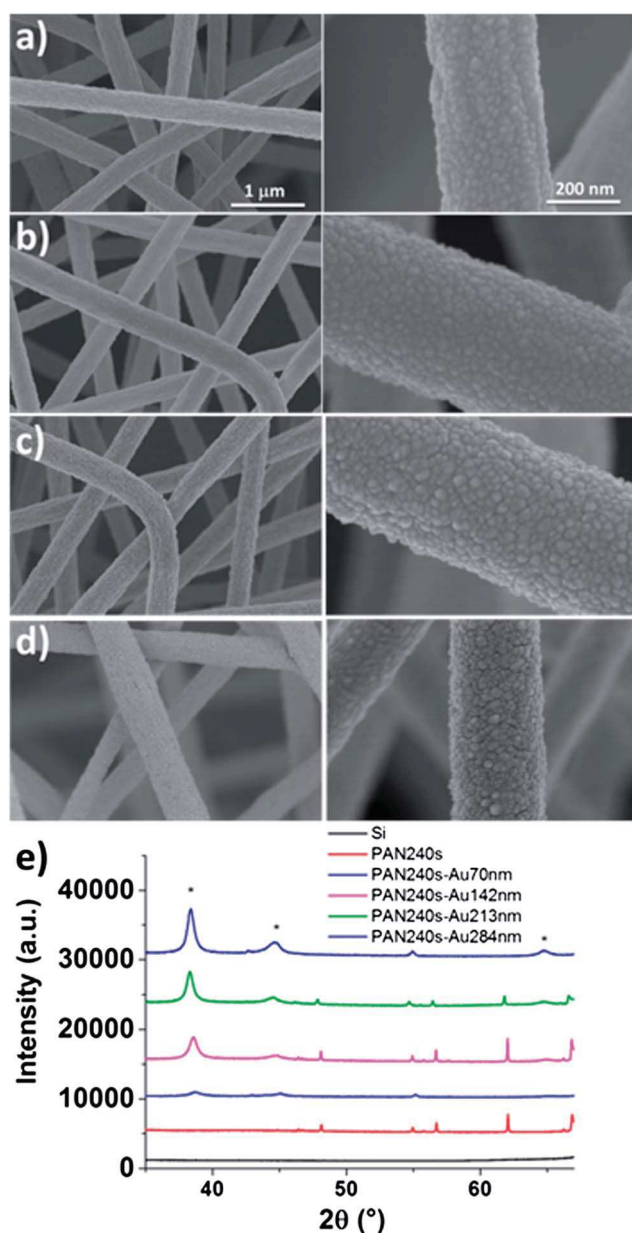


Fig. 2 SEM images at different magnifications of PAN/Au NFs obtained by electrospinning for 240 s followed by sputtering of 70 (a), 142 (b), 213 (c) and 284 nm (d) of gold. (e) XRD patterns of the obtained Au/PAN/Si electrodes.

Table 2 Electrical conductivity of PAN/Au NFs as a function of PAN electrospinning time for an Au film thickness of 142 nm

PAN electrospinning time (s)	G (ohm ⁻¹)
30	0.08
60	0.07
120	0.03
240	0.015
600	4.5×10^{-4}

cathodes, like a direct 4-electrons reduction mechanism, reducing O_2 completely to H_2O .²⁸ The pathway for electron transfer between the PAN/Au NF biocathode and O_2 is illustrated in Fig. 3a. Electrons are transferred from the cathode to reduce $ABTS_{ox}$. Next, four equivalents of $ABTS_{red}$ are transferred to the four active $Cu(II)$ ions of laccase that acquires the necessary electrons to reduce dioxygen to water.^{29,30} The PAN/Au NFs were covered on the surface by a mixture of laccase, and ABTS entrapped in the Nafion® polymer. The enzyme was previously mixed with carbon black nanomaterials as efficient hosts for enzymes, providing an electrical connection between the enzymes and the electrode and providing an additional surface area for adsorption of active laccase.^{6,17}

The electrochemical response of the constructed biocathode (based on the geometric surface area) in phosphate buffer solution pH 5 under O_2 is shown in Fig. 3b and compared to the control biocathode prepared by the same immobilization technique on a thin film of gold in the absence of PAN NFs. No current response towards O_2 was observed at electrodes in the absence of laccase (data not shown). From the polarization curves, the oxygen reduction current begins at 0.59 V vs. ECS, without overpotential, and the current densities feature a semi-plateau that indicates the control of the electrocatalytic reaction by diffusion of the oxygen to the electrode surface. The electrospun PAN fiber biocathode shows the highest performance increase (3 mA cm^{-2}) by 3-fold compared to the control. This result can be attributed to the porous structure of the PAN that affords a close contact between the electrode material and the enzymes, and relieves the mass-transfer limitation of the species through the mat. This result shows the high benefit and the future applications of electrospun fibers to increase the performances of enzyme electrodes. In addition, the stability of

the biocathode was also investigated (Fig. 3c) from the evolution of the polarization curve on the same day and after keeping the electrode in a humid atmosphere at 5°C for 3 and 6 days. Successive scans lead to a loss of 17% of the initial electrochemical activity. This loss increases to 36% and 42% after 3 and 6 days, respectively, associated with a lower open-circuit voltage value $V_{oc} = 0.55 \text{ V}$. This phenomenon is mainly attributed to ABTS leaching from the matrix.¹⁴ The direct wiring of laccase on gold/PAN fibers without any addition of ABTS was evaluated but the biocathode activity towards O_2 reduction showed very low current densities (Fig. S4, ESI†).

In order to have a clear idea on the effect of electrospun PAN/Au NFs on the performance of a biofuel cell, the present biocathode was evaluated with respect to a bioanode prepared in a similar manner based on alcohol dehydrogenase (ADH), and the complete BFC was evaluated towards ethanol fuel. Ethanol is oxidized to aldehyde in the presence of ADH and its cofactor NAD^+ . The regeneration of the cofactor is well achieved using an additional redox protein diaphorase which operates efficiently in the presence of the mediator VK_3 .³¹ In this work, the immobilization technique afforded the entrapment of all the reactive species at the electrode surface. The electrochemical behavior of the PAN NF bioanode (based on the geometric surface area) has been studied in phosphate buffer solution pH 9 (Fig. S5, ESI†) and compared to the control bioanode made on a thin film of gold. The bioanode exhibits activity for ethanol oxidation with a V_{oc} of around -0.3 V vs. ECS and a current density of 3.4 mA cm^{-2} . However, the evolution of the polarization curves with time and after keeping the electrode in a humid atmosphere at 5°C for 10 days shows a stable V_{oc} but a pronounced loss of current densities mainly due to the loss of NAD^+ (as adding NAD^+ in solution leads to 85% of the initial electrochemical activity).

The complete BFC was tested in the presence of a membrane to separate the two bioelectrodes and operated with only ethanol in the anode compartment and dissolved oxygen in the cathode compartment. Fig. 4 shows the cell voltage and the resulting power density of the ethanol/ O_2 BFC versus the current density. In the absence of electrospun PAN NFs on the gold electrode, the V_{oc} of the cell is 0.90 V and the polarization curve shows a potential drop corresponding to activation losses which

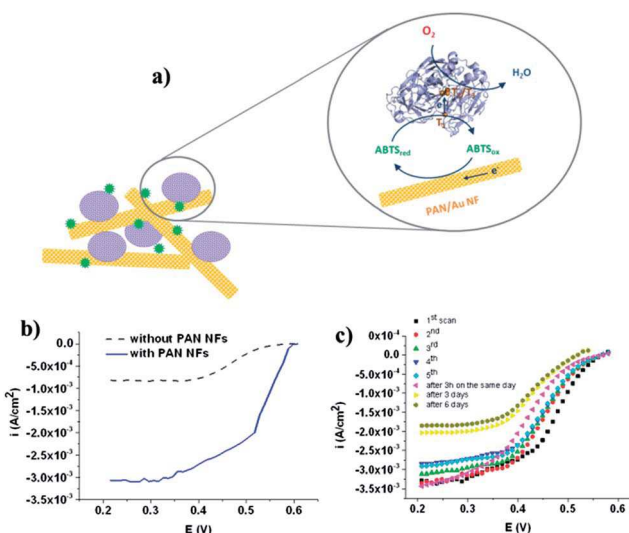


Fig. 3 (a) Schematic pathway for electron transfer between the PAN/Au NFs and O_2 . (b) Polarization curves of a biocathode with and without PAN NFs in O_2 -saturated phosphate solution (pH 5, 0.1 M). Scan rate 3.3 mV s^{-1} . (c) Stability of the PAN/Au NFs bioelectrode evaluated from polarization curves plotted the 1st day after repeated scans, after 3 h, and the 3rd and 6th days.

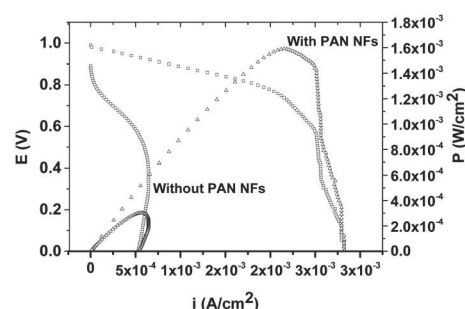


Fig. 4 Typical cell voltage (\square) and resulting power density (Δ) versus current density of the constructed laccase biocathodes with respect to ADH bioanodes, built with and without PAN/Au NFs in compartmented BFC. Scan rate 3.3 mV s^{-1} .

are the consequence of sluggish electrode kinetics. As expected, the BFC based on electrospun PAN/Au NFs presents a higher V_{oc} (0.99 V) but especially a region of ohmic polarization significantly extended from 1 to 0.7 V, followed by clear mass transport limitation of ethanol and O_2 through the films identified at current densities around 2.2 mA cm^{-2} . The maximum power density delivered is 1.6 mW cm^{-2} at 0.75 V, which is five times the power density delivered by the BFC built from bioelectrodes without PAN/Au NFs. The higher current densities measured for the nanofibers-modified electrodes are attributed to the porous structure of the PAN/Au that contributes to high enzyme loadings and to efficient mass-transfer of the species through the mat. The steady-state behavior of the BFC was also evaluated from the power curve obtained at constant load discharges (Fig. S6, ESI†). In that case, the BFC efficiency is lower due to the equilibrium time to reach the steady state that contributes to the instability of the bioanode.

The ethanol/ O_2 BFC, developed in this work, works from enzymatic reactions performed at both the cathode and anode with immobilization of the respective enzymes on three-dimensional nanostructured electrodes synthesized by our group. Although comparison with the literature is not straightforward, this ethanol/ O_2 BFC presents high and competitive efficiency with reported ethanol/ O_2 BFCs based on the modification of commercial conductive materials as carbon fiber paper.^{10,11,32,33}

Conclusions

In summary, the introduction of electrospun PAN NFs/Au to construct bioelectrodes provides a high surface area for enzyme immobilization and a better conductivity that result in reduced ohmic losses under polarization conditions. A significantly improved performance in the BFCs has been observed. We can conclude that the increase of the specific surface area of the electrode, which is provided by the network of the PAN NFs, is an efficient approach to improve the power density of the BFCs. However, the immobilization procedure was not sufficiently efficient to prevent the leaching of the redox mediators NAD^+ and ABTS that contributes to a low stability of the BFCs with time.

The possibility of tuning the surface area, the conductivity, and the chemical composition should allow the applications of these nanostructured electrodes in other fields such as sensors, hydrogen production,³⁴ and photocatalytic and photovoltaic applications.³⁵

Acknowledgements

Financial support by the European Commission in the framework of an AVerroes grant is gratefully acknowledged. DS and AA contributed to this work equally.

Notes and references

- 1 I. Ivanov, T. Vidakovic-Koch and K. Sundmacher, *Energies*, 2010, **3**, 803–846.

- 2 E. Hao Yu and K. Scott, *Energies*, 2010, **3**, 23–42.
- 3 B. E. Logan, B. Hamelers, R. Rozendal, U. Schröder, J. Keller, S. Freguia, P. Aelterman, W. Verstraete and K. Rabaey, *Environ. Sci. Technol.*, 2006, **40**, 5181–5192.
- 4 Z. Du, H. Li and T. Gu, *Biotechnol. Adv.*, 2007, **25**, 464–482.
- 5 M. H. Osman, A. A. Shah and F. C. Walsh, *Biosens. Bioelectron.*, 2011, **26**, 3087–3102.
- 6 S. D. Minter, P. Atanassov, H. R. Luckarift and G. R. Johnson, *Mater. Today*, 2012, **15**, 166–173.
- 7 J. Y. Lee, H. Y. Shin, S. W. Kang, C. Park and S. W. Kim, *J. Power Sources*, 2010, **195**, 750–755.
- 8 D. Ivnitski, B. Branch, P. Atanassov and C. Apblett, *Electrochem. Commun.*, 2006, **8**, 1204–1210.
- 9 A.-F. Che, V. Germain, M. Cretin, D. Cornu, C. Innocent and S. Tingry, *New J. Chem.*, 2011, **35**, 2848–2853.
- 10 S. Topcagic and S. D. Minter, *Electrochim. Acta*, 2006, **51**, 2168–2172.
- 11 L. Deng, F. Wang, H. Chen, L. Shang, L. Wang, T. Wang and S. Dong, *Biosens. Bioelectron.*, 2008, **24**, 329–333.
- 12 K. Murata, K. Kajiya, N. Nakamura and H. Ohno, *Energy Environ. Sci.*, 2009, **2**, 1280–1285.
- 13 A. Zebda, C. Gondran, A. Le Goff, M. Holzinger, P. Cinquin and S. Cosnier, *Nat. Commun.*, 2011, **2**, 370.
- 14 J. Kim and K.-H. Yoo, *Phys. Chem. Chem. Phys.*, 2013, **15**, 3510–3517.
- 15 L. Deng, L. Shang, D. Wen, J. Zhai and S. Dong, *Biosens. Bioelectron.*, 2010, **26**, 70–73.
- 16 A. Greiner and J. H. Wendorff, *Angew. Chem., Int. Ed.*, 2007, **46**, 5670–5703.
- 17 J. Kim, H. Jia and P. Wang, *Biotechnol. Adv.*, 2006, **24**, 296–308.
- 18 Z.-G. Wang, L.-S. Wan, Z.-M. Liu, X.-J. Huang and Z.-K. Xu, *J. Mol. Catal. B: Enzym.*, 2009, **56**, 189–195.
- 19 Z.-G. Wang, Z.-K. Xu, L.-S. Wan, J. Wu, C. Innocent and P. Seta, *Macromol. Rapid Commun.*, 2006, **27**, 516–521.
- 20 L.-S. Wan, B.-B. Ke and Z.-K. Xu, *Enzyme Microb. Technol.*, 2008, **42**, 332–339.
- 21 Z.-G. Wang, B.-B. Ke and Z.-K. Xu, *Biotechnol. Bioeng.*, 2007, **97**, 708–720.
- 22 C. Lau, E. R. Adkins, R. P. Ramasamy, H. R. Luckarift, G. R. Johnson and P. Atanassov, *Adv. Energy Mater.*, 2012, **2**, 162–168.
- 23 W. Nogala, A. Celebanska, G. Wittstock and M. Opallo, *Fuel Cells*, 2010, **10**, 1157–1163.
- 24 M. Smolander, H. Boer, M. Valkiainen, R. Roozeman, M. Bergelin, J.-E. Eriksson, X.-C. Zhang, A. Koivula and L. Viikari, *Enzyme Microb. Technol.*, 2008, **43**, 93–102.
- 25 K. Szot, W. Nogala, J. Niedziolka-Jönsson, M. Jönsson-Niedziolka, F. Marken, J. Rogalski, C. N. Kirchner, G. Wittstock and M. Opallo, *Electrochim. Acta*, 2009, **54**, 4620–4625.
- 26 M. Bechelany, X. Maeder, J. Riesterer, J. Hankache, D. Lerose, S. Christiansen, J. Michler and L. Philippe, *Cryst. Growth Des.*, 2010, **10**, 587–596.
- 27 X. Wang, C. J. Summers and Z. L. Wang, *Nano Lett.*, 2004, **4**, 423–426.

- 28 V. Soukharev, N. Mano and A. Heller, *J. Am. Chem. Soc.*, 2004, **126**, 8368–8369.
- 29 E. I. Solomon, U. M. Sundaram and T. E. Machonkin, *Chem. Rev.*, 1996, **96**, 2563–2605.
- 30 S. Shleev, J. Tkac, A. Christenson, T. Ruzgas, A. I. Yaropolov, J. W. Whittaker and L. Gorton, *Biosens. Bioelectron.*, 2005, **20**, 2517–2554.
- 31 M. Togo, A. Takamura, T. Asai, H. Kaji and M. Nishizawa, *Electrochim. Acta*, 2007, **52**, 4669–4674.
- 32 N. L. Akers, C. M. Moore and S. D. Minteer, *Electrochim. Acta*, 2005, **50**, 2521–2525.
- 33 S. Aquino Neto, J. C. Forti, V. Zucolotto, P. Cincaglini and A. R. de Andrade, *Biosens. Bioelectron.*, 2011, **26**, 2922–2926.
- 34 M. Bechelany, A. Abou Chaaya, F. Frances, O. Akdim, D. Cot, U. B. Demirci and P. Miele, *J. Mater. Chem. A*, 2013, **1**, 2133–2138.
- 35 J. Elias, M. Bechelany, I. Utke, R. Erni, D. Hosseini, J. Michler and L. Philippe, *Nano Energy*, 2012, **1**, 696–705.